The development of a transcatheter mitral valve

A thesis submitted for the degree of doctor of philosophy

Georgia Lucia Preston-Maher

7/20/2017

Disclaimer

I, Georgia Lucia Preston-Maher confirm that the work presented in this thesis is my own. Where information has been derived from other sources, I confirm that this has been indicated in the thesis.

Signed GEORGIA LUCIA PRESTON-MAHER

Abstract [1]

Transcatheter heart valve replacements avoid the main risks associated with conventional open heart surgery and so is the preferred replacement technique for high-risk patients with aortic stenosis. Due to technical challenges, adaptation for the mitral position is still in early stages of research.

The aim of this project was to develop the novel UCL transcatheter mitral valve (TMV) based on a prior conceptual design. The UCL TMV is designed to treat mitral regurgitation (MR) and is based on the UCL transcatheter aortic valve (TAV) which is retrievable, repositionable and has enhanced anchoring and sealing.

The UCL TMV leaflets, which ensure unidirectional blood flow, are novel because they mimic native mitral valve morphology by having two leaflets, being D-shaped and conical. Their optimal design criterion and two key design parameters were identified using a failure mode and effects analysis and numerical simulations were used to select a design with acceptable stress levels and maximum coaptation area. The optimal leaflets were prototyped as a surgical valve to evaluate their performance against available commercial device designs and were then incorporated in TMV prototypes, and assessed for hydrodynamic performance, both of which exceeded international standard requirements. Durability assessment of the TMV is ongoing and very encouraging; currently withstanding > 80 million cardiac cycles.

In conclusion, the results presented and ongoing durability assessments for the UCL TMV indicate it could be a new and effective treatment option for severe MR in high-risk patients whom are declined surgical interventions.

[1] Abstract word count: 243 words.

Acknowledgements

I would sincerely like to thank my supervisors Gaetano Burriesci and Ryo Torii for their support, guidance and educative discussions as well as my transfer examiners Rebecca Shipley and Ben Hanson and the following people:

University College London, Mechanical Engineering Department: all staff especially; Cardiovascular Engineering Laboratory: Selim Bozkurt (Lab Coordinator), Benyamin Rahmani (Lab Coordinator), Rashmi Raju (Research Student), Jake Salmon (Research Student), Wenbo Zhou (Research Student), Spyros Tzamtzis (Lab Coordinator 2009-2014), department collaborators: Andrea Ducci (Lecturer) and previous group members Kevin Lau (Research Student), Lia Volpatti (Research Student – UCL & Politecnico Di Milano), Analisa Dimasi (Research Student – UCL & Politecnico Di Milano), Talayeh Shams (Research Student), Xin Wang (Research Student).

The Bartlett School of Architecture: Martin Watmough (Director).

Department of Medical Physics and Bioengineering: Eve Hatten (Teaching Laboratory Technician).

The Heart Hospital: Chris McGregor (Professor and Chair of Cardiothoracic Surgery/Director of Surgery), Mike Mullen (Consultant Cardiologist), Antonis Pantazis (Imaging Consultant Cardiologist), Silvia Schievano (Senior Lecturer), Giorgia Bosi (Research Student), Claudio Capelli (Research Associate), Giovanni Biglino (Research Associate), Mun Hong Cheang (Cardiologist), John Yap (Consultant Cardiac Surgeon), Andrew Cook (Senior Lecturer), Nicola Delahunty (Percutaneous Valve CNS), Markus Reinthaler (Cardiac Surgeon).

External collaborators: Morten Jensen (Associate Professor of Biomedical Engineering, Department of Clinical Medicine, Aarhus University, Denmark).

Institute of Making: Richard Gamester (Technician), Zachary Eastwood-Bloom (Technician), George Walker (Makespace Assistant).

Nimrodental: Nimrod Tal (Director), Hugo Patrao (R&D Manager), Laura Macho (Technician).

Lithotech Group: Valery Diamant (CTO & R&D Manager).

MSC. Software: Douglas Marriot (Technical Consultant).

I would also like to thank the UCL alumni for my studentship and the British Heart Foundation and Lithotech Group Inc. for financing the project.

List of Figures

List of Tables

Thesis Aim

There are approximately eight million people worldwide with symptomatic mitral regurgitation (Lloyd-Jones et al 2010, Nkomo et al 2006, Lung et al 2003) and due to the prevalence increasing with age and the presence of an aging population the number of cases is expected to rise significantly in the future. Up to 50% of patients with severe mitral regurgitation, whom would advisably have a replacement, are currently declined surgery because they are judged too ill or weak to withstand the stress of the open heart procedure required (Taramasso et al 2010, Mirabel et al 2007, Lung et al 2003) (3).

Transcatheter aortic valves (TAV) have provided a treatment option for similar patients with aortic valve disease; however these devices are not suitable for the mitral position. The UCL TAV was developed for the treatment of calcified aortic valves and improves on the first generation of commercially available devices by being retrievable, repositionable and has enhanced anchoring and sealing. Following successful animals trials of the UCL TAV, it was adapted for the mitral position, to have two-leaflets and be D-shaped (Chapter 2).

The aim of this project was to develop a proof of concept prototype of the UCL transcatheter mitral valve (TMV) by completing an initial design cycle consisting of design (Chapter 3 and 4), prototyping and testing (Chapter 6 and 7).

Dissemination

Journal Publications

1. Bozkurt S, Preston-Maher GL, Torii R and Burriesci G. **Design, analysis and testing of a novel mitral valve for transcatheter implantation.** Annals of Biomedical Engineering. Mar 2017. URL: http://dx.doi.org/10.1007/s10439-017-1828-2.
2. Sturla F, Ronzoni M, Vitali M, Dimasi A, Vismara R, Preston-Maher G, Burriesci G, Votta E and Redaelli A. **Impact of different aortic valve calcification patterns on the outcome of transcatheter aortic valve implantation: a finite element study**. Journal of Biomechanics. 49(12):2520-2530, Aug 2016. URL: http://dx.doi.org/10.1016/j.jbiomech.2016.03.036.
3. Preston-Maher GL, Torii R and Burriesci G. **A technical review of minimally invasive mitral valve replacements**. Cardiovascular Engineering and Technology. 6(2):174-184. Jun 2015. URL: http://dx.doi.org/10.1007/s13239-014-0203-9.

Conferences

1. Preston-Maher G, Bozkurt S, Rahmani B, Torii R, Mullen M and Burriesci G. **Development and hydrodynamic assessment of a novel transcatheter mitral valve.** European Society for Vascular Surgery Spring Meeting, London, UK, 13 May 2016 – 14 May 2016. 14 May 2016.
2. Bozkurt S, Preston-Maher G, Torii R and Burriesci G. **A novel mitral valve for transcatheter implantation.** European Society of Biomechanics Conference, Lyon, France, 10 Jul 2016 – 13 Jul 2016. 10 Jul 2016.
3. Bozkurt S, Preston-Maher GL, Rahmani B, Torii R, Burriesci G. **Design, Analysis and Hydrodynamic Assessment of a Novel Transcatheter Mitral Valve**. 28th Conference of the International Society for Medical Innovation and Technology, Delft, Netherland, 5-8 Oct 2016. 7 Oct 2016.

Chapter 1 Background

The transcatheter mitral valve developed in this project is designed to treat severe mitral regurgitation in high-risk patients. Therefore, the aim of this chapter is to explain the anatomy and function of healthy mitral valves, define mitral regurgitation in terms of its statistical significance and pathology, and introduces the current surgical and minimally invasive treatment options as well as the emerging UCL solutions.

1.1 Mitral valve

This section describes the mitral valve anatomy and kinetics associated with the annulus, leaflets, chordae tendineae and papillary muscles and describes the associated left ventricle (LV) dynamics.

1.1.1 Anatomy

The mitral valve is located in the left side of the heart. It regulates the flow of oxygenated blood from the left atrium (LA) into the LV (Figure 1.1), which pumps the blood through the aortic valve and around the circulatory system.

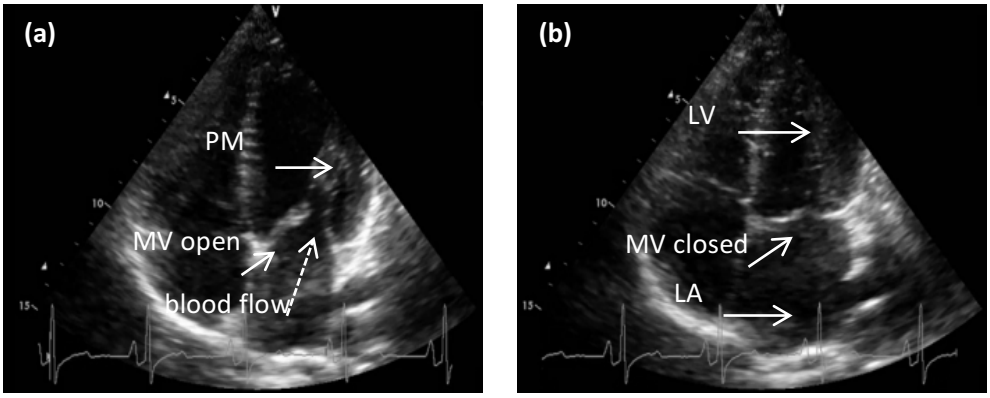

Figure 1.1: 2D echocardiogram of a healthy mitral valve **(a)** direction of blood flow through open mitral valve (MV), papillary muscles (PM) **(b)** left atrium (LA), closed mitral valve (MV), left ventricle (LV) (acknowledgements: Gibbons R, Brunel University London).

1.1.1.1 Annulus

The mitral valve is essentially part of the LV and is often described as having an annulus. In fact it is a saddle D-shaped orifice called the left atrioventricular junction, formed between the walls of the LV and the supporting LV structures (Van Mieghem et al 2010), that supports the thin tissue leaflets.

1.1.1.2 Leaflets

The vascularized leaflets are made from fibrous tissue (collagen type I, III and V), smooth muscle cells and nonmylinated nerve fibres. The conical leaflet structure is formed of an aortic leaflet, which is in fibrous continuity with two of the aortic valve leaflets, and is divided into three regions; A1 (lateral), A2 (middle) and A3 (medial), connected via the anterolateral and posteromedial commissures to the opposing mural leaflet similarly divided into three regions P1, P2 and P3 and has two scallops (indentations) (Figure 1.2). The aortic leaflet is relatively longer and covers one-third of the atrioventricular junction, compared to the shorter and less extensible mural leaflet which covers the remaining two thirds. The leaflets are described by three regions; the base (closest to the annulus), belly (central region) and the free edge (distal to the annulus), the latter being the most extensible. The leaflets are further described by two zones; clear and rough. The clear zone occurs between the annulus and line of coaptation, which have minimal chordae attachment, are thin with regular texture and translucent. The rough zones have numerous chordal insertions, with a higher density in the mural leaflet, and therefore are thicker, irregular and textured.

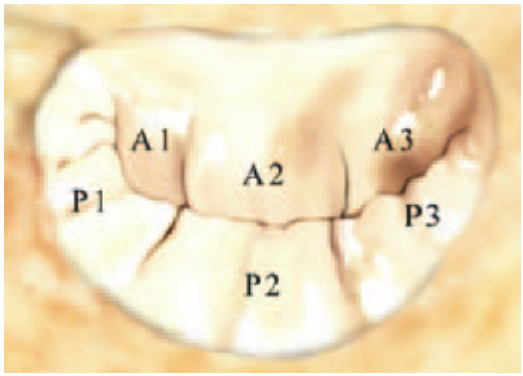

Figure 1.2: Mitral valve leaflet regions: **(posterior leaflet)** lateral (P1), middle (P2) and medial (P3) **(anterior leaflet)** similarly A1, A2 and A3 (Fedak et al 2008).

1.1.1.3 Chordae tendineae

The fibrous tendinous cords extend down from the rough zones connecting the edges of the leaflets to the LV wall by gathering them into two papillary muscles; posteromedial and anterolateral, anchoring them in the cardiac muscle (Figure 1.3).

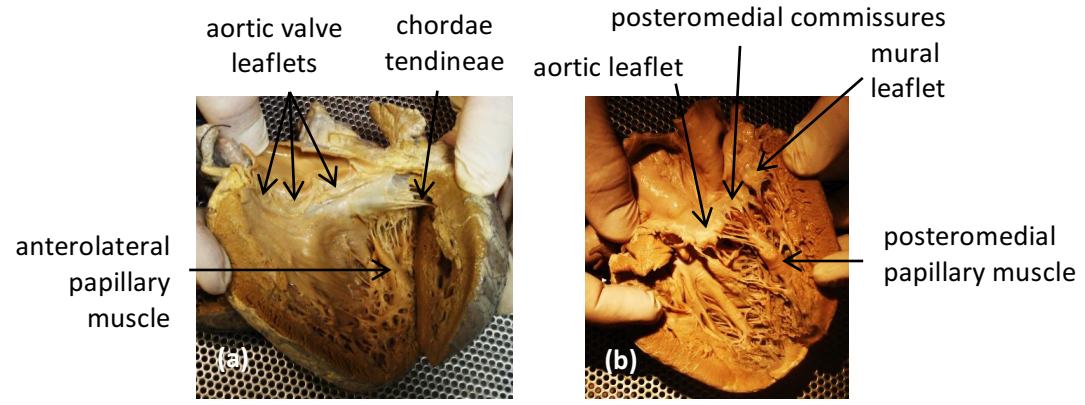

Figure 1.3: Morphology of the left heart **(a)** dissected left ventricle with intact mitral valve **(b)** dissected left ventricle and mitral valve (acknowledgements: Cook A, UCL).

1.1.2 Dynamic behaviour of mitral valve components

The mitral valve opens and closes throughout the cardiac cycle. During diastole, when the atrial pressure is greater than in the ventricle, the mitral valve opens, a jet is formed and the valve reaches its maximum open position (Figure 1.4.a). Vortices begin to form once peak flow has been achieved (Figure 1.4.b), the mitral flow then diminishes and the leaflets gradually start to close under the action of vortices and/or an adverse pressure gradient, the mitral jet becomes slower and narrower (Figure 1.4.c). Atrial contraction then causes acceleration of flow reopening the mitral valve, but without convective vortex generation (Figure 1.4.d). The ventricle begins to contract reversing the atrio-ventricular pressure gradient causing the valve to close (Figure 1.4.e). Once the mitral valve is fully closed isovolumic contraction occurs rising the ventricular pressure above the aorta pressure opening the aortic valve (Figure 1.4.f).

Below are detailed descriptions of the mitral valve components, including the mitral annulus, leaflets, chordae tendineae and papillary muscles.

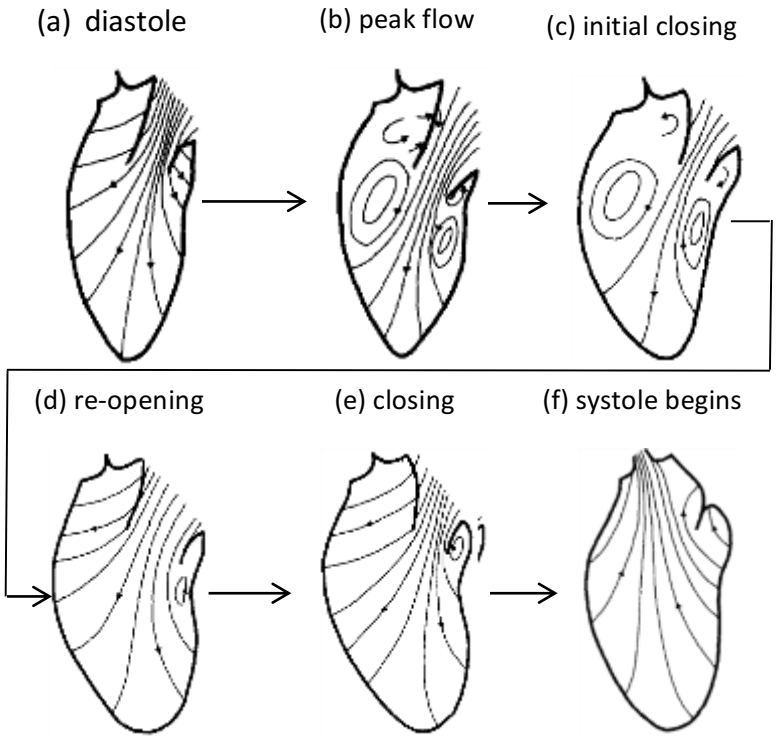

Figure 1.4: Six main stages of the mitral valve cardiac cycle dynamics (adapted from Reul et al 1981).

1.1.2.1 Annulus

The mitral annulus contracts and bends throughout the cardiac cycle (Figure 1.5), varying the mitral orifice area and circumference by as much as 26% and 13%, respectively (Rabbah et al 2013). The saddle shape, defined by the annular height to commissural width ratio (AHCWR) (Figure 1.6), can vary by as much as 30% (Rabbah et al 2013) throughout the cardiac cycle and has an essential role in reducing the stresses in the leaflets and evenly distributing the forces among the chordae, the flattening of which has been associated with an increase in the severity of mitral regurgitation (Jensen et al 2013).

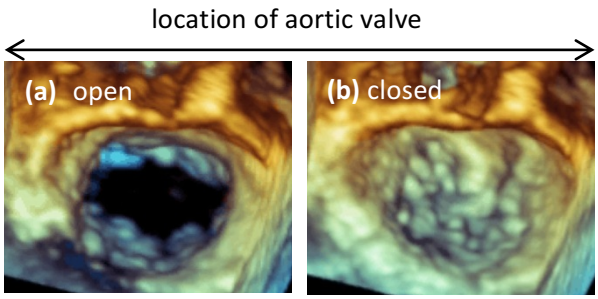

Figure 1.5: 3D echocardiogram of a healthy mitral valve **(a)** more circular in diastole (blood flow into the page) **(b)** more kidney-shaped in systole (acknowledgements: Pantazis A, The Heart Hospital, London).

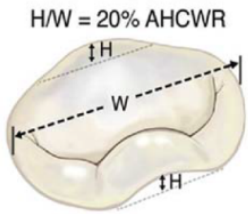

Figure 1.6: Mitral valve saddle shape defined as the ratio of annular height (H) to commissural width (W) (adapted from Padala et al 2009).

1.1.2.2 Leaflets

The passive membrane leaflets undergo membrane deformation, more specifically, the coapting force on the leaflets is caused by the apically contracting papillary muscles and the basally directed pressure forces (Figure 1.7). The mobility and redundancy of the aortic and mural leaflets respectively (Kunzelman et al 1994), combined with the presence of the commissures provides an optimal seal to withstand the transmitral pressure gradient.

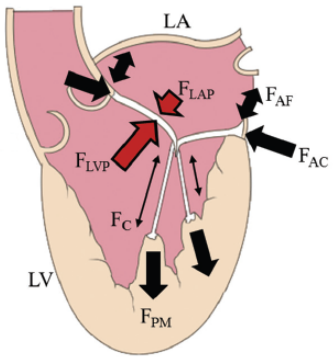

Figure 1.7: Forces **(F)** acting on the mitral apparatus **(F_{LAP})** left atrium pressure **(F_{LVP})** left ventricle pressure **(F_C)** chordae **(F_{PM})** papillary muscles **(F_{AC})** annular contraction **(F_{AF})** apical-basal force **(LA)** left atrium **(LV)** left ventricle (Rabbah et al 2013).

1.1.2.3 Chordae tendineae

The collagenous chordae (Padala et al 2010) exert restraining tensile forces during systole preventing the upward displacement of the leaflets into the LA and have recently been measured *in vivo* (Askov et al 2013). They also facilitate leaflet opening, along with the commissures, during diastole.

1.1.2.4 Papillary muscles

The papillary muscles stabilise mitral valve function by adjusting the tension on chordae and leaflets. They contract apically by as much as 2-5 mm during systole, thereby maintaining valvular-ventricular force continuity, then, before diastole the crimped collagen fibrils straighten and the high crosslinking of collagen prevent creep during valve closure.

There are various pathologies associated with the mitral valve which alter these healthy anatomies, dynamics and kinetics, the most common pathology being mitral regurgitation (MR).

1.2 Mitral regurgitation

This section summarises the statistics associated with MR, one of the most common forms of heart valve disorder, and describes the pathology in terms of anatomical abnormalities and their subsequent effect on the pressures and volumes within the LV.

1.2.1 Statistics

It is estimated that symptomatic MR affects over four million Europeans and a similar number of Americans (Lloyd-Jones et al 2010, Nkomo et al 2006, Lung et al 2003) and due to the continuous ageing of the western population; the number of cases is expected to rise significantly in the future. In fact, MR prevalence increases with age, rising from 0.5% for young patients (18-44 year olds) to 9.3% for patients older than 75 years (Nkomo et al 2006). Therefore, a significant proportion of symptomatic patients are in their late age, with relevant co-morbidities and previous surgery (Lung et al 2003, Edwards et al 2003, Roques et al 1999, Körfer et al 1995). As a result, up to 50% of them are currently declined surgery because they are judged too ill or weak to withstand the stress of the invasive treatment (Taramasso et al 2010, Mirabel et al 2007, Lung et al 2003).

1.2.2 Pathology

MR is the flow of blood in the wrong direction from the LV through the mitral valve into the LA and results in additional turbulence in the LA during systole (Dyverfeldt et al 2011). Degenerative MR is associated with alterations of the mitral valve leaflet structure, whereas functional MR, classified by Carpentier's four functional classes (Figure 1.8), occurs

due to changes in shape of the heart chambers or damage to the heart muscle (e.g. from myocardial infarction) resulting in annular dilatation and papillary muscle displacement, which compromises correct leaflet coaptation.

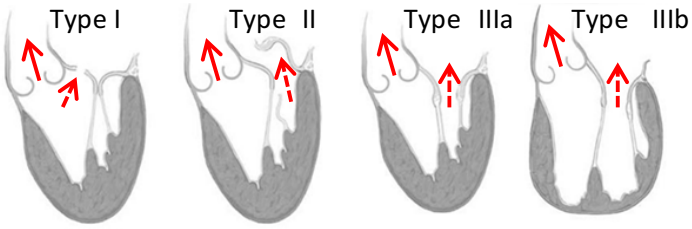

Figure 1.8: Carpentier's functional classification of mitral regurgitation **(Type I)** annular dilation or leaflet perforation **(Type II)** leaflet prolapse **(Type III)** restricted leaflet motion **(a)** subvalvular involvement **(b)** ventricular dilation**.** Dashed arrow: undesired regurgitant flow; solid arrow: desired flow into aorta (adapted from Cohn et al 2003).

MR alters the healthy pressures and flows that occur in the LV during the cardiac cycle, which are commonly represented by pressure-volume diagrams (Figure 1.9). Firstly, MR prevents isovolumetric contraction and relaxation; which can be observed in Figure 1.9 as volumetric changes between 2 and 3 and between 4 and 1 respectively. MR also increases the afterload i.e. the pressure in the LV during ejection, which can cause a smaller than normal end-systolic volume (point 1, Figure 1.9). The elevated pressure in the atrium, caused by the regurgitant flow, is transmitted to the ventricle during diastole, when the mitral valve is open, causing the end-diastolic pressure and volume in the ventricle to increase (point 2, Figure 1.9), the latter is exacerbated by increased compliance associated with dilated ventricles in the case of chronic MR. This means that despite the stroke volume increasing the volume ejected into the aorta reduces. In addition to raising the systolic pressure and volumetric capacity the cardiac system also uses systemic vasoconstriction[2], increased blood volume and heart rate and inotropy[3] in order to compensate for loss of blood flow. Therefore Figure 1.9 is only one example of what a given set of conditions for MR may look like.

[2] Systemic vasoconstriction is the narrowing of blood vessel throughout the circulatory system.
[3] Inotropy is cardiac contractility.

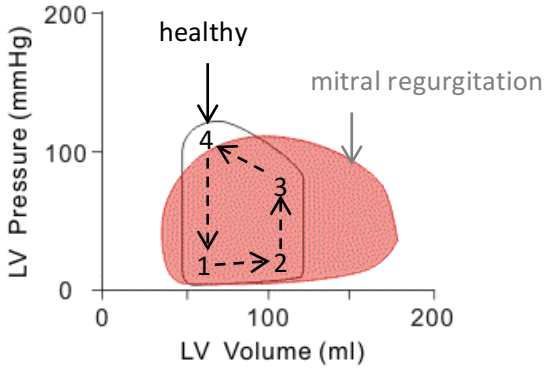

Figure 1.9: Pressure-volume diagram for a healthy heart compared to one with mitral regurgitation **(1-2)** mitral valve open **(2-3)** **"**isovolumic" contraction **(3-4)** aortic valve open **(4-1)** **"**isovolumic" relaxation (adapted from Klabunde 2011).

The area of the pressure-volume diagram is equivalent to the energy generated by the pumping action of the LV during one cardiac cycle. All healthy circulatory systems have energy losses, which occur when mechanical energy in the form of static pressure (generated by ventricular contraction), is irreversibly converted to frictional energy in the form of heat (via viscosity and flow separation) during the desirable conversion to kinetic energy (Akins et al 2008). Pathologies are sources of additional energy loss and in the case of MR, cause abnormal remodelling of the LV and circulatory system, resulting in an undesirable increase in stress on the myocardium. In fact, this concept of energy loss has been used to assess MR in symptomatic patients (MacIsaac et al 1992).

If untreated, MR increases the risk of heart failure and leads to a deterioration in life expectancy and quality of life. In severe cases, the leaking native valve can be replaced by a prosthetic device; optimal devices being those with minimal energy losses (Akins et al 2008).

1.3 Surgical treatments

In severe cases of mitral heart valve disease, the clinician may suggest the patients' native valve to be replaced by a prosthetic device. Current options include mechanical and stentless or stented bioprosthetic heart valves (Figure 1.10).

Figure 1.10: Surgical mitral valve replacements **(top)** mechanical; *left:* bi-leaflet, *middle:* tilting disk, *right:* ball and cage **(bottom)** bioprosthetic; *left:* stentless, *right:* stented (Pericarbon MORE Mitral).

Mechanical valves have the best durability; lasting 30-40 years compared to bioprosthetic valves which only last 15 years (Hoffmann et al 2008). However, the synthetic materials of mechanical valves require anticoagulation therapy, the side effects of which decrease the patients' quality of life. Such therapy is not required for bioprosthetic valves, made from biological tissue and furthermore they have more favourable hemodynamic performance (Hulsmann et al 2012), therefore in some cases are the best treatment option.

The Pericarbon MORE Mitral (Figure 1.10) successfully mitigated the early mechanical failures that hampered the durability of first-generation pericardial valves and is the only bioprosthetic device specifically adapted from its initial aortic version for the mitral position (Caimmi et al 1998). In general, manufacturers design devices for the aortic position, for which there is a higher commercial demand, and assess them according to the minimum performance requirements for the mitral position, with higher pressure gradients than the aortic position. Therefore, these circular three leafleted aortic valves can be used in the opposite orientation in the mitral position; a typical sizer used to select the correct sized device is shown in Figure 1.11. Subsequently all bioprosthetic heart valves implanted in the mitral position force the natural D-shape, see Figure 1.5, to become circular and replace the native two leaflets with three, the effect of which is unknown.

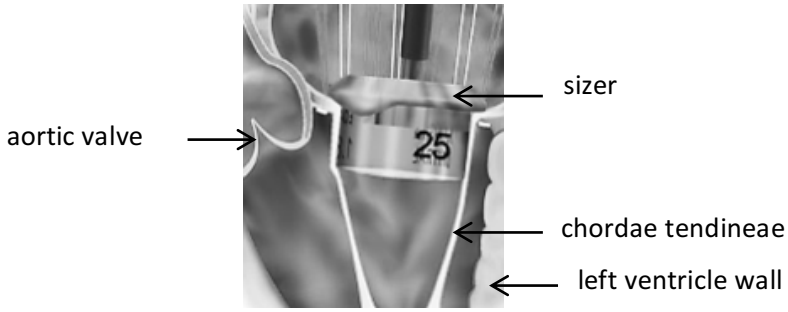

Figure 1.11: Sizer in a native mitral valve to determine the size of the surgical mitral valve replacement required (25 mm) (adapted from Edwards website: www.edwards.com 5/5/16).

Prosthetic heart valves present a greater resistance to blood flow compared to the native valve and therefore cause additional energy losses, dependant on valve type, size, orientation and position, consequently affecting ventricular function. Stentless bioprostheses provide the least resistance, followed by bileaflet and tilting disk mechanical valves and stented bioprostheses present the greatest resistance, as tested *in vitro* (Akins et al 2008, Yoganathan et al 2002).

All of the above mitral valve replacements require open heart surgery which presents too many risks for half the patients that require a replacement (Mirabel et al 2007). These patients are currently treated with limited medical alternatives, i.e. drugs, which merely aim to relieve their symptoms and in fact in some cases have no benefit at all (Nishimura et al 2014). Therefore, there is a clinical need for a minimally invasive alternative.

1.4 Minimally invasive treatments

In recent years, the growing need for less invasive therapeutic approaches has led to the development of a number of reconstructive percutaneous treatments for MR. However; these procedures generally only relieve the symptoms of very specific forms of mitral valve disease and anatomic subset, and are still surpassed in efficacy by surgical repair (Herrmann 2009, Masson et al 2009). A minimally invasive mitral valve functional replacement would allow the treatment of a broader spectrum of patients, disease etiology and anatomical variations, with significant benefits for the substantial patient population unable to undergo invasive surgery (Davidson et al 2006, Lung et al 1996). This approach would reduce both the procedural and recovery time for heart valve replacements (Modi et al

2008), with significant potential for cost saving (Osnabrugge et al 2013) as well as being a more accessible procedure both in terms of patient populations, pathologies and global location (Claramunt et al 2012), surpassing the relatively excessive risk factors and resource-intensive requirements of conventional open heart surgical replacements. Moreover, as shown in the case of the pulmonary valve, they can represent an excellent bridge treatment before surgery for children.

The first minimally invasive heart valve replacement for the pulmonary valve in 2000 (Bonhoeffer et al 2000), was developed into the current transcatheter aortic valve implantation (TAVI) technology and has been in the European market since 2007, approved for use in high-risk patients unfit for open heart surgery (Steinberg et al 2014).

1.4.1 Percutaneous mitral valve repair

The first percutaneous mitral valve procedure is dated back to the early '80s, when Inoue and colleagues performed the first balloon valvuloplasty for treatment of mitral stenosis (Inoue et al 1984), accessing the valve region via antegrade venous route (with transseptal puncture). This approach has quickly become the solution of choice for congenital stenotic mitral valves (Block et al 1988, Mckay 1991) in patients with isolated mitral stenosis and suitable anatomy (Vahanian et al 2004). However, this disease is now uncommon in developed countries and the procedure is not free from complications, including failure to relieve stenosis, formation of mitral regurgitation and systemic embolization (Vahanian et al 2004, Axford et al 2004). Mitral valve regurgitation represents a much more common disease in the western world (Davidson et al 2008), which affects patients often untreatable surgically (Lung et al 2003, Mirabel et al 2007, Taramasso et al 2010). Hence, a number of minimally invasive procedures have recently been developed to target this disease. These are essentially reconstructive treatments (valve *repair*) that aim to improve the leaflets apposition by remodelling one of the functional substructures. Hence, below they are classified in terms of the substructure they target to achieve their function.

1.4.1.1 Leaflets plication procedures

The main percutaneous approach currently adopted for mitral repair is based on the edge-to-edge technique (Figure 1.12). This consists in the apposition of the central portion of the anterior and posterior mitral valve leaflets to create a double-orifice valve with reduced

leaflet excursion and reduced regurgitation (Alfieri et al 2001). This is achieved by manipulating a grasping clip (MitraClip, Abbott Vascular) (Coats et al 2007) or suturing device (Mobius, Edwards) (Chiam et al 2011, Davidson et al 2006). The main limitation of this procedure is it being restricted to patients without severe dilatation of mitral annulus, relatively normal leaflets, mitral valve prolapse and central regurgitation (Block 2005). Moreover, clinical results indicate the inability of the technique to eliminate regurgitation in all patients (Feldman et al 2005). In fact, the edge-to-edge technique was developed as an adjunct to standard surgical repair procedures, and its use as a stand-alone technique is still debated (Block 2005, Cohn 2001).

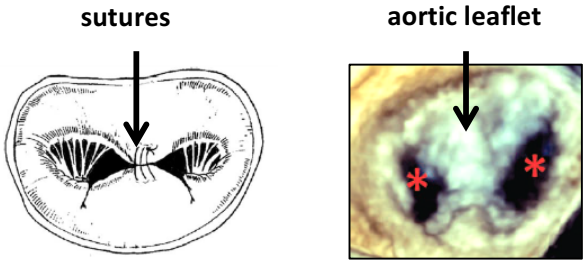

Figure 1.12: The edge-to-edge technique for mitral valve repair resulting in a "double-orifice" (*) **(left)** suturing method (surgical) (adapted from De Bonis 2002) **(right)** 3D transesophageal echocardiogram of a MitraClip® (Abbott Laboratories) (transcatheter) (adapted from Bartel et al 2014).

In 2008 the Abbott's MitraClip percutaneous repair device obtained CE marking, followed by FDA approval in 2013. This remains the only percutaneous reconstructive device currently available on the market.

1.4.1.2 Annulus reshaping procedures

Other popular approaches aim to restore the leaflets coaptation by reshaping the mitral annulus. In the first solutions, this was achieved by implanting into the coronary sinus a stent-like device (such as the Carillon, Cardiac Dimensions and the Monarc, Edwards) that forces the reshaping of the posterior region of the annulus, producing an approximation of the mitral valve leaflets (Kaye et al 2003, Liddicoat et al 2003). However, this approach is considerably limited by the great anatomical variability of the coronary sinus, and is not applicable in about half of the patients. Lastly, the consequence of long-term placement of such an aggressive prosthesis into the coronary sinus, whose walls are very thin, is still unknown and raises some concern (Coats et al 2007, Block 2005, Axford et al 2004).

Other devices achieve the reduction of the anteroposterior diameter by applying an epicardial pressure that modifies the shape of the left ventricle and, consequently, the annulus. This is obtained by tethering cords passed into the ventricle (iCoapsys, Myocor) or inflating silicone bands placed around the atrioventricular groove (BACE, Mardil).

Alternative recent methodologies replicate more closely surgical annuloplasty, which achieve leaflet coaptation by undersizing the annulus perimeter. These are based on transannular or subannular cinching by means of sutures that are anchored and tethered (e.g. Mitralign System, Mitralign and Accucinch System, Guided Delivery Systems), or by anchored Dacron bands of adjustable length (Cardioband, Valtech). The main limitation of these approaches is that they only allow partial cinching (posterior leaflet only) (Chiam et al 2011, Herrmann et al 2009).

Other solutions achieve the annulus undersizing by shrinking its collagen fibres with the heat generated by radio frequencies or ultrasound (e.g. QuantumCor Device, QuantumCor and ReCor Device, ReCor Medical). The drawback of this approach is the potential over-constriction or undercorrection, as well as possible damage to the surrounding structures (Chiam et al 2011). The long-term outcome for these devices is still unknown, and their development has been discontinued.

1.4.2 History of pulmonary and aortic valves

The first human valve replacement using a percutaneous procedure was reported in 2000 by Professor Philipp Bonhoeffer (Bonhoeffer et al 2000), who successfully implanted a stented valve in the pulmonary artery prosthetic conduit of a 12-year-old boy with stenosis and insufficiency. The valve was an 18 mm bovine jugular vein valve, sutured to a Numed CP platinum stent. The prosthesis, Contegra® (Medtronic), received CE marking in 2006 and FDA approval under Humanitarian Device Exemption in 2010, and is now widely used.

The approach was soon adopted for treating the aortic valve, with the first human implantation described by Dr Alain Cribier and colleagues in 2002. They delivered a bovine pericardial valve sewn into a stainless steel stent using a venous transseptal (antegrade) approach. The patient, who had been judged to be too weak to withstand the stress of open-heart surgery, was a 57-year-old man who presented with cardiogenic shock due to

severe calcific aortic stenosis with a bicuspid aortic valve. Since then, transcatheter aortic valve implantation (TAVI) has been established as the treatment of preference for calcified aortic valves in high risk patients (Helton et al 2011, Ghanbari et al 2009, Zajarias et al 2009). Two valve devices, the balloon-expandable Edwards SAPIEN (a direct evolution of the prosthesis implanted by Dr Cribier) and the self-expanding Medtronic CoreValve, with bovine and porcine pericardium leaflets respectively, have been in the European market since 2007 (FDA approval was granted in 2011 and 2014, respectively) and a number of second generation devices are already emerging; such as Boston Scientific's LOTUS Edge and the Medtronic Evolut R (Table 1.1). The SAPIEN has an advantageously shorter length, best for causing minimal vascular damage during delivery and they are both limited by their inability to reposition once deployed and are similarly subject to paravalvular leakage (PVL). The major limitations are discussed in more detail in the following sections.

Table 1.1: Commercially available transcatheter aortic valves (up to date at time of writing).

Company	Edwards Lifesciences	Medtronic	Boston Scientific
Models	[1]  **SAPIEN 3**  **SAPIEN XT**	[2]  **CoreValve**  **Evolute R**	[3]  **LOTUS Edge™**
Stent type (material)	Balloon-expandable (stainless-steel, Co-Cr)	Self-expanding (nitinol)	Mechanically expanded (braided nitinol)
Leaflets (material)	Bioprosthetic (bovine pericardium)	Bioprosthetic (porcine pericardium)	Bioprosthetic (bovine pericardium)
Device size (annulus size)	20, 23, 26, 29 (18-27) mm	23, 26, 29, 31 (18-29) mm	23, 25, 27 (19-23 and 23-27) mm
Length	14-19 mm	45-55 mm (62 collapsed)	-
Delivery diameter	16-18 Fr	18 Fr	18-20 Fr
[1] www.edwards.com, 12/9/16. [2] www.corevalve.com, 12/9/16. [3] www.bostonscientific.com, 2/3/17.			

1.4.2.1 Fluid dynamic requirement

TAVIs push the native leaflets to the side restricting the formation of oval vortices in the sinus (Ducci et al 2013), which, when present, induce an even pressure on the leaflets. This means the native leaflets act as a wall, reducing the area in which a vortex can form causing the blood to flow in a more vertical manner; creating a greater force on the belly (i.e. the middle) of the leaflets than in other areas, instigating the characteristic belly-first behaviour during both closure and opening, which is more prominent in TAVI valves such as the SAPIEN XT (Edwards Lifescience) and CoreValve (Medtronic) compared to surgical valves. Namely because when the latter are implanted the native leaflets are removed and so more natural sinus hemodynamics occur, resulting in more natural leaflet opening and closing morphology.

1.4.2.2 Conformity

The calcified deposits on stenotic aortic valves prevent TAVIs from conforming to the native annulus and so a small gap often remains between the native diseased leaflets and stent of the device, causing paravalvular leakage (PVL). Medtronic have recently released a new version; CoreValve® EvolutTM (Medtronic CoreValve Evolut) (Table 1.1, Figure 1.13), which is designed to address this problem by virtue of new stent geometry, size and material properties improving its conformability, fit and radial force for minimal PVL.

Figure 1.13: Conformability of CoreValve Evolut to the native aortic annulus (www.corevalve.com, 12/9/16.)

1.4.2.3 Applicable patients

Initially TAVIs were only implanted in elderly high-risk patients. For example; the patients in the Placement of AoRTic TraNscathetER valve (PARTNER) trial, were aged 83.1 ± 8.6 years (Leon et al 2010). Then, six years later, once their efficacy and safety had been demonstrated, the SAPIEN XT and SAPIEN 3 were granted U.S. Food and Drug Administration (FDA) approval for use in intermediate risk patients.

A similar initial patient population will have to be used for the trial of transcatheter mitral valve implants (TMVI). Then it is predicated that similar to TAVIs, their target patient population will be expanded to include medium and eventually also low risk patients.

1.4.3 The UCL transcatheter aortic valve

The transcatheter aortic valve (TAV) designed and manufactured at UCL, the TRISKELE, is retrievable, repositionable and has enhanced anchoring and sealing (Figure 1.14) (Burriesci et al 2012, Burriesci et al 2010, Ghanbari et al 2008), thereby overcomes the main limitations associated with some of the commercially available devices. The leaflets are currently made from a novel synthetic functional nanocomposite polymer, developed by the group of Professor Seifalian at UCL (Rahmani et al 2013).

Figure 1.14: The UCL transcatheter aortic valve 'TRISKELE'.

According to *in vitro* tests, the UCL TAV has a similar effective orifice area and smaller regurgitant fraction compared to first generation TAVI devices in the market at the time of testing in 2012 (Rahmani et al 2012). The UCL TAV resulted in lower ventricular energy loss during the cardiac cycle and therefore was deemed to have better overall performance.

In 2013 the UCL TAV was implanted into sheep by Mike Mullen and John Yap (UCLH Heart Hospital), at IMM Recherche, Paris (Mullen et al 2014). All prototypes were successfully implanted, retrieved back into the catheter and repositioned. Their hemodynamic performance was assessed for their optimal position, demonstrating good acute valve function with no significant regurgitation (Mullen et al 2014).

Despite the pertinent clinical need (Block et al 2006, Block 2005), the translation of transcatheter valve technologies to the mitral position has been hindered by the need for

alternative engineering strategies, taking into account the complex morphology of the valve, higher transvalvular pressure and larger sized devices (Siminiak et al 2007). Also, this application necessitates adaptation of the delivery and deployment methods, sizing algorithms, intraprocedural imaging, failure modes and post procedural assessment parameters, all of which are unique to the mitral position.

1.4.4 The UCL transcatheter mitral valve

The *in vitro* and *in vivo* data for the UCL TAV proved the effectiveness of its wireframe design in enabling retrieval, repositioning, good anchoring and low paravalvular leakage (PVL) in absence of calcification. Therefore a similar retrievable and repositionable design was used for the wireframe of the UCL transcatheter mitral valve (TMV); GEMINI (Figure 1.15). Furthermore, it is novel in mimicking the morphology of the native mitral valve; being D-shaped and having two leaflets.

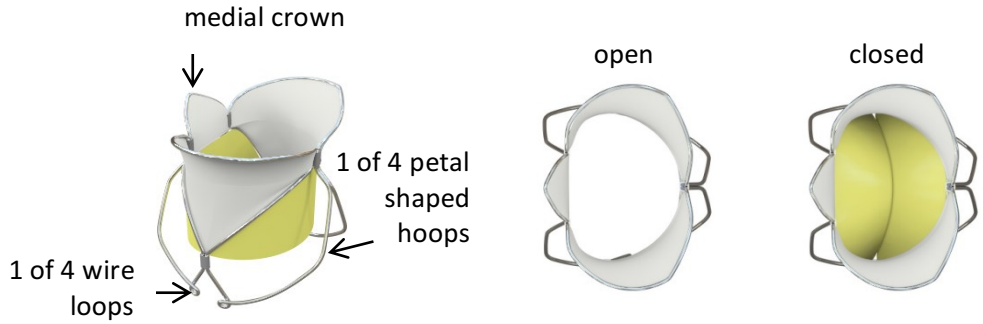

Figure 1.15: Initial concept for the UCL TMV **(left)** perspective view (leaflets open) **(middle)** atrial view (leaflets open) **(right)** atrial view (artist's impression of leaflets closed position).

The TMV frame has three functions; it facilitates folding of the device for transapical minimally invasive delivery, is a structure supporting the leaflets and is a means for anchoring the device in situ. The word 'frame', rather than stent is used to emphasise its intricate relationship with the function of the leaflets, namely as an axis for their hinge-like motion. This is contrary to the metallic stent components of other devices that have the primary function of exerting a radial force on surrounding anatomy. The medial crown (Figure 1.15) acts as a webbed spring which can deform and then return to its former shape. This harbours the classical physics of springs in a non-coiled form, predicted to

enable the proposed device to adapt to a mobile environment (previously described and depicted in Figure 1.5), absorbing load, whilst providing a constant radial force securing the device against the mitral annulus, thus creating a seal.

The implantation procedure for the proposed device would take place in a catheterisation laboratory using a delivery system similar to that for the UCL TAV (Burriesci et al 2012). Just prior to the procedure, a set of tethers would be threaded through the delivery catheter and attached to four wire loops. The device would then be submerged in water at 4 ^{o}C whilst the tethers are pulled together, folding the wireframe as it is pulled inside the catheter. To minimise the catheter diameter, the aortic and mural loops were designed to lay side-by-side when folded, thereby reducing risk of damage to surrounding tissues as it is inserted. The loaded catheter would then be guided towards the mitral orifice using fluoroscopic and transesophageal echocardiography (TEE).

The current position of the loops necessitates a transapical implantation procedure; once the device is positioned in the mitral orifice the deployment can begin (Figure 1.16.a). Firstly, the three crown sections of the frame would be released inside the atrium; generating one side of the clamping force (Figure 1.16.b). The petal shaped hoops would then expand inside the ventricle and project radially into the native leaflets, pushing them to the side, generating the other side of the clamping force, securing the device to the native mitral annulus (Figure 1.16.c) and once the loop sections are released they will keep the native leaflets taut, preventing left ventricular outflow tract obstruction (LVOTO) (Figure 1.16.d).

The correct positioning of the device is vital to anchor the device securely. In anticipation that the device does not deploy in the correct position, the tethers are designed so the device can be drawn back inside the catheter, moved to a more optimal position, and re-deployed, this could be done several times. Once the device is deployed in the correct position the tethers would then be cut and removed, after which the loops would function as springs, absorbing motions that occur in the light frame structure.

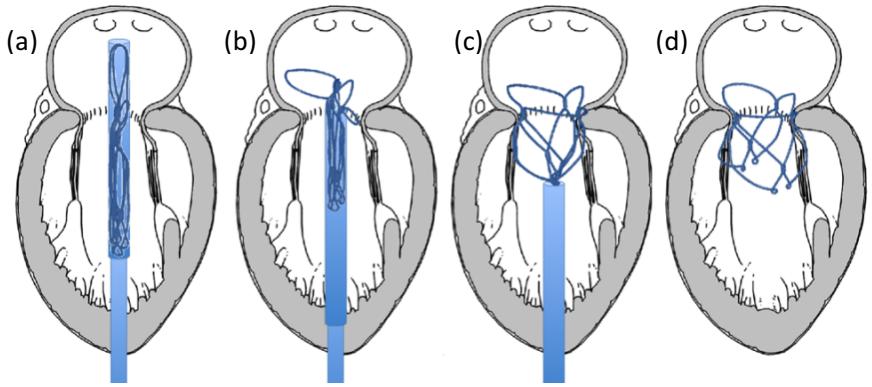

Figure 1.16: Transapical implantation for the UCL transcatheter mitral valve **(a)** wireframe collapsed in catheter in the mitral orifice **(b)** crowns released **(c)** petal shaped hoops released **(d)** final configuration keeps native leaflets taut.

1.5 Summary

This background chapter expounded relevant information regarding the anatomy and dynamic behaviours of the mitral valve components. The disease state being addressed, namely mitral regurgitation was described and current surgical and minimally invasive treatments were explained, including the UCL transcatheter solutions which are at both working prototype (UCL TAV, TRISKELE) and conceptual stages of design (UCL TMV, GEMINI). This has provided the required background information to form the context for the following literature review and thesis.

Chapter 2 Literature review

The UCL transcatheter mitral valve (TMV) aims to mimic the conical bileaflet native mitral anatomy (previously described in section 1.1.1). Therefore, the first section of this chapter reviews previous attempts to do this for surgical devices and the evolutionary development into the initial concept for the UCL TMV. The other TMVs in development are then reviewed in terms of their structural components, anchoring approaches, regurgitation prevention, delivery methods and *in vivo* evaluations. Implications for the regulations specifically for minimally invasive heart valves implanted in the mitral position are discussed; namely the devices diastolic and systolic performance, risk management issues and the choice of a relevant reference valve, which is followed by a summary and the future work required for the evolution of TMV implantation technology.

2.1 Bileaflet and quadrileaflet bioprosthetic mitral valves

There have been several attempts to mimic the native mitral valve morphology in bioprosthetic valves, although none have achieved technology transfer. All of the stented and stentless mitral valves discussed below were made from bovine pericardium with either two or four leaflets.

2.1.1 Stented

2.1.1.1 The bubble valve

In 1983 a circular bileaflet stented surgical mitral valve (SMV) was developed at the University of Victoria, Canada (Walker et al 1983), the leaflets for which were designed to form two symmetrical bubbles when in the closed position, as would occur for the stent profile. The shape of the bubbles was initially measured experimentally from a five times scale model and later a computational technique was used, which defined the stent boundary as shown in Figure 2.1. This 'bubble valve' successfully achieved comparable, and in some cases exceeded, the performance of the Bjork-Shiley convexo-concave tilting-disc and the Ionescu-Shirley three leaflet pericardial xenograft valves i.e. the commercially available mitral valves at the time.

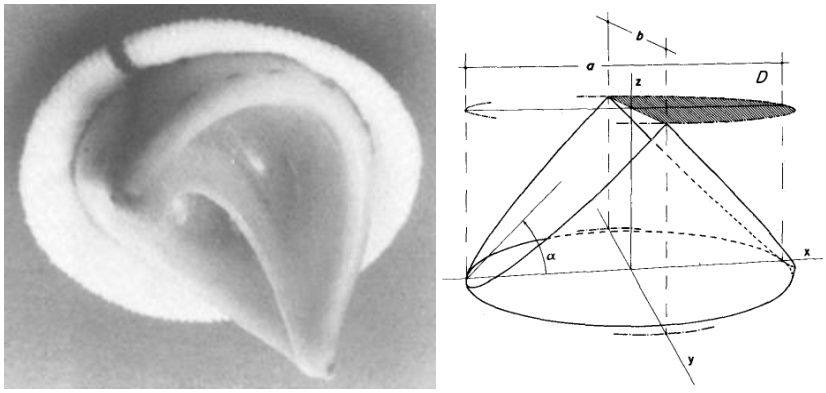

Figure 2.1: Stented bileaflet surgical mitral valve **(left)** 'bubble valve' developed at the University of Victoria, Canada (adapted from Walker et al 1983) **(right) c**o-ordinate system used for bubble surface: ellipse (short side (a) long side (b)) is an idealised projection of stent boundary on x-y plane, α is angle between plane of the stent and the x-y plane and D denotes the symmetry, i.e. the half of the ellipse calculated (Walker et al 1983).

2.1.1.2 The Sheffield valve

Later in 1986, another circular bileaflet stented SMV was developed at Sheffield University (Black et al 1986), the open shape for which is slightly conical (i.e. "*the fustrum of a cone, with a small cone angle*" (Black et al 1991, Figure 2.2). Both two (Huang et al 1990) and three-dimensional (Black et al 1991) finite element analyses have been completed. An investigation into the influence of orthotropy in pericardium on its mechanical behaviour (Burriesci et al 1999) and was reported to have endured a peak maximum principal stress of approximately 2 MPa, associated with the critical loading mode when the leaflets are fully closed, formed in a pattern of contours traversing the belly from the commissures to peaks at the base. The prototypes withstood more than 400 million opening and closing cycles (5 years) *in vitro* as well as *in vivo* function in calves, with survival times that met the Food and Drug Administration requirements (Black et al 1986).

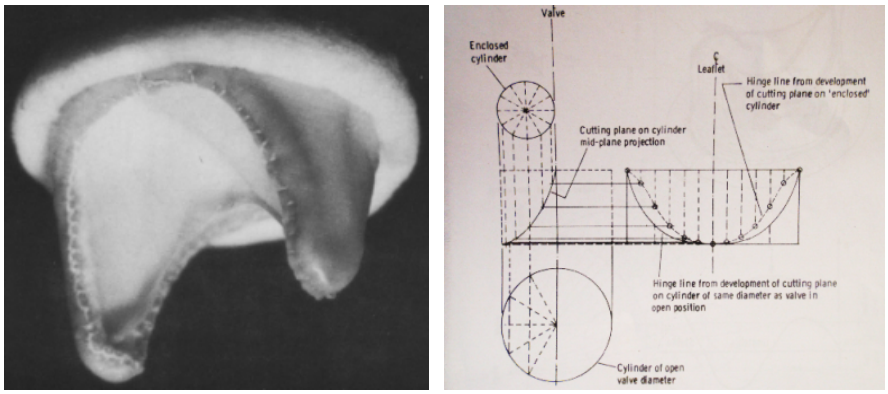

Figure 2.2: Stented bileaflet surgical mitral valve **(left)** Sheffield valve (adapted from Black et al 1991) **(right)** Cylindrical surface developments of the Sheffield valve (Black et al 1986).

2.1.1.3 The California valve

A bileaflet SMV was developed at the University of California, which had a flexible saddle annulus (Kheradvar et al 2012) (Figure 2.3 and Figure 2.4) and two diverging supporting prongs to prevent leaflet prolaspse, the latter being in direct contrast to the slightly conical design of the Sheffield valve. The computational analyses and *in vitro* hemodynamic studies showed leaflet length and the dynamic saddle annulus were critical in minimising stress distribution at leaflet tips (Kheradvar et al 2012).

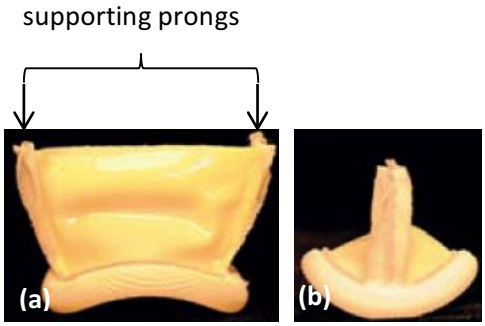

Figure 2.3: The California bileaflet mitral valve with a dynamic saddle shaped annulus **(a)** front view **(b)** side view (adapted from Kheradvar et al 2012).

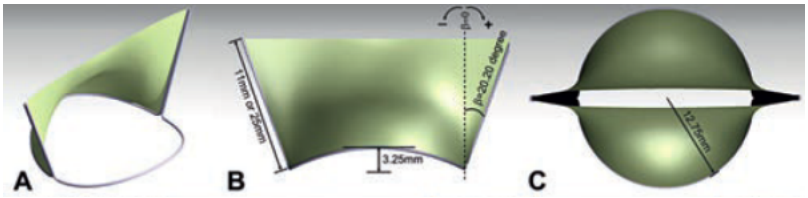

Figure 2.4: The California bileaflet mitral bioprosthetic with saddle shape annulus **(A)** mid-section of the valve showing the Nitinol core surrounded by pericardial tissue **(B)** open configuration from convex side, depicting valve dimensions and angle of motion **(C)** schematic from the top when the valve is fully open (Kheradvar et al 2012).

2.1.2 Stentless

2.1.2.1 The Quattro™ valve

The first D-shaped quadrileaflet stentless bovine pericardial SMV; Quattro™ (St. Jude Medical Inc.), was implanted into a total of 76 patients between 1998 and 2005 and used a different approach which requires the device's papillary flaps (Figure 2.5) to be attached to the native papillary muscles. Although the initial results were promising (Middlemost et al 2003, Walther et al 2003, Hofmann et al 2001, Aybek et al 2000, Middlemost et al 2000, Middlemost et al Mar 1999, Middlemost Mar 1999, Middlemost et al Oct 1999, Walther et al Oct 1999, Walther et al Dec 1999), it was later shown to be associated with a high risk of endocarditis, reoperations, valve degeneration and malfunction

due to the papillary flap attachment to the ventricle leading to insufficiency or subvalvular stenosis (Alsoufi et al 2010, Goldberg et al 2002). Due to the joining of the papillary flaps, the Quattro™ is effectively conical and therefore, more similar to the Sheffield stented SMV than the California SMV.

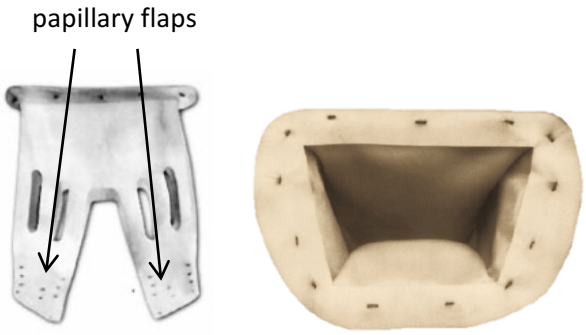

Figure 2.5: Quattro™ surgical mitral valve **(left)** lateral view (adapted from Hofmann et al 2001) **(right)** inflow side of valve (adapted from Walther et al 2003).

Despite the failure of the quadrileaflet Quattro™ mitral valve, similar designs have continued to be researched across China using both finite element analyses and *in vitro* assessments (Wang et al 2013, Huang et al 2013, Kuai et al 2008, Kuai et al 2006). The foremost, the Beijing valve being the only D-shaped valve, similar to the Quattro™, in contrast to the Hunan and Xiamen valves, which are circular (Figure 2.6).

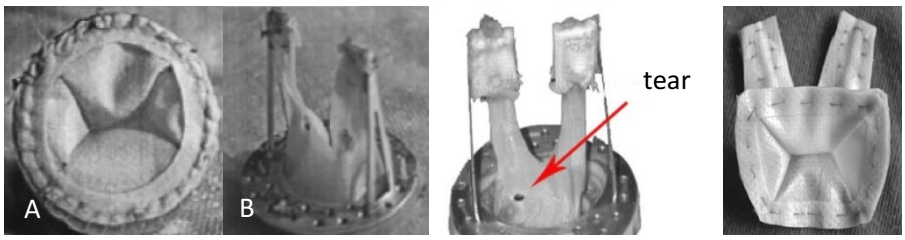

Figure 2.6: Quadrileaflet valves researched in China: **(left)** Hunan valve: **(A)** inflow **(B)** outflow aspects of valve (adapted from Kuai et al 2008) **(middle)** Xiamen quadrileaflet valve (adapted from Huang et al 2013) **(right)** Beijing quadrileaflet valve (adapted from Wang et al 2013).

2.1.2.2 The Cleveland valves

The Cleveland valves are stentless kidney-shaped bileaflet mitral valves (Figure 2.7) based on the morphology of the native valve and, therefore, designed to similarly form a "*continuous veil as a muff to the circumference of the mitral annulus*" (Navia et al 2010). In 2010, two of these devices were tested in 12 sheep (Navia et al 2010); one with and one without chordae (Figure 2.7). The foremost required the surgical removal of both the native leaflets and chordae tendinae; however,

for the latter the native chordae and leaflet free edge to which they attach were not removed but sutured to the free edge of the prosthesis. Both designs achieved good performance, with further chronic studies suggested.

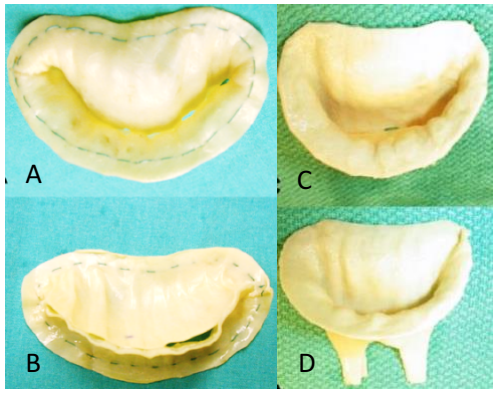

Figure 2.7: The Cleveland stentless bileaflet valves: no chordae **(left)** A: atrial and B: ventricular surfaces, with chordae **(right)** C: atrial and D: ventricular surfaces (adapted from Navia et al 2010).

2.1.3 Evolution to the UCL bileaflet transcatheter mitral valve

The UCL TMV presents an evolution of the aforementioned two and four leafleted SMVs, by combining the successful features which replicate the native morphology into a transcatheter device. In particular, it has two leaflets, similar to the California, Sheffield and Cleveland valves, but moves away from the circular design of the former two, employing a D-shape more akin to the latter. Furthermore, it improves on the very angular D-shape of the Quattro^{TM} and other quadrileaflet valves, which would result in a quadrangular orifice, by having two rather than four leaflets resulting in an elliptical orifice, making it more representative of a healthy native orifice in the open state (Figure 1.5). In addition to these morphological improvements to the previous designs, the UCL TMV also incorporates them into a frame which is suitable for transcatheter delivery, thereby significantly advancing the development of mitral valve replacements which replicate the native morphology, aiming to produce more physiological function.

2.2 Transcatheter mitral valves in development

A number of research groups and companies are currently working on the adaptation of percutaneous valve solutions specifically for the mitral position. In this section, the TMVs known at a most advanced stage of development and the technical solutions on which they are based are described and discussed (Table 2.1 and Figure 2.8).

Table 2.1: Transcatheter mitral valves at the most advanced stage of development and description of their main features.

Product name	Company	Frame	Leaflets	Anchoring	Delivery	Trials
AccuFit	Sino Medical Science Technology Inc., Tianjin, China	SE NiTi	P	Atrial & ventricular flanges	Transapical, RPR	Animals only
Caisson TMVR	Caisson	Not specified		Atrial flange and native valve anchors	Transseptal	Preclinical
CardiAQ Prosthesis	Edwards Lifesciences, California, US	SE NiTi	GA fixed PP	Atrial & ventricular flanges	Transseptal/Transapical	First-in-human in 2012
Cardiovalve	Valtech Cardio Ltd, Or Yehuda, Israel		GA fixed P	Atrial flange (full details not currently available)	Not specified	Animals only
Direct Flow Mitral	Direct Flow Medical Inc., California, US	Polyester	GA fixed BP	Atrial & ventricular flanges	Transapical, RPR	First-in-man expected Q4 2016
Double-Crowned Mitral Valve Implantation	Zhejiang University, Hangzhou, China & Centre Hospitalier Universitaire Vaudois (CHUV), Lausanne, Switzerland	SE NiTi	Porcine pulmonary & aortic homografts		Left atriotomy	Animals only
Endovalve	Micro Interventional Devices, Langhorne, Pennsylvania, US		GA fixed P	Arrow-head anchors	Transapical	
Fortis	Edwards Lifesciences, California, US		GA fixed BP	Atrial flange and native valve anchors		First-in-human in 2014
Gorman	The Trustees of The University of Pennsylvania, Philadelphia, US		GA fixed P	Atrial & ventricular flanges	Left atriotomy	Animals only
HighLife	HighLife Medical Inc., California, US					
Medtronic TMVR	Medtronic Inc., Minneapolis, US			Atrial flange & native anchors		
MitraCath	Emory University, Georgia, US	Prototype under development				
MitralSeal	Avalon Medical Ltd., Stillwater, Minneapolis, US	SE NiTi	GA fixed P	Atrial flange & ventricular tethers	Transapical	Animals only
MitrAssist	MitrAssist Medical Ltd, Misgav, Israel			Atrial flange & native valve anchors	Not specified	
MiVAR	Trinity College Dublin, EIRE			Atrial cage		
NaviGate TMVR	NaviGate Cardiac Structures Inc., Cleveland, Ohio, US	BE CoCr		Atrial & ventricular flanges	Transseptal	None currently reported
Tendyne	Abbott Laboratories, US	SE NiTi	GA fixed BP	Atrial flange & ventricular tethers	Transapical	First-in-human in 2013
Tiara	NeoVasc Inc., Richmond, British Columbia, Canada			Atrial flange & native valve anchors		First-in-human in 2013
Tresillo	Transcatheter Technologies GmbH, Regensburg, Germany		Not specified		Transseptal, RPR	None currently reported
Twelve Intrepid	Medtronic, US	SE			Transapical	First-in-human in 2016

Key: GA = Glutaraldehyde, BP = bovine pericardium, PP = porcine pericardium, P = pericardium (animal not specified), SE = self-expandable, BE = balloon expandable, NiTi = superelastic alloy, CoCr = cobalt chromium alloy, RPR = repositionable and retrievable.

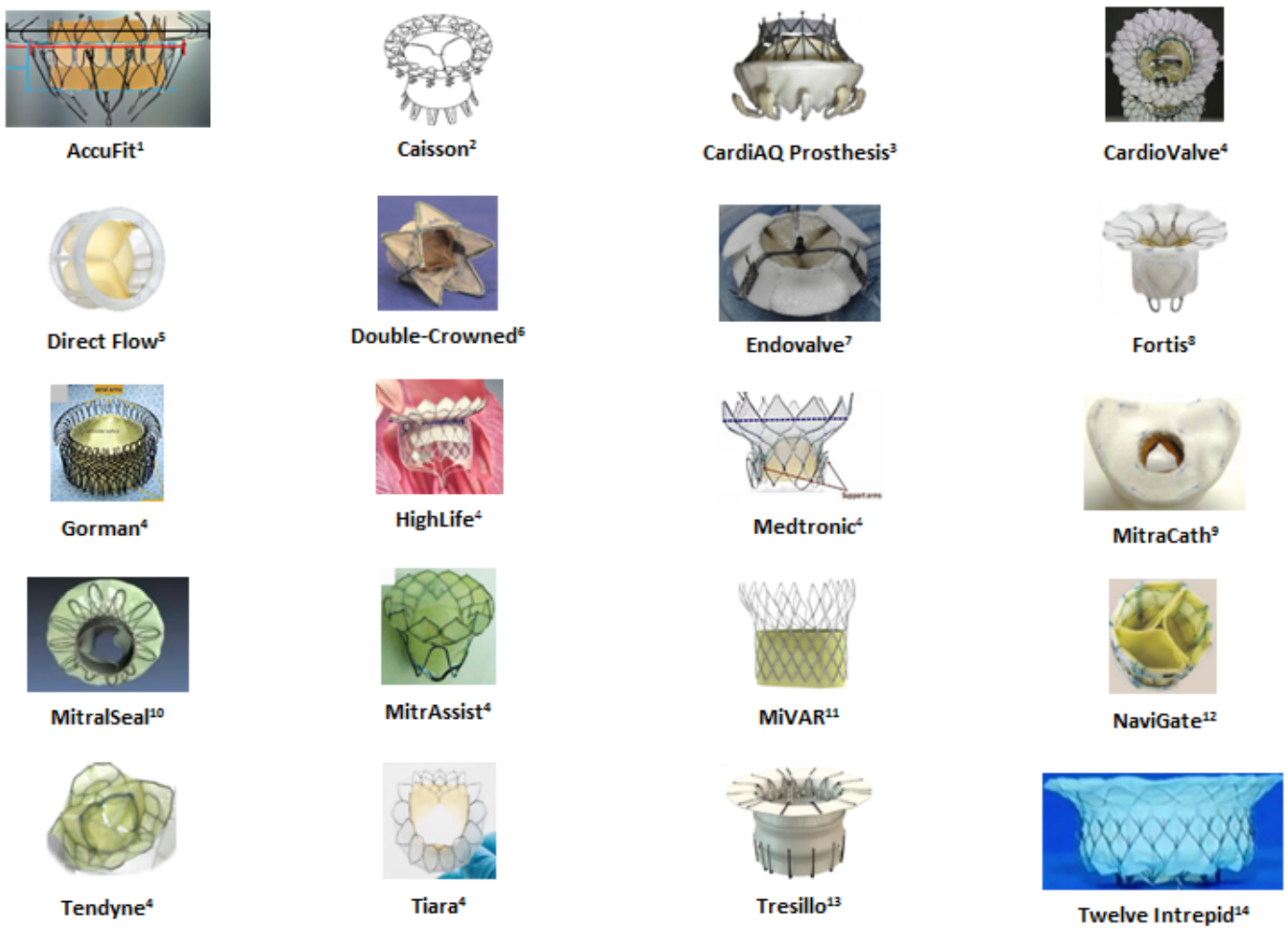

Figure 2.8: Transcatheter mitral valves in development: [1](Abdelghani et al 2015), [2](Hacohen et al 2011), [3](www.dicardiolody .com), [4](De Backer et al 2014), [5](Kheradvar et al 2015), [6](Ma et al 2005), [7](Chiam et al 2011), [8](Maisano et al 2015), [9](www.avalonmed.com), [10](www.atlanticpediatricdeviceconsortium.org), [11](www.knowledgetransferireland.com), [12](www.health.clevelandclinic.org), [13](www.transcathetertechnologies.com), [14](www.2015.icimeeting.com). (All websites accessed 13/06/16).

As in all prosthetic heart valves, in order to restore unidirectional blood flow through the cardiac chambers, the devices are comprised of an occluding component, a supporting structure and a securing means that avoids valve dehiscence. The presence of a sealing component to minimise paravalvular leakage is also preferable, especially for mitral valve applications.

The occluding component of all described solutions consists of three membrane leaflets (apart from the MitrAssist which has two asymmetrical leaflets) made from glutaraldehyde fixed bovine or porcine pericardium, sewn onto a supporting frame. This functional solution is optimal for percutaneous valves because the flexibility of the membranes allows them to be folded easily. Moreover, membrane valves can operate in different configurations, accommodating specific anatomical shapes and dimensions. This feature offers the possibility for the valve to adapt to an implantation site with dimensions and tissue elasticity which cannot be accurately determined and are likely to change during the device's life.

All of the supporting frames, excluding the NaviGate TMVR, are self-expanding structures made from nitinol; a near-equiatomic Ni-Ti alloy that exhibits enhanced recoverable elastic strains up to 8% (about 20 times larger than for stainless steel), commonly referred to as super-elastic behaviour. Thanks to this property, the valves are delivered after crimping them inside a covering sheath, which once the prosthesis has reached the anatomical site, is pulled back allowing the frame to re-expand into its unstressed configuration. This self-expanding approach provides the ability to better adapt to geometrical changes that may occur in the implantation site during the valve life.

In the case of the NaviGate TMVR the frame is made from a balloon-expandable Co-Cr alloy. During implantation, the valve is collapsed around an empty balloon with a crimping device, which plastically deforms the frame by producing plastic hinges. The valve is then re-deformed to the expanded configuration by inflating the balloon with a liquid solution. Balloon-expandable approaches allow the operator to administer the deployment pressure, but in the case of the mitral valve they require particular care to avoid excessive deformation of the neighbouring aortic valve. Moreover, they are typically less suitable for the implementation of retrievable devices.

2.2.1 Anchoring approach

The anchoring methods required for percutaneous mitral valves are distinct from those used in TAVI devices due to the more irregular and dynamic morphology. The substantial amount of calcium present in a stenotic native aortic valve can generate the large radial reaction forces that are commonly used to fix aortic prostheses. In the case of the mitral valve, the stiffening mineral is normally insufficient to provide radial forces able to secure a device. Moreover, high levels of radial forces would not be advisable as they could cause left ventricular outflow obstruction (LVOTO) (Ducas et al 2009) due to the native anterior leaflet being pushed radially into the LVOT, as well as possible aortic valve impairment, due to the device extending into the aorto-mitral curtain (Timek et al 2003).

Hence, anchoring in percutaneous mitral valves is commonly achieved by application of counteracting axial forces and/or tensioning the device between proximal and distal constraints. In the case of the Tendyne and MitralSeal the proximal constraint is represented by a flange, which lies flat against the atrial surface of the native mitral annulus, while the valve is fixed distally to the apex of the left ventricle, through a set of tensioned threads (Figure 2.9.a). Although these threads look similar to chordae tendineae, they have the function to anchor the frame, with no direct action on the valve leaflets. This solution may contribute to the reduction of paravalvular leakage (PVL), thanks to the presence of the atrial flange, pressed on the inlet wall. A potential drawback might be represented by possible variations in the tension applied to the distal threads in the event of left ventricle remodelling.

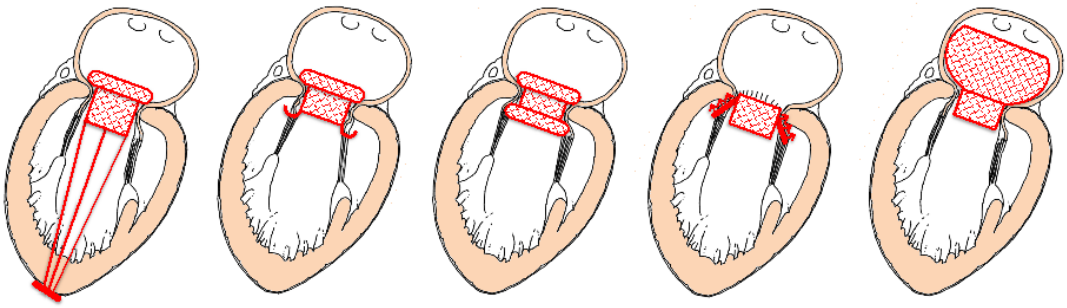

Figure 2.9: Percutaneous mitral valve anchoring systems **(a)** atrial flange and ventricular tethers **(b)** atrial flange and native valve anchors **(c)** atrial and ventricular flanges **(d)** subannular hooks **(e)** atrial cage.

An alternative approach is adopted in the Fortis, Gorman, Medtronic TMVR, MitrAssist, Tiara and Tresillo which, instead of threads, use ventricular distal anchors that grasp the free margins of the native leaflets (Figure 2.9.b). The Fortis is secured by two ventricular tabs that capture the aortic and mural leaflets, combined with an atrial flange. The Gorman valve is secured using upper and lower wire-weave flanges. The Tiara uses ventricular tabs that capture the aortic and mural leaflets, combined with three atrial flanges that anchor the device on the right and left fibrous trigones and native posterior leaflet. An additional feature of the Tiara anchoring system is its saddle-shape, designed to better conform to the native annulus (Jensen et al 2013). However, this makes the implantation of the device more challenging, as the saddle shaped device demands accurate orientation. The Tresillo, also uses ventricular anchors to restrain the native leaflets, although are longer and more numerous than in the Tiara valve. A potential advantage of clamping the native leaflets could be derived by reducing the risk of LVOTO, though the long-term effect of the force acting on the subvalvular components still needs to be ascertained (Rabbah et al 2013).

The Double-Crowned Mitral Valve and the HighLife adopt clamping mechanisms that engage with the upstream and downstream sides of the mitral annulus, reducing the interaction with the subvalvular apparatus (Figure 2.9.c). This is achieved by squeezing the mitral annulus between two Z-stents. The deployment of the Double-Crowned Mitral Valve Implantation requires the presence of an annuloplasty ring in the mitral annulus, thus making its application limited to only a sub-set of patients. The HighLife relies on the alignment of a groove with the annulus to anchor the device and provide a seal between the left atrium and ventricle. The same securing principle is used by the CardiAQ Prosthesis, Cardiovalve and NaviGate TMVR, which incorporate two sets of barbs or ‘wings’ protruding from the main body to improve the grasp. The advantage of this approach is a reduced interference with the subvalvular apparatus, which avoids potential issues associated with re-modelling. However, the solution does not prevent LVOTO, and the presence of barbs may represent a risk for surrounding structures such as the coronary sinus

In the case of the Endovalve, fixation is provided by a series of anchors around the edge of the valve consisting of a solid core and flexible barb (Figure 2.9.d). The flexible barb hugs the core, thereby enabling the anchors to pierce the mitral valve tissue as the device is deployed. Once inserted inside the tissue, the barb springs away from the core, forming an

arrowhead which prevents retraction and ensures the anchors do not disengage. This anchoring method could be effective in preventing PVL, but it does not facilitate multiple deployment or retrieval. Therefore, incorrect release would foreseeably require open-heart surgery.

An alternative approach is provided by the MiVAR valve, which relies on an atrial fixation system (Figure 2.9.e); based on a nitinol cage that conforms to the atrial chamber, preventing axial displacement of the valve. A potential disadvantage of this design is that, every time the left ventricle contracts, the associated apical-basal motion (Lung et al 1996) and pressure gradient may cause the device to move relative to the wall of the left atrium, the consequences of which are to be determined. This solution makes the valve operation totally independent from any remodelling that may occur to the subvalvular apparatus or left ventricle, and could help to reduce PVL. However, its presence could impair the atrial function, as well as the aortic valve.

2.2.2 Regurgitation prevention

Contrary to standard surgical valves, which are normally sutured onto the annulus (after dissection of the native leaflets), transcatheter valves are expanded into the diseased valve leaflets. This may result in gaps between the prosthesis and surrounding native tissues, with consequent PVL.

PVL has been identified as a major shortcoming of TAVI, and its impact is potentially more prominent in the mitral position due to the higher transvalvular pressure difference (De Bonis et al 2012). Therefore it is of paramount importance that any leakage around the edge of the device is actively mitigated in the design. Most of the devices, including the Cardiovalve, Endovalve, Fortis, HighLife, Medtronic TMVR, MitralSeal, Tendyne, Tiara and Tresillo prevent PVL using a fabric flange sutured onto the atrial portion of the metal frame. A unique method is employed by the Gorman valve, which relies on the flexibility of a nitinol wire-weave stent body to conform to the complex host geometry and create a seal. The other valves do not report any specific measure taken to mitigate PVL.

2.2.3 Delivery

TMVIs need to conform to more irregular anatomical sites and larger orifices than TAVI. This requires more material for the valve components, which translates into larger diameters of the collapsed device and subsequently wider access routes are required. With sufficiently low valve profiles an endovascular retrograde approach allows to conveniently reach the aortic valve from the femoral vein, after puncturing of the inter-atrial septum (Figure 2.10.a). This approach has been very popular in the early experience with TAVI devices, because the larger dimensions and greater elasticity of the veins allows the passage of relatively large collapsed stents. In the case of the mitral valve, this is the most favourable access, because it does not require navigation through the subvalvular apparatus. However, this procedure requires the device to fit inside a catheter equal to or smaller than 24 Fr (8 mm diameter), while current valves still require relatively larger catheters of 30-33 Fr (10-11 mm diameter), with the exception of the MitrAssist, for which a delivery system of 18 Fr (6 mm diameter) is declared. Currently, only four of the devices have achieved a percutaneous delivery; Caisson, CardiAQ Prosthesis, NaviGate TMVR and MiVAR, all but the later use transseptal approaches (Maisano et al 2015, De Backer et al 2014) and this approach is also claimed to be achievable for the Tresillo.

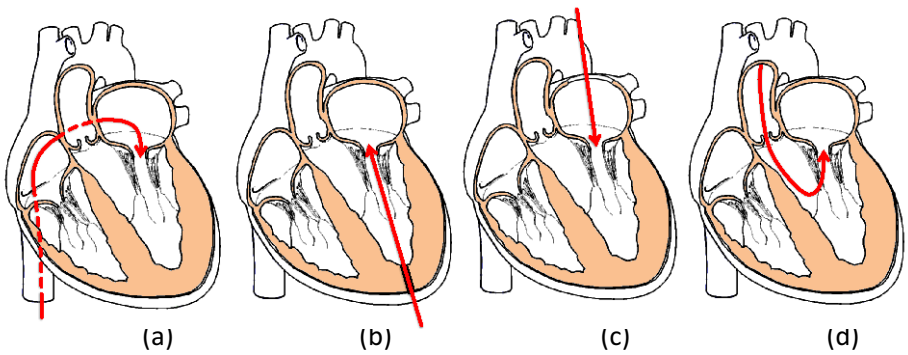

Figure 2.10: Percutaneous mitral valve delivery **(a)** transseptal **(b)** transapical **(c)** left atriotomy **(d)** transaortic.

The transapical route (Figure 2.10.b), widely used for the implantation of aortic valves, allows the passage of larger valves; and therefore is currently the most adopted approach. However, access to the mitral valve requires navigating the delivery system through the subvalvular apparatus. To prevent the device becoming entangled in the chordae tendineae, expert interpretation of the fluoroscopic and transesophageal echocardiographic guidance (TEE) is required. Despite this challenge, the transapical

approach has been used for implanting the CardiAQ Prosthesis, Direct Flow Mitral, Fortis, Tiara and Twelve Intrepid (Banai et al 2014) and is necessary for the anchoring systems of the Tendyne, MitralSeal and Endovalve.

A left atriotomy (Figure 2.10.c) is required to implant the Double-Crowned Mitral Valve Implantation, Gorman, HighLife and Medtronic TMVR valves. This approach involves an incision of approximately 10 cm, making it the most invasive access for transcatheter valve implantation.

A unique choice of surgical approach is adopted for the MitrAssist, which currently uses a transaortic implant (Figure 2.10.d) where a minimally invasive surgical incision into the aorta is made to insert the device.

2.2.4 In vivo evaluation

Evaluation of transcatheter prosthetic mitral valves in large animals has been reported for the CardiAQ Prosthesis, Cardiovalve, Double-Crowned Mitral Valve Implantation, Endovalve, Fortis, Gorman, HighLife, Medtronic TMVR, MitrAssist, Tendyne and Tiara, similarly indicating the approach is feasible and promising, whilst highlighting current deficiencies (De Backer et al 2014, Banai et al 2014, Gillespie et al 2013, Zou et al 2013, Iino et al 2012, Banai et al 2012, Ma et al 2005). A common failure mode of the devices was inadequate anchoring mechanisms, resulting in device migration, which is also one of the main causes of LVOTO. However, some of these failure modes may be due to inappropriate sizing. For example, the relatively high rate of PVL in chronic in animal evaluation of the Tiara was attributed to only one size device being available for the range of native valves (De Backer et al 2014). The MitralSeal is routinely employed for veterinary applications in dogs, which are characterised by similar mitral valve pathologies to humans (Pedersen et al 2000) and acute animal studies for AccuFit are currently in their final stages (Abdelghani et al 2015).

Generally, in animals, experience with TMVIs indicate that current devices require substantial design improvements, namely to position and anchor them. These improvements may partly be achieved by developing appropriate algorithms for selecting device size to be implanted for a particular native valve. For the Tiara device, implants in

human cadavers are reported (Banai et al 2014), which demonstrated appropriate geometric positioning.

In humans, evaluation of minimally invasive mitral valve replacements has occurred since 2012 when the CardiAQ prosthesis was the first to be implanted in a human, followed by the Tendyne in 2013, the Tiara and Fortis in 2014 and most recently in 2016 the Twelve Intrepid. The AccuFit and Direct Flow Mitral were expected to achieve their first-in-man later in 2016 (Abdelghani et al 2015). The Cardiovalve, Double-Crowned Mitral Valve Implantation, Endovalve, Gorman, HighLife, Medtronic TMVR, MitrAssist and MiVAR all remain in animal trials, whilst no *in vivo* data are yet reported for the NaviGate TMVR.

The first-in-man experience of the CardiAQ Prosthesis was performed by the team of Lars Søndergaard at the Heart Centre in Copenhagen, Denmark, in June 2012. The valve was implanted into an 86-year-old high-risk patient suffering from severe mitral regurgitation (MR). The device successfully alleviated the patient's severe regurgitation, although some remained and three days later the patient died from multi-organ failure (Sondergaard 2012). More recently, in 2014, three elderly patients aged 78-89 years, with severe MR were given the CardiAQ mitral valve on compassionate grounds. All were positioned and deployed accurately, successfully eliminating MR, two of the patients made full clinical recovery with good valve function monitored up to 60 days post-procedure and the other patient died nine days after the operation from pneumonia (Sondergaard et al 2015).

In 2013 two Tendyne valves were implanted at the French Hospital in Asuncion, Paraguay (De Backer et al 2014). The 57 year-old man and 55 year-old woman, with severe MR, agreed to have the Tendyne valve implanted for 2 hours prior to removal of their native valves for conventional surgical replacement. The severity of their MR grade was successfully reduced from four to one in one patient and completely eliminated in the other (Lutter et al 2014).

The Tiara was implanted into a 73-year-old-man and a 61-year-old-woman with severe functional MR at St. Paul's Hospital, Vancouver, British Columbia, Canada (De Backer et al 2014) at the beginning of 2014 and successfully eliminated MR as well as achieving improved LV stroke volumes (Cheung et al 2014), according to data up to 2 months after the procedure.

Later in 2014, a total of five Fortis valves were implanted, four by the Heart Team at St. Thomas' Hospital in London, UK and one at St Michael's Hospital in Toronto, Canada (Bapat et al 2014). The patients had presented with severe mitral valve disease and showed promising initial recovery after the implantation of Fortis, although three patients died between four and 76 days after the procedure. Failure modes and causes of death have not been reported. More recently in 2015, three patients with functional MR (mean age 71 ± 9 years, 2 men) had the Fortis implanted under a compassionate use program (Altisent et al 2015). The devices were implanted with no complications and successfully removed MR in one patient with trace residual MR in the other two and remained alive at 6-month follow-up (Altisent et al 2015). However, thrombus formation was a significant issue with the Fortis device, which signifies that a well-tailored anticoagulation regime may be required after TMVIs.

Most recently, in February 2016 results were presented for a pilot study of eleven Twelve Intrepid valves (NHS, UK), for which three patients died, one of which was due to deployment failure and one of the patients still experiences symptoms as per NYHA[4] class II heart failure (Wood 2016).

These human trials have demonstrated the clinical need, reflected by elderly patients agreeing to the implantation, and the potential of TMVIs to diminish MR to a similar level achieved by surgical replacements. However, only with larger numbers of patients and longer follow-up times can the effectiveness of TMVI technology be assessed as a truly compassionate treatment option for elderly patients with severe MR at too high risk for surgical replacements.

2.3 Regulatory issues for transcatheter mitral valves

Prior to reaching the market, the safety and efficacy of any prospective heart valve substitute must be ascertained by means of *in vitro* and *in vivo* investigations. Guidelines and recommendations for the qualification of the design and manufacture of permanent prosthetic valve devices are provided by International Standards ISO 5840-Cardiovascular implants-Cardiac valve prostheses. This imposes the design and minimum performance

[4] New York Heart Association (NYHA) Functional Classification class II has the following mild symptoms; mild shortness of breath and/or angina and slight limitation during ordinary activity.

specifications for aortic and mitral valves, and outlines the approach required to assess the properties of prostheses and their materials, and those for *in vivo* evaluation. The standard, first enforced in 1984 and initially based on a 'requirement based' approach, has recently adopted a 'risk based' approach (ISO 5840:2005), more in line with FDA guidance and better suited for recent transformative developments of the technologies. The substantial technological and functional differences between surgical and minimally invasive valve prostheses have driven the drafting and publication of an additional updated part of the standard, ISO 5840-3:2013, specifically created for qualification of transcatheter heart valve substitutes and valid since March 2013.

Most of the specifications and assessment approaches described in the International Standards ISO 5840:2005 and ISO 5840-3:2013 are applicable to minimally invasive mitral valve replacements. However, as they are based on existing clinical evidence, mainly available only for surgical valves and TAVI, revision may be needed to better address this emerging class of devices.

2.3.1 Diastolic performance

The current standards prefer measurement of the effective orifice area (EOA) to assess the hydrodynamic performance of valves, during the forward flow phase (diastolic phase for the mitral valve). However, due to its larger orifice, the EOA is a less critical parameter for the healthy function of the mitral valve compared to the aortic valve, and is often sacrificed in favour of better leaflet coaptation. For example, in the edge-to-edge repair technique, the EOA of the mitral valve can be reduced by as much as 60% after an edge-to-edge repair, without detrimental consequences. Therefore, assessment based on the effective surface area using the proximal isovelocity surface area (PISA) method (Lancellotti et al 2010, Recusani et al 1998) may be more relevant for the intraoperative evaluation of mitral devices.

2.3.2 Systolic performance

The performance of the valve during the closing and closed phase is verified and controlled by limiting the regurgitant fraction. The ISO 5840-3:2013 acknowledges the inevitability of higher degrees of paravalvular leakage in transcatheter devices, accepting larger

regurgitant fractions (for large sizes, up to 25% at a CO of 5 lpm) than for corresponding surgical valves. This is compensated by more severe demands in terms of EOA.

As discussed above, though this approach is acceptable for TAVIs, in the case of the mitral valve increases in EOA would possibly be unnecessary and insufficient to compensate significant levels of leakage, which should instead be mitigated.

2.3.3 Risk management aspects

The potential hazards, associated failure modes and subsequent evaluation methods currently described in ISO 5840-3:2013 (Annex G) are defined based on TAVI experience. In order to better reflect lessons learnt from current *in vivo* experiences with TMVIs, the risks associated with unintended anatomical interactions should also consider failure modes such as: left ventricular out flow tract obstruction (LVOTO), which can lead to heart failure and death; left circumflex (LCx) artery compression, which would inhibit blood supply to the posterolateral left ventricle and anterolateral papillary muscle; and coronary sinus (CS) compression, which would hinder deoxygenated blood flow from the heart muscles to the right atrium.

2.3.4 Reference valve predicament

The standards require that a heart valve substitute with known clinical experience is used for comparative preclinical and clinical evaluations. No such reference valve for transcatheter mitral valves (TMV) has been suggested in the literature to date.

The clinical experience most similar to a TMV is evidence of transcatheter aortic valves (TAV) performing well in the mitral position when implanted inside existing annuloplasty rings or valvular prosthesis (Tang et al 2013). However, these valve-in-mitral-valves are not appropriate reference valves because they are not specifically designed for the mitral position and have an unfair advantage in terms of likely lower regurgitation and reduced risk of migration due to being implanted inside existing devices. For similar reasons, comparison with balloon-expandable aortic valve systems, used in patients with severely calcified mitral valves (Fassa et al 2014, Guerrero et al 2014, Himbert et al 2014, Ribeiro et al 2014, Hasan et al 2013, Sinning et al 2013) are not appropriate either.

The next most similar device to a TMV is a bio-prosthetic surgical mitral valve (SMV) replacement. There are four commercially available pericardial valves used in the mitral position. Edwards Lifesciences Corporation manufactures three of them; the Magna Mitral Ease, Perimount Plus and Perimount Theon, and Sorin Group (now LivaNova PLC) manufacture the Pericarbon MORE Mitral, all of which are circular devices with three leaflets. The latter being the only bio-prosthetic valve to be specifically adapted for the mitral position from its initial aortic version, with successful clinical experience (Caimmi et al 1998). In fact nearly all bioprosthetic heart valves are suitable for the mitral position even though in general they are not specifically designed for it.

However, direct comparison between a surgical and transcatheter mitral valve would not be valid due to different minimum device performance requirements made by ISO 5840:2009 and 5840-3:2013 respectively (Table 2.2 and Table 2.3). Namely, the latter standard for transcatheter valves accounts for inevitably greater leakage compared to surgical valves by allowing more regurgitation for a given device size but demanding a greater effective orifice area to compensate for the additional work required by left ventricle to maintain normal cellular metabolism. For example; a size 25 mm (tissue annulus diameter) SMV must have a regurgitant fraction (RF) less than or equal to 15% (Table 2.2) but a size 25 mm (deployed valve diameter within implant site) TMV can have a RF as high as 20% (Table 2.3), however, it must have an effective orifice area (EOA) greater than or equal to 1.25 cm^2 (Table 2.3) compared to only 1.2 cm^2 for a SMV (Table 2.2).

Table 2.2: Minimum device performance requirements for surgical mitral valve replacements (adapted from ISO 5840:2009).

Valve size	Tissue Annulus Diameter (mm)	25	27	29	31
	Effective orifice area (cm^2) ≥	1.2	1.4	1.6	1.8
	Regurgitant fraction (%) ≤	15	15	20	20

Table 2.3: Minimum device performance requirements for transcatheter mitral valve replacements (adapted from ISO 5840-3:2013).

Valve size	Deployed valve diameter within implant site (mm)	23	25	27	29	31	33
	Effective orifice area (cm^2) ≥	1.05	1.25	1.45	1.65	1.90	2.15
	Regurgitant fraction (%) ≤	20	20	20	25	25	25

At this early stage in the development of TMVs, and therefore in absence of a relevant reference valve to date, they have been assessed *in vivo* in reference to improving the previously untreated disease state (Sondergaard et al 2012, Sondergaard et al 2015, De Backet et al 2014, Lutter et al 2014, Cheung et al 2014, Bapat et al 2014, Altisent et al 2015, Wood 2016).

2.4 Summary of transcatheter mitral valve technology

After the rapid development of pulmonary and aortic transcatheter heart valve implantations, the advantages of percutaneous procedures are finally being transferred to the functional replacement of mitral valves. The experience gained with TAVI devices is fundamental to the development of this approach, which presents unique challenges requiring new technical solutions, due to the more complex morphology and function of the mitral valve.

Similarly to the first generation of percutaneous aortic valves, PVL and embolisation[5] remain major hurdles, the impact of which is amplified by more severe transvalvular pressures and valve dynamics. The accuracy of medical imaging technologies and sizing criteria will play a major role in reducing these complications, by allowing selection of the most suitable TMVI for each patient. In fact, for a correct fitting, most of the valves under development require proper geometrical matching with the irregular mitral annulus (normally characterised by an asymmetric bean-shape, laying on a saddle-shape surface), as well as the subvalvular structures and heart chambers. All these components are characterised by significant variations of their dimensions during the cardiac cycle, due to the dynamic nature of the mitral valve apparatus and surrounding anatomy. Therefore, for each prosthetic valve, it is essential to identify what parameters are the most relevant for ensuring proper anchoring and sealing. Accurate and comprehensive sizing algorithms will need to be developed, to ensure the safety and proper functionality of TMVIs. This will necessarily require continuous revision and refining, based on both *in vivo* experience and *in vitro* assessment.

Future designs will also need to focus on reducing the device's collapsed profile, enabling endovascular access with minimal incision size. This will foreseeably follow the

[5] Embolisation is the lodging of an embolus (a blood clot) within the bloodstream.

developmental trend that has characterised aortic solutions, which have achieved substantial advances in reducing the loaded valve size and delivery system, offering new alternative implantation approaches with reduced vascular injury. An important feature to inherit from the latest generation of TAVIs will be the ability to reposition valves during the implantation procedure. In fact, as most of the anchoring approaches adopted for the mitral application require a precise axial and angular positioning, inappropriate release is more likely to lead to functional complications and increased PVL.

Concerns about safety and durability in the functionally more stressed mitral position will be revealed only after medium and long term clinical outcome, but the positive results of TAVI devices suggest that metal frames can be suitable to withstand heavy loading conditions. Also, as for TAVIs, TMVs might result in a high rate of silent cerebral ischemic lesions. These, in fact, appear to be independent from catheter manipulation and the severity of calcification (Rodes-Cabau et al 2010), and are possibly associated with the hemodynamic disturbance[6] produced by the valve-in-valve configuration (Ducci et al 2013).

In order to be established as a sustainable therapy, it is essential that TMV replacement fully demonstrates its safety and efficacy, guaranteeing at the same time affordable costs. In fact, contrary to TAVI devices, which only compete with other replacement strategies, mitral valves will have to operate in a more aggressive commercial climate, contending the role to a range of surgical and transcatheter, replacement and repair solutions, with various degrees of invasivity. However, it can be envisaged that, similarly to what has happened for aortic valve therapies, currently established mitral treatments will strongly benefit from novel technical solutions developed for TMVIs. In fact, dimensional reduction of the supportive structure of the leaflets and the availability of collapsible sutureless mitral valves may contribute to the development of procedurally safer and less invasive surgical applications.

In summary, first experiences with TMV replacements have been very encouraging, demonstrating the feasibility and potential benefit of the approach. However, due to anatomical variations between animals, comparison of *in vivo* data for current devices in development (Table 2.1) would be insufficient to determine the best solution; *in vitro*

[6] Disturbance here meaning alteration of physiological flow, thereby including stagnation of flow.

assessment is required to obtain comparative data, which may consequently better determine an optimal anchoring method for the mitral position. Undoubtedly, substantial progress will be needed in order to overcome current limitations and establish this solution as a competitive treatment. The process will have to be assisted by regulatory standards that better reflect the specific clinical needs and recent experiences with this approach.

2.5 Summary of key findings

There were two main findings from the background and literature review which directly influenced the design and form the context of the work presented.

1. **Conical Design**

The background research regarding the anatomy of a healthy native mitral valve indicated that conicity would make the proposed UCL bileaflet design more physiologically similar. This feature can be seen clearly in Figure 1.5, which depicts the mitral valve in its open position, and shows the leaflets acting as a funnel for transporting blood from the left atrium into the left ventricle. This novel design feature was consequently added to the initial UCL TMV concept (section 1.4.4).

2. **Annulus size**

It was clear from current *in vivo* data for developmental TMVs, that implantation site size had a significant impact on the device's performance. Therefore, it was chosen as the focus for the *in vitro* tests, and thereby instigated the design and manufacture of various sized mock native mitral valve holders in which the UCL TMV prototypes were tested. There by resulting in a novel contribution to the experimental design for TMVs.

2.6 Thesis outline

This thesis describes how the materials used to make the UCL TMVs were characterised; namely pericardium, polyester mesh and nitinol wire, the requirements for which are also outlined in Chapter 3. Chapter 4 then discusses the leaflet design and how finite element analyses' were used as a design tool resulting in the selection of a conical bileaflet design,

uniquely defined by two parameters; its scale factor and coaptation length. Chapter 5 then describes the equipment used and made to assess the prototypes. This includes the design and manufacture of surgical mitral valves, designed to provide a relevant reference valve for the UCL TMV. Furthermore, it describes the experimental conditions used to simulate the left side of a normal healthy adult heart and the parameters measured to assess prosthetic heart valve's performance. The minimum performance requirements are also expounded as well as the limitations of these methods.

Chapter 6 outlines the main aim of the UCL TMVs, that is, to assess its potential as a treatment option for high-risk patients with severe mitral regurgitation. The design of the prototypes and their functional assessment are then described and the results are then presented and discussed. Chapter 7 describes how and why the 1st generation device (Chapter 6) was developed into a 2nd generation device, for which preliminary results and a discussion are provided.

Chapter 8 discusses current and future work to develop the UCL TMV; including development of the surgical version as well as functional assessment methods, delivery system and durability assessments. Lastly, chapter 9 concludes design and functional performance and the appendices contain numerical codes and graphs, unnecessary in the main body of the thesis and are all referred to where relevant.

To summaries, the aim of this project was to develop a proof of concept prototype of the UCL transcatheter mitral valve (TMV) by completing the following objectives; an initial design cycle consisting of design of both devices and testing equipment (Chapter 3-5), prototyping (Chapter 6) and testing (Chapter 6 and 7). This aim was achieved, and the main findings, limitations and recommendations for future work required to further develop the UCL TMV are outlined in Chapter 8.

Chapter 3 Material characterisation

The UCL TMV has two pericardial leaflets, a self-expanding nitinol wireframe and polyester mesh skirt sections (Figure 3.1). Characterisation of these materials is crucial in the initial stage of the design cycle, therefore, contained within this chapter are their requirements and characterisation. More specifically, the thermo-mechanical properties of pericardium, the nominal Poisson's ratio of a mesh structure and the effect of variable strain history on the cyclic tensile mechanical properties of nitinol wire are discussed.

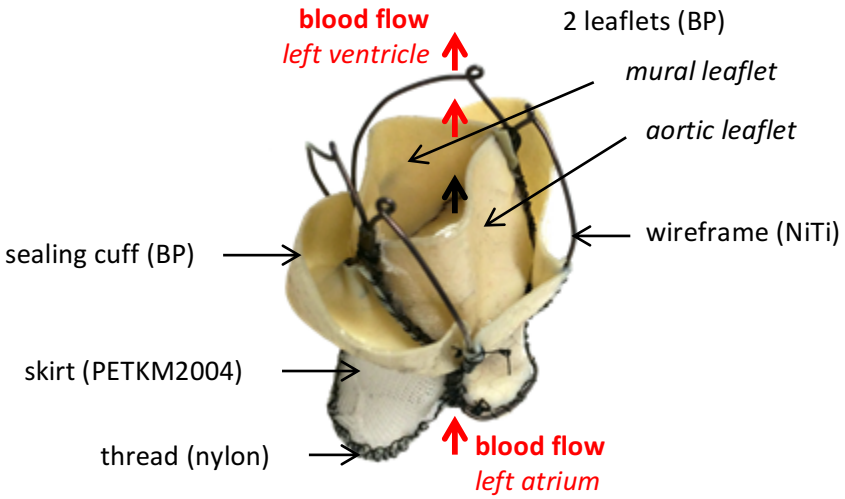

Figure 3.1: The UCL transcatheter mitral valve made from bovine pericardium (BP), nitinol (NiTi) wire and polyester knitted mesh (PETKM2004).

3.1 Pericardium

This section explains why pericardium was chosen for the prosthetic mitral valve leaflets, describes characterisation of its thermo-mechanical behaviour and identification of four parameters for an Ogden equation to model its constitutive stress-strain relationship, both in relation to developing bioprosthetic heart valves.

3.1.1 Requirements

The leaflets for the prototype prosthetic mitral valves had to be constructed from a material which has known successful clinical experience. Therefore glutaraldehyde (GA) fixed bovine pericardium (BP) soft tissue was chosen due to its common use in bioprosthetic heart valves and favourable hemodynamic performance (Hulsmann et al

2012). In general, prosthetic heart valves are required to withstand and perform well at a healthy body temperature[7] of approximately 37 ^{o}C and must not be damaged when at room temperature, 21 ^{o}C nor when folded into a catheter at 4 ^{o}C, the latter temperature being required to collapse the nitinol frame. Therefore, these temperatures are highly relevant for modelling and testing.

3.1.2 Characterisation

The mechanical behavior of pericardium tissue is complex; nonlinear, with nearly elastic behaviors over small strains, hysteresis over cyclic loads, creep under constant loads and stress relaxation at fixed deformations. The aim of this section, which describes the uniaxial characterisation of BP, is firstly to describe and quantify its thermo-mechanical behavior and secondly to provide data to identify four parameters for an Ogden hyperelastic material model for use in finite element analyses later.

Technically, pericardium is orthotropic and, therefore, in order to investigate its direction dependant properties, a biaxial tensile test would be required; for example Baek et al (2005) presented the first biaxial study on the stress relaxation behaviour of collagenous tissue before and after thermal damage. However, a uniaxial tensile test was sufficient to provide information for average behaviour, accurate enough to achieve aims previously described.

3.1.2.1 Thermo-mechanical behaviour

Cyclic uniaxial tensile tests have previously been conducted on GA fixed BP (Claramunt et al 2012, Trowbridge et al 1985) and its mechanical properties have been described as having a transition point (TP) between a more extensible and stiffer region (Black et al 1991, Trowbridge et al 1985) with various amounts of hysteresis (Claramunt et al 2012). However, the thermo-mechanical properties have not been reported and the strain at which the TP occurs has not been quantified, both of which are addressed in the study described below.

The thermo-mechanical behaviour of BP can be quantitatively described by changes in strain at a TP between an approximately linear region at small strains and non-linear (transition) region at higher strains (Figure 3.2). To identify the TP in an objective manner

[7] According to ISO 5840 the patient's body temperature may vary between 34 ^{o}C and 42 ^{o}C.

we defined it as the strain at the maximum of the second derivative of a four parameter equation, which models the stress-strain relationship for BP (Figure 3.2 and 3.3 and Equation 3.1).

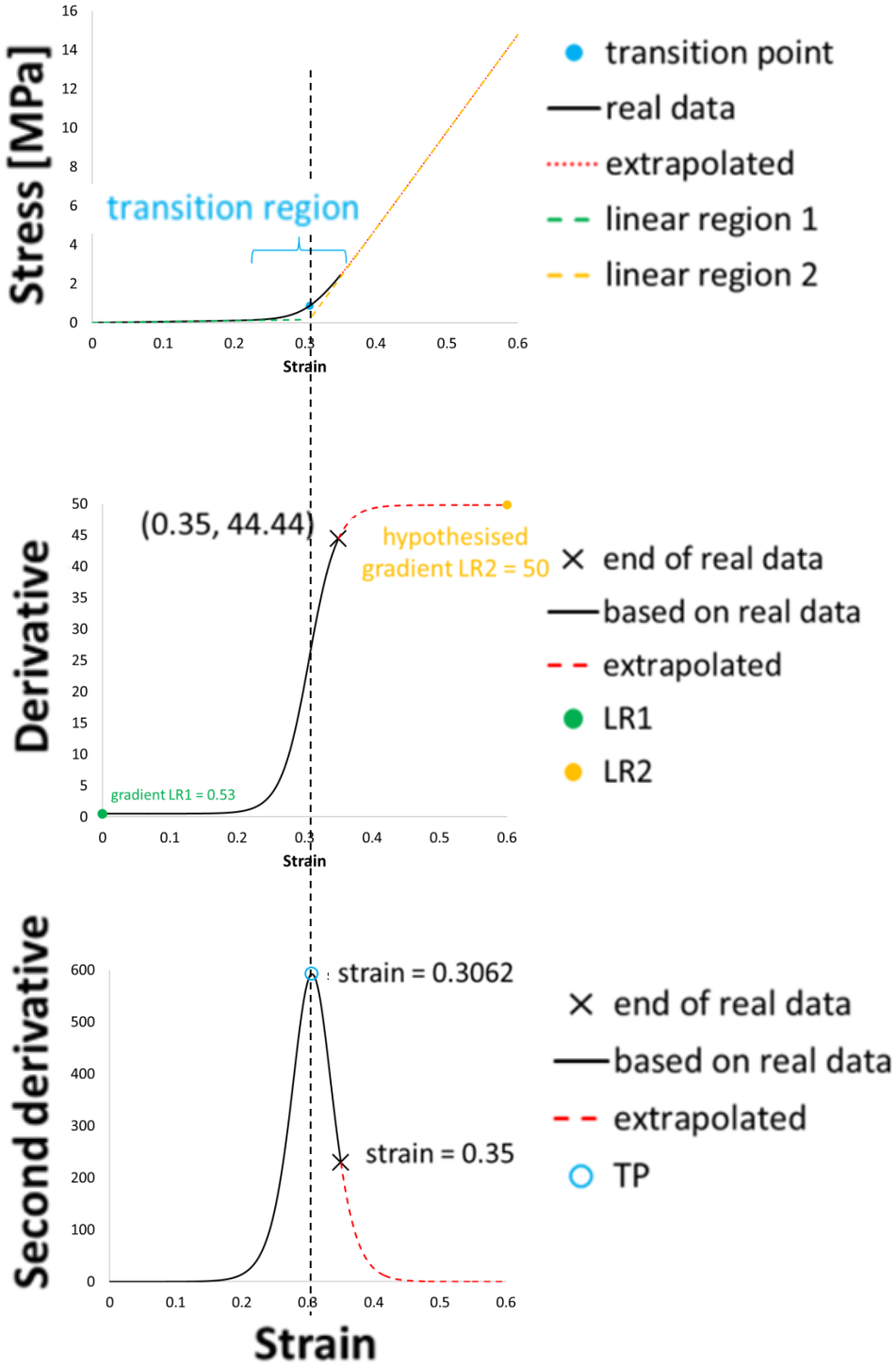

Figure 3.2: Definition of transition point for pericardium shown on original data **(top)** real data/soft tissue equation 3.1: definition of linear region 1 (LR1), transition point (TP) and theoretical linear region 2 (LR2) **(middle)** derivative of soft tissue equation 3.1 **(bottom)** second derivative of soft tissue equation 3.1.

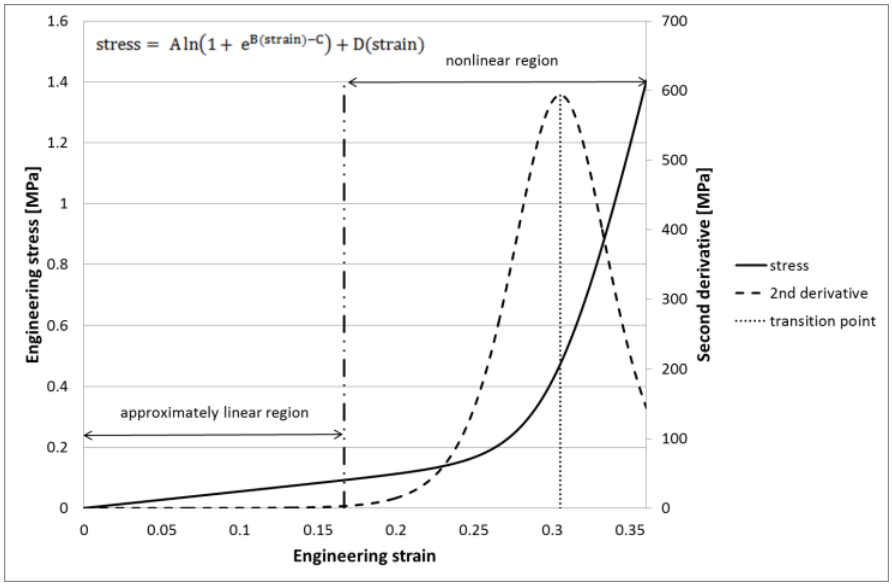

Figure 3.3: Characterisation of the strain vs stress relationship for pericardium using a transition point between an approximately linear region and the non-linear transition region which occurs prior to the theoretical second linear region which is not actually reached in the tests conducted.

The engineering stress is defined as;

$$\sigma = A \ln(1 + e^{B\epsilon - C}) + D\epsilon \tag{3.1}$$

where;

A = y-direction stretch/compression transformation of the integral of the logistic function (Equation 3.2) for A > 1 and A < 1 respectively,

B = x-direction stretch/compression transformation of the integral of the logistic function for 0 < B < 1 and B > 1 respectively,

ϵ = engineering strain,

C = translation in the positive x-direction of the integral of the logistic function, and

D = constant to multiply strain by to provide an initial straight line with a (0, 0) intercept.

This proposed 'soft tissue equation' is based on graphical transformations of the integral of the logistic function (Equations 3.2 and 3.3).

$$y = \frac{1}{1 + e^{-x}} \tag{3.2}$$

When integrated becomes;

$$\int y = \ln(1 + e^{x}) \tag{3.3}$$

The logistic function being the most common sigmoid function (Equation 3.4), chosen because it is a bound differential real function that is defined for real input values and has a positive derivative at each point.

$$f(x) = \frac{L}{1 + e^{-k(x-x_0)}} \tag{3.4}$$

Where;

x_o = x-value of the sigmoid's midpoint (0 for logistic function),

L = curve's maximum value (1 for logistic function), and

k = the steepness of the curve (1 for logistic function).

3.1.2.1.1 Protocol

A total of three dumbbells[8] were extracted from GA fixed BP patches using a die cutter and fixed in the clamps of a Zwick Z5.0 mechanical testing machine, with the aid of acetate templates (Figure 3.4), then submerged in a water bath at 4 ^{o}C and subjected to a mechanical cyclic test, with 10[foot note 9] conditioning and full cycles up to 3 and 6 N respectively. The conditioning cycles were done to remove the variation that occurs in the first cycles (Claramunt et al 2012) and the latter force was chosen because it induced stresses (approximately 3 MPa) similar to that experienced by bioprosthetic heart valve leaflets (Burriesci et al 1999, Black et al 1986). These cyclic tests were repeated a total of eight times on each of the three dumbbells according to the three temperature cyclic history shown in Figure 3.45. Then one of the samples was tested again a total of 19 times according to the ten-temperature cyclic history shown in Figure 3.4.

[8] A dumbbell shape was chosen as it had previously been used by the research group.

[9] The number of conditioning/full cycles, i.e. 10, was chosen based on the current protocol used by the research group.

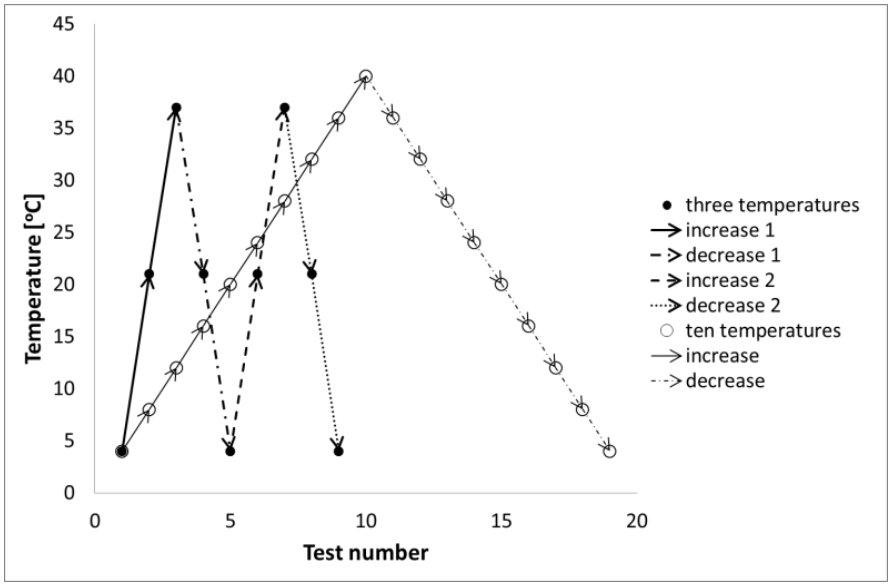

Figure 3.4: Cyclic temperature histories; three and ten temperature tests.

The temperatures chosen for the three temperature cyclic history were 4, 21 and 37 °C, corresponding to the temperature at which the device is crimped, prepared and functions at respectively. The ten temperatures chosen for the ten temperature test were chosen to provide an even number of data points between 4 and 37 °C.

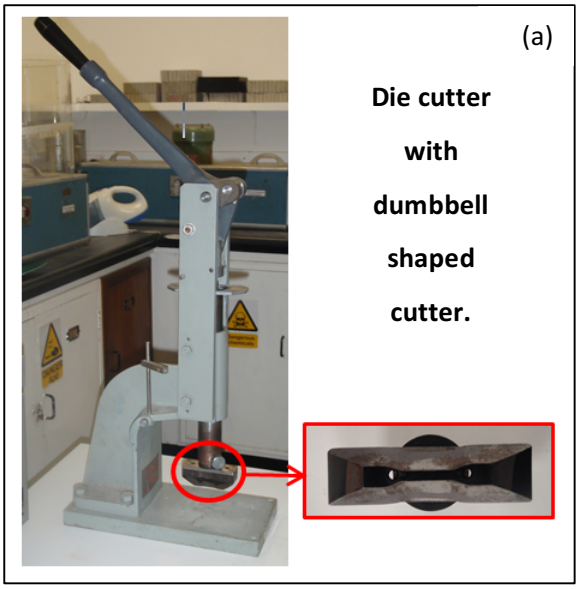

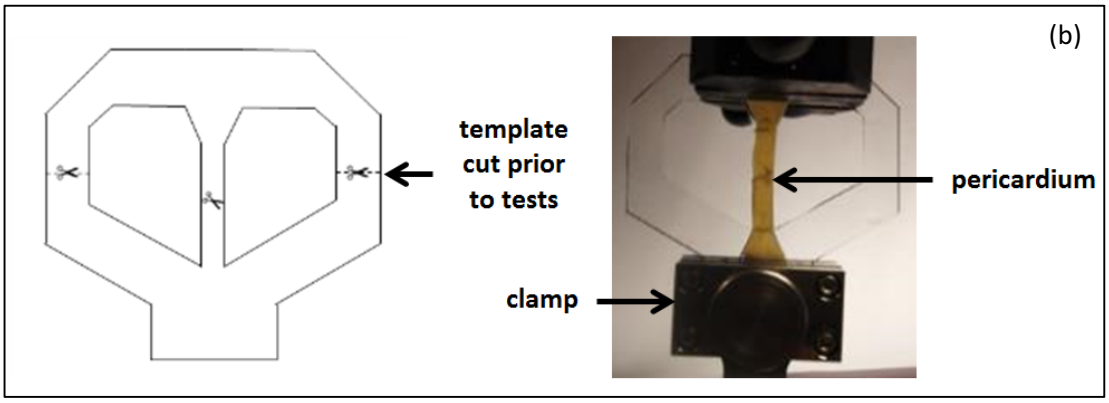

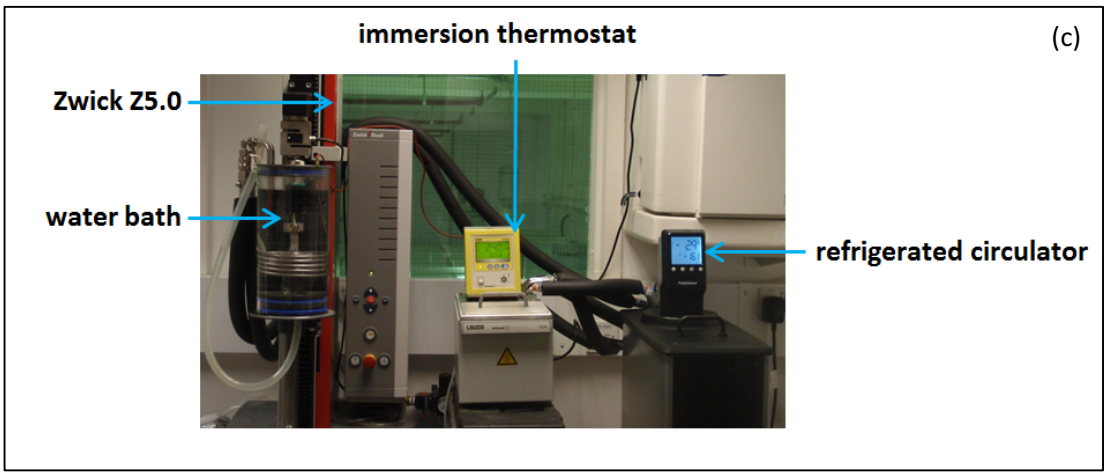

Figure 3.5: Uniaxial tensile test set up for measuring thermo-mechanical properties of pericardium **(a)** dumbbell die cutter **(b)** acetate template and dumbbell pericardium sample and template clamped in a Zwick Z5.0 **(c)** equipment; Zwick Z5.0, water bath, immersion thermostat and refrigerated circulator.

3.1.2.1.2 Analysis

A MATLAB script was written to find the parameters for the soft tissue equation 3.1 which fit the data for the 10 full cycles (approximately 6000 data points per loading/unloading cycle) in a least-squares sense i.e. the fit which minimised the sum of squared residuals (the difference between the observed value and the value predicted by the model); achieved using the '`lsqcurvefit`' function. Provided that initial estimates ≤ 5 integers from the final values were given, then the scrip (Appendix A) worked well. Test cycles with parameters greater than 1.5 standard deviations (Equation 3.5) from the associated mean were considered outliers and therefore excluded from further analysis. This criterion meant in each test there was an average of 5 and not less than 3 cycles used for the analysis. The parameters for these loading and unloading cycles were then averaged to represent each cycle with one curve (Figures 3.2, 3.3 and 3.6), the maximum of the second derivative of which indicated the TP. The mean and standard deviation of the hysteresis (Equation 3.6) was also calculated; the integrals for which were computed numerically using adaptive Simpson quadrature.

$$s = \sqrt{\frac{1}{N\text{-}1}\sum_{i=1}^{N}(x_i - \bar{x})^2} \tag{3.5}$$

$$h = \int_0^{\epsilon_{max}} \text{loading curve} - \int_0^{\epsilon_{max}} \text{unloading curve} \tag{3.6}$$

where ϵ_{max} is the maximum strain and h is the hysteresis.

3.1.2.1.3 Results and discussion

The four parameter soft tissue equation 3.1 fitted the data very well for both loading and unloading cycles (Appendix B, Figure B.2), with 'adjusted R^2' (Equation 3.7) values of at least 0.999, which on visual comparison was much better than the fit achieved by Zioupos and Barbenel (1994) and Rabkin et al (1975), however they did not report R^2 values so direct comparison is not possible. Although the parameters A, B, C and D did not correlate

significantly with changes in temperature, the gradient of the linear region and TP did and are discussed later.

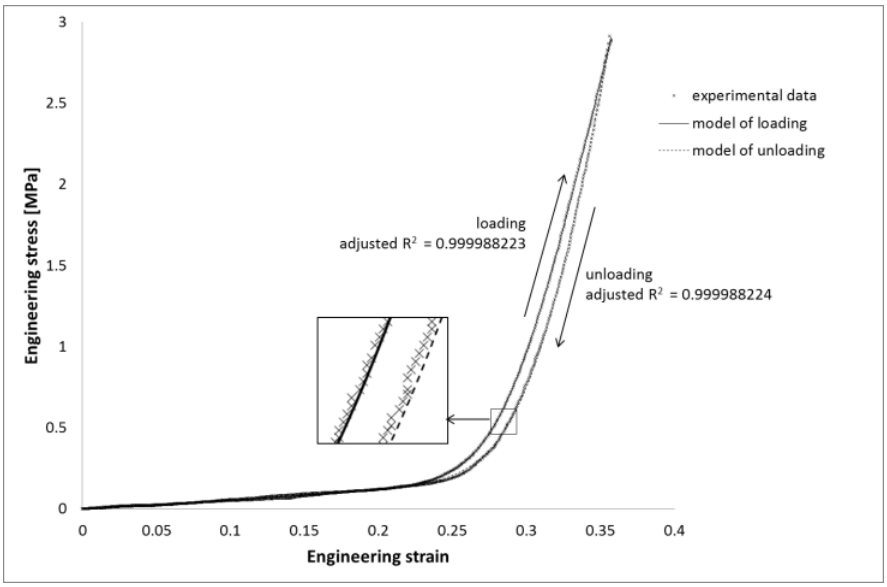

Figure 3.6: Example of soft tissue equation curve fit for loading and unloading curves of bovine pericardium dumbbell 1, test 1 at 4 °C, cycle 1.

$$\text{adj. } R^2 = 1 - \frac{SS_{res}/_{n-k}}{SS_{tot}/_{n-1}} \tag{3.7}$$

Where;

SS_{res} = sum of squares of residuals,

SS_{tot} = total sum of squares,

k = number of parameters, and

n = number of data points.

There was no statistically significant variation in the gradient of the initial highly elastic linear region for the three-temperature and the first increasing temperature cycle of the ten-temperature tests. However, there was a non-linear (3rd order polynomial) relationship for the second, decreasing, temperature cycle for the ten-temperature test (Appendix B, Figure B.3 and Table B.1).

All samples demonstrated that on average for 1 ^{o}C increase in temperature there was a statistically significant increase in the TP of 0.0004 (Appendix B, Figure B.4-B.6 and Table B.2). The average TP for dumbbell 2 was 0.2978 and was on average 6% and 43% higher for dumbbells 1 and 3 respectively (Appendix B, Figure B.5). This variation between dumbbells and even greater variation between patches was confirmed as significant at the 5% level using Student's t-tests (Appendix B, Table B.3) and the linear relationship was confirmed by the ten-temperature test (Appendix B, Figure B.6).

Furthermore, for all dumbbells the rate of change of TP with temperature decreased and remained constant after the first temperature cycle, for which the null hypothesis was rejected by a Student's t-test with a p-value of 0.04, and is therefore statistically significant at the 5% level (Appendix B, Figure B.4-B.6). However, the actual increase in TP between the first and remaining cycles was only significant at 4 and 21 ^{o}C (Appendix B, Table B.4). There was also a significant increase of the TP after 21 days storage at 4 ^{o}C in phosphate-buffered saline (PBS) (Appendix B, Table B.5).

The calculation of hysteresis was based on curves with 'adjusted R^{2}' values of at least 0.999, and therefore was a more accurate method compared to that used in Claramunt et al (2012), which achieved various coefficients of determination between 0.916 and 0.993. The three and ten-temperature tests revealed no significant variation in hysteresis with temperature or stress history, the later concurring with previous findings (Claramunt et al 2012). However, the three-temperature test did successfully indicate the natural and significant variation in hysteresis between patches ranging between 0.2 and 5.1 kPa, which was on average 24% lower for dumbbell 1 and 98% lower for dumbbell 3, the latter being from a different patch, when compared to dumbbell 2 (Appendix B, Table B.6). There was also a decrease in the hysteresis of dumbbell 2 after 21 days storage in PBS at 4 ^{o}C, although only significant at 21 and 36 ^{o}C with p-values of 0.005 and 0.0007 respectively.

3.1.2.1.4 Summary

1. Thermo-mechanical properties of pericardium

The stress-strain relationship for pericardium soft tissue can be modelled as approximately linear for small strains followed by a non-linear region using the four parameter 'soft tissue equation 3.1, the maximum of the second derivative of which can determine the strain at

the transition (TP) between the two regions and enables quantification of hysteresis between loading and unloading curves. More specifically:

- The linear region only varied with temperature after an initial temperature cycle from 4 to 40 ^{o}C (3rd order polynomial).

- In general the TP increased linearly with temperature at a rate of 0.0004 per ^{o}C and more specifically it:

    - varied between dumbbells and even more so between patches,
    - increased at 21 ^{o}C and 4 ^{o}C after an initial temperature cycle up to 37 ^{o}C,
    - increased with storage at 4 ^{o}C in PBS.

- The hysteresis varied between dumbbells and even more so between patches and storage at 4 ^{o}C in PBS decreased the hysteresis at 21 and 37 ^{o}C.

2. Implications for *in vitro* testing of bioprosthetic heart valves

Although the TP of pericardium is affected by temperature, on average the standard deviation of the transition point at 4, 21 and 37 ^{o}C was 0.007 ±0.0007 which is a factor of ten smaller than between patches; 0.06. Therefore, in terms of the TP, changes in the mechanical properties of pericardium due to temperature differences, in the range relevant for bio-prosthetic heart valves, are insignificant compared to variations that occur between patches and subsequently between prostheses.

Consequently, the *in vitro* assessment of bio-prosthetic heart valves can justifiably be conducted at room temperature, rather than a body temperature of 37 ^{o}C. In fact, in terms of using a working fluid, i.e. the fluid in the pulse duplicator, with a similar kinematic viscosity to blood (2.8 – 3.8 m^2/s x 10^{-6}) water at 21 ^{o}C (0.98 m^2/s x 10^{-6}) is more similar than if heated to 37 ^{o}C (0.70 m^2/s x 10^{-6}). Furthermore, any particular pulse duplicator set-up is only accurate in providing comparative data (Simenauer et al 1987), therefore the same comparative conclusions would be drawn whether tested at an elevated temperature or not. However, the impact of temperature on the material properties of the other components of the bioprosthetic valve would have to be considered.

In summary, increase in temperature, a cyclic temperature history and storage all make pericardium tissue less stiff. However, due to variation in the thermo-mechanical properties

between patches used to make individual bioprosthetic heart valves, the effect of temperature is negligible. Therefore, *in vitro* testing of bioprosthetic heart valves at room temperature is acceptable in terms of its effect on the leaflets mechanical properties.

3.1.2.2 Ogden model

The Ogden constitutive equation was chosen instead of, for example, a neo-Hookean[10] or any other Mooney Rivlin equations, because it models the hyperelastic, non-linear stress-strain behaviour of complex materials such as rubbers, polymers and biological soft tissue. It assumes the material behaviour can be described by means of a strain energy density function, from which the stress-strain relationship can be derived. The properties of blood vessel wall tissues can be approximated as isotropic (Lally et al 2004) and, therefore, the same approach has been followed as a first approximation. Furthermore, pericardium can generally be approximated as incompressible and strain rate independent, allowing for several simplifications to the Ogden equation.

3.1.2.2.1 Aim

Four parameters for an Ogden model were identified from the previously described uniaxial tensile test data for BP. The aim was to implement this as a finite element material model to simulate the mechanical behaviour of the proposed bio-prosthetic mitral valve leaflets described in Chapter 4.

3.1.2.2.2 Calculation

In the Ogden model, the strain energy density (W) (Equation 3.8) is expressed in terms of the principal stretches: $\boldsymbol{\lambda_1, \lambda_2 \text{ and } \lambda_3}$ (Figure 3.7) and material constants $\boldsymbol{\mu_p}$ and $\boldsymbol{\alpha_p}$, where the stretch/extension ratio ($\boldsymbol{\lambda}$) is defined in terms of the final and original lengths, L and L_o respectively (Equation 3.9).

$$W(\lambda_1, \lambda_2, \lambda_3) = \sum_{p=1}^{N} \frac{\mu_p}{\alpha_p} (\lambda_1^{\alpha_p} + \lambda_2^{\alpha_p} + \lambda_3^{\alpha_p} - 3) \qquad (3.8)$$

[10] The neo-Hookean, a special case of the Mooney Rivlin, constitutive relationship has a characteristic plateau at higher strains which is not representative of pericardium.

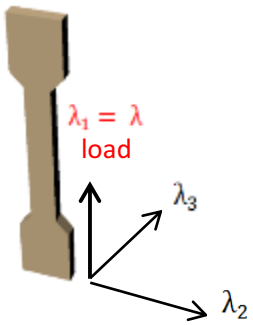

Figure 3.7: Direction of principal stretches for pericardium dumbells subjected to uniaxial tensile tests.

$$\lambda = \frac{L}{L_o} \tag{3.9}$$

To identify the constants for a four parameter Ogden model the order of bulk modulus, N, was set to two in Equation 3.8 such that it results in Equation 3.10 which requires four constants to be identified.

$$W = \left(\frac{\mu_1}{\alpha_1}\right)\left(\lambda_1^{\alpha_1} + \lambda_2^{\alpha_1} + \lambda_3^{\alpha_1}\text{-}3\right) + \left(\frac{\mu_2}{\alpha_2}\right)\left(\lambda_1^{\alpha_2} + \lambda_2^{\alpha_2} + \lambda_3^{\alpha_2}\text{-}3\right) \tag{3. 10}$$

To fit the model to the experimental data three assumptions were made. Firstly pericardium was assumed to exhibit isotropic behaviour (the same material properties in all directions) and so λ_1 and λ_2 were considered to be equal (Equation 3.11).

$$\lambda_2 = \lambda_3 \tag{3. 11}$$

Secondly, it was assumed to be incompressible (i.e. no change in volume) such that the determinant of the deformation gradient tensor F becomes equal to the Jacobian (J) and equal to 1 (Equation 3.12).

$$F = \begin{bmatrix} \lambda_1 & 0 & 0 \\ 0 & \lambda_2 & 0 \\ 0 & 0 & \lambda_3 \end{bmatrix} \tag{3.12}$$

$$\det(F) = 1 = \lambda_1\lambda_2\lambda_3 \tag{3.13}$$

The calculation of the above determinant can be simplified using the isotropic assumption (Equation 3.11 and 3.14-3.16).

$$\lambda_1\lambda_2^2 = 1 \tag{3.14}$$

$$\lambda_2 = \frac{1}{\sqrt{\lambda_1}} \tag{3.15}$$

$$\lambda_3 = \lambda_2 = \frac{1}{\sqrt{\lambda_1}} \tag{3.16}$$

This results in simpler equations for the principal stretches (Equations 3.17-3.19);

$$\lambda_1 = \lambda \tag{3.17}$$

$$\lambda_2 = \frac{1}{\sqrt{\lambda}} \tag{3.18}$$

$$\lambda_3 = \frac{1}{\sqrt{\lambda}} \tag{3.19}$$

which when substituted into Equation 3.8 the strain energy density becomes;

$$W(\lambda) = \sum_{p=1}^{N} \frac{\mu_p}{\alpha_p}(\lambda^{\alpha_p} + \left(\frac{1}{\sqrt{\lambda}}\right)^{\alpha_p} + \left(\frac{1}{\sqrt{\lambda}}\right)^{\alpha_p} \text{-}3) \tag{3.20}$$

In general, the shear modulus (μ) (Equation 3.21) results from the constants of the Ogden model.

$$2\mu = \sum_{p=1}^{N} \mu_p \alpha_p \tag{3.21}$$

Then using the Ogden material model, the three principal Cauchy stresses (Equation 3.22) can now be computed (Equations 3.23-3.25).

$$\sigma = \begin{bmatrix} \sigma_{11} & \sigma_{12} & \sigma_{13} \\ \sigma_{21} & \sigma_{22} & \sigma_{23} \\ \sigma_{31} & \sigma_{32} & \sigma_{33} \end{bmatrix} \tag{3.22}$$

$$\sigma_{11} = p + \lambda_1 \frac{\partial W}{\partial \lambda_1} \tag{3.23}$$

$$\sigma_{22} = p + \lambda_2 \frac{\partial W}{\partial \lambda_2} \tag{3.24}$$

$$\sigma_{33} = p + \lambda_3 \frac{\partial W}{\partial \lambda_3} \tag{3.25}$$

The third assumption is that pericardium tissue is a membrane and therefore the third principal Cauchy stress is effectively zero (Equation 3.26).

$$\sigma_{33} = p + \lambda_3 \frac{\partial W}{\partial \lambda_3} = 0 \tag{3.26}$$

Therefore, a value for p can be obtained (Equation 3.27).

$$p = -\lambda_3 \frac{\partial W}{\partial \lambda_3} \tag{3.27}$$

Substituting Equation 3.27 into Equation 3.4 gives Equation 3.28.

$$\sigma_{11} = \lambda_1 \frac{\partial W}{\partial \lambda_1} - \lambda_3 \frac{\partial W}{\partial \lambda_3} \tag{3.28}$$

The derivatives for Equation 3.28 are calculated from Equation 3.10 as in Equations 3.29 and 3.30.

$$\frac{\partial W}{\partial \lambda_1} = \mu_1 \left(\lambda_1^{(\alpha_1 - 1)}\right) + \mu_2 \left(\lambda_1^{(\alpha_2 - 1)}\right) \tag{3.29}$$

$$\frac{\partial W}{\partial \lambda_3} = \mu_1 \left(\lambda_3^{(\alpha_1 - 1)}\right) + \mu_2 \left(\lambda_3^{(\alpha_2 - 1)}\right) \tag{3.30}$$

The extension of the pericardium dumbbells was measured by the Zwick tensile testing machine and so the first principal stretch was known (original length of the test section was 20 mm) and so the second and third could be calculated.

The above equations (Equations 3.18-3.20 and 3.27-3.29) were implemented in Excel to minimise the sum of the difference squared (Equation 3.31) between the first principal experimental ($\sigma_{11,\exp}$) and Cauchy true stresses (σ_{11}).

$$\sum \Delta\sigma^2 = \sum (\sigma_{11,\exp} - \sigma_{11})^2 \tag{3. 31}$$

The resulting four parameters for the Ogden model are displayed on Figure 3.8 and were used to study the impact of different aortic valve calcification patterns on the outcome of transcatheter aortic valve implantations (Sturla et al 2016).

In summary, the four parameter 'soft tissue equation' (equation 3.1) modelled the engineering stress-strain relationship for BP reasonably well and enabled the quantitative study of its thermo-mechanical properties; becoming less stiff at higher temperatures, although the difference is not significant enough to warrant *in vitro* testing of bioprosthetic valve leaflets at body temperature. Despite this derived engineering relationship having a better fit compared to the four parameter Ogden model identified, with 'adjusted R^{2}' values of 0.999 and 0.981 respectively, the true stress-strain represented by the latter model was required for the finite element analysis of the non-linear behaviour because the engineering stress-strain does not represent the physics at large strains, where the

instantaneous area of the cross section is significantly different to the original. Therefore, the Ogden model was used in the finite element analyses described in Chapter 4.

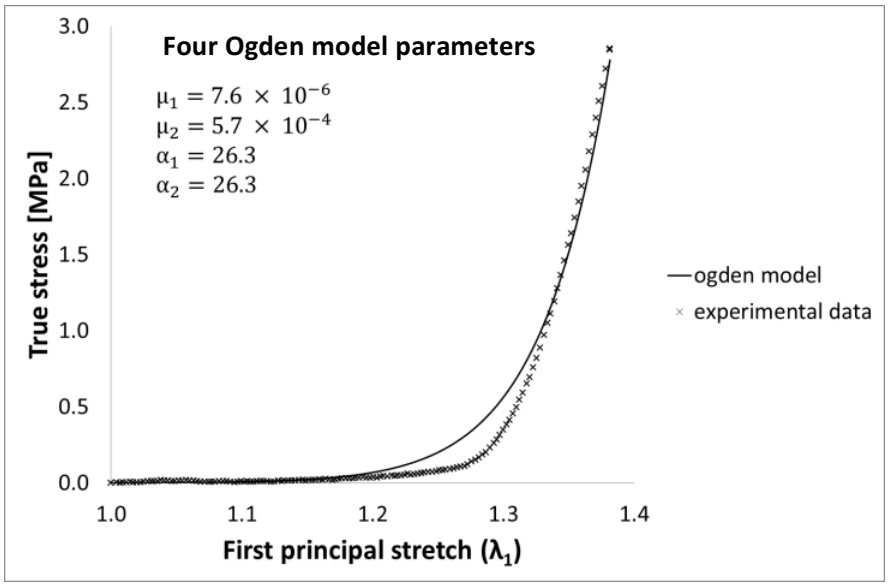

Figure 3.8: Ogden material model compared to experimental data for a uniaxial tensile test of bovine pericardium.

3.1.3 Harvesting and chemical processing of pericardium

To generate an inert biomaterial from a xenogeneic origin the xenogeneic antigen epitopes present in, for example, bovine pericardium (BP) must either be removed or masked to minimise immunological reactions from a patient's body. This can be achieved by decellularisation or masked using chemical crosslinking methods such as glutaraldehyde (GA) treatment; a 0.5% solution being standard (Hulsmann et al 2012). The protocol and equipment made for processing BP used to make prototype mitral valves is described below.

BP sacs were cut to lay flat on a workbench and any fat and parietal pericardium, which attaches fat to the fibrous pericardium, were removed by hand (Figure 3.9).

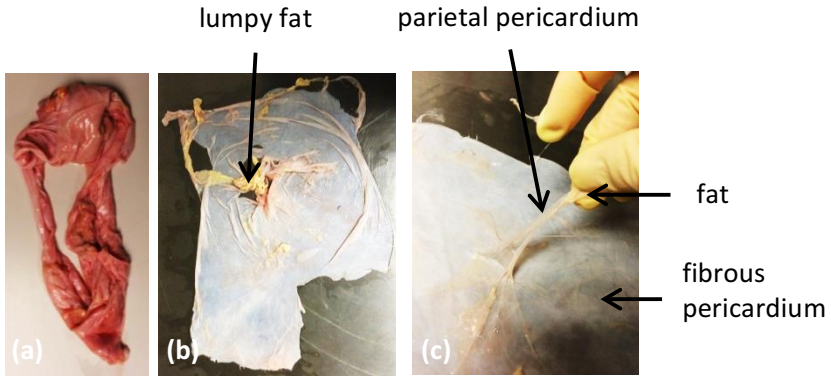

Figure 3.9: Bovine pericardium manual processing **(a)** whole sac **(b)** dissected sac **(c)** fat and parietal pericardium removal from fibrous pericardium.

Number grid patches were printed onto the glued side of overhead projector acetate, transferred onto the nearly dry and smoothest sections of pericardium and cut-out. Their thickness was measured three times at each location using a thickness gauge (Mitutoyo Corporation, Tokyo, Japan) specially adapted for pericardium; with the addition of a 3D printed resin circular plunger head whilst submerged in saline (Figure 3.10). The new plunger head being preferable to the original metal one which would have cut through the soft tissue.

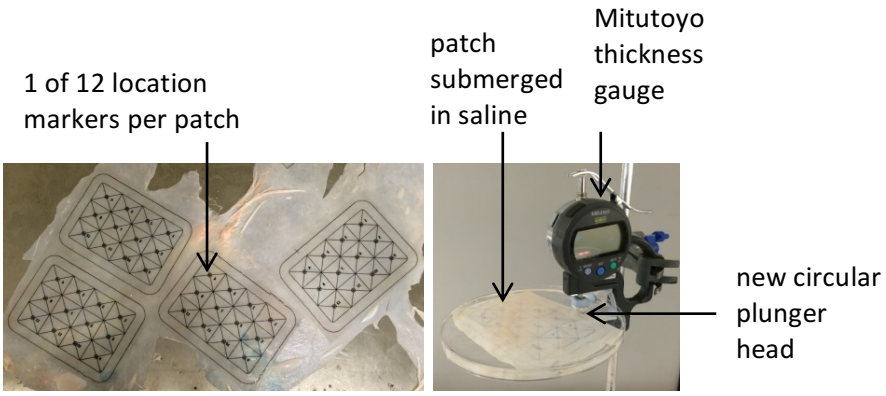

Figure 3.10: Bovine pericardium patch preparation **(left)** patch selection **(right)** thickness measurement using an adapted Mitutoyo thickness gauge.

Magnetic frames, based on a design previously used by the research group, were made by gluing together laser cut Perspex® (Universal Laser Systems Inc.) (Figure 3.11), were then used to keep the pericardium taut during fixation in a 0.5% solution of GA for 48 hours. Due to this wet and salty environment the magnets would be prone to rusting; therefore a novel protective layer of silicone was added to the design to increase durability (Figure 3.11).

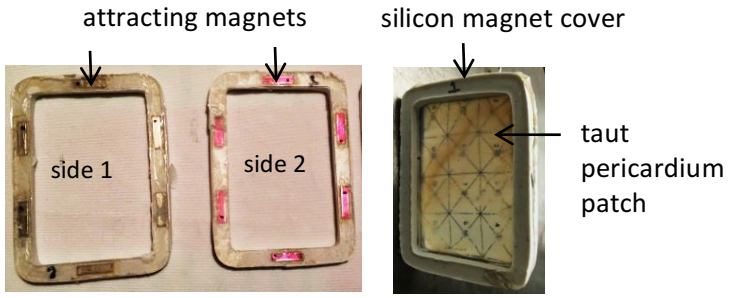

Figure 3.11: Magnetic frames **(left)** two sides of frames separate **(right)** two side of frames holding a pericardium patch taut.

The thickness of nine pericardium patches was measured again after fixation (Figure 3.12 and Appendix C); average thickness becoming 0.35 ± 0.11 mm and ranged between 0.18 and 0.69 mm, the average increase compared to before fixation was 0.04 ± 0.03 mm the average value before fixation was 0.31 ± 0.06 mm. Theses variations are statistically significant because they are greater than the average error between three measurements taken in a single location, which was 0.01 mm. The thickness/location data for fixed patches was later used to select regions 0.4 mm thick for making prototype mitral valve leaflets.

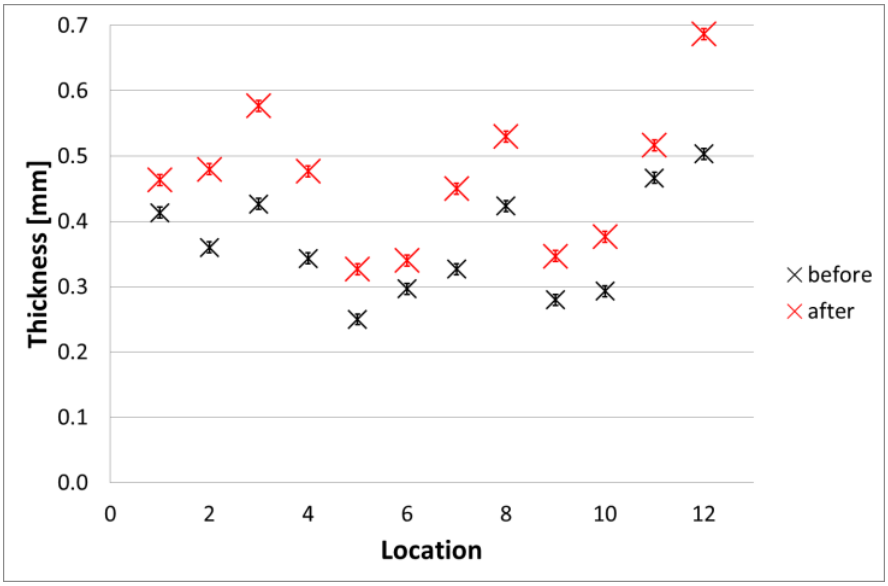

Figure 3.12: Effect of glutaraldehyde fixation on the thickness of bovine pericardium, patch 1 see Appendix B for results for patches 2 to 9 (there were no errors in the locations measured).

3.2 Polyester mesh

This section describes the requirements and characterisation of polyester knitted mesh used for the skirt regions of the UCL TMV (Figure 3.1). This research into the characterisation of mesh structures is also relevant for the characterisation of other meshes used in clinical practice.

3.2.1 Requirements

The skirt region of the UCL TMV is required to extend in the axial direction by approximately 65% when the device is fully crimped (Figure 1.15) (estimated from CAD model). In order to minimise the collapsed diameter of the device, to reduce damage to surrounding tissue during implantation, the skirt region would ideally also contract in the transverse direction. Therefore, a biocompatible mesh structure was identified as a suitable material.

A total of twelve biocompatible polyester knitted and woven meshes were considered (Textile Development Associates Inc.) (Figure 3.13). The woven meshes were not suitable due to their inextensibility; therefore one of the knitted meshes, PETKM2004, was chosen because it had the smallest pore size compared to the other knitted meshes. There are numerous reasons why the smallest pore size was advantageous for the UCL TMV:

- It better facilitated secure suture retention for attachment to the wireframe.
- The more dense structure of mesh better distributes the gentle anchoring force over the annulus compared to a more sparse structure of meshes with larger pores.
- For the purpose of *in vitro* assessment, and therefore in the absence of tissue ingrowth, smaller pore sizes would be advantageous in terms of minimising regurgitation.

The ability of PETKM2004 to meet the required extension was subsequently characterised as described in the following section.

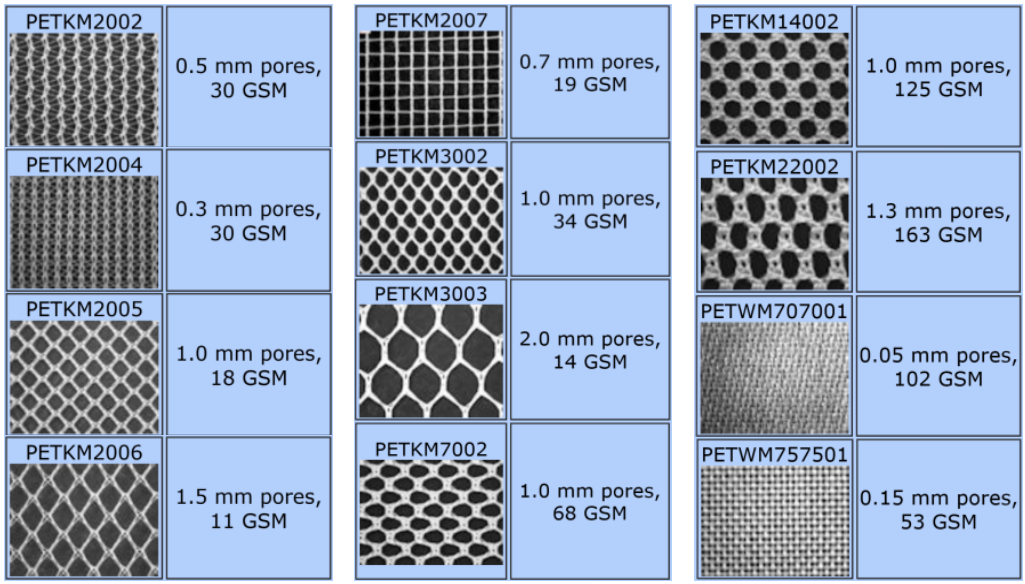

Figure 3.13: Polyester meshes from Textile Development Associates, Inc. (GSM = grams per square meter) (http://www.surgicalmesh.com/pet_mesh.htm, 9/10/16).

3.2.2 Characterisation

Biocompatible synthetic meshes are commonly used to treat ventral hernias[11] and their general mechanical properties have been characterised (Ibrahim et al 2015). However, the nominal Poisson's ratio i.e. that associated with the mesh structure has not previously been measured and is of critical importance for crimping the UCL TMV because as the frame is folded the mesh must elongate in the axial direction of the device and contract in the transverse direction (Figure 3.14).

[11] A ventral hernia is a buldge through an opening in the muscles of the abdomen.

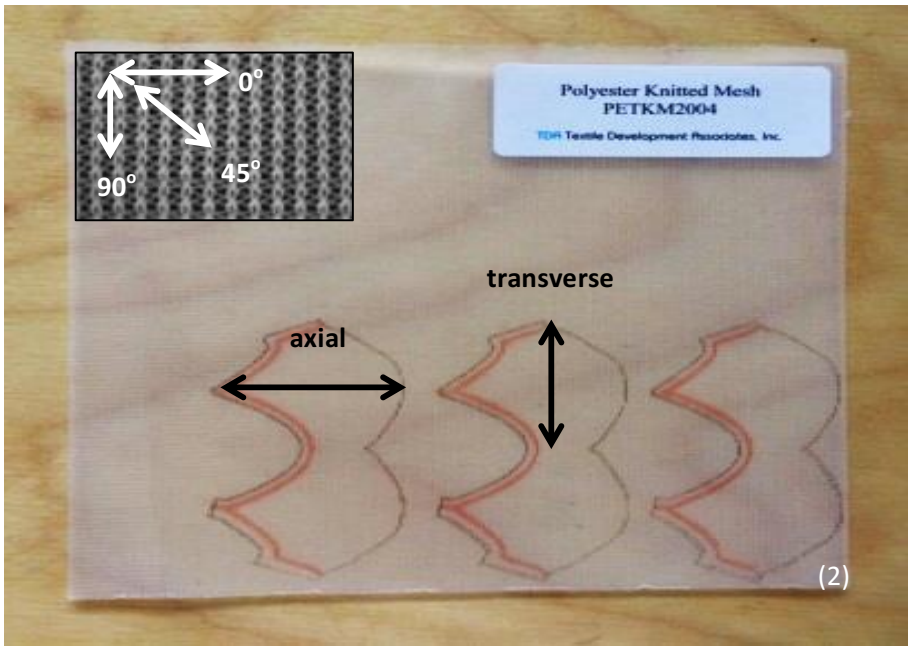

Figure 3.14: PETKM2004 sample orientation **(1)** magnification of mesh structure (http://www.surgicalmesh.com/pet_mesh.htm, 9/10/16) **(2)** orientation of skirt cutting pattern on sample.

3.2.2.1 Uniaxial tensile tests

Initial uniaxial tensile tests were done to the required 65% extension (section 3.2.1) for three orientations of the PETKM2004 mesh; 0°, 45° and 90° (Figure 3.14Figure 3.15), which identified the 0° orientation to be the most extensible and therefore most suitable for axial orientation in the UCL TMV skirt.

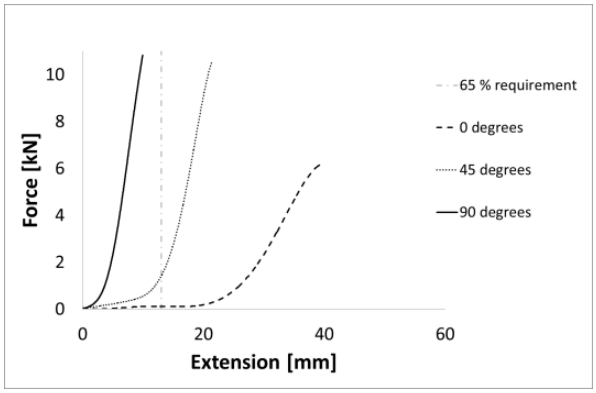

Figure 3.15: Uniaxial tensile test to failure for 3 orientations of PETKM2004 measured using a Zwick Z5.0 mechanical testing machine.

To confirm the PETKM2004 samples had not slipped in the uniaxial clamps and that it was the mesh structure rather than the polyester material properties that were measured and to enable calculation of the nominal Poisson's ratio, a sample at 0^{o} was mounted on a bi-axial mechanical testing machine (BioTester, CellScale Biomaterials Testing) using BioRakes, which allowed lateral movement (Figure 3.16), and was extended to 70%, demonstrating it could in fact exceed the requirement.

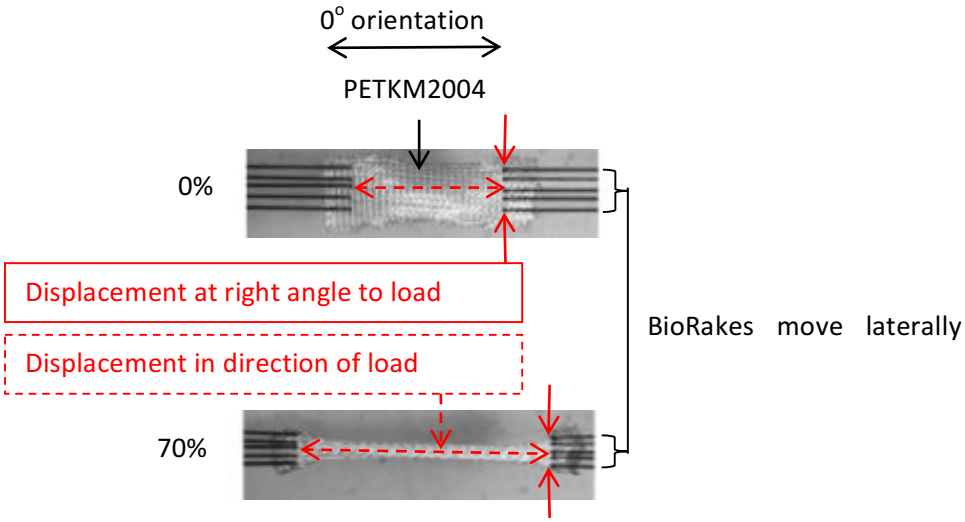

Figure 3.16: Biaxial tensile test (BioTester, CellScale Biomaterials Testing) of PETKM2004 cut at 0^{o} from sample indicating locations to measure displacements for nominal Possion's ratio.

3.2.2.2 Nominal Poission's ratio

Firstly, it should be noted that when a Poisson's ratio is describing a material it cannot be greater than 0.5 due to the requirement that Young's modulus, shear modulus and bulk modulus have positive values[12]. However, here it is applied to a mesh structure rather than the material itself.

The nominal Poisson's ratio (Equation 3.32) of the PETKM2004 mesh structure was 2.7, based on relative axial and transverse dimensions of the sample, measured relative to the BioRakes as indicated in Figure 3.16 from the BioTester video footage. In practice, this means that when the TMV is loaded into a catheter, the axial dimension of the skirt will extend from approximately 21 to 32 mm and decrease from 33 to 26 mm in the transverse

[12] Interestingly, some materials have negative Poission's ratios, called auxetic materials, and are being researched by the UCL Cardiovascular Engineering Laboratory (Karnessis et al 2013, Burriesci et al 2007, Scarpa et al 2003, Smith et al 2002).

direction. Therefore, two sections of skirt material of approximately 2.6 cm wide and 0.14 mm thick need to fit inside the catheter along with the other components.

$$\nu = \frac{\mathrm{d} \in_{\mathrm{trans}}}{\mathrm{d} \in_{\mathrm{axial}}} \tag{3. 32}$$

Where;

$d \in_{trans}$ = strain in direction of load, and
$d \in_{axial}$ = strain at right angle to load.

3.3 Nitinol wire

This section explains how nitinol wire fulfils the requirements for the UCL TMV frame and describes its characteristic mechanical behaviour aided by an investigation into the effect of cyclic uniaxial variable strain history tensile tests. An exemplar analysis for determining the material properties for use in finite element analyses of the nitinol frame, which simulated its collapse into a catheter (Bozkurt et al 2016), is provided as background information. Lastly, the limitations associated with using Nitinol are described.

3.3.1 Requirements

It is arguably preferable for the frame of any TMV to be self-expanding rather than balloon-expanding because the radial forces associated with the latter are not appropriate for the mitral position. Furthermore the frame of a TMV should be made from a material with known successful clinical experience, both of which have been achieved by the nitinol stented CoreValve (Medtronic Inc.) TAV device (Liao et al 2016) and is popular in second generation and investigational devices (Kheradvar et al 2015, Preston-Maher et al 2015). However, the CoreValve stent is significantly different to the UCL TMV because it is laser cut from a nitinol tube, rather than constructed from a single wire, and also has a diamond mesh structure rather than the relatively light-frame structure of the UCL TMV. That said; it is also arguable that the control one has over the radial force produced by balloon-expandable devices is advantageous to the uncontrolled and therefore variable radial forces induced by self-expanding devices. The superelastic abilities of nitinol enable it to be

crimped to a diameter ≤ 8 mm, smaller diameters being associated with reduced damage to surrounding tissues during transcatheter implantation. Lastly, it should also be repositionable and possible to re-start the implantation procedure, i.e. retrievable, all of which were previously shown to be feasible with the nitinol wireframe design of the UCL TAV (Rahmani et al 2013, Burriesci et al 2012, Burriesci et al 2010, Ghanbari et al 2008), on which the UCL TMV frame is based.

3.3.2 Characterisation

Nitinol (NiTi), a composite metal of Nickel (Ni) and Titanium (Ti), is characterised by shape memory (Huang et al 2003), superelasticity, stress hysteresis and damping. Its material properties are non-linear, path and temperature dependant; determined by the specific composition and thermo-mechanical processing. Its superelasticity is achieved by its ability to inter-change its crystal structure between austenite (simple cubic) and martensite (body-centered tetragonal), this reversible solid-state phase transition therefore differs from conventional elasticity achieved by stretching of atomic bonds. In the absence of stress, the martensitic transformation of nitinol can also be induced by temperature changes, resulting in shape memory (Stoeckel et al 2008, Duerig et al 2000).

As in most biomedical applications, the fatigue behaviour of nitinol is highly relevant due to the cyclic loads often induced and more specifically is relevant for the repeatable loading/deployment of the UCL TMV. The highly complex fatigue behaviour of nitinol has recently been reviewed (Mahtabi et al 2015). However, they do not mention the investigation into the effect of cyclic variable strain amplitudes, conducted by Lin et al (2012). In fact, this appears to be the only research into the effect of cyclic variable strain history for nitinol, which assessed the fatigue life of stent-like diamond and Z-shaped nitinol specimens. The investigation, described in the following sections, into the effect of cyclic uniaxial variable strain history tensile tests on the mechanical properties of nitinol wire assesses the induced variation in mechanical properties (rather than fatigue) and uses a different specimen shape (a single nitinol wire) compared to those used by Lin et al (2012) and Schlun et al (2011).

3.3.2.1 Aim

The aim was to investigate how the mechanical properties of nitinol wire are affected by a series of cyclic uniaxial tensile tests up to various maximum strains. The results from which also provided exemplar data for explaining the material properties of nitinol wire and their derivation for use in numerical simulations used to optimise the UCL TMV frame (Bozkurt et al 2016).

3.3.2.1 Protocol

A nitinol wire[13], 70 mm long 0.45 ± 0.0004 mm diameter was subjected to 5 cyclic loads up to strains of 2, 4, 6, 8 and 10%, using the Zwick Z5.0 mechanical testing machine at room temperature. These tests were done prior to the UCL TMV prototypes being made and samples of the optimised wire used for the UCL TAV were not available; therefore, the sample tested was one of the suboptimal wires for the UCL TAV.

3.3.2.1 Results and Discussion

3.3.2.1.1 Hysteresis

The typical stress hysteresis for nitinol (Figure 3.17) and associated hyperelastic behaviour was observed in the sample tested. Initially, the stress increased linearly with strain after which there was a loading plateau, characterised by small increases in stress for relatively large increases in strain (Figure 3.17). In the cases of strains ≥ 7% the end of the loading plateau was reached and linear extension of the martensitic phase was observed (Figure 3.18). As the strain began to reduce, the stress decreased rapidly until an unloading plateau was reached (Figure 3.17), which recovered the strain with only small decreases in stress. Finally, the last portion of strain was recovered linearly, although, when strained to 10% the final linear region is no longer co-linear with the initial linear region, which interestingly is characteristic of nitinol when tested at a temperature T, which is $M_f < T < A_f$; where M_f is the martensitic finish temperature (below this the nitinol is fully martensitic) and A_f is the austenitic finish temperature (above which the nitinol is austenitic) (Mahtabi et al 2015).

[13] The nitinol wire (Fort Wayne Metals Ireland Limited) had the following chemical composition (percent): C(0.0240), Cr(0.0014), Ni(55.96), Fe(0.0110), Ti(Bal), Cu(0.0014), Co(0.004), H(0.0005), O(0.0263) and austenitic peak temperature -17 ^{o}C.

3.3.2.1.2 Stress relaxation and memory

Stress relaxation occurred as the sample was repeatedly cycled to each maximum strain; for example, the upper plateau strength (UPS) for the fifth cycle to 6% strain was 7 MPa less than for the first cycle (Figure 3.18). The samples also demonstrated memory of the "relaxed" UPS for the first cycle of the consecutive series of cyclic tensile tests to a higher maximum strain, but once the strain exceeded that previously experienced there was a step increase (Figure 3.19) in the UPS back to the same stress level (σ_S^{AS}) associated with the very first cycle to 2%.

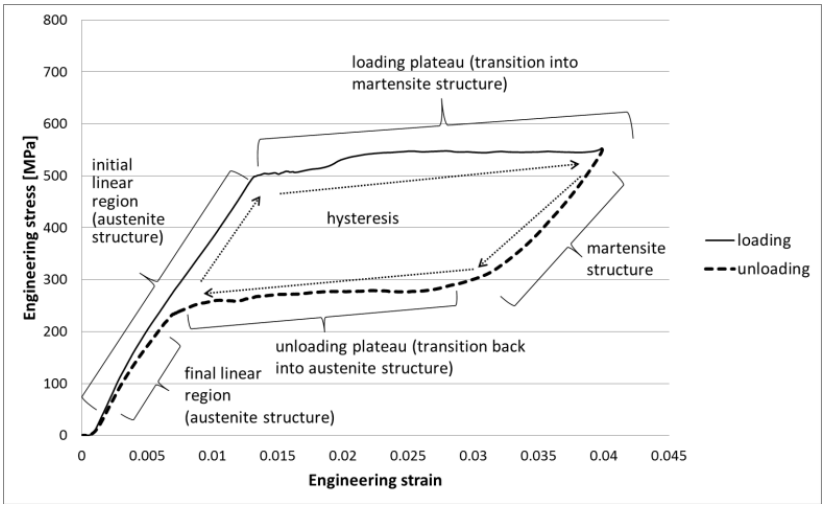

Figure 3.17: Stress-strain relationship showing the superelastic transformation of a nitinol wire up to 4% strain, average of 5 cycles.

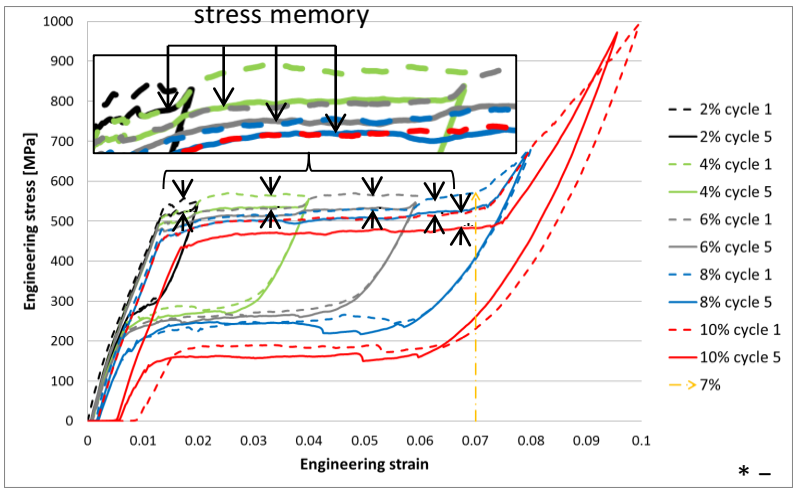

Figure 3.18: Stress-strain relationship for nitinol wire for maximum strains of 2, 4, 6, 8 and 10% showing just the first and last cycles for each, demonstrating stress relaxation over cyclic loads to a specific strain, and stress memory.

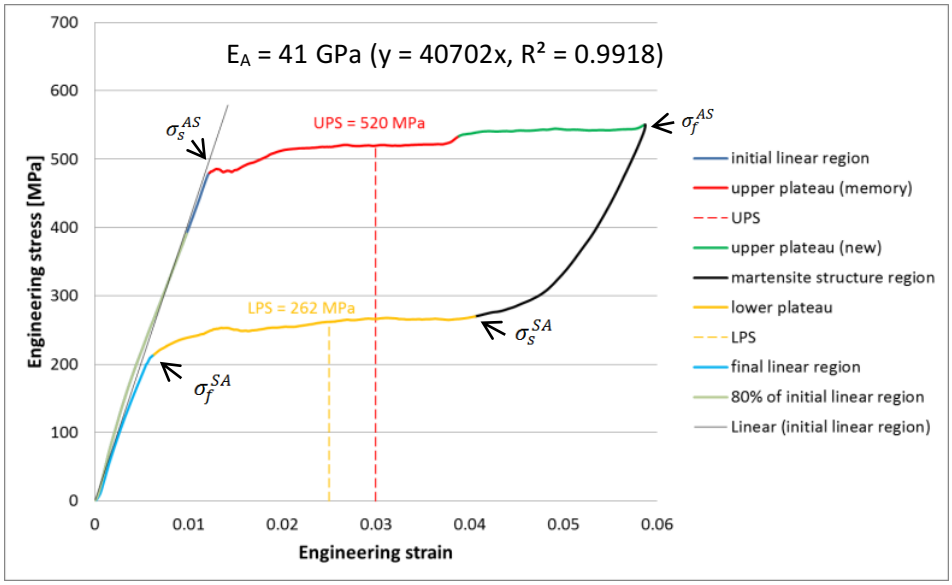

Figure 3.19: Stress-strain relationship for nitinol wire up to 6% strain, average of 5 cycles, indicating the definition of properties for mathematical modelling and simulation.

3.3.2.1 Properties for mathematical modelling

This section presents an example of how the material properties for nitinol wire were determined for use in numerical model optimisation of the nitinol frame which simulated its collapse into a catheter (Bozkurt et al 2016). The values in the table below correspond to nitinol wire strained to 6% (Figure 3.19).

Table 3.1: Exemplar material properties for nitinol wire strained to 6%.

Material Property	Definition	Exemplar values
Upper plateau strength (UPS)	stress at 3% strain during loading	520 MPa, slightly higher than the UPS used to model the CoreValve nitinol stent by Tzamtzis et al (2012); 390 MPa
Lower plateau strength (LPS)	stress at 2.5% strain during unloading	262 MPa
Residual elongation (El_r)	difference between the strain at a stress of 7 MPa during unloading and loading	0.014%
Ultimate tensile strength (UTS)	maximum stress sustained just prior to necking, or fracture, or both	The UTS and associated **uniform elongation (El_u)** were not reached.
Young's Modulus for the initial austenite region (E_A)	slope of 80% of the stress-strain curve up to the UPS	41 GPa
Young's Modulus of the later martensitic region (E_M)	slope of 80% of the curve between the **stress at the finish of transformation from austenite to martensite (σ_f^{AS})** and the UTS	550 MPa, the latter was not obtained for the wire tested therefore E_M was not calculated
Stress at the start of the transformation from austenite to martensite	σ_s^{AS}	481 MPa
Stress at the start of the transformation from martensite to austenite	σ_s^{SA}	270 MPa
Stress at the finish of the transformation from martensite to austenite	σ_f^{SA}	212 MPa
Elastic transformation region	difference between the strain at σ_f^{AS} and σ_s^{AS}	ϵ_l = 0.047

The final material properties for the UCL TMV frames were unknown at this initial prototyping stage because the specific composition and thermo-mechanical processes require optimisation. However, material properties resulting from the optimised manufacturing methods used for the similar UCL TAV frame were available (E_A = 50 GPa, E_M = 12 GPa, σ_s^{AS} = 527 MPa, σ_f^{AS} = 525 MPa, σ_s^{SA} = 279 MPa, σ_f^{SA} = 297 MPa and ϵ_l = 0.075) and subsequently used as approximate inputs for the finite element analyses used to optimise the UCL TMV frame in terms of having minimal stresses whilst crimped in an 8 mm tube and to adequately match the mitral valve anatomy (Bozkurt et al 2016).

3.4 Summary

This chapter characterised and outlined the requirements for the components of the UCL TMV prototypes; namely the self-expanding nitinol wireframe, polyester mesh skirt and pericardial leaflets (Figure 3.1). The two main outcomes from this chapter were;

1. **Characterisation of the thermomechanical properties of pericardium:**
    a. Provided input data for numerically modelling the mechanical properties of pericardium tissue for use in finite element analyses used as a design tool for developing the UCL TMV bileaflet design (Chapter 4).
    b. Indicated *in vitro* haemodynamic assessment of prototypes could be justifiably conducted at room temperature, rather than at an elevated body temperature of 37 ^{o}C (Chapter 5).
2. **Characterisation of polyester mesh:** indicated that PETKM2004 was suitable for the UCL TMV prototypes (Chapter 6).

Chapter 4 will now discuss the leaflet design and how finite element analyses' were used as a design tool resulting in the selection of a conical bileaflet design, uniquely defined by two parameters; its scale factor and coaptation length.

Chapter 4 Leaflet design using finite element analysis

The UCL TMV leaflets, presented in this chapter, have an original combination of features being D-shaped, with two leaflets and slightly conical. Further, this is the first such morphologically similar leaflet design to be used in a transcatheter device. This chapter firstly describes their requirements and then the design approach and finite element simulations used are expounded, the results for which are presented and discussed.

4.1 Requirements

The requirements for the TMV leaflets in terms of their material properties were previously described in section 3.1.1. A device with an inter-trigonal diameter of 26 mm (Figure 4.1) was required because it is small enough to mount in the mitral position of the pulse duplicator, used to assess its performance, and is appropriate for future animal trials as well as for small human patients, most likely female adults.

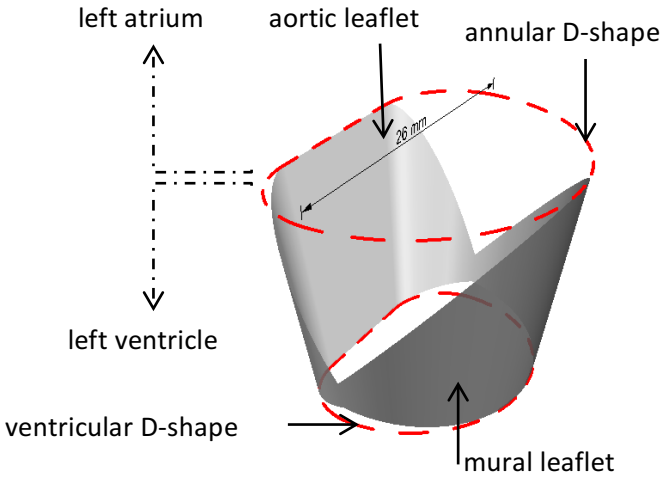

Figure 4.1: The 26 mm (inter-trigonal diameter) UCL transcatheter mitral valve.

4.2 Design

A risk rather than requirements based design approach is required for the recent transformative developments of transcatheter heart valves and is in accordance with ISO 5840-3:2013, further described in ISO 14971:2012 'Medical devices – application of risk management to medical devices'. Therefore a risk based approach was used to select the optimal design criteria and determine the parametric design. This is summarised in Table 4.1 using a failure mode and effects analysis and described in detail in the following section.

Table 4.1: Failure mode and effects analysis to obtain the optimal design criteria (mitigation/requirements) and parametric design (parameter for further investigation/evidence of mitigating risk) for transcatheter mitral valves.

Potential failure mode	**Potential cause(s)/mechanism**	**Cardiac cycle phase**	**Local effects of failure**	**Next higher level effect**	**System level end effect**	**Probability (estimate) (P)**	**Severity (S)**	**Relevance for patient population (R)**	**Risk Level (P+S+R)**	**Mitigation /Requirements**	**Parameter for further investigation /evidence of mitigating risk**
Structural	Tearing, perforations and/or calcification	Systolic	Regurgitation	Additional work required by left ventricle	Reduced blood flow, ending in inadequate supply of nutrients for cellular metabolism. Risk of heart failure.	1 (Kapadia SR et al 2015)	5 (worst case)	2	8	Minimise excessive stresses	Conicity and coaptation length
Functional	Incomplete coaptation and/or prolapse					5 (sections **Error! Reference source not found.**-2.4)		5	15	Maximise coaptation area	
Key:	Probability rating (meaning based on occurrences in similar devices with clinical experience)	1 = Extremely unlikely (none known), 2 = Remote (relatively few), 3 = Occasional, 4 = Reasonably Possible (repeated failures), 5 = Frequent (almost inevitable).									
	Severity rating	1 = No relevant effect, 2 = Minor (may require use of pharmaceutical drugs to maintain health), 3 = Moderate (loss of optimal performance of device resulting in return of symptoms untreatable with pharmaceutical drugs), 4 = Critical (loss of optimal performance of device resulting in a replacement being required), 5 = Catastrophic (device no longer performs required function resulting in death).									
	Relevance rating	1 = None, 2 = Little, 3 = Considerably, 4 = Very, 5 = Extremely.									

4.2.1 Optimal design criteria for leaflets

On reflection of the failure mode and effects analysis (Table 4.1), two main risks were identified for the leaflets of a TMV; structural and functional failure. Optimal design criteria associated with these two failure modes were identified as the peak maximum principal stress (MPS) and coaptation area (CA) respectively, both of which are measurable from finite element analyses (FEA) and are unobtainable experimentally. The criteria for the peak MPS and CA are further described below.

4.2.1.1 Peak maximum principal stress (MPS)

Bioprosthetic heart valves must endure a complex cyclic loading and deformation during the cardiac cycle, opening and closing more than 100,000 times per day. The resulting stress states are multi-axial and their failure (on average bioprosthetic valve functional life is only 12 years (Chandran et al 2010)), is governed by a combination of various stress components, including tensile and compressive in-plane, bending and shear.

There are no failure theories relevant for bioprosthetic heart valves. The ability to determine why and how materials fail i.e. the complete separation of a member, has been an area of research for several decades, continuing to the present day, resulting in numerous failure theories some only for specific applications and all with advantages and disadvantages. They all have the common theme that a material will fail when some physical variable reaches a limiting value; whether this is a certain stress, strain or energy is specific to each theory.

There are two main failure criteria theories[14], one based on stress, the maximum principal stress theory, and one based on shear strains, the maximum distortion energy theory. The maximum principal stress theory, is based on the idea that failure will occur when either of the principal stresses, σ_1 or σ_2, reaches or exceeds the yield strength, known as the Rankine failure criteria. In contrast, the maximum distortion energy theory assumes that failure will occur when the distortional energy associated with the principal stress equals or exceeds the distortional energy corresponding to that for the yield strength of the material in uniaxial tension or compression, known as the von Mises failure criteria. In general, the

[14] Other failure theories include Coulomb-Mohr, Beltrami (maximum strain energy), Tresca (maximum shear stress) and St Venant (maximum principal strain theory) to name a few.

Rankine criterion provides a good prediction for the failure of brittle materials, whereas the von Mises criterion is better for ductile materials.

The von Mises failure criterion has previously been used for designing the tissue leaflets of a percutaneous aortic valve (Smuts et al 2011). However, the Rankine criteria has shown relevance in the structural failure in explanted bioprosthetic heart valves (Bernacca et al 1992, Thubrikar et al 1983), observed as tearing, perforations and/or calcification[15], shown to be associated with locations of peak MPS (Burriesci et al 1999). Despite their theoretical difference, the peak MPS and von Mises stresses in a commercially successful transcatheter bioprosthetic heart valve are shown in section 4.4.1 to be the same order of magnitude. Furthermore, pericardium cannot be defined solely as a ductile nor brittle material. Whilst fracture is preceded by little plastic deformation (Zioupos et al Jan 1994, Zioupos et al Apr 1994) characteristic of a brittle material, necking occurs before failure which is characteristic of a ductile material. Therefore, either the Rankine or von Mises criterion may be relevant. However, it is the concentration of principal stresses that are responsible for delamination (Mirnajafi et al 2010) and the consequent blood flow through the open pores which leads to calcification. Therefore, the Rankine criterion is arguably the most relevant for designing bioprosthetic heart valve leaflets.

A leaflet design similar to the UCL TMV leaflets (Burriesci et al 1999), was reported to have endured a peak MPS of approximately 2 MPa, associated with the critical loading mode when the leaflets are fully closed, which withstood more than 400 million opening and closing cycles (5 years) *in vitro* as well as *in vivo* function in calves, with survival times that met the Food and Drug Administration requirements (Black et al 1986). Therefore, the order of magnitude of the peak MPS for the optimal leaflet design had to be 2 MPa or less.

This order of magnitude risk assessment for structural failure is appropriate for several reasons. Firstly, when FEA is applied to the design of bioprosthetic heart valve leaflets, the results are only relevant as a prediction for the order of magnitude of stresses that will occur. Secondly, higher accuracy would be futile due to the natural variability in material properties across devices as well as within a single set of leaflets. Finally, the requirement

[15] It has been shown that structural and functional failure can occur in unison; calcific deposits (structural failure) can inhibit the full closure of the leaflet (functional failure) (Shah et al 2008, Vesely et al 1988, Thubrikar et al 1983).

of withstanding 400 million cycles was revised in the current standard (ISO 5840-3:2013, Annex O) to a minimum of 200 million cycles with no sign of excessive structural damage and/or functional impairment, therefore this order of magnitude criteria is conservative.

4.2.1.1 Coaptation area

The CA has previously been used to assess the effect of the positioning strategy for the SAPIEN TAV (Auricchio et al 2013), which ranged between 3.4 and 2.6 cm^2. The CA for the TMV leaflets is the area of contact between the aortic and mural leaflets. This provides a surface seal, sustains the closing pressure load and provides a safety margin against valvular regurgitation. If removed the valve would be incompetent, also referred to as functional[16] failure. Therefore, it appeared to be logical inference to assume that larger CAs would be associated with less regurgitation and therefore the optimal leaflet design would have the maximum CA.

4.2.2 Parametric design

The parametric design was developed after reflection of the failure mode and effects analysis (Table 4.1) and therefore conicity was added to the initial concept for the UCL TMV (section 1.4.4) making it even more physiologically similar and novel compared to others in development (section 2.2) (although conicity is in fact present in the Cleveland, Sheffield, Quattro™ and the other quadrileaflet surgical valves previously reviewed (section 2.1)). The use of a parametric design to create a bileaflet mitral valve based on a failure mode and effects analysis (Table 4.1) improves on the clinically irrelevant reasoning behind the 'bubble valve' (section 2.1.1, Walker et al 1983) and Sheffield surgical valve (Black et al 1986) designs.

The idea for creating a conical design was inspired by the 3D echo of a healthy mitral valve (Figure 1.5) and the following section describes how the optimal leaflet design was drawn using computer-aided design (CAD) 3-D modelling software Rhinoceros 4.0 (Robert McNeel & Associates).

[16] The second functional failure mode is heart failure, caused by adverse pressure gradients which cause the heart to work harder. This is associated with the diastolic orifice area, which is taken into account in limiting the scale factor to not be less than 0.745.

4.2.2.2 Design parameters

The leaflets for the UCL TMV were drawn in their assembled configuration as surfaces using computer-aided design (CAD) 3-D modelling software Rhinoceros 4.0 (Robert McNeel & Associates) based on a standard D-shape (Figure 4.2 and following instructions).

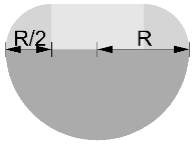

Figure 4.2: Standard D-shape proportions constructed from a semi-circle with radius R, two quarter circles and a rectangle.

1 In the **top view** draw a semi-circle of diameter 26 mm.

2 Draw a line from the centre of the circle to the edge. This is line1.

3 Draw a quarter circle centred on the middle of line1.

4 Mirror the quarter circle along the x-axis.

5 Draw a straight line between the two quarter circles.

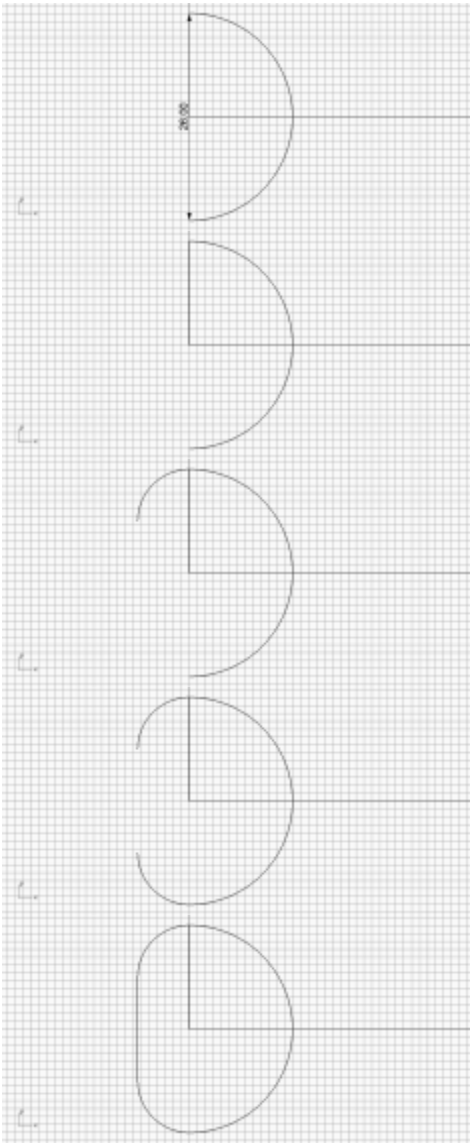

6 Join the four sections of the D-shape together.

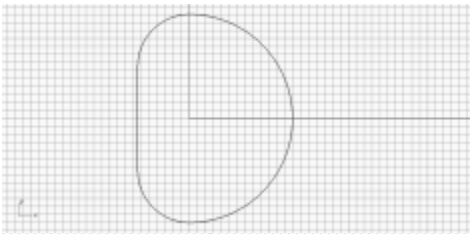

7 Scale the D-shape, using the centre of the semi-circle as the origin and a scale factor (SF) of 0.745.

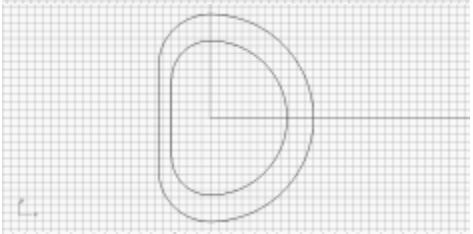

8 In the front view, move the larger and smaller D-shapes 14 and 4 (CL) mm above and below the origin respectively.

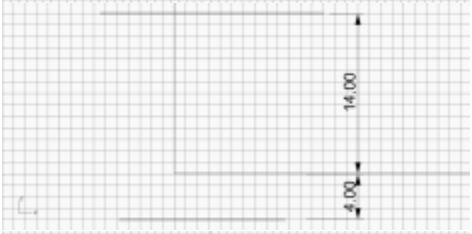

9 In the top view, draw a line between the ends of the two semi-circles. This is line2.

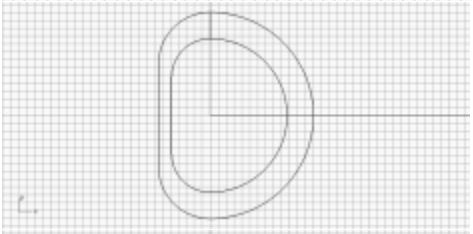

10 Mirror this line along the x-axis. This is line3.

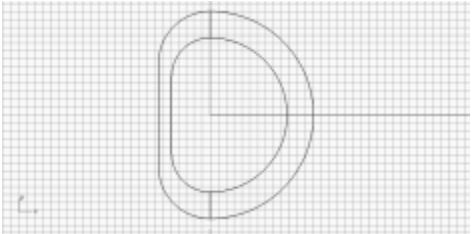

11 Using **Sweep2**, use line2 and line3 as the rails and the two D-shapes as the cross-sections. This is the conical surface.

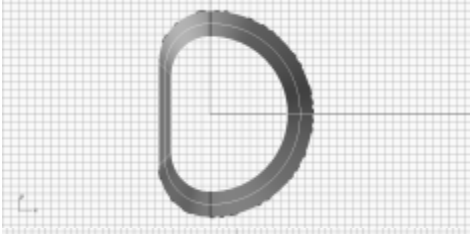

12 In the right view, display line2 and line3.

13 Draw a plane, selecting the tops of line2 and line3 as the first two points and entering in 10 for the width. This is called plane1.

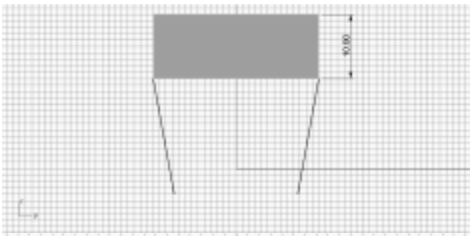

14 Display line1, line2 and line3.

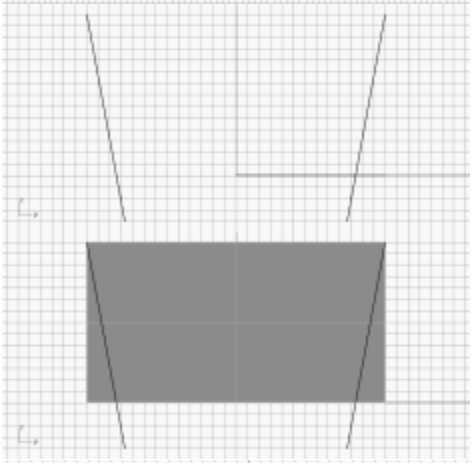

15 Draw a plane using; **surface/plane/3 points**; selecting the top of line2 and line3 and the far right end of line1. This is plane2.

16 Hide the lines. Draw a vertical line down 2.5 mm (cuff length) from the bottom left corner of plane2. This is line4.

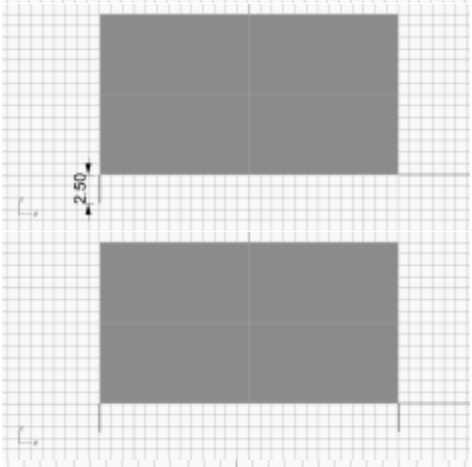

17 Mirror this line along the y-axis. This is line5.

18 Display the smaller D-shape, line4 and line5.

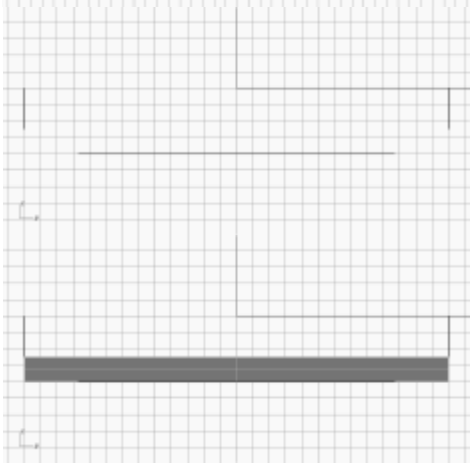

19 Draw a plane, select the bottom end of line4 and line5 and the intercept with the centre of smaller D-shape. This is plane3.

20 Display the conical surface. Draw a plane that will intersect the displayed layers. This is plane4.

21 In the **front view**, **Split** the conical surface with plane2, plane3 and plane4.

22 Create a layer for the region to the left of the y-axis, this is the **aortic leaflet**. Then “hide” it.

23 Create a layer for the region to the right of the y-axis, when split in a similar way, this will be the **mural leaflet**. Then “hide” it.

24 Create a layer for the regions above the x-axis. Then “hide” them. The remaining surfaces can be discarded.

25 In the right view, display line2 and line3. Draw a plane selecting the top ends of them and a width of 10. This is plane5.

26 Display line1, line2 and line3.

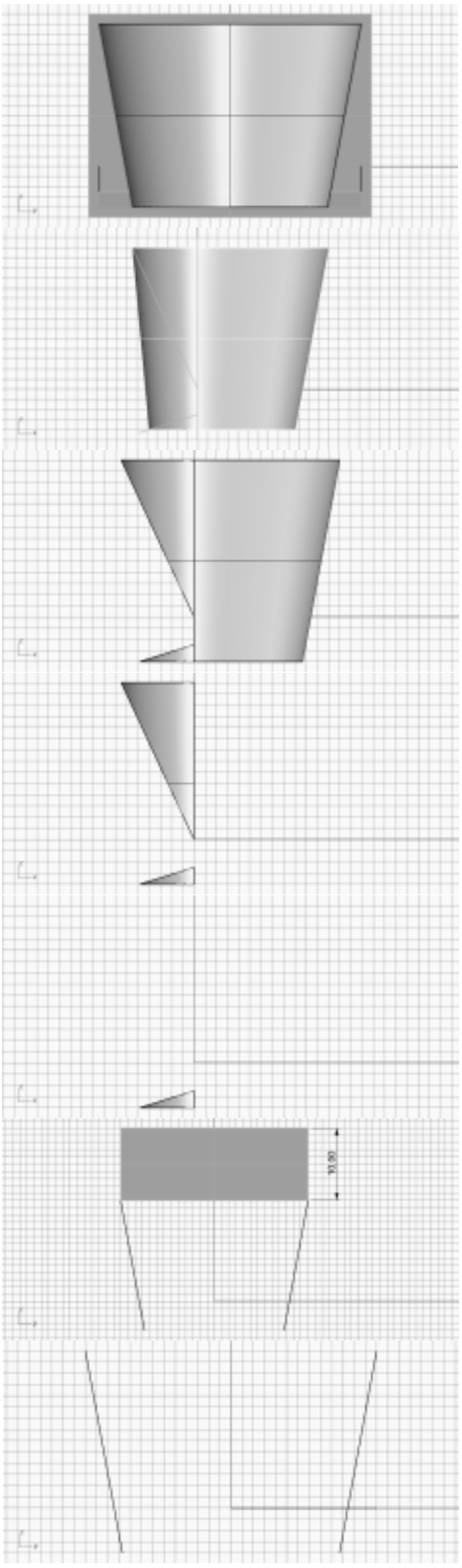

27 Draw a plane, selecting the top ends of line2 and line3 and the far right end of line1. This is plane6.

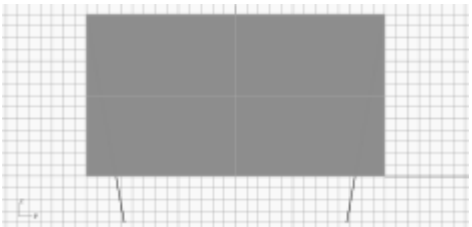

28 Hide line2 and line3. Draw a vertical line down 2.5 mm from the bottom left corner of plane6. This is line6.

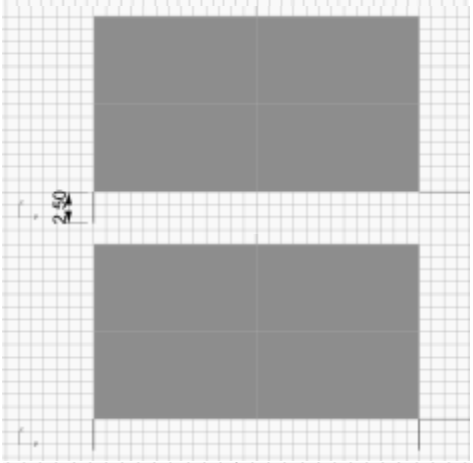

29 Mirror this line along the y-axis. This is line7.

30 Display the smaller D-shape and line6 and line7.

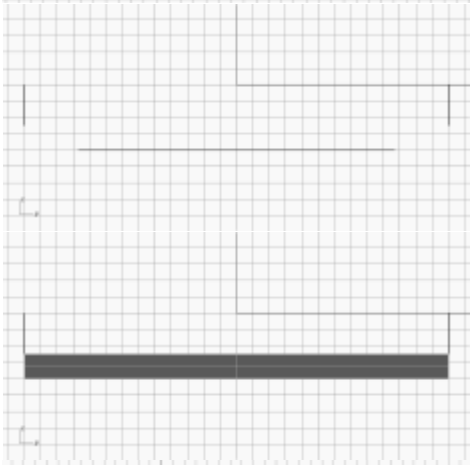

31 Draw a plane selecting the bottom ends of line6 and line7 and the centre of the small D-shape. This is plane7.

32 In the front view, display the mural surface, plane6 and plane7. Split the mural surface using plane6 and plane7.

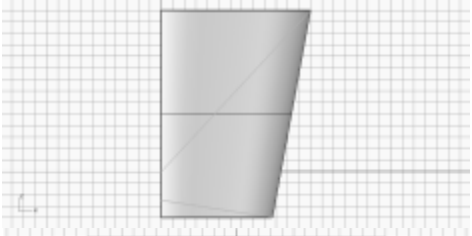

33 Look at the right view. Create a layer for the central section, this is the mural leaflet. Then “hide” it.

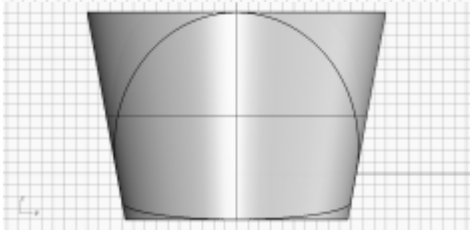

34	Place the sections above the x-axis in the **commissures** layer. The bottom section can be discarded.	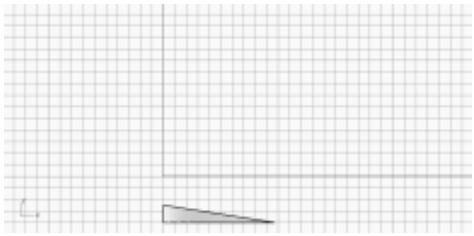

4.2.2.1 Aim

The aim of the parametric leaflet design was to enable a series of incrementally different designs to be created using parameters that would be associated with the design criteria previously discussed. Thereby aiming to minimise the peak MPS and maximise the coaptation area, with the aid of finite element simulations (section 4.3).

4.2.2.1.1 Scale factor

The SF[17] between the annular and ventricular D-shapes quantifies the conicity of the leaflets (Figure 4.1 and Figure 4.3). The addition of conicity was inspired by the shape of a healthy native mitral valve (Figure 1.1 and Figure 1.3, Votta et al 2008) and is in direct contrast to the divergent design by Kheradvar et al (2012) (Figure 2.3). The conical design was speculated to prevent excessive oscillation of the orifice area during diastole and thereby reduce potential turbulence and associated risk of blood damage[18]. Furthermore, the conical design may prevent left ventricular outflow tract obstruction (LVOTO) and prolapse; by counter acting the tendency for the free leaflet edges to diverge from their manufactured configuration when placed inside an annulus with an interference fit, as is common practice.

The SF must not be greater than 1; if it were the native leaflets would turn outwards and may cause LVOTO. They should not be less than 0.745, which will ensure the native mitral valve diastolic orifice area is not reduced by more than 60%; for which mitral valves repaired using the edge-to-edge technique (Figure 1.12) still function without adverse pressure gradients[19] (Alfieri et al 2001). This minimum SF was calculated for the largest

[17] A scale factor was used to place the leaflets at an angle, because due to geometric restrictions, it is not possible to angle the leaflets individually and have coapting lengths which can be formed from a flat sheet of pericardium.

[18] High turbulence is associated with high shear stress, which is associated with two types of blood damage; hemolysis and platelet activation (Leverett et al 2008).

[19] Acknowledgements The Heart Hospital, London for allowing me to observe a patient undergoing a transesophageal echocardiogram (TEE) as well as a MitraClip® procedure.

native annulus into which the proposed device would be implanted (25 mm, resulting in an interference fit of 1 mm) by approximating the native D-shape to be similar to the D-shape used for the construction of the prosthetic leaflets (Figure 4.2). This calculation ignored the conicity of the native valve, and therefore was a conservative estimate.

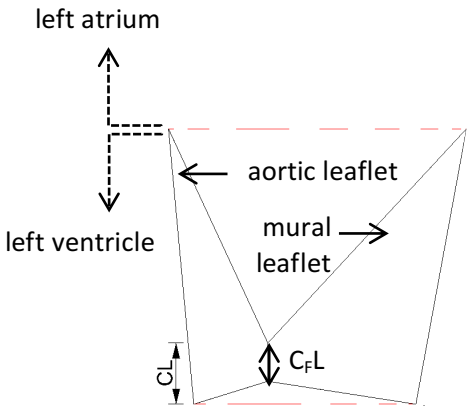

Figure 4.3: Leaflets for the UCL transcatheter mitral valve and the conical bileaflet (CB) surgical mitral valve: coaptation length (CL) = 4 mm, cuff length (C_FL) = 2.5 mm.

To enable the generation of a set of designs which would be incrementally different, the following even distribution of five SFs, in the range described, were chosen for investigation; 0.745, 0.79875, 0.8525, 0.90625 and 0.96.

4.2.2.1.2 Coaptation length

The CL is commonly used to describe the morphology of a native mitral valve (Wang et al 2013). For the proposed leaflet design, CL refers to the vertical distance from the arris between the aortic and mural leaflets to the middle of the leaflets free edge (the longest part of each leaflet). It was hypothesised that longer CLs would provide better coaptation between the leaflets (Gogoladze et al 2010), quantifiable as a larger coaptation area, and would also allow the valve to function in a larger range of host annulus geometries.

Leaflets with CLs longer than the cuff-length[20] (C_FL) of 2.5 mm were cut at an angle mainly because the leaflets have to be made from a single flat sheet of pericardium, the edges of which must be joined together and attach securely to the frame. Furthermore, removal of

[20] The cuffs used for the similar UCL TAV were 2.5 mm long and therefore it was assumed similar ones would be used for the UCL TMV.

excess leaflet tissue will prevent structural and/or functional failure that may occur due to rubbing on the frame and is also advantageous for achieving a minimum crimped profile, thereby reducing damage to surrounding tissue during implantation.

There are several reasons to limit the maximum leaflet length; too much redundant material may cause premature degradation of the leaflets and would result in more localised bending or folding, such as buckling or pin wheeling (twisting of the leaflets free edges due to excessive leaflet tissue, ISO 5840-3:2013), which was associated with failure of pericardial leaflets (Shah et al 2008, Vyavahare et al 1999, Vesely et al 1988). Also longer leaflets are more likely to cause LVOTO. Another reason to limit their length is that viscous energy losses are directly proportional to vessel length (Akins 2008); therefore on this basis shorter leaflets will have lower diastolic energy losses. Subsequently, the CL was limited to 4 mm. The following five CLs were chosen; 0, 1, 2, 3 and 4 mm, which when combined with the five different SFs, resulted in 25 incrementally different bileaflet CAD models. These were then turned into finite element models and their closure simulated.

4.3 Finite element simulations

Computational simulations of prosthetic heart valve dynamics play an important role in their design and evaluation, previously reviewed in (Chandran 2010). In the case of a TMV, both the boundary conditions and operating configuration are highly complex, unknown and patient specific and therefore use of the finite element method in this context is limited to being an initial design tool (Smuts et al 2011).

4.3.1 Aim

The aim of using finite element simulations to assess the critical loading mode (fully closed) of 25 incrementally different bileaflet designs (section 4.2.2) was to select an optimal design which reduced the risk of functional and structural failure (section 4.2.1), i.e. maximised the coaptation area and minimised the peak maximum principal stress respectively (Table 4.1). This subsequently saved time and money that would have been required for prototyping unsuccessful designs and provided data unobtainable experimentally.

4.3.2 Finite element model

4.3.2.1 Software

An explicit code, traditionally used for impact and crash analyses, was chosen rather than an implicit code mainly because of its superior ability to deal with contact problems, which is crucial for simulating the critical loading mode of heart valve leaflets in their fully closed position. Furthermore, an explicit code provides a cost effective analysis technique for short duration events that have significant non-linearities with large deformations; ideal for simulating the closure of pericardial leaflets which have large strains in bending of 5% or greater at high strain rates with contact interactions and plasticity. LS-DYNA (Livermore Software Technology Corporation) is one such FE code, previously used successfully for simulation of bioprosthetic heart valves (Burriesci et al 1999) and therefore was employed in this study (Appendix D).

Small time steps are required to maintain stability and provide a robust solution procedure even for a high degree of nonlinearities. Explicit integration is used; where a system of explicit algebraic equations is written for all nodes in the mesh at time level t + Δt. Each equation is solved in-turn for the unknown node point displacements. The time step (Δt) must be less than the length of time it takes a signal traveling at the speed of sound (c) in the material to traverse the distance between the node points (L; the smallest element length, Equation 4.1).

$$\Delta t \leq \frac{L}{c} \tag{4.1}$$

4.3.2.2 Material

Despite pericardium being orthotropic, an isotropic material model will provide sufficient information for average behaviour of pericardial leaflets; a good approximation both in terms of stresses and displacements (Burriesci et al 1999). Therefore, the constitutive relationship of the leaflets was modelled as isotropic, non-linear, hyperelastic, incompressible and capable of recoverable strain using the Ogden model previously described (Figure 3.8).

4.3.2.3 Boundary conditions

The boundary between the movable leaflets and stationary frame was simplified i.e. the individual stiches which attach the pericardium to the nitinol were modelled as a uniform hinge which allowed rotations and restricted the x, y and z locations of the nodes. The coaptation of the leaflets was modelled using a contact boundary condition which checked the nodes for potential contact with the neighbouring leaflet as well as self-contact at each increment in load and in the absence of a fluid the wetness of contact was modelled using a zero coefficient of friction, previously used in a simulation of a similar mitral valve design (Burriesci et al 1999). Although the boundary between blood and leaflets was not modelled, the effect of blood's inertia in reducing system oscillations was represented by multiplying the velocity of each node by a damping coefficient of 0.9965, previously used successfully for the simulation of a similar pair of leaflets (Burriesci et al 1999).

4.3.2.4 Discretisation

Shell elements provided a good model of the membrane structure of pericardium. They have previously been used successfully for their ability to model thin structures, with thickness small compared to length, and efficiently provide accurate results for shear and large strains in bending, which can be greater than 5% in heart valve leaflets, caused by the large and complex deformations during the cardiac cycle (Howard et al 2003, Burriesci et al 1999, Patterson et al 1996, Black et al 1991, Huang et al 1990). Therefore, an iso-mesh of quadrilateral (CQUAD4) 2D constant strain Belytschko-Lin-Tsay (BLT) shell elements with grid points of 6 degrees of freedom, based on the C^{o}-Mindlin shell formulation with one point Gauss quadrature (Belytschko and Tsay 1981), were chosen to model the 0.4 mm thick leaflets. The BLT shell elements use a bilinear (i.e. first-order) interpolation function, to define the mid-surface velocity, angular velocity and element's coordinates.

The out-of-plane stresses were represented by one constitutive evaluation for each of the five integration points through the thickness of the shell elements. However, this geometry is limited by reduced accuracy when warping is involved, caused by assuming the shell is flat.

Initially, a 2 mm iso-mesh was sufficient to compare the trends in behaviour in the initial 25 leaflet designs and had a reasonable computational time of approximately 30 minutes. This resulted in, on average, 300 shell elements per leaflet, a factor of ten fewer than previously

used to predict actual behaviour of prosthetic aortic valve leaflets (Auricchio et al 2014, Burriesci et al 1999). This mesh was later refined to 0.5 mm for the optimal leaflet design. Finer meshes were not used because they would not represent the physics of the thin, 0.4 mm thick, pericardium leaflets, the elements for which should be wider than they are thick. In fact a mesh refinement conducted for a similar valve revealed that finer meshes provided an inferior representation of the valves closed morphology (section 4.4.1).

4.3.2.5 Load

In general, for assessment of prosthetic heart valve leaflets the closing phase dynamics are the most significant during the cardiac cycle and more specifically, idealised models of bioprosthetic heart valves (Hamid et al 1986) and synthetic valve designs (Chandran et al 1991) have identified the critical loading mode to occur when there is a maximum pressure difference across the fully closed leaflets. Therefore, simulation of just leaflet closure, using a time dependent and spatially uniform pressure difference applied to the ventricular side of the leaflets, was sufficient to enable selection of an optimal leaflet design based on critical loading mode performance. To close the leaflets starting from their fully open position a small opening pressure was applied prior to ramping to 200 mmHg (27 kPa) (Figure 4.4; based on pulse duplicator data previously obtained by the research group).

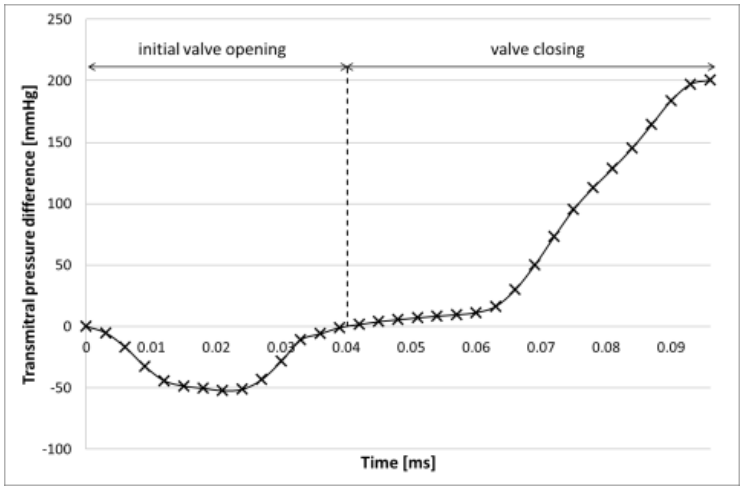

Figure 4.4: Transmitral pressure difference derived from pulse duplicator data, applied to the ventricular side of the leaflets in their manufactured configuration.

4.4 Results

4.4.1 Confirmation of peak maximum principal stress optimal design criteria

The maximum allowable stress in the bileaflet designs was set to be the same precision as 2 MPa, for reasons previously discussed (section 4.2.1). This design criterion was further supported by a FEA of the critical loading mode of a similar device, the SAPIEN, a pericardial three-leafleted TAV[21], which has achieved up to five years implantation without structural deterioration (Kapadia et al 2015).

The same software, material, boundary conditions and structure as previously described were applied to a FEM of the SAPIEN leaflets, only with two adjustments. Firstly, the pressure applied was a transaortic pressure derived from pulse duplicator data, which had associated video footage (Figure 4.5) and, secondly a finer mesh of 0.5 mm was used to obtain a more accurate measure of stress. Finer meshes were not used because they would not represent the physics of the thin, 0.4 mm thick, pericardium leaflets, the elements for which should be wider than they are thick (discussed further in the 'mesh refinement' section below).

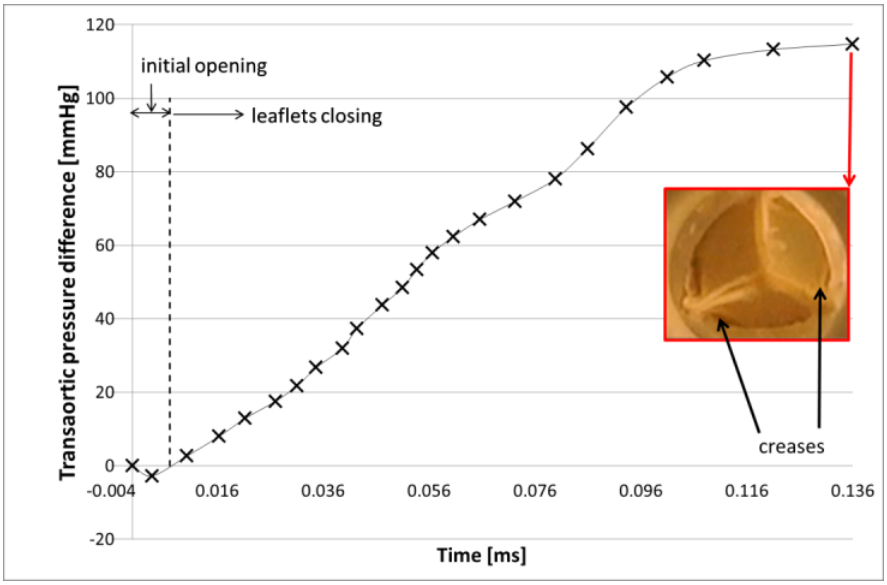

Figure 4.5: Transaortic pressure difference derived from pulse duplicator data, applied to the aorta side of the SAPIEN leaflets in their manufactured configuration and the associated video frame when closed. (Data previously obtained by the research group).

[21] Although designed for the aortic position, it has also been implanted in the opposite orientation in the mitral position to treat severe calcification (Hasan et al, 2013).

The resulting FEA successfully represented the morphology of the fully closed SAPIEN leaflets, replicating a similar free-edge curvature as well as the characteristic creases in the leaflet surface, which combined with the models reasonable material description means it can be assumed the magnitude of the peak MPS measured from the FEA, 1.4 MPa, was also realistic (Krucinski et al 1993, Figure 4.6). Thus, this FEA is validated. Furthermore, this FEA validates the simulations used to design the bileaflets prior to experimental validation of their similar FEMs. Note that due to the singularities that occurred at the top of the stent posts and at the edge of the bases, peak values for the MPS and von Misses stress were measured one element away. More specifically, the peak MPS was 2.1 MPa at the corner of the stent post, it was 1.4 MPa one element diagonally inwards; similarly the von Mises stress was 2.4 MPa at the very edge of the base, and was a maximum of 1.1 MPa one element away.

The peak von Mises stress and MPS were the same order of magnitude, identical to one significant figure and both concur with recently reported literature (Abbasi et al 2015,

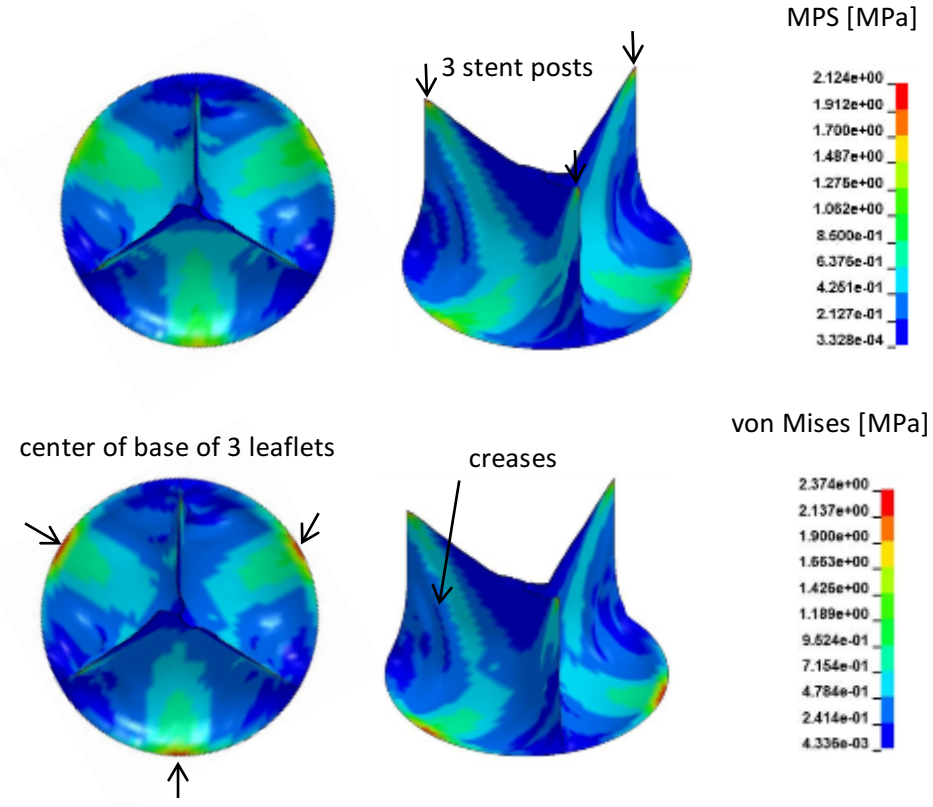

Figure 4.6: SAPIEN leaflets in their critical loading mode **(top)** maximum principal stress (MPS) peaks at top of stent posts 1.4 MPa **(bottom)** von Mises stress peaks at center of base of leaflets 1.1 MPa **(left column)** views from aorta **(right column)** isometric views.

Auricchio et al 2014). The location of stress concentrations for the MPS and von Misses stress differ, being located at the top of the stent posts and center of the base of each leaflet, respectively. However, neither the Rankine nor von Mises failure theories can be confirmed as applicable without *in vivo* failure observations, which have not yet occurred for the SAPIEN valve (Kapadia et al 2015), there is also no known *in vitro* durability data either. Therefore, the MPS and von Mises stress theories can equally provide an estimate for the order of magnitude of stresses sustainable for a period of 5 years in the SAPIEN valve.

4.4.1.1 Mesh refinement

The mesh for the SAPIEN valve was refined (Figure 4.7) and although it did not converge in terms of stress, a mesh size of 0.4 mm was chosen. Not only did this best represent the experimentally observed morphology of the closed leaflets it also meant the width of the shells (i.e. mesh size) remained at least the same size as their thickness. This means the elements remained thin structures; if the mesh were smaller than 0.4 mm the elements become narrower than they are thick, which no longer represents the physics of 0.4 mm *thin* pericardium tissue (Figure 4.7 and Figure 4.8). Therefore, based on correctly representing the physics and correlations with experimental observations, rather than mesh convergence, a mesh of 0.4 mm was used for the SAPIEN and also for the optimal bileaflet design.

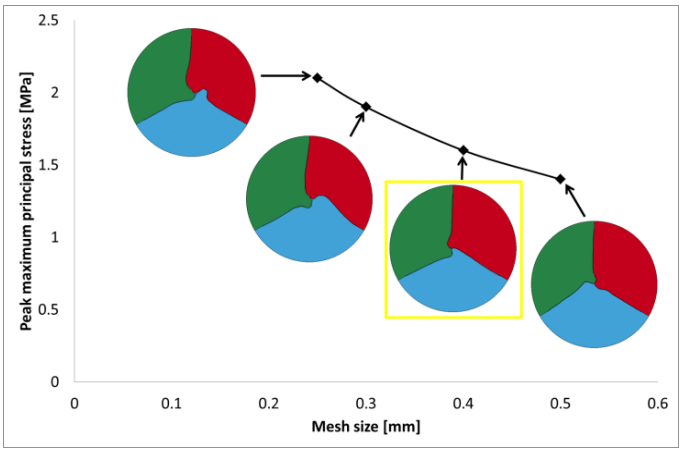

Figure 4.7: Mesh refinement for the SAPIEN valve leaflets, indicating the morphology of and peak maximum principal stress associated with its critical operating condition when fully closed, highlighting the 0.4 mm mesh size chosen.

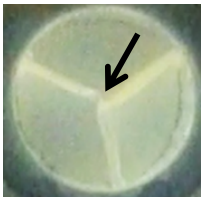

Figure 4.8: Pulse duplicator footage of SAPIEN valve in its fully closed position indicating twist of leaflet coaptation.

4.4.2 Optimal leaflet design

As previously described, FEMs of the 25 bileaflet designs were created and a FEA of their closure simulated. The critical loading mode results were then analysed as follows. Firstly, each model was inspected visually and those which did not occlude the orifice were rejected because this was an essential design requirement. Secondly, the stresses in the remaining 17 designs were analysed, which confirmed they had a peak MPS of the same precision as 2 MPa (ranging between 3 and 1 MPa) and, therefore, none were rejected. Lastly, the CA associated with each design was measured as the total area of the elements in contact (Figure 4.9).

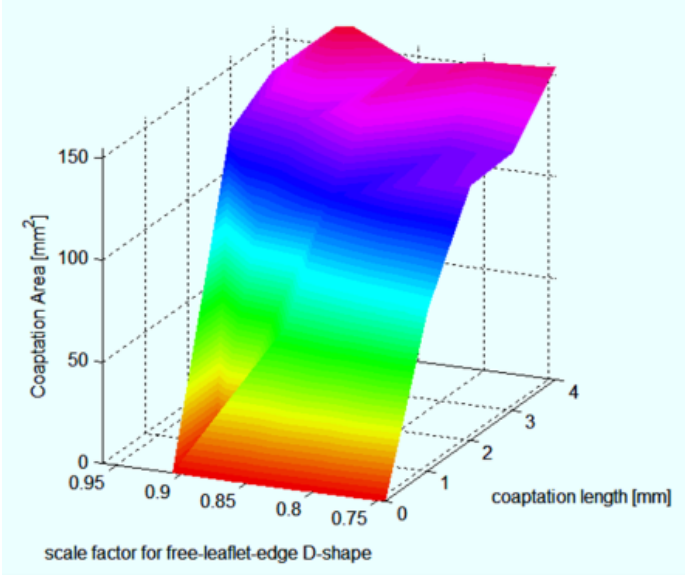

Figure 4.9: Leaflet optimisation of coaptation length, scale factor and coaptation area. (Colour variation relates to changes in coaptation area and was included to help visualisation).

Ideally the optimal design would have both the minimum peak MPS and maximum CA. However, in reality the maximum CA (1.62 cm^2) was achieved by the design with a SF of 0.90625 and CL of 4 mm (abbreviated to: SF_0.90625_CL_4) and the minimum peak MPS (0.6 MPa) was achieved by a design SF_0.745_CL_3 (Figure 4.10). If minimisation of peak MPS and maximisation of CA were of equal importance, then the optimal design would be the one closest to the origin in Figure 4.10 and therefore design SF_0.8525_CL_4 would be optimal (only 7 units from the origin), compared to the other two closest designs SF_0.745_CL_4 and SF_0.79875_CL4, which were 30 and 11 units from the origin, respectively. However, the peak MPS in these three designs were all 1 MPa (1 s.f.). Therefore, due to FEA results for bioprosthetic heart valve leaflets only being relevant as an order of magnitude approximation for stresses, the CA was used as the principal design criteria.

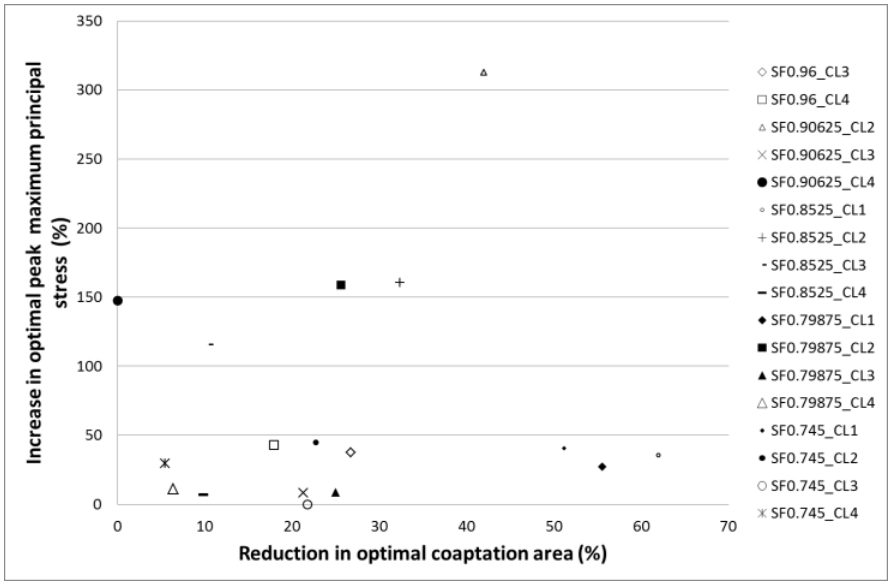

Figure 4.10: Variation in peak maximum principal stress and coaptation area for 17 incrementally different bileaflet designs relative to the optimal values achieved.

Selection of the optimal design based on CA is further justified by its acute relevance in minimising regurgitation, preventing functional failure and enabling proper coaptation for a range of different host annulus geometries, the foremost being of significant importance in the mitral position. Furthermore, considering that transcatheter devices are currently only implanted in elderly patients, mostly for compassionate reasons (rather than with the intention of significantly increasing their life span); precision engineering the leaflets for maximum durability is arguably irrelevant compared to engineering them for minimal

regurgitation. In fact, designing them for minimal regurgitation would be the best design strategy for improving the patient's quality of life, especially considering the initial high-risk patient population will have limited life expectancy due to various co-morbidities. Therefore the prevention of regurgitation was chosen as the principal design criteria. In which case, the design SF_0.745_CL_4 was the optimal design; with a CA of 1.54 cm^2 compared to 1.46 and 1.52 cm^2 for designs SF_0.8525_CL_4 and SF_0.79875_CL4 respectively.

The initial 2 mm mesh of the optimal leaflet design was subsequently refined to 0.5 mm (and no smaller due to reasons previously discussed in section 4.4.1), which confirmed the peak MPS to be 2 MPa, still meeting the design criteria, and had a larger CA of 2 cm^2. Unlike the SAPIEN FEA, location of stress concentrations for both the MPS and von Misses stress were both located at the arris between the leaflets, and again although technically different were the same order of magnitude (Figure 4.11).

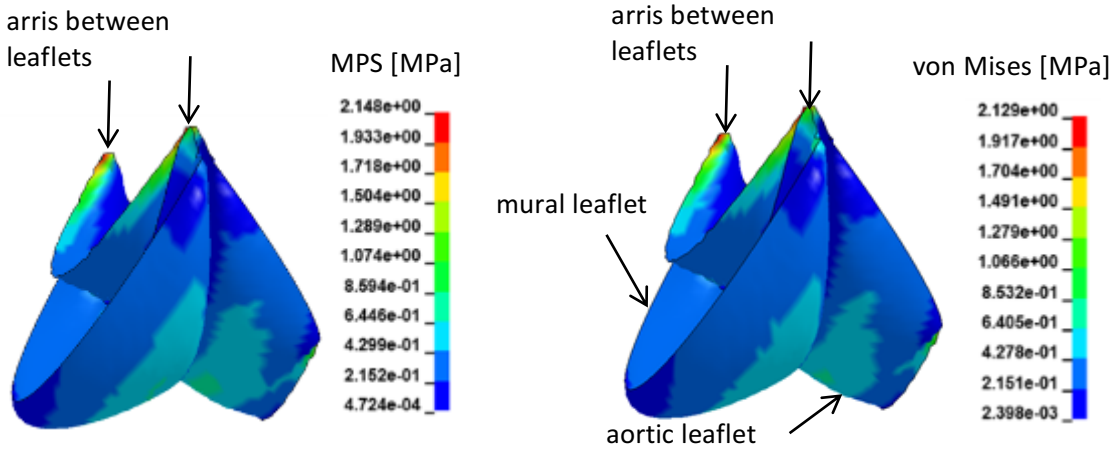

Figure 4.11: FEA results for the optimal bileaflet design with a 0.5 mm mesh **(left)** maximum principal stress (MPS), peak 2.15 MPa **(right)** von Mises stress, peak 2.13 MPa, arrows indicate regions of stress concentration and location of peak values.

4.5 Discussion

4.5.1 Parametric design

The nature inspired conical design, implemented using a scale factor, effectively reduced excess material at the leaflets free edge, smoothing the central buckle previously observed

in the Sheffield bileaflet valve (Figure 4.12), thereby possibly reducing associated peak stresses (Burriesci et al 1999).

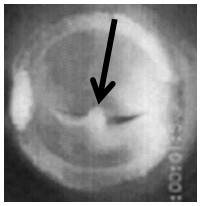

Figure 4.12: Sheffield valve indicating the central buckle in leaflets (adapted from Burriesci et al 1999).

The UCL TMV aortic and mural leaflet angles, 5.2° and 10.4° respectively (Figure 4.13), are in different proportions compared to those previously quantified *in vivo*, which were 8.3° and 5.3° respectively (Votta et al 2008). This highlights the impact of using a scale factor to angle the leaflets, rather than placing them at an angle individually. In fact it was not possible to angle the leaflets individually due to geometric restrictions involved in having a coaptation length, making leaflets from a single flat sheet of pericardium tissue and ensuring that their edges joined together along the cuff length (Figure 4.3).

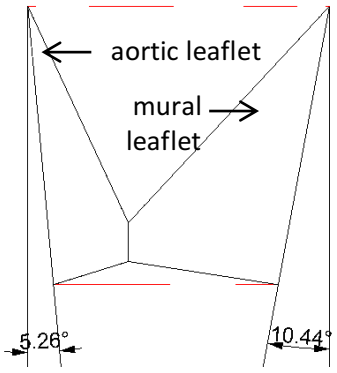

Figure 4.13: UCL transcatheter mitral valve leaflet angles resulting from a scale factor between annular and ventricular D-shapes of 0.745: aortic = 5.26° and mural = 10.44°.

4.5.2 Finite element simulations

The structural FEAs were adequate to predict whether the leaflets closed and fully occluded the orifice. However, they did not predict leaflet morphology during closure, which concurs with Smuts et al (2011); that when modelling the closure of heart valve leaflets the finite

element method is limited to being an initial design tool. Reasons for disparities between the numerical model and experimental observations are discussed below.

4.5.2.1 Correlation with experimental observations

The leaflets of the surgical version of the chosen leaflets curved in the opposite direction compared to that predicted by the simulations (Figure 4.11 and Figure 4.14.a) i.e. they curved towards the aortic leaflet. However, the curvature of the transcatheter leaflets concurred with the simulations (Figure 4.14.b), which also moved towards the mural leaflet.

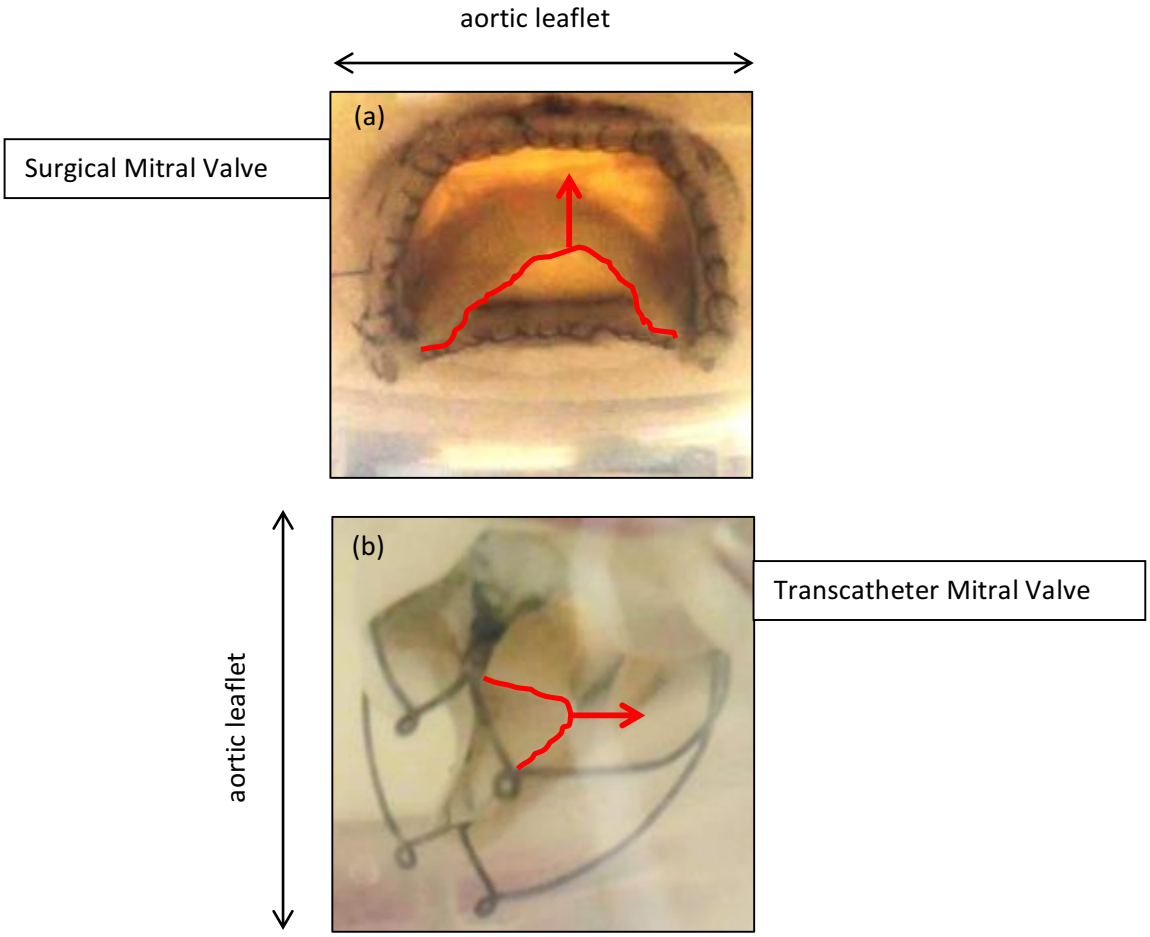

Figure 4.14: Direction of curvature of leaflets for the **(a)** surgical and **(b)** transcatheter mitral valves, indicated by red arrows. Red lines indicate the free leaflet edge of the coapting leaflets.

4.6 Summary

This chapter described the morphological requirements for the UCL TMV leaflets. The risk based design approach was justified and expounded and its use in selecting the optimal design criteria, in terms of peak MPS and CA, was explained followed by the consequent

parametric design, which was created using a scale factor and coaptation length in 3-D modelling software. The conversion of these 3-D models into FEMs were then described along with their accomanying simulations, which acted as a design tool, the results which are discussed and resulted in the selection of a conical bileaflet design, uniquely defined by two parameters; a scale factor of 0.745 and coaptation length of 4 mm.

Chapter 5 will now describe the equipment used, designed and made to assess the prototypes. This includes the design and manufacture of surgical mitral valves, designed to provide a relevant reference valve for the UCL TMV. Furthermore, it describes the experimental conditions used to simulate the left side of a normal healthy adult heart and the parameters measured to assess a prosthetic heart valve's performance. The minimum performance requirements are also expounded as well as the limitations of these methods.

Chapter 5 Haemodynamic assessment of valve leaflets

This chapter describes the equipment used to assess the functional performance of the surgical and transcatheter mitral valves, including the successful design and manufacture of a range of different sized mock native mitral valve implantation sites used to assess the effect of annulus size on the functional performance of the UCL TMV. The pulsatile flow conditions, resulting test parameters and minimum performance requirements for surgical and transcatheter mitral valves are expounded. The surgical mitral valve (SMV) section then describes the aim and manufacture for the bileaflet and trileaflet SMVs, for which preliminary flow visualisation of the left ventricle was done as well as the aforementioned function assessment. The experimental results are then presented and discussed, followed by the conclusions drawn and suggested future work. Finally, the limitations of the functional assessments are outlined along with current and future work.

5.1 Pulse duplicator

A commercially available hydro-mechanical cardiovascular pulse duplicator system (*ViVitro Superpump SP3891, ViVitro, BC, Canada*) (Figure 5.1) was used to assess the mitral heart valves made. Its main components are a pump, flowmeter and pressure transducers, the function of which are outlined in this section. The manufacture of silicon holders designed to mount the heart valves in the mitral position are also described. All prototypes were assessed with a mechanical bileaflet valve (Sorin Bicarbon 25) in the aortic position (Figure 1.10) using phosphate-buffered saline (PBS) as the working fluid; water based salt solution with the same osmolarity and ion concentration as the human body (but different viscosity and density).

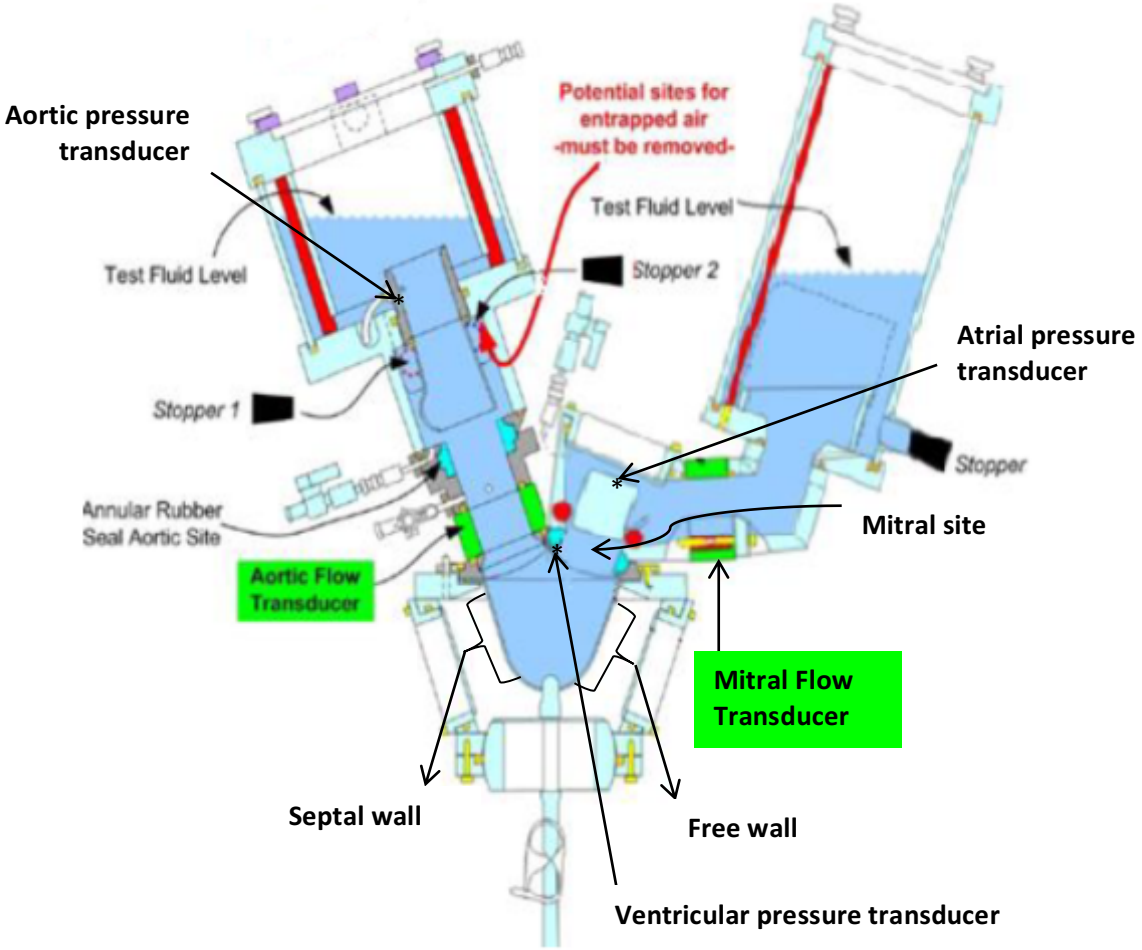

Figure 5.1: Schematic of ViVitro pulse duplicator (ViVitro Superpump SP3891, ViVitro, BC, Canada) (adapted from Pulse Duplicator User Manual, ViVitro Labs Inc. 2015).

5.1.1 Pump

The hydro-mechanical cardiovascular pulse duplicator system (*ViVitro Superpump SP3891, ViVitro, BC,* Canada) replicates muscular relaxation and contraction of the native left ventricle, which are 65% and 35% of the cardiac cycle respectively under rest conditions (Figure 5.2), by using lateral motion of a piston head acting on a body of water to compress and expand a flexible silicon sac (Figure 5.3). The piston head speed determines heart rate and the magnitude of stroke determines cardiac output/pump stroke volume; ultimately inducing pressure differences required to open and close the passive aortic and mitral valves. The pump was reasonably accurate at replicating the desired 35% systolic duration, achieving 35.03% ± 0.11%.

It is assumed the fluid outside the ventricle sac, in direct contact with the piston head, is incompressible and therefore the volume of fluid displaced as the piston head moves is directly correlated to the volume of fluid displaced within the flexible ventricle sac, i.e. the area of the piston head (38 cm^2) multiplied by the lateral displacement (Figure 5.2), which can range between 0 mm and 40 mm (±20 mm from neutral position).

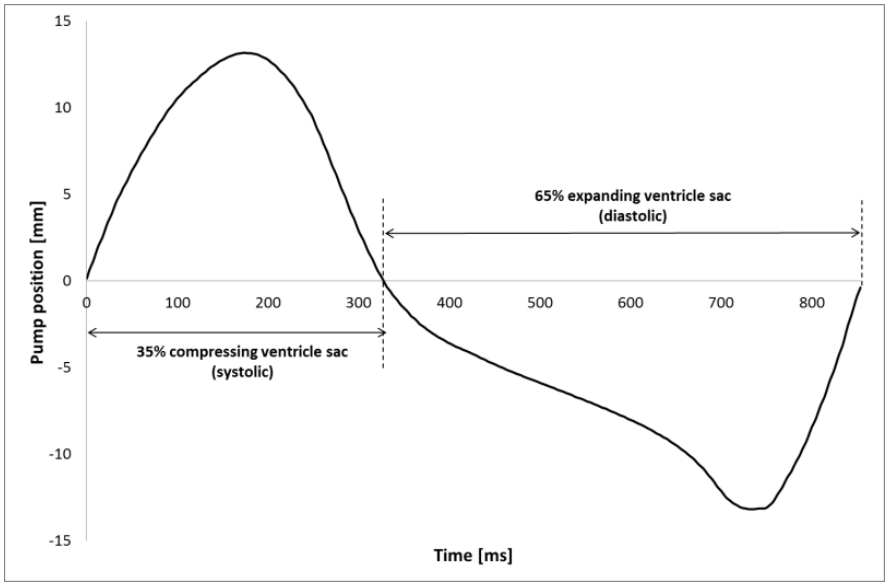

Figure 5.2: Pump position over one cardiac cycle at 5 lpm; 35% systolic, 65% diastolic, representative of a healthy normal adult at rest.

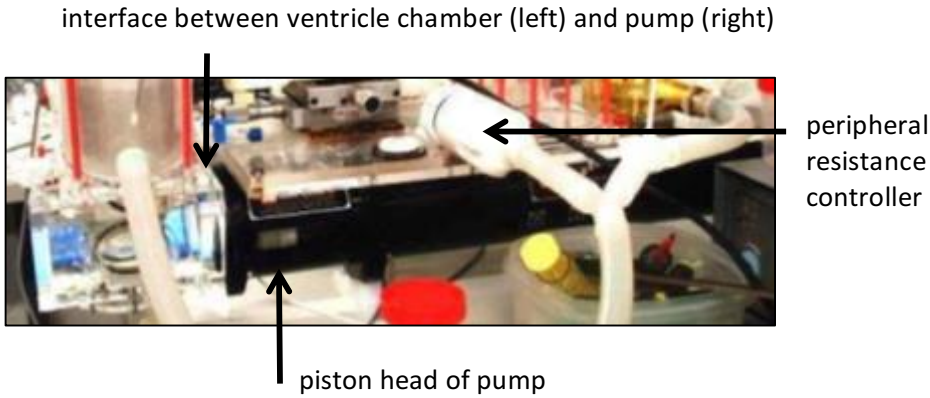

Figure 5.3: Pulse duplicator pump and peripheral resistance controller.

5.1.2 Magnetic flowmeter

The electromagnetic flowmeter (Carolina Medical Electronics Inc.) measured flow through the mitral position (Figure 5.5). Following Faraday's law of electromagnetic induction, flow of conductive PBS through the magnetic field generated within the cylindrical flowmeter, generates a voltage signal directly proportional to flow rate i.e. a faster flow generates a higher voltage, sensed by electrodes on the flow tube walls. This voltage, received by the data acquisition system, is calibrated to flow (Figure 5.4) with an average sample rate of 300 Hz, and achieves high accuracy, as can be seen from achieved cardiac outputs and their standard deviations (Table 5.1).

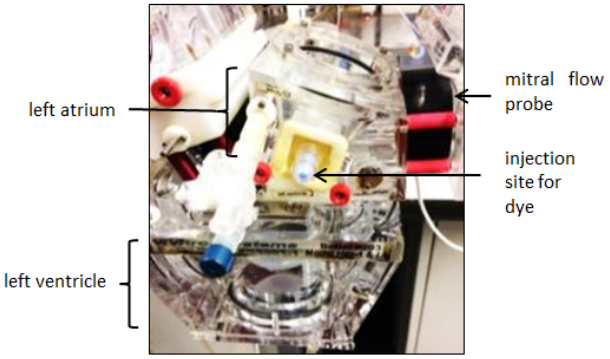

Figure 5.5: ViVitro pulse duplicator mitral flow probe (black cylinder).

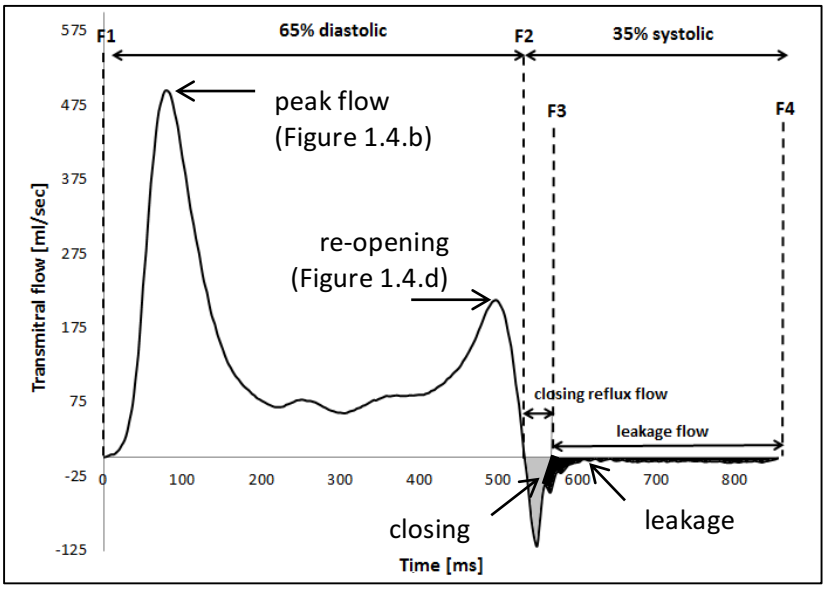

Figure 5.4: Exemplar reading from the mitral flow probe at 5 lpm indicating the 65% diastolic and 35% systolic phases, closing and leakage flows, the linear extrapolation between the latter two and flow markers F1 to F4.

Table 5.1: Accuracy of flow measurement, exemplar cardiac output statistics for 10 cardiac cycles.

Cardiac output (lpm)		Standard Deviation
Target value	*Average*	
2	2.009	0.029
3	2.996	0.001
4	4.002	0.021
5	4.961	0.012
6	5.993	0.062
7	6.959	0.041

5.1.3 Pressure transducers

There are three pressure transducers (Mikro-Tip® pressure catheter, Millar Inc.) (atrial, ventricular and aortic) (Figure 5.1 and Figure 5.6) that deflect under pressure altering their electrical outputs, which are calibrated to pressure in millimeters of mercury[22] (mmHg) (Figure 5.7). The sample rate being the same as the flow meters, 300 Hz. The pressure transducers exceeded the required accuracy of ±2 mmHg; (ISO 5840) for example the mean ventricular pressure for 10 consecutive cardiac cycles was measured at 36.71 ± 0.36 mmHg.

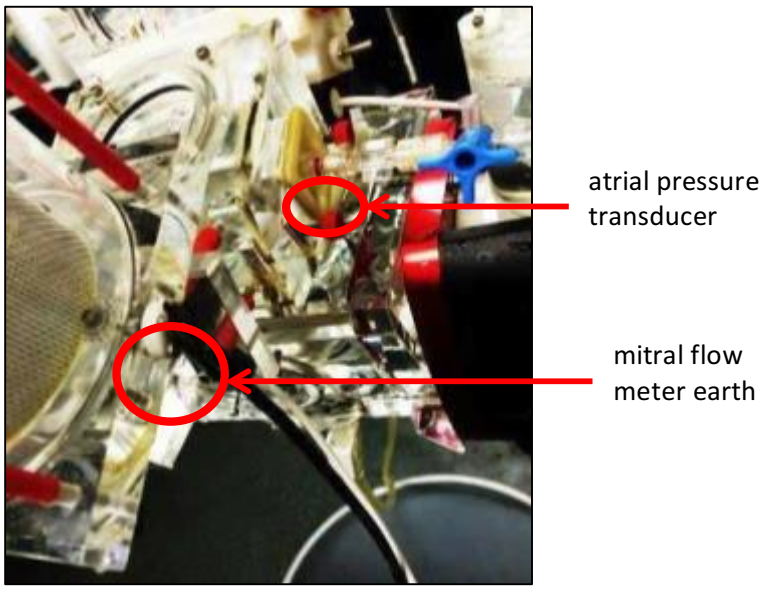

Figure 5.6: ViVitro pulse duplicator atrial pressure transducer and earth for flow meter.

[22] A millimetre of mercury (mmHg) is the pressure generated by a column of mercury one millimetre high (approximately 133 pascals (Pa)).

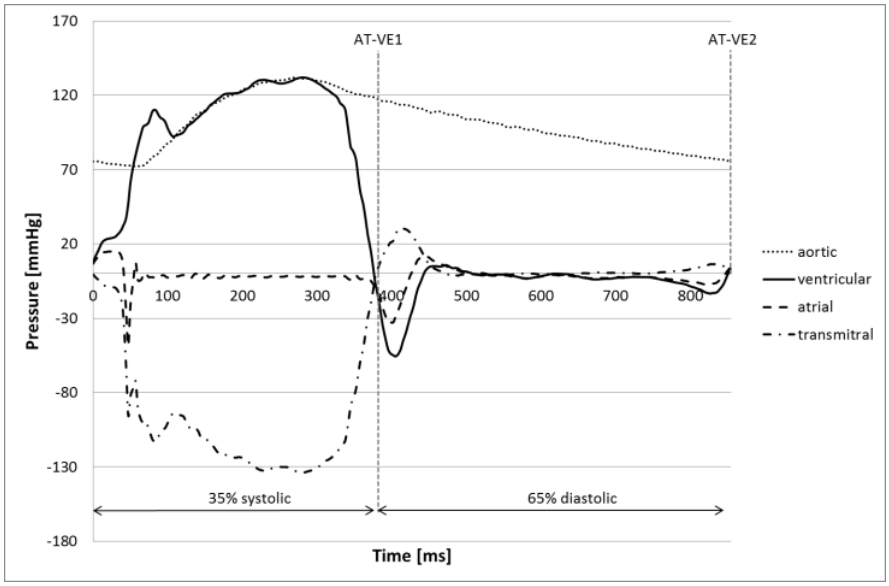

Figure 5.7: Pressure recorded by the three pressure transducers; aortic, ventricular and atrial, and the transmitral (atrial minus ventricular), indicating the two pressure markers AT-VE1 and AT-VE2.

5.1.4 Surgical Mitral Valve Holders

Holders were required to mount the surgical prototypes in the pulse duplicator's mitral position, the angle of which can be seen in Figure 5.1. They had to create a fluid seal between the left ventricle and atrium as well as between prototypes and their holders. Therefore, the SMV stents were designed with flanges which slotted into silicon holders.

The holders were made by syringing in a liquid silicone mixture (RTV Silicon Mould Rubber T28 mixed with 5% weight T6 catalyst) into 3D printed moulds (Figure 5.8), which were cured in 24 hours at room temperature. To aid removal of cured holders, all mould parts were sprayed with Ambersil Formula 5 prior to syringing in the silicon.

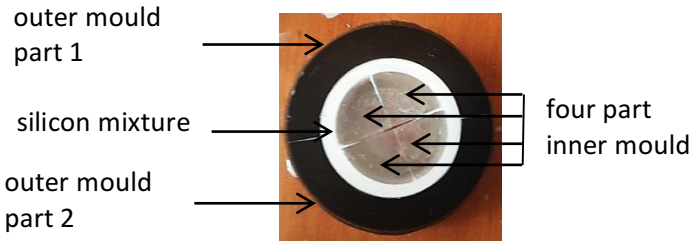

Figure 5.8: Moulds for making a holder for a circular surgical mitral valve assembled and filled with silicon; outer moulds (Object30 3D (Stratasys Ltd.)), inner moulds (Form1+ (Formlabs Inc.)).

The outer sections of the mould were made on the Object30 3D (Stratasys Ltd.). As the mould design developed the more cost effective Form1+ (Formlabs Inc.) desktop 3D printer became available and so was used to make the inner sections. Due to the Form1+'s limitations the inner sections had to be made in four parts and partially hollowed, which also saved material (clear photopolymer resin) and time required for printing (Figure 5.9). The same outer moulds were used to create the holders for both the D-shaped and circular SMVs, just different inner moulds were required, thereby saving material, money and time.

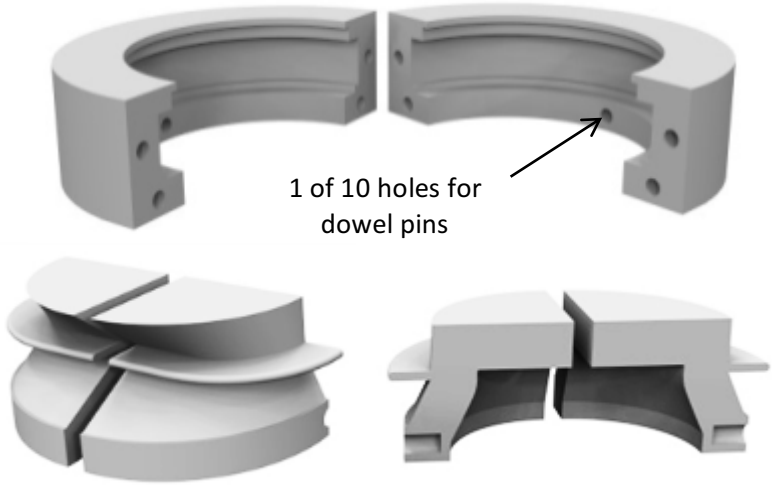

Figure 5.9: Moulds to make D-shaped surgical mitral valve holder **(top)** two outer sections **(bottom)** four hollow inner sections.

5.1.5 Mock native mitral valve implantation sites

It is common practice to design one sized prosthetic heart valve to fit a range of patient sized valves. For example, the latest SAPIEN 3, 26 mm device is suitable for implantation in annulus sizes 21-25 mm and the CoreValve Evolute 23 mm is for 18-20 mm annuluses (Table 1.1). These interference fits anchor the devices and prevent paravalvular leakage, similarly the UCL TMV will be larger than the native mitral valve into which it is implanted and therefore will operate in a semi-folded configuration, unique to each patient. As previously reviewed, the functional performance of TMVs is highly dependent on the difference between the size of the device and the implantation site and indifference to this fact resulted in failure of devices (De Backer et al 2014). Therefore, the 26 mm UCL TMV prototypes were assessed in six different sized mock native mitral valve implantation sites with inter-trigonal diameters ranging between 20 and 25 mm in 1 mm intervals, which

thereby addressed a potential failure mode thus keeping with the risk based approach outlined in ISO 5840-3:2013 (Annex A, A.1). Increments of 1 mm were chosen because this is the accuracy achievable using echocardiographic imaging[23], and therefore smaller increments would not have clinical relevance.

Firstly D-shaped silicon holders were made using similar moulds and methods as previously described (Figure 5.10.a/b), then mock native mitral valve leaflets were added by painting 5 layers of silicone onto paper templates (Figure 5.10.c and Figure 5.11), which peeled away easily from the silicon once dry. In fact, without mock native leaflets the UCL TMV migrated into the atrium. Therefore they were essential to correctly model the geometry of the implantation site and thereby securely anchor the device.

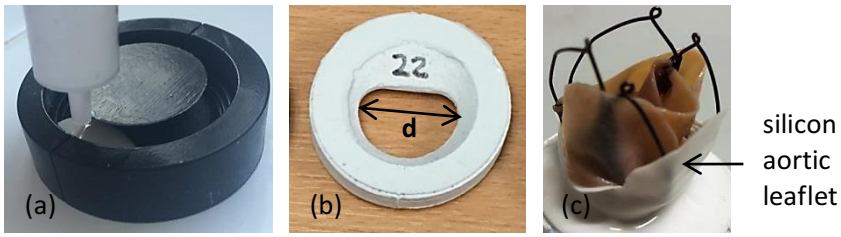

Figure 5.10: Mock native mitral valves **(a)** silicon syringed into three part mould **(b)** resulting D-shaped holder indicating inter-trigonal diameter 'd' **(c)** UCL transcatheter mitral valve 2 in a 25 mm annulus with mock leaflets.

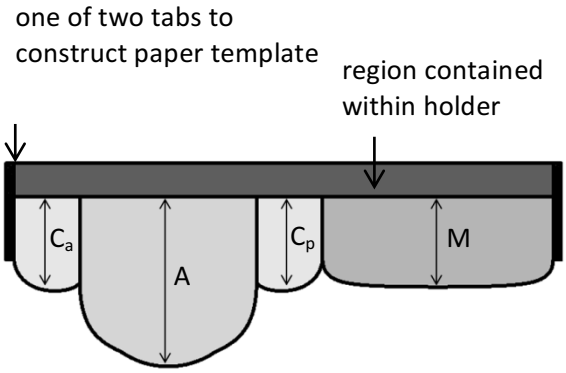

Figure 5.11: Mock native mitral valve leaflet template indicating leaflet lengths for; **Ca:** anterior commissure, **A:** aortic leaflet, **Cp:** posterior commissure and **M:** mural leaflet.

[23] Acknowledgements Pantazis A (Imaging Consultant Cardiologist, The Heart Hospital, London).

Numerical simulations (Bozkurt et al 2016) of the TMV frame[24] deployed inside similar D-shaped orifices (20-25 mm) confirmed for all annulus sizes that stresses in the nitinol frame would be acceptable; the highest stress being approximately half of the yield strength.

5.2 Pulsatile flow conditions

5.2.1 Pressure test

All hydrodynamic parameters were measured at a heart rate of 70 bpm with a mean aortic pressure[25] of 100 mmHg and systolic duration of 35%, representative of a normal healthy adult as required by regulatory standards. These test parameters were achieved by combined adjustment of the peripheral resistance controller and piston amplifier (Figure 5.3); more specifically an increase in the constriction of the peripheral system increased the mean aortic pressure but reduced flow and therefore reduced cardiac output (CO).

In vivo CO will vary between each individual depending on their physical fitness and level of activity; maximum values range from approximately 35 lpm for a trained athlete to 20 lpm for an average person. Typically CO at rest is 5 lpm and a normal range of outputs is between 4 and 8 lpm. Therefore CO was varied between 2 and 7 lpm in 1 lpm intervals, providing the minimum of four readings between 2 and 7 lpm as required by ISO 5840, whilst the previously mentioned flow conditions were held constant. It should be noted that because the pulsatile flow conditions were held constant across cardiac outputs[26], a full set of measurements at 2, 3, 4, 5, 6 and 7 lpm (for the same device) are not representative of the same physiology.

5.2.2 Regurgitant test

Minimisation of regurgitation in mitral prostheses is important. Therefore, a regurgitation test was performed to determine the regurgitant volumes associated with mean back

[24] Different software to that used for the pericardial leaflets was required to simulate the Nitinol frame i.e. one which used an implicit code was required.
[25] A mean aortic pressure of 100 mmHg is normotensive, compared to 70 mmHg for hypotensive and between 113 and 190 mmHg for hypertension.
[26] In clinical practice a Cardiac Index (l/min/m^2) is used to relate cardiac output (lpm) to body surface area (m^2), usually between 2.6 and 4.2 l/min/m^2 at rest, and thus assesses the heart performance relative to the size of the individual.

pressures of 80, 120 and 160 mmHg and heart rates of 40, 70 and 120 bpm at a normal cardiac output of 5 lpm and systolic duration of 35% (ISO 5840-3:2013; N.4.3.3).

5.3 Test parameters

The test parameters reported were selected with the aim of characterising diastolic, systolic and global performance of the prosthetic mitral valves. The effective orifice area (EOA) and mean transmitral diastolic pressure drop characterise forward flow impedance imposed by prostheses and would be maximal and minimal respectively for an optimal device. The regurgitant fraction (RF) and associated volumes (closing, leakage and total) characterise the incompetence of valves during systole which contribute to closing, leakage and total energy losses, the later which is also due to diastolic losses and would all be minimal for an optimal device. These test parameters are further defined and described below.

5.3.1 Mean transvalvular diastolic pressure drop

The mean transvalvular diastolic pressure drop is the average pressure difference between the left atrium (inflow) and left ventricle (outflow) during diastole, when the mitral valve is open. This is reported, instead of the mean over the entire cardiac cycle, as previously expounded by Walker et al (1983), because the diastolic mean pressure measures the valves' resistance to forward flow. Optimal prosthetic heart valves have minimal pressure differences, associated with maintaining a healthy blood pressure. Therefore, the mean transvalvular diastolic pressure drop is a more specific and relevant quantification of the devices performance.

5.3.2 Effective orifice area

The EOA is the vena contracta area; the minimum cross sectional area associated with the jet of blood through a heart valve where velocity is maximum and is always smaller than anatomical/geometric orifice areas (Figure 5.12) and can be estimated using Gorlin's equation (Equation 5.1).

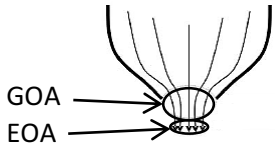

Figure 5.12: 2D representation of the location of the geometric orifice area (GOA) and effective orifice area (EOA) i.e. the area of the vena contracta (adapted from Akins et al 2008).

$$\mathrm{EOA} = \frac{\mathrm{Q_{rms}}}{51.6\sqrt{\frac{\Delta p}{\rho}}} \tag{5.1}$$

where;

EOA = effective orifice area (cm^2),

Q_{rms} = root mean square forward flow (ml/s) during the positive differential pressure period,

Δp = mean pressure difference (mmHg) measured during the positive differential pressure period,

ρ = density of the test fluid (g/cm^2) and

51.6 = non-dimensionless constant, therefore it is only valid with the units specified.

$$\mathrm{Q_{rms}} = \sqrt{\frac{\int_{t1}^{t2} \mathrm{Q(t)^2 dt}}{t_2\text{-}t_1}} \tag{5. 2}$$

Where;

$\mathrm{Q(t)}$ = instantaneous flow at time t,

t_1 = time at start of positive pressure (AT-VE1 in Figure 5.13) and

t_2 = time at end of positive pressure (AT-VE2 in Figure 5.13).

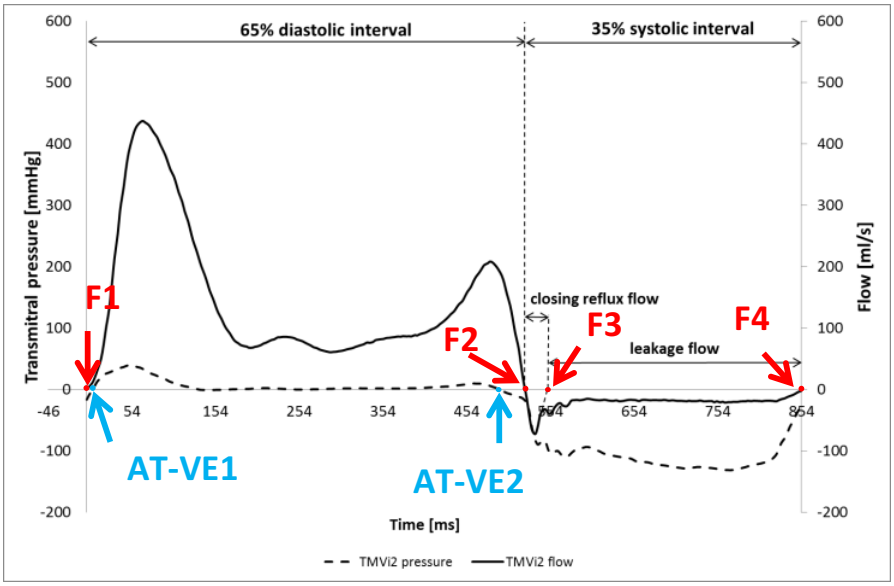

Figure 5.13: Average transmitral pressure and flows across ten cardiac cycles for the UCL transcatheter mitral valve prototype 2 at a cardiac output of 5 lpm for one cardiac cycle, systolic/diastolic phases marked based on flow.

The time interval used to calculate the flow and pressure during the positive differential pressure period in Equation 5.2 is determined using pressure markers AT-VE1 and AT-VE2 (Figure 5.13), which provides repeatable and consistent results compared to the flow (F), hybrid (H) and pressure/flow (PF) alternatives:

- (F) uses F1 and F2 (Figure 5.13),
- (H) uses AT-VE1 and F2 and
- (PF) uses the AT-VE1 and AT-VE2 to calculate the pressure component and uses F1 and F2 to calculate the flow component.

However, there are limitations to calculating the EOA based on pressure, mainly due to it being based on a simplified version of Bernoulli's equation and therefore will not equate to EOAs calculated *in vivo*, although this formulae is also used to calculate EOAs *in vivo*. Alternative EOA equations were proposed by Aaslid et al (1975) and Gabbay et al (1978), which whilst theoretically more correct are not clinically practical, due to the sophisticated flow measuring device required (Dieter 1990) and so Gorlin's equation was still used, which is relevant for comparison to the minimum performance requirements in ISO 5840. It should be noted that in clinical practice an EOA indexed to body surface area is commonly used (Dumesnil et al 1992).

In summary, the EOA is a functional valve area used to measure how much a particular prosthesis impedes forward flow and thereby quantifies the quality of a prosthesis; higher EOAs corresponding with desirable smaller energy losses.

5.3.3 Regurgitation fraction

The RF is a measure of inevitable reverse flow during one cardiac cycle, defined as the sum of closing and leakage volumes expressed as a percentage of forward flow volume (Equation (5.3). Optimal devices are associated with minimal RFs because they have smaller energy losses i.e. require less work from the left ventricle.

$$\mathrm{RF}[\%] = \frac{(\text{closing volume} + \text{leakage volume})*100}{\text{forward volume}} \tag{5.3}$$

5.3.4 Volumes

The total regurgitant volume is the total reverse flow from the left ventricle into the left atrium during one cardiac cycle and is the sum of closing and leakage volumes as measured by the mitral flow meter; being total reverse flow due to valve closure dynamics and total reverse flow through the closed valve respectively (Figure 5.4).

5.3.5 Energy losses

Contraction of the left ventricle muscle generates static pressure, which once increased above the aorta pressure, forces the aortic valve open thereby converting pressure energy into kinetic energy of the ejection fraction, typically 67 ± 4.6 % of total ventricle volume, which flows around the body at a rate to enable normal cellular metabolism. This conversion of static pressure to kinetic energy during one cardiac cycle is commonly depicted in terms of the pressure *within* and the volume *of* the left ventricle; the integral of this pressure-volume diagram (Figure 1.9) is equivalent to the energy generated by the ventricle during one cardiac cycle (Equation 5.4). Similarly, diastolic, closing, leakage and total energy losses (EL_D, EL_C, EL_L and EL_T) are calculated by integrating flow times transvalvular pressure over a relevant flow interval; Equations 5.5-5.8 respectively. However, these equations are limited because they do not account for the ventricular compliance.

$$\mathrm{VE} = 0.1333 \int_{\mathrm{F1}}^{\mathrm{F4}} \mathrm{P_{vent}} \cdot \mathrm{DL\_DT} \cdot \mathrm{dt} \tag{5.4}$$

Where;

0.1333 = constant to convert energy from mmHg.ml to milli joules (mJ)[27],

F1 and F4 = flow intervals defined in Figure 5.13, integrals are evaluated by the ViViTest software using the trapezoidal rule,

$\mathrm{P_{vent}}$ = ventricular pressure (mmHg),

DL_DT = signal provided by SuperPump Controller indicating pump's flow rate (ml/sec) and dt = 1/sample rate.

$$\mathrm{EL_D} = 0.1333 \int_{\mathrm{F1}}^{\mathrm{F2}} \Delta \mathrm{P}_i \cdot \mathrm{flow} \cdot \mathrm{dt} \tag{5.5}$$

$$\mathrm{EL_C} = 0.1333 \int_{\mathrm{F2}}^{\mathrm{F3}} \Delta \mathrm{P}_i \cdot \mathrm{flow} \cdot \mathrm{dt} \tag{5.6}$$

$$\mathrm{EL_L} = 0.1333 \int_{\mathrm{F3}}^{\mathrm{F4}} \Delta \mathrm{P}_i \cdot \mathrm{flow} \cdot \mathrm{dt} \tag{5.7}$$

$$\mathrm{EL_T} = \mathrm{EL_D} + \mathrm{EL_C} + \mathrm{EL_L} \tag{5.8}$$

Where;

$\Delta \mathrm{P}_i$ = pressure difference (mmHg) across mitral valve during the relevant flow interval and flow = flow rate (ml/sec) across mitral valve during the relevant flow interval.

In summary, some of the pressure energy generated by the left ventricle is not converted to kinetic energy; it is lost as blood travels through the circulatory system. The ventricle compensates for additional losses due to pathologic conditions such as valvular regurgitation or presence of prosthesis by raising systolic pressure and/or volumetric

[27] 1 J = 1 N.m = 1 Pa.m^3 = 1 (kg.m^2)/s^2 where J represents joules (units of energy), N is Newtons (units of force), m is meters (units of distance), Pa is Pascals (units of pressure), kg is kilograms (units of mass) and s is seconds (units of time).

capacity, both of which result in an undesirable increase in work on the myocardium. Therefore an optimal prosthetic heart valve would have minimal energy losses.

5.4 Minimum performance requirements

The minimum performance requirements for prosthetic mitral valves corresponding to the applied pulsatile flow conditions for a normal healthy adult are outlined in two standards; one for surgical devices, ISO 5840:2009 'Cardiovascular implants – cardiac valve prostheses', and one for transcatheter devices, ISO 5840-3:2013 'Cardiovascular implants – cardiac valve prostheses Part 3: Heart valve substitutes implanted by transcatheter techniques'. In both cases, just two requirements are set, one for diastolic and one for systolic performances, namely the EOA and RF respectively.

5.4.1 Surgical mitral valves

The minimum performance requirements stipulated in ISO 5840:2009 are relative to the device tissue annulus diameter (TAD; the smallest flow area within the patient's valve annulus), which assumes they are circular. Therefore, to determine requirements for a D-shaped valve it was necessary to convert the TADs to perimeters (Table 5.2).

Table 5.2: Minimum device performance requirements for surgical mitral valve replacements (adapted from ISO 5840:2009).

Valve size	TAD[1] (mm)	25	27	29	31
	Perimeter (mm)	79	85	91	97
Effective orifice area (cm^2) ≥		1.2	1.4	1.6	1.8
Regurgitation fraction (%) ≤		15	15	20	20
[1]Tissue Annulus Diameter					

All the SMVs tested had the same outer perimeter of 86 mm and therefore should meet the same minimum performance requirements of an EOA ≥ 1.4-1.6 cm^2 and a RF ≤ 15-20%.

5.4.2 Transcatheter mitral valves

The allowable RF for transcatheter valves is higher than for surgical devices because their implantation technique inevitably leads to greater paravalvular leakage due to a difference

between the perimeters of the device and implantation site. Therefore the required EOA is higher to compensate for leniency in systolic performance.

The minimum performance requirements stipulated in ISO 5840-3:2013 are based on published literature (American College of Cardiology 2006)(Yoganathan et al 2002) (Table 5.3) and are relative to the deployed valve diameter within implant site. The requirements for 25 and 23 mm devices are an EOA ≥ 1.25 cm^2 and 1.05 cm^2 respectively and both require a RF ≤ 20%. No requirements are set for annulus sizes 20-22 mm.

Table 5.3: Minimum device performance requirements for transcatheter mitral valve replacements (adapted from ISO 5840-3:2013).

Valve size	Deployed valve diameter within implant site (mm)	23	25	27	29	31	33
	Effective orifice area (cm^2) ≥	1.05	1.25	1.45	1.65	1.90	2.15
	Regurgitation fraction (%) ≤	20	20	20	25	25	25

5.5 Surgical mitral valves

5.5.1 Aim

There are no predicate devices to compare with the UCL TMV. Therefore, in order to assess the validity of the design process, the surgical valve is used for comparison. Thus, the aim of the SMVs was to provide a pseudo reference valve for the UCL TMV leaflets (section 2.3.4) by comparing the conical bileaflet (CB) SMV to a replica of the Pericarbon MORE Mitral (PMM) (Sorin Group, now LivaNova PLC), named hereafter as the trileaflet (T) valve.

5.5.1.1 Hypotheses

It was hypothesised that for the same size implantation site the more physiological morphology of the bileaflet valves would have advantageous functional performance compared to the circular trileaflet valves. This was based on previous research into a similar bileaflet mitral valve, which demonstrated the leaflet length and proximity to the ventricular wall will have a significant effect on the energy dissipation that occurs as blood flows from the left atrium to the aorta (Kheradvar et al 2012) as well as evidence previously discussed in section 5.5.3.

5.5.1.2 Bileaflet valve

The stented, bileaflet, D-shaped, conical mitral valves described in this section advance the study of SMVs which mimic the native morphology by providing an original set of features, combining the conical design of the Sheffield (section 2.1.1) and stentless mitral valves with the D-shape of the Quattro™ (St. Jude Medical Inc.) (section 2.1.2). Also, the combined results of the CB and T valves provide a solution to the reference valve predicament, discussed below.

The CB SMV houses the leaflets chosen for the UCL TMV (Figure 4.1Figure 4.3). However, the conicity of these leaflets is only suitable for a transcatheter device; chosen to address the needs of their patient population i.e. severe mitral regurgitation, and would not have been chosen if designing a surgical device. In practice, the leaflets for the TMV are designed to operate with some compression of the base (a size 26 mm fits into a maximum sized annulus of 25 mm) which makes the leaflets less conical. Consequently, it is inevitable that the diastolic performance of the CB valve, measured in terms of its effective orifice area (EOA) will be significantly surpassed by the straight T valve.

5.5.1.3 Trileaflet valve

The T valve was a scaled replica of the PMM (Figure 1.10), with the same external perimeter as the bileaflet valves, making their comparison clinically relevant i.e. they could both potentially be implanted in the same patient. Furthermore, a replica was required to enable comparison independently from stent design, material selection and processing and assembly methods.

More specifically, commercial valves typically have multi-staged fixation resulting in their unstressed state being the closed position[28]. Typically, the flat sheet of pericardium is firstly fixed with 0.2% GA (within 4 hours of slaughter), cut and formed into leaflets which are then pressurised to close and fixed again with 0.5% GA. In contrast, the leaflets for the prototypes were not subjected to pre-stressing during assembly; therefore their unstressed state was the open position.

[28] In general, commercially available valves are fixed in their closed position because surgeons prefer to see the valve is going to be competent before implantation.

5.5.2 Prototyping

5.5.2.1 Stents

The SMV stents, with annular perimeters of 86 mm, had flanges to mount them in the pulse duplicator using specifically designed silicon holders (Figure 5.14), made from clear photopolymer resin using stereolithography (Form 1+, Formlabs Inc.); a form of additive manufacturing that creates artefacts by directing a laser across a tank of liquid resin, which polymerises thin layers onto a build platform that pulls the model upwards out of the tank. The resin is not approved for use in medical applications and so the prototypes are only suitable for *in vitro* assessment.

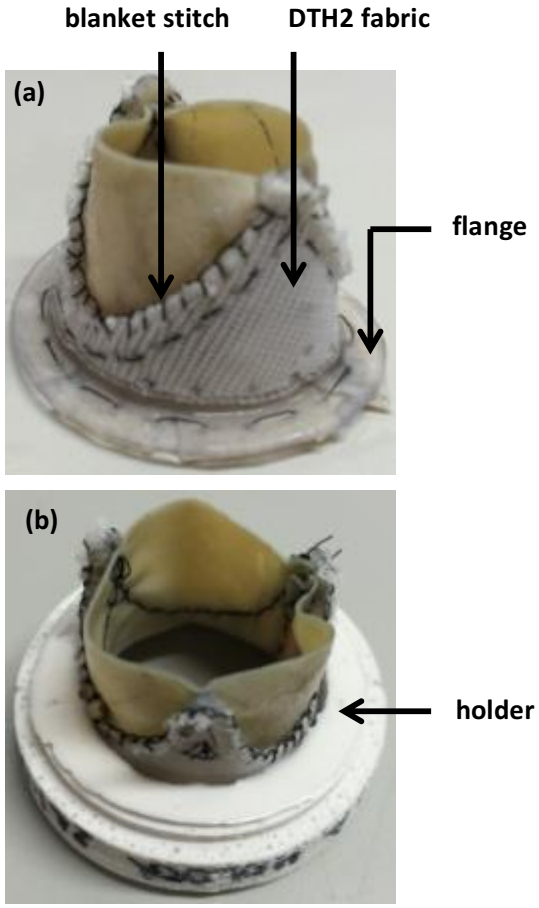

Figure 5.14: Surgical mitral valves (SMVs) **(a)** conical bileaflet valve, indicating DTH2 fabric, nylon blanket stitch and flange which secure the SMVs in their silicon holders **(b)** trileaflet valve indicating its silicon holder.

Thinner stents are preferable because they maximise the geometric orifice area, and consequently the EOA. The thinnest the Form1+ could make the stents was 1 mm, which is 0.3 mm thicker than achieved in most polymeric commercial stents (e.g. made from Delrin, one commercial form of polyoxymethylene), although the Pericarbon MORE has a stent 1.2

mm thick for large sizes. Due to this sub-optimal thickness achievable at this prototyping stage, the usual layer of material on the inside of the stent was omitted.

5.5.2.2 Fabric

The stents were covered in a biocompatible PET knitted material used for heart valve sewing rings; DTH2 (Vascutek Ltd, A Terumo company). This was preferable to the alternative DTL1 because it is 0.17 mm thicker, with a thickness of 0.466 mm and has a water permeability of 0.96 $ml/cm^2/min$ which is 0.71 $ml/cm^2/min$ lower, both advantageous in terms of reducing intervalvular leakage, which may occur through the assembly holes of the stents. Also DTH2 has suture retention of 25 N which is 11 N stronger than DTL1, advantageous for securely joining it to the inner pericardium band using a blanket stitch (Figure 5.14).

5.5.2.3 Nylon thread

The name nylon refers to a family of similar artificial aliphatic polyamides[29] and is one of several materials used to make surgical sutures. At this initial *in vitro* prototyping stage non-medical grade nylon thread was sufficient and could foreseeably be replaced with biocompatible thread if the designs progress to *in vivo* trials.

5.5.2.4 Inner band

The PMM has an inner band made from pericardium, which relative to using fabric not only reduces paravalvular regurgitation but also leaflet wear due to contact during diastole. Therefore an inner pericardium band was also used in the replica T design (Figure 5.15) and adapted for the bileaflet designs.

5.5.2.5 Assembly

The 0.4 mm BP leaflets and inner bands were cut from patches previously processed (section 3.1.3) and stitched together using nylon thread along their leaflet profiles (Figure 5.15). The short edges were stitched together, then the cylindrical/conical tissue structures were stitched to the main body of their stents, flange and finally the inner band and DTH2 fabric were joined using a blanket stitch.

[29] Polyamides also occur naturally, for example wool and silk.

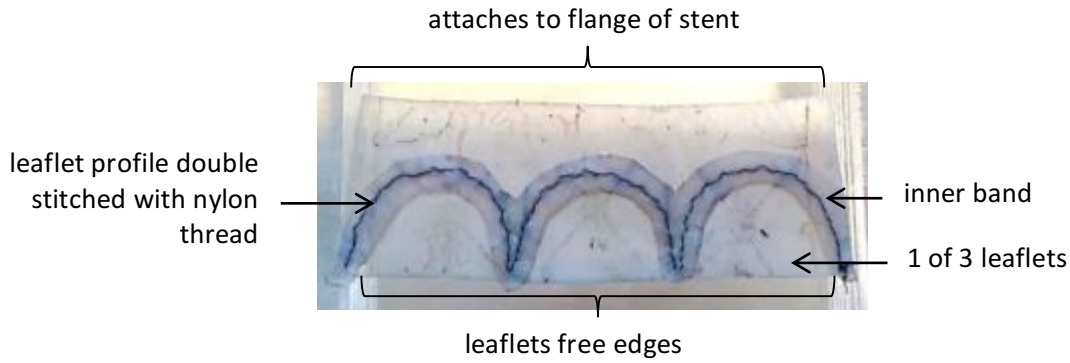

Figure 5.15: Trileaflet surgical mitral valve leaflets and inner band double stitched together with nylon thread, prior to assembly on stent.

5.5.3 Flow visualisation

This section describes the relevance, aims, hypothesis and protocol for visualising flow in the pulse duplicator's ventricle using dye.

5.5.3.1 Clinical relevance

All current heart valve prostheses are associated with clinical complications due to non-physiologic flow patterns caused by their implantation (Dasi et al 2009). More specifically, SMV replacements have been observed to reverse vertical flow inside the left ventricle, increasing energy dissipation, i.e. increasing energy required by the left ventricle to change the momentum of fluid within the ventricle, which in a normal healthy heart is minimised by timely alignment of flow towards the aortic valve by the end of diastole ready for systolic ejection, which also avoids excessive regional wall stress. The reversal of the vertical flow also effects the spatial pressure distribution, subsequently possibly influencing post procedural complications (Pendrizzetti et al 2010), such as blood damage, which can be caused by excessive turbulence, as well as other problems related to blood flow including platelet activation, thrombus formation, hemolysis and increased myocardial stress leading to left ventricular hypertrophy and remodelling. These changes in transmitral vortices are affected by variation in transmitral pressure gradient (Dyverfeldt et al 2011) as well as length and proximity of leaflets to the ventricle wall, as per a similar bileaflet mitral valve design (Kheradvar et al 2012).

It has previously been inferred that a more physiological bileaflet mitral prosthesis would result in flow patterns that close the valve as efficiently as the natural valve (Peskin et al 1981, Bellhouse 1980, Lee et al 1979, Reul et al 1979, Laniado et al 1976, Tsakiris AG et al 1976), although the exact mechanisms are undetermined. Furthermore, more recently the potential benefits of flow patterns resulting from a bileaflet valve (Kheradvar et al Feb 2012, Kheradvar et al 2010, Pasipoularides et al 2003) compared to trileaflet valves (Kheradvar et al 2009, Kheradvar et al Jan 2007, Kheradvar et al Dec 2007, Pasipoularides et al 2003) have been found.

5.5.3.2 Aim

The aim of visualising ventricle flow associated with the bileaflet and trileaflet SMVs was to qualitatively compare their diastolic streaklines. Flow visualisation using dye injection was not feasible for the TMVs due to skirt porosity, which would allow dye to leak from the atrium through the skirt into the ventricle prior to valve opening, muddying the ventricle fluid making diastolic jet streaks unobservable.

5.5.3.3 Hypothesis

The flow patterns, in particular wash out of particularly stagnant areas will be different for the bileaflet and trileaflet SMVs.

5.5.3.4 Protocol

Ideally particle image velocimetry (PIV) would be used to visualise and quantify the ventricle flow, however due to technical limitations (section 0) dye injection was used as a preliminary method of obtaining qualitative streak line data.

Once the pulsatile flow conditions representative of a normal healthy adult were set for a CO of 4 lpm[30] and a high speed camera (TSI) had begun recording whilst linked with Insight Experiment MVUR VI software, blue dye (Cole-Parmer blue tracer dye concentrate) was injected into the atrium just above the mitral valve (Figures 5.4 and Figure 5.16). A few free standing light sources were used to help illuminate the flow.

[30] A cardiac output of 5 lpm was attempted but the quality of the images was worse than at 4 lpm.

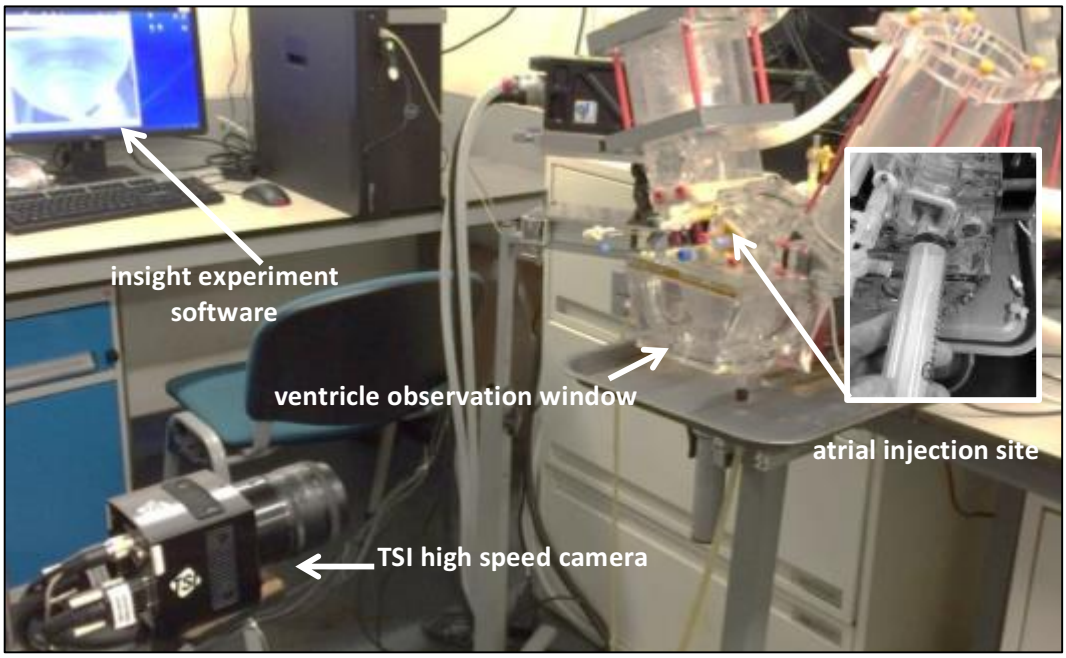

Figure 5.16: Dye injection flow visualisation ViVitro pulse duplicator left ventricle using TSI high speed camera and insight experiment software.

5.5.4 Results

This section presents the functional performance and flow visualisation results for the SMVs.

5.5.4.1 Anomalies

Most of the data plotted in section 5.5.4 is the average of three prototypes and their associated standard deviation. However, there were some anomalies for the trileaflet valve 2 (T2), identified because they caused the standard deviation for the three prototypes to be larger than the average value for the parameter i.e. the standard deviation statistic spanned into the negative regions of leakage volume and energy loss, which are nonsensical and so were removed. The anomalies identified were as follows.

At 3 lpm T2 had an abnormally high leakage volume of 2.1 ml compared to 0.2 and 0.1 ml for T1 and T3 respectively, and similarly for a CO of 4lpm (Figure 5.23). This was also the case for the total energy losses at these COs, for example at 3 lpm T2 had a total energy loss of 52 mJ (6 %VE) compare to 25 mJ (3 %VE) and 14 mJ (2 %VE) for T1 and T3 respectively (Figure 5.29). These elevated leakages and consequently higher energy losses are most likely due to inaccuracy of the assembly of T3. More specifically the leaflets were

not perfectly aligned due to inaccuracy of the suturing, the consequent elevated leakage was exacerbated by lower ventricular pressure at lower COs which meant the leaflets did not coapt as firmly, enabling more fluid to pass back into the atrium.

The forward energy losses for prototypes 1 and 2 at COs of 2 and 3 lpm were negative and therefore were removed, which is why there are no error bars plotted (Figure 5.26, the standard deviation across ten cardiac cycles for prototype 3 for the forward energy losses were ±0.61 mJ and ±0.11 %VE). These negative energy losses occurred due to errors in the position of the flow markers used by the software to calculate energy losses (Equations 5.5-5.8 and Figure 5.13).

5.5.4.2 Functional performance

The holders designed for the SMVs successfully mounted them with a seal between the pulse duplicator atrium and ventricle chambers and prevented paravalvular leakage (Figure 5.17 and Figure 5.18).

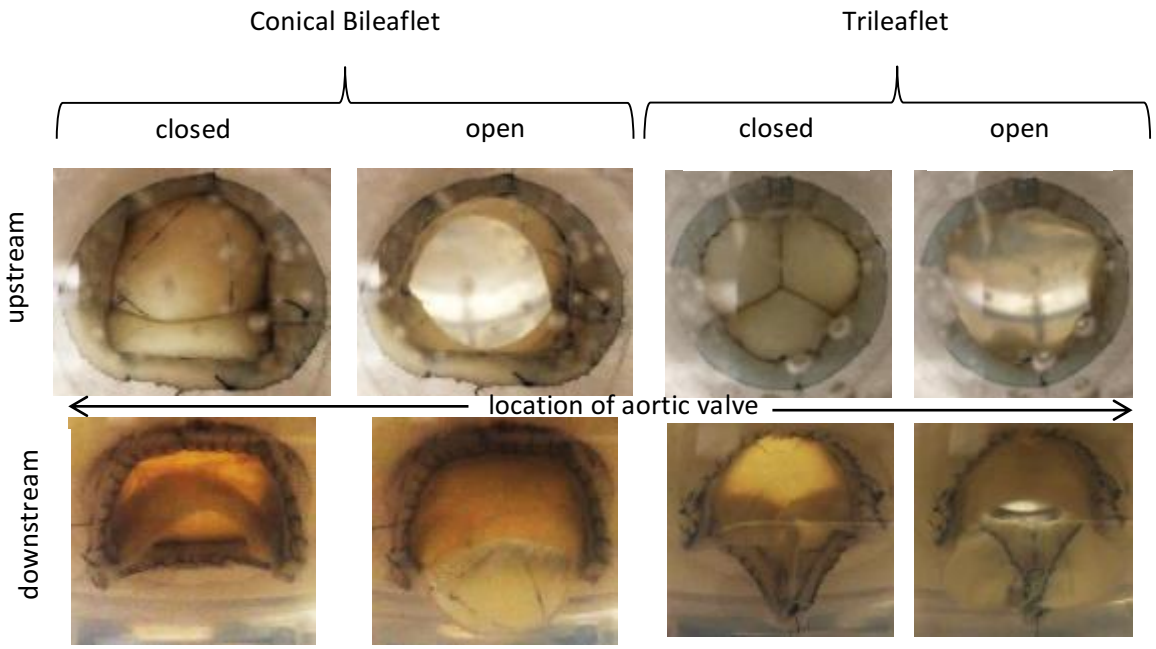

Figure 5.17: Open and closed morphology of the conical bileaflet and trileaflet designs at a cardiac output of 5 lpm, viewed in a pulse duplicator from **(top row)** atrium and **(bottom row)** ventricle.

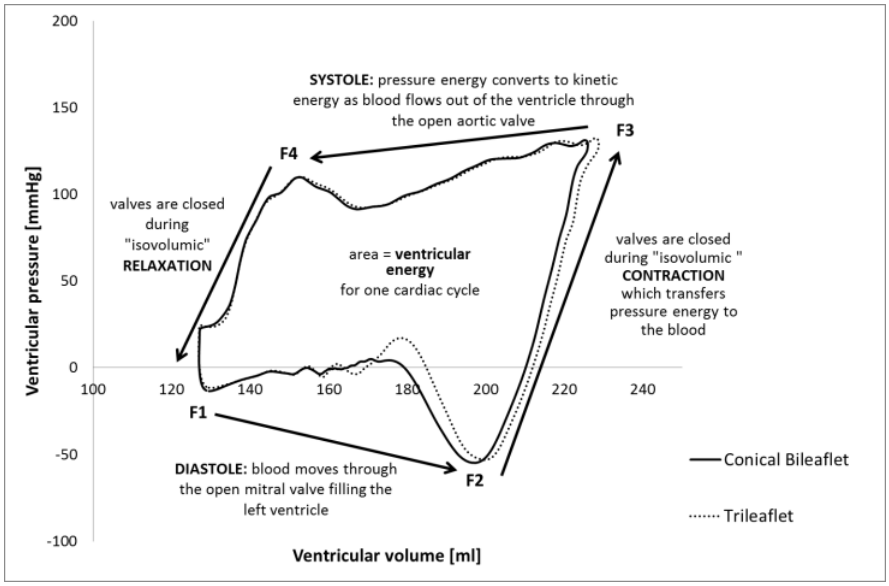

Figure 5.18: Pressure-volume diagram for two surgical mitral valve designs for a cardiac output of 5 lpm. (Irregular in shape compare with a "normal" native valve in Figure 1.9, which is rectangular).

5.5.4.2.1 Effective orifice area

The effective orifice area (EOA) increased slightly with cardiac output (CO) and was larger in the trileaflet design ranging between 1.99 and 3.07 cm^2 compared to between 1.43 and 2.07 cm^2 for the bileaflet design (Figure 5.20). When the EOA is analysed as a percentage of the geometric orifice area (GOA), ideally 100%, (Figure 5.19) the designs perform to a more similar standard (Figure 5.21). Furthermore, when the EOA of the bileaflet design is analysed as a percentage of its design orifice area (DOA) (Figure 5.19) it in fact exceeds that achieved by the trileaflet design (Figure 5.21). Both designs met the minimum EOA performance requirements for a CO of 5 lpm, i.e. they open sufficiently well.

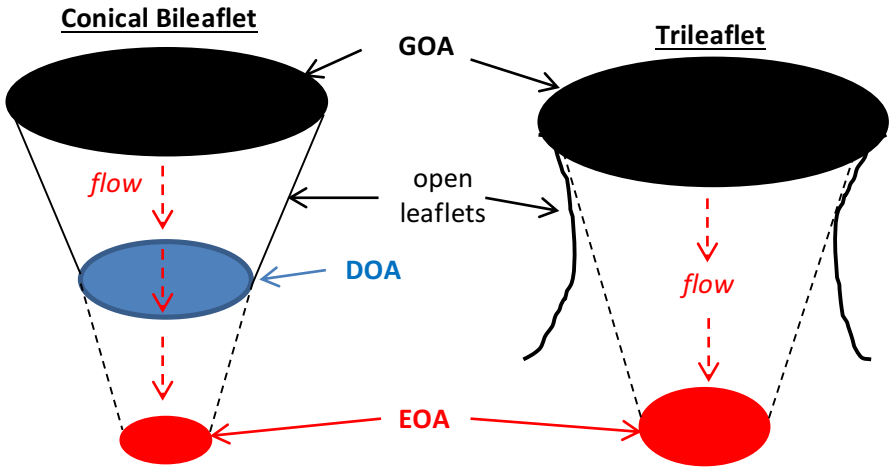

Figure 5.19: Definition of areas for the conical bileaflet and trileaflet mitral valves **(GOA)** Geometric Orifice Area **(DOA)** Design Orifice Area and **(EOA)** Effective Orifice Area.

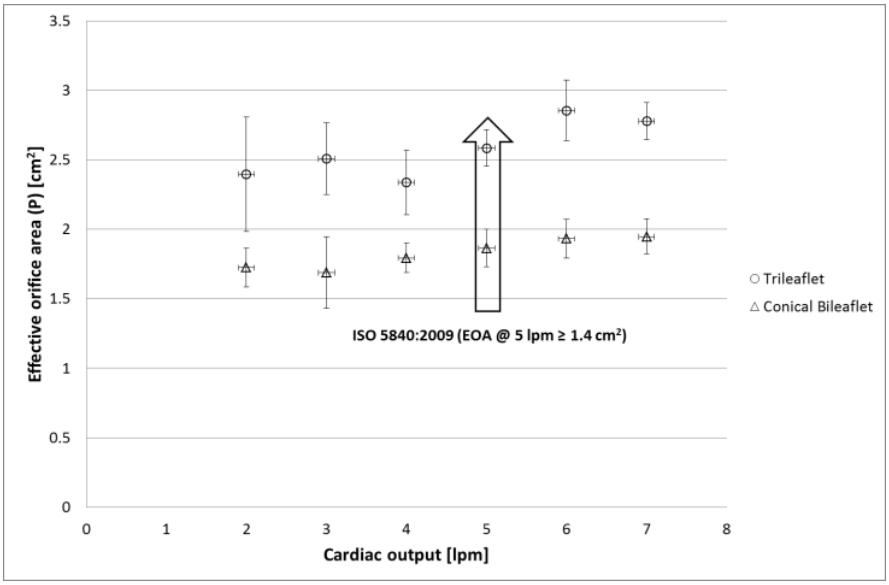

Figure 5.20: Effective orifice area for two surgical mitral valve designs, average of three prototypes each.

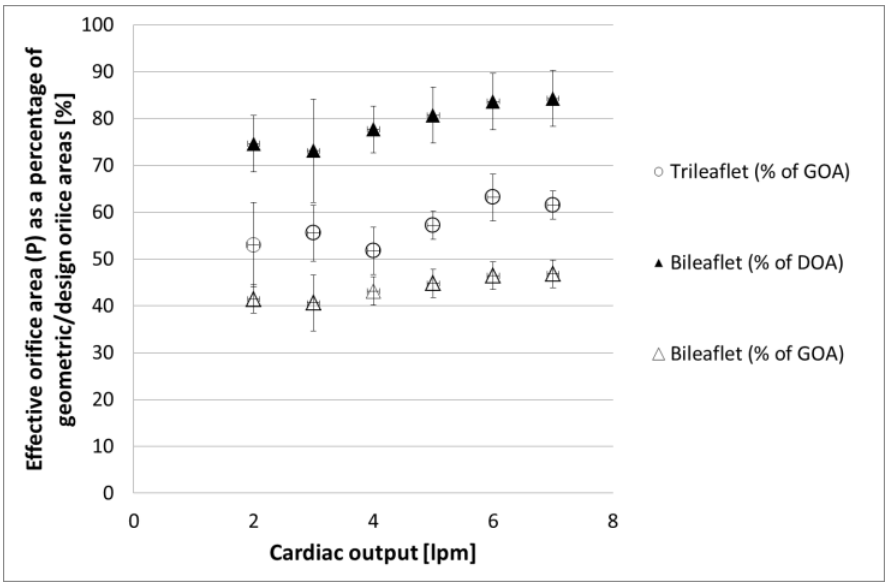

Figure 5.21: Effective orifice area (P) as a percentage of geometric/design orifice areas for two surgical mitral valve designs, average of three prototypes each.

5.5.4.2.2 Reverse flow volumes

For a CO of 5 lpm, in general, there was no statistically significant difference between the reverse flow volumes for the two designs (Figure 5.22). Although on average the trileaflet design had a larger closing volume than the bileaflet design but had less leakage and therefore the total regurgitant flow was less; however, the performance of the trileaflet design was more variable i.e. had larger standard deviations across cardiac cycles. In general, this pattern was observed for all COs.

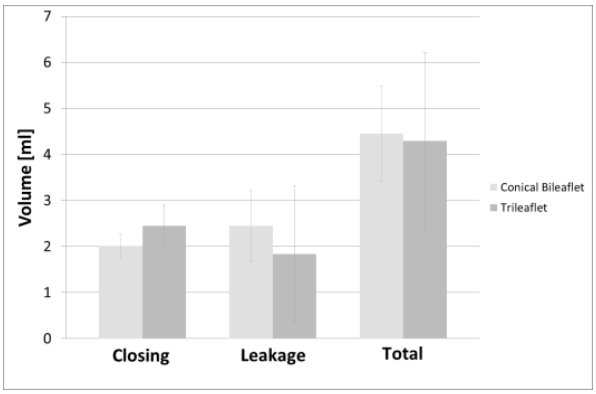

Figure 5.22: Reverse flow volumes for a cardiac output of 5 lpm, for two surgical mitral valve designs, average of three prototypes each.

The closing volume, i.e. the total reverse flow due to valve closure dynamics, decreased as the CO increased (**Error! Reference source not found.**), ranging between approximately 4.5 and 1.5 ml, and was more variable (larger standard deviations across cardiac cycles) at lower COs for the trileaflet design compared to the bileaflet design, for which the closing volume was significantly less for COs between 4 and 7 lpm.

For COs between 3 and 7 lpm leakage volume, i.e. the total reverse flow through the closed valve increased as CO increased (Figure 5.23), ranging between 0.1 and 4.5 ml, and was more variable at higher COs for the trileaflet design and overall less variable for the bileaflet design, which was significantly less for COs of 3 and 4 lpm. Furthermore, the leakage volumes for the Trileaflet valve were statistically significantly lower than for the Bileaflet valve at COs of 3 and 4 lpm, for no apparent reason. The leakage volumes for a CO at 2 lpm were in between those at 4 and 5 lpm.

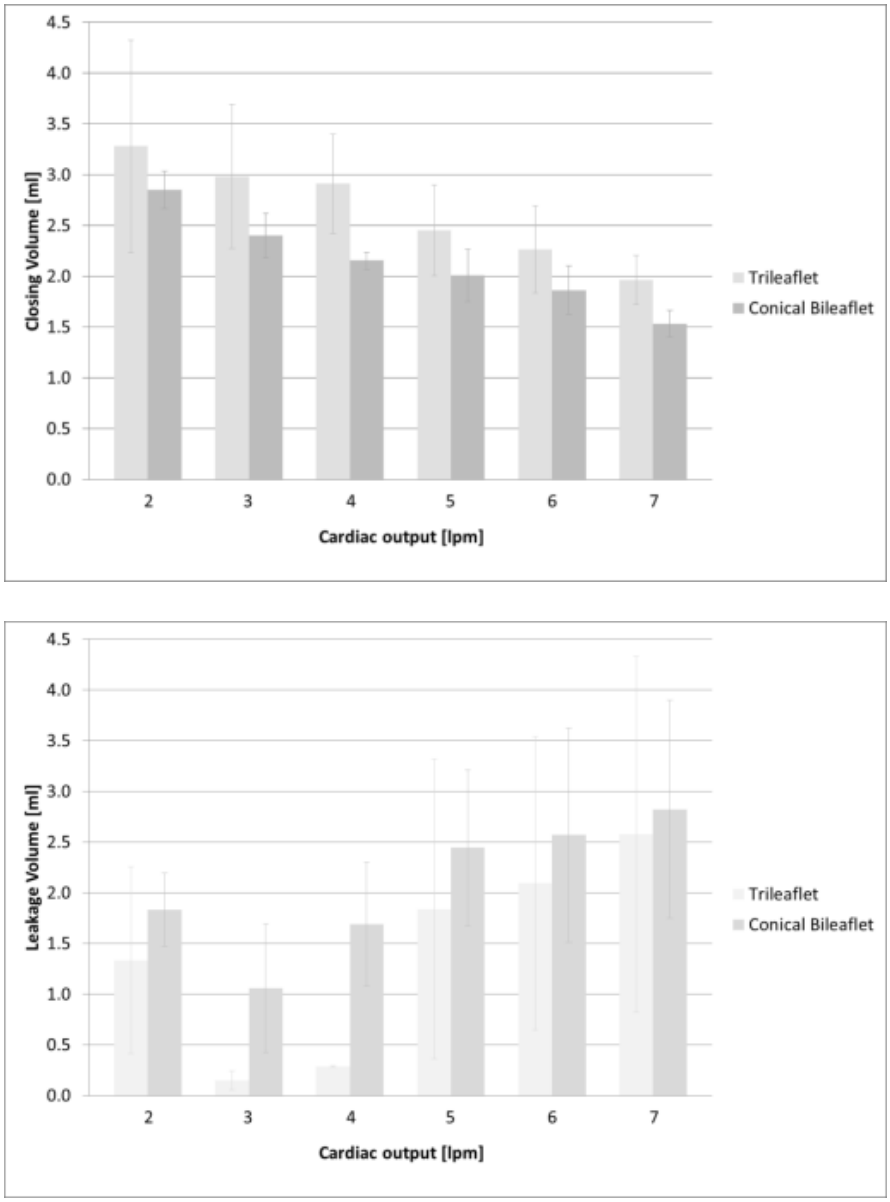

Figure 5.23: (top) closing volumes for two surgical mitral valve designs at six different cardiac outputs, average of three prototypes each **(bottom)** leakage volume for two surgical mitral valve designs at six different cardiac outputs, average of three prototypes each.

The total regurgitant volume ranged between approximately 2.3 and 6.6 ml, which occurred at COs of 3 and 2 lpm respectively. The total regurgitant volume at 4 lpm was similar to that at 3 lpm and was slightly higher and approximately constant for COs between 5 and 7 lpm.

5.5.4.2.3 Mean transmitral diastolic pressure difference

In general, the mean transmitral diastolic pressure difference increased with CO (Figure 5.24) ranging between approximately 1 and 4 mmHg and was significantly higher in the bileaflet compared to the trileaflet design for COs of 3, 6 and 7 lpm.

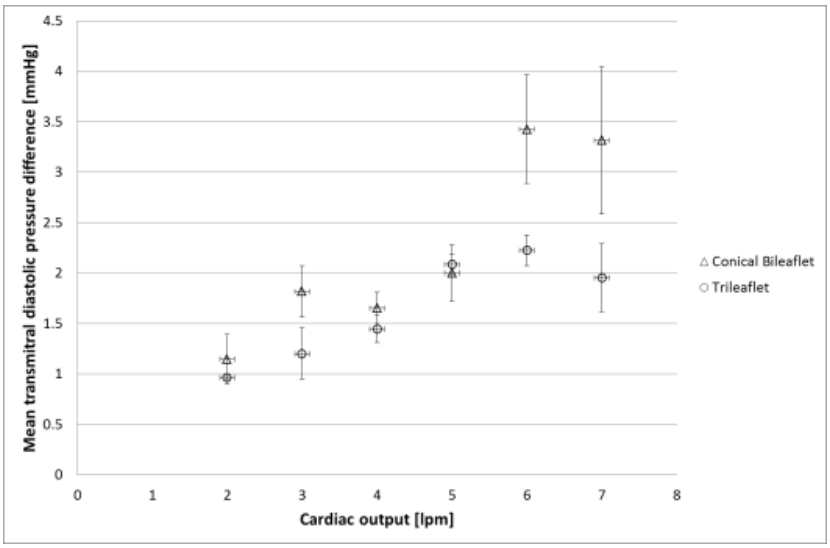

Figure 5.24: Mean transmitral diastolic pressure difference for two surgical mitral valve designs, average of three prototypes each.

5.5.4.2.4 Energy losses

At a CO of 5 lpm, in general most energy loss occurred during forward flow phase with minimal contribution due to closing (Figure 5.25), ranging between 85 and 15 mJ (i.e. 1-6 percent of ventricular energy (%VE)), with intermediate values for energy loss due to leakage. The total energy loss for the trileaflet design was significantly lower compared to the bileaflet design. In general, these patterns were observed for all COs.

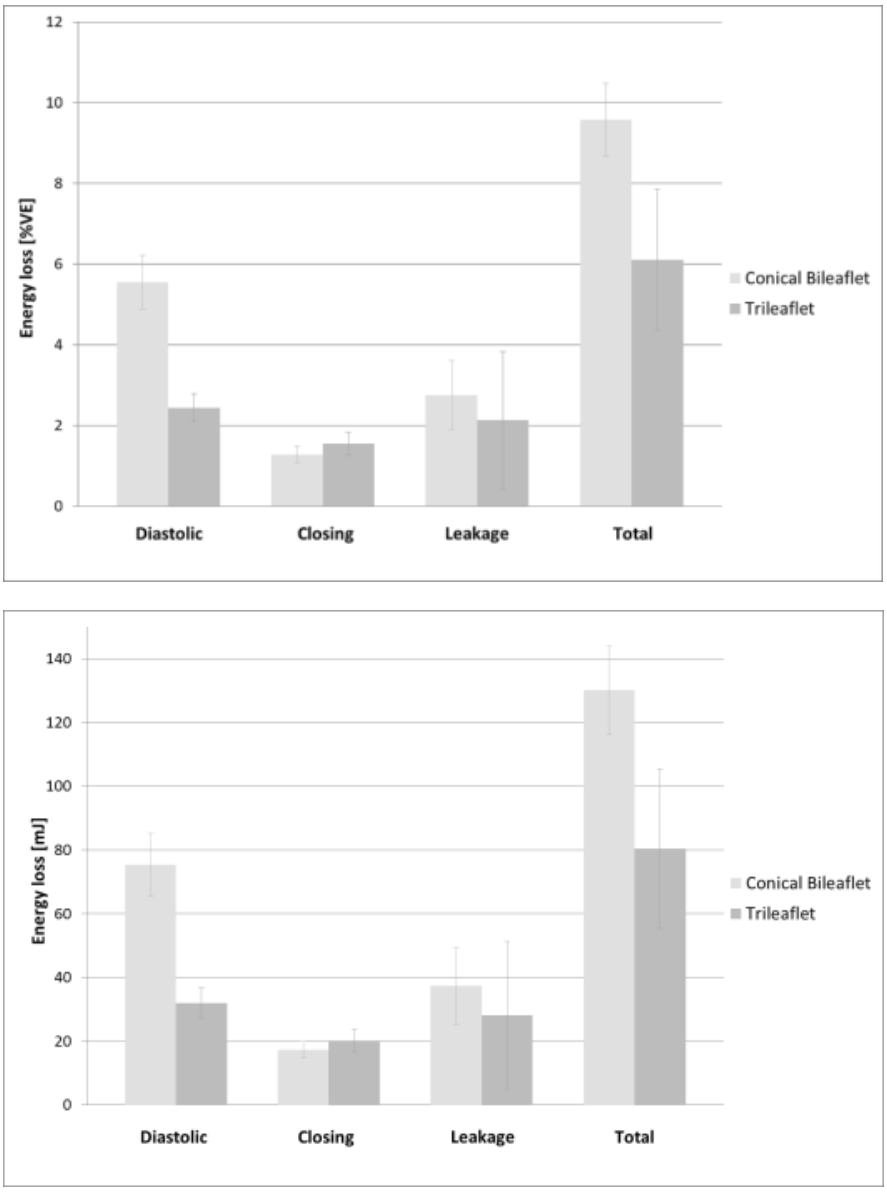

Figure 5.25: (bottom) energy losses in millijoules for two surgical mitral valve designs for a cardiac output of 5 lpm, average of 3 prototypes each **(top)** energy losses as a percentage of ventricular energy for two surgical mitral valve designs for a cardiac output of 5 lpm, average of three prototypes each.

The diastolic energy losses increased with CO ranging between 1 and 196 mJ (i.e. 0.1 and 9.1 %VE) (Figure 5.26).

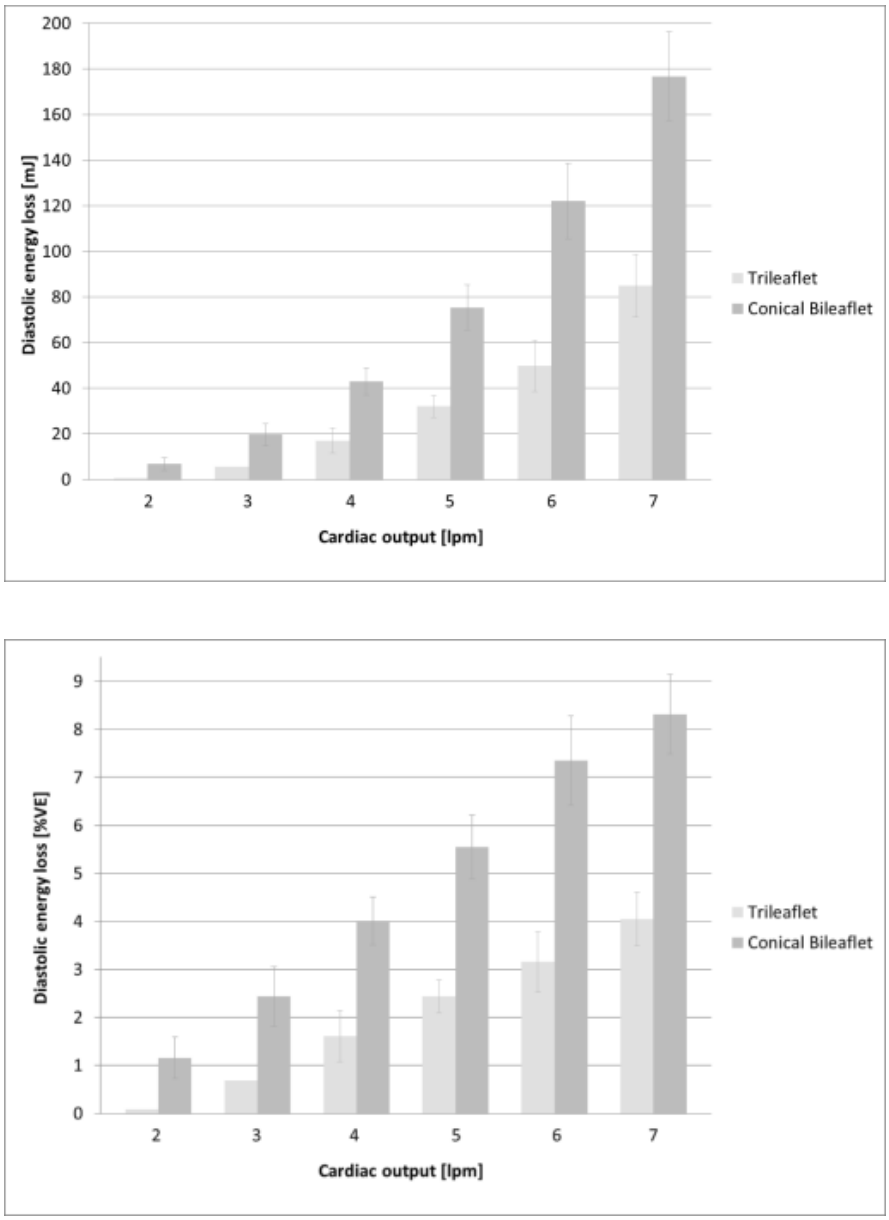

Figure 5.26: diastolic energy losses for two surgical mitral valve designs at six different cardiac outputs, average of three prototypes each. Omitted error bars for trileaflet results at 2 and 3 lpm discussed in section 5.5.5 **(top)** in millijoules **(bottom)** as a percentage of ventricular energy.

The closing energy losses were approximately constant for all COs with average values of 18 mJ, 2 %VE (Figure 5.27).

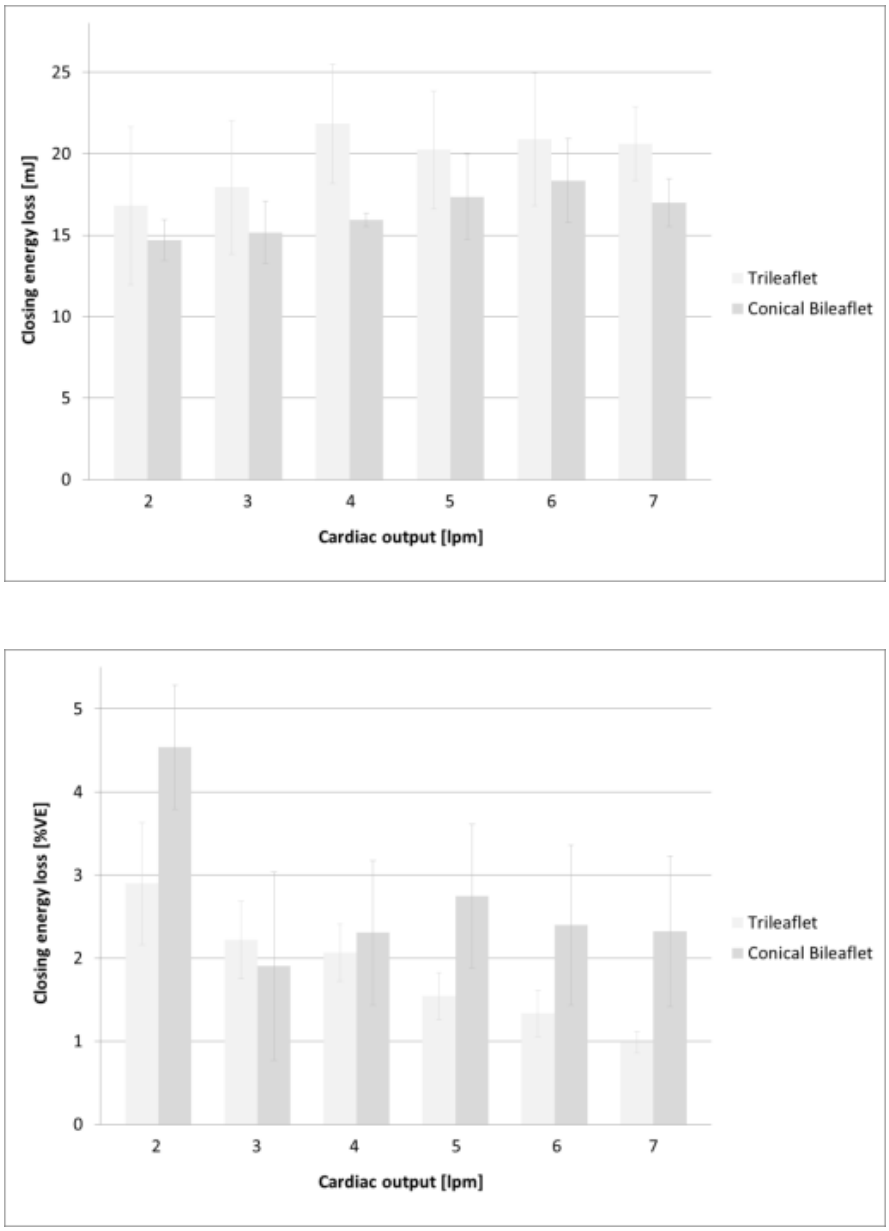

Figure 5.27: Closing energy losses for two surgical mitral valve designs at six different cardiac outputs, average of three prototypes each **(top)** in millijoules **(bottom)** as a percentage of ventricular energy.

The leakage energy losses increased as CO increased from 3 to 7 lpm ranging between 0.3 and 79 mJ i.e. 0.04 and 4 %VE (Figure 5.28), with losses at 2 lpm between those at 4 and 5 lpm. In general the total energy loss increased with CO ranging between approximately 11 and 265 mJ i.e. 1 and 12 %VE (Figure 5.29).

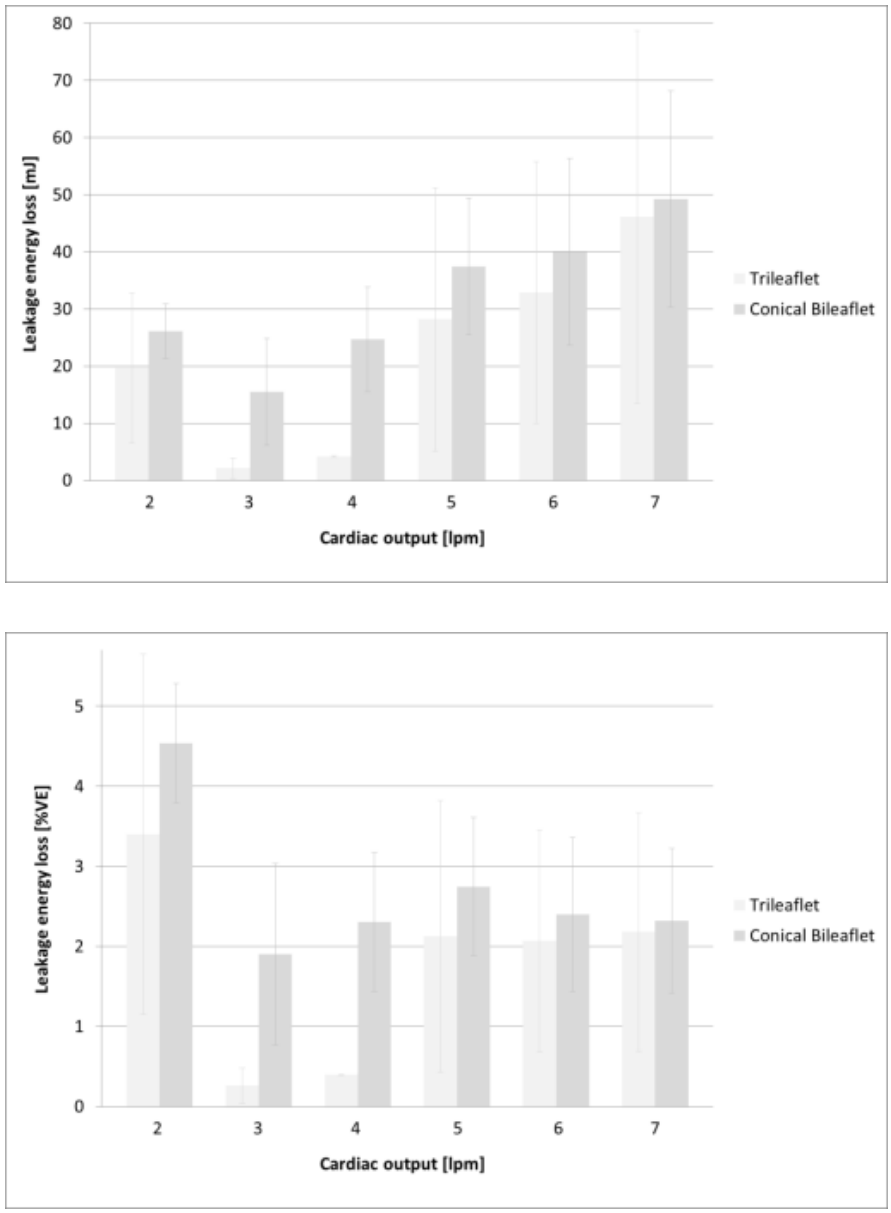

Figure 5.28: Leakage energy losses for two surgical mitral valve designs at six different cardiac outputs, average of three prototypes each **(top)** in millijoules **(bottom)** as a percentage of ventricular energy.

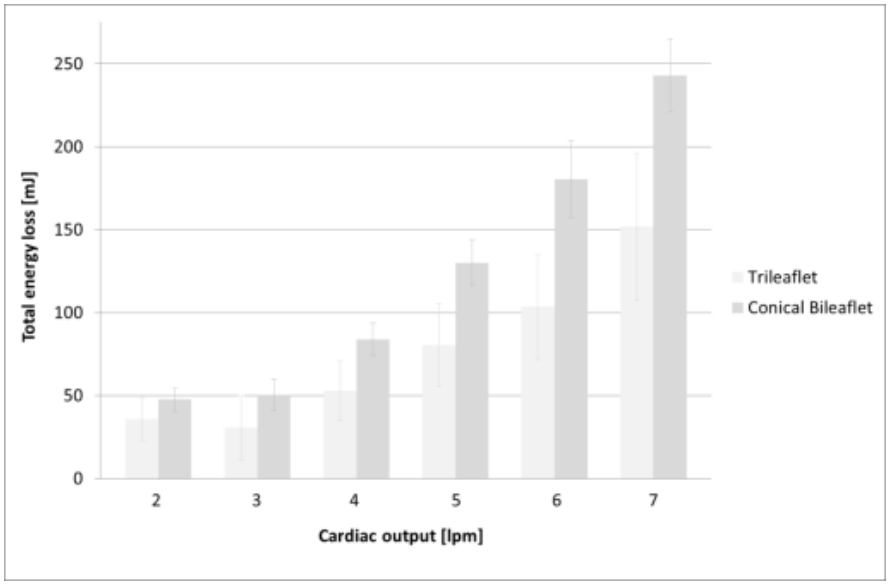

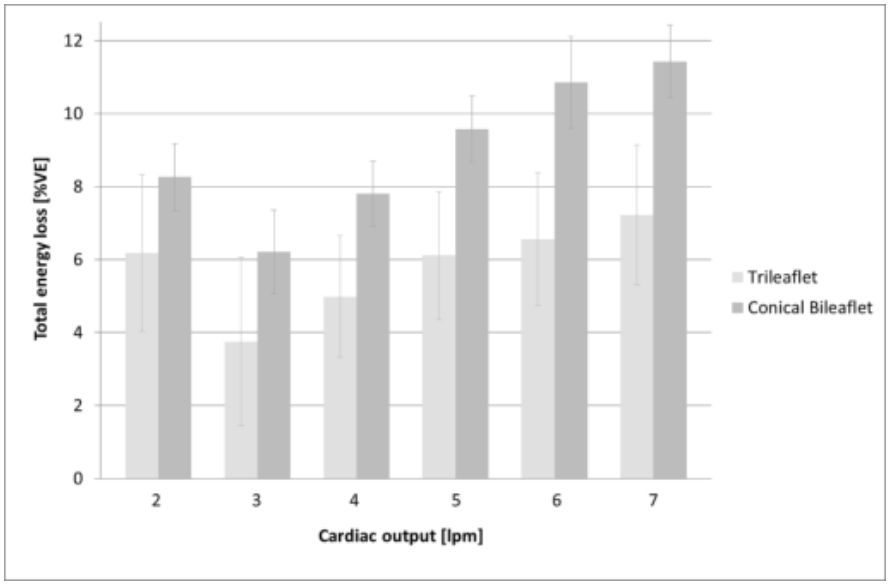

Figure 5.29: Total energy losses for two surgical mitral valve designs at six different cardiac outputs, average of three prototypes each **(top)** in millijoules **(bottom)** as a percentage of ventricular energy.

5.5.4.2.4 Regurgitant fraction

The regurgitant fractions decreased with CO ranging between 2.9 and 17.2% and were not significantly different for the two designs (Figure 5.30).

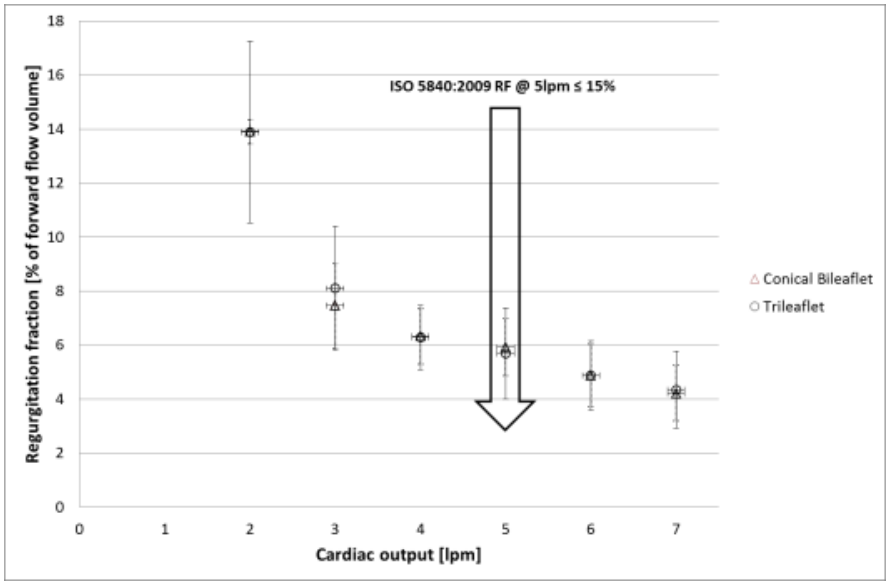

Figure 5.30: Regurgitation fraction for two surgical mitral valve designs for a cardiac output of 5 lpm, average of three prototypes each.

5.5.4.3 Flow visualisation

The streakline (Figure 5.31, frame 1) for the trileaflet SMV jet at the beginning of diastole was narrow, short and straight. As the streakline became longer and wider it drifted towards the free wall and once it came in contact with the ventricle apex a vortex formed directing flow towards the aortic valve. Later lack of circulation of dye can be observed at the base of ventricle near the free wall.

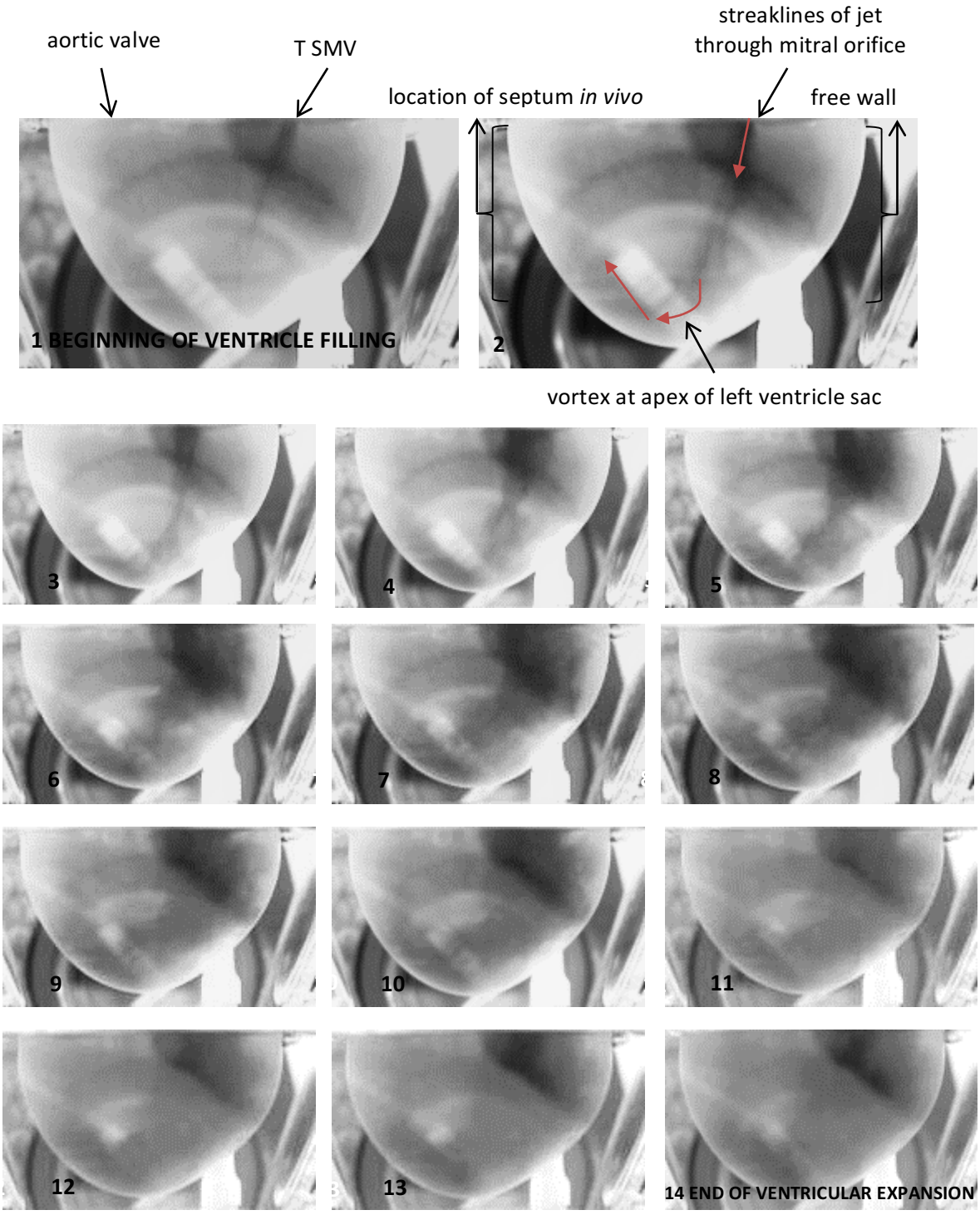

Figure 5.31: Dye injection flow visualisation of the trileaflet (T) surgical mitral valve (SMV) prototype 2 at 4 lpm, time between frames is 10 ms, taken using a TSI high speed camera, which produces black and white images.

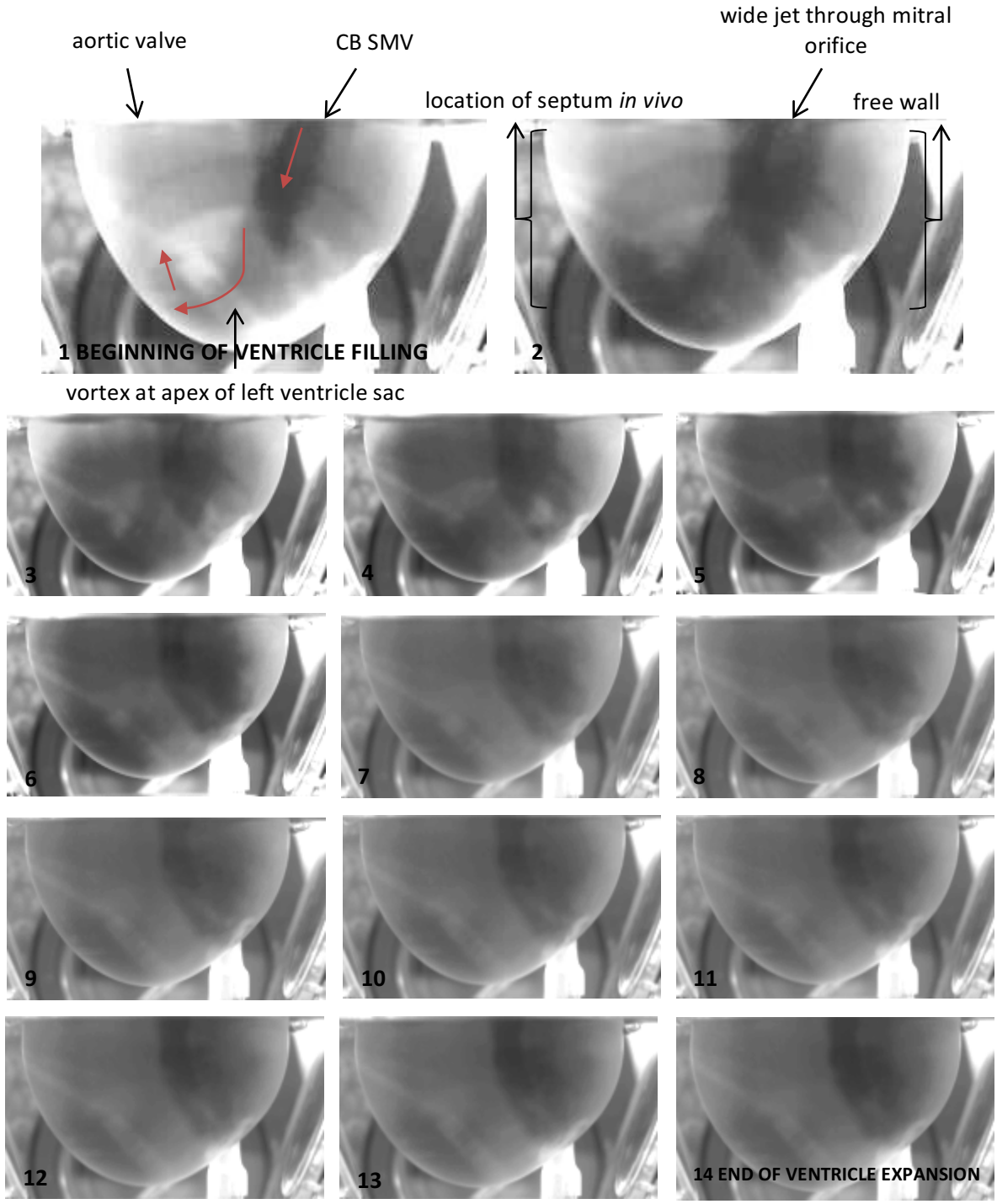

Figure 5.32: Dye injection flow visualisation of the conical bileaflet (CB) surgical mitral valve (SMV) prototype 2 at 4 lpm, time between frames is 10 ms, taken using a TSI high speed camera, which produces black and white images.

The streakline (Figure 5.32, frame 1) for the conical bileaflet SMV jet at the beginning of diastole was wide, long and divergent, immediately coming into contact with the ventricle apex and generating a vortex directing the flow towards the aortic valve. After which, the ventricle fluid was circulated to such an extent that no more streaklines could be observed.

5.5.5 Discussion

This section provides a discussion of the experimental results for the surgical prototypes including their functional performance and associated flow visualisation. The reasons for translating a bileaflet design to the transcatheter device are then discussed.

5.5.5.1 Functional performance

The trileaflet and bileaflet valves were the same size i.e. had the same external perimeter, and so had the same minimum performance requirements of an effective orifice area (EOA) ≥ 1.4-1.6 cm^2 and a regurgitant fraction (RF) ≤ 15-20%. These were exceeded by the trileaflet valve with values of 2.5 cm^2 and 5.7%, which performed better than the conical bileaflet valve which also exceeded the minimum requirements with values of 1.8 cm^2 and 5.9%. In words, the bileaflet design successfully matched the systolic performance of a commercially available valve, although performed less well during diastole. However, as discussed previously, the heart is resilient to reduction in mitral valve orifice area (Figure 1.12) and therefore the relatively lower EOA of the bileaflet design is not cause for rejecting it.

The RF was lower at higher cardiac outputs (COs), most likely due to higher systolic transmitral pressure difference coapting the leaflets more tightly. Despite this total energy loss (TEL) increased with CO, most likely because of losses due to viscosity[31]; turbulence[32] and flow separation[33] all increase as CO increases (Akins et al 2008), indicating TEL is less affected by regurgitation compared to other sources of loss. Although the two designs had similar RFs the origin of reverse flow differed, mostly due to closing and leakage for trileaflet and bileaflet valves respectively (for all COs).

[31] Viscous energy losses are directly proportional to the flow rate, vessel length and fluid viscosity (Akins et al 2008).
[32] Energy loss due to turbulence is proportional to the square of the flow rate (Akins et al 2008).
[33] Energy loss due to flow separation is proportional to the square of the flow rate (Akins et al 2008).

The trileaflet valve presented a significantly advantageously smaller resistance to forward flow for COs of 3, 6 and 7 lpm, i.e. had a smaller mean diastolic transmitral pressure difference, although did not perform significantly different to the bileaflet valve for COs of 2, 4 and 5 lpm.

The smaller closing volume associated with the conical bileaflet valves, compared to the trileaflet valves, supports previous studies which state that flow patterns associated with a bileaflet valve will result in efficient closure (Peskin et al 1981, Bellhouse 1980, Lee et al 1979, Reul et al 1979, Laniado et al 1976, Tsakiris et al 1976).

The bileaflet valves caused greater energy losses compared to the trileaflet design, mostly due to higher diastolic losses, as well as higher leakage losses. Although the bileaflet design had favourably smaller closing energy losses in millijoules (also reflected as smaller closing volume), when considered as a percentage of ventricular energy (%VE) it was in fact larger compared to the trileaflet valves.

The exemplar data (Figure 5.18) shows an instance where the bileaflet valve had a marginally lower VE compared to the trileaflet valve. However, due to variation between cardiac cycles of individual prototypes and even greater variation between prototypes, overall there was no significant difference between designs as it increased with CO. The isovolumic contraction and relaxation that occur in a healthy heart with competent valves clearly does not occur for the prosthetic devices i.e. lines from F4 to F1 and F2 to F3 are not vertical (Figure 5.18). This was caused by leakage though both the mitral prototypes as well as the mechanical aortic valve.

5.5.5.1.1 Comparison with in vivo data

The EOA, RF, transmitral pressure difference and energy loss are commonly understood and used in clinical practice as well as in laboratory studies. Despite *in vitro* assessments being relevant only in terms of comparative performance for two or more devices tested in any particular pulse duplicator set-up (Simenauer et al 1987), the trileaflet valve, a 27 mm diameter replica of the Pericarbon MORE Mitral, had a similar pressure gradient and EOA to those observed *in vivo* for an actual 29 mm bioprosthesis (based on postoperative data from 21 patients in stable conditions, Table 5.4, Caimmi et al 1998). However, this comparison is limited due to the inevitably different pulsatile flow conditions, most notably

the EOA for the larger device *in vivo* is smaller than that for the smaller device *in vitro*, which is likely to be due to the higher pressure gradients *in vivo* and/or could also be due to a lower CO. Also, most notably there is a difference in fluid viscosity; blood being approximately four times more viscous than water.

Table 5.4: Comparison between in vitro data for a 27 mm replica Pericarbon MORE Mitral (PMM) i.e. the trileaflet valve and in vivo data for an actual 29 mm PMM.

Variable	*In vivo* echo-color doppler study (Caimmi et al 1998)	*In vitro* pulse duplicator study at 5 lpm
Size (mm)	29	27
Peak gradient (mmHg)	10.2 ± 1.0	8.2 ± 1.7
Mean gradient (mmHg)	3.4 ± 0.2	2.1 ± 0.2
Effective orifice area (cm^2)	2.1 ± 0.2	2.5 ±0.1

5.5.5.1.2 Comparison with in vitro data

In absence of a reference valve for the bileaflet valve a comparison is made here with the only other known reported data for a bileaflet mitral valve, the 'bubble valve' (BV, Walker et al 1983, section 2.1.3, Table 5.5, the EOA was not reported). The BV had lower energy losses, most likely due to the conicity of the bileaflet design, although the latter had favourably smaller regurgitant volume thereby demonstrating that it achieved its main design aim. However this comparison is limited because, as previously stated, data for valves tested in different pulse duplicator set-ups are not strictly comparable (Simenauer et al 1987) and, furthermore, the only pulsatile flow condition stated by Walker et al 1983 was heart rate.

Table 5.5: The functional performance of the bileaflet design compared to the 'bubble valve' in terms of regurgitant volume, diastolic and total energy losses.

Variable	'Bubble valve' (Walker et al 1983)		Bileaflet valve at a cardiac output of 5 lpm
Size (nominal diameter) (mm)	29		27
Heart rate (bpm)	60	80	70
Regurgitant volume (ml)	6±1	7±1	4±1
Diastolic energy loss (% of ventricular energy)	1.5±1		5.5±0.7
Total energy loss (% of ventricular energy)	6.5±0.8	7±1	9.6±0.9

5.5.5.2 Flow visualisation

Both valves were associated with formation of vortices when their mitral jets made contact with the ventricle apex, directing flow towards the aortic valve, although the timings of their generation and dissipation varied and their direction prior to aortic valve opening was not determinable. For the trileaflet design, stagnation of flow was observable near the ventricle free wall (Figure 5.31, please refer to the electronic version for clearer images), which is undesirable because blood stasis was associated with platelet activation and thrombus formation (Lowe 2003). However, the Pericarbon MORE Mitral has been used successfully for the past 16 years with no significant haemolytic consequences. Further investigation (section 8.4) may therefore indicate relatively low residence times.

5.5.5.3 Translation to a transcatheter device

The bileaflet design successfully fulfilled its targeted optimal systolic performance i.e. minimal regurgitation, demonstrated by having near equivalent RF to the trileaflet valve (a replica of a commercially available device). Also, its two instead of three stent posts may make it preferable for specific patients whom are declined circular replacements due to their specific anatomical requirements (Walker et al 1983, Figure 1.2). Although the bileaflet design was surpassed by the trileaflet design in its EOA, it was still used for the leaflets of the transcatheter prototype for several reasons.

Translation of a bileaflet design to the transcatheter device is supported by previous evidence which demonstrates that a bileaflet design is preferable to the more common trileaflet solutions due to its ability to have proper leaflet coaptation for a wider range of anatomical configurations (Burriesci and Zervides et al 2010) and it has also been inferred that it will generate more physiological left ventricle haemodynamics (Carmody et al 2006, Burriesci et al 2003, Peskin et al 1981, Bellhouse 1980, Lee et al 1979, Reul et al 1979, Laniado et al 1976, Tsakiris et al 1976), unsurprising considering native mitral valves also have two leaflets. Therefore the proposed TMV is expected to exceed the performance of other devices in development because it has two rather than three leaflets.

A D-shaped device would present less restriction of the LVOT compared to a circular device (Figure 5.33), and although a D-shaped device would have a smaller geometric orifice area compared to circular device with the same perimeter, it would in fact use the space available more efficiently.

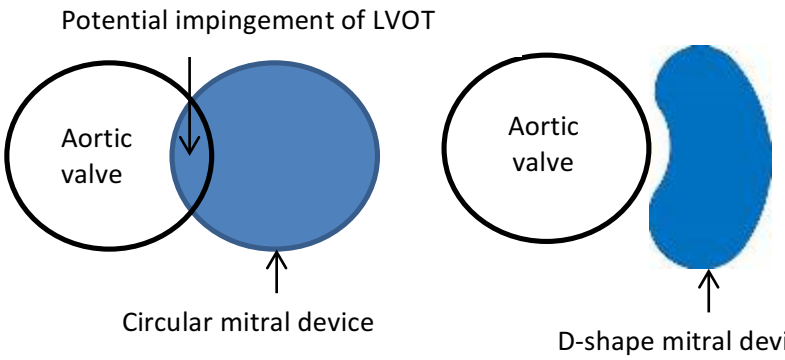

Figure 5.33: Advantage of D-shaped mitral valve replacements compared to circular **(left)** potential impingement of left ventricular outflow tract by circular device **(right)** efficient use of space by a D-shaped device.

Developers of other TMV designs most likely choose trileaflet circular configurations because they are relatively easier to design for minimal crimped profiles, which are necessary for delivery through narrow vascular passages. Three leafleted, circular devices also tend to have repeatable uniform deployment.

5.5.6 Conclusions

5.5.6.1 Nature-inspired design

The functional assessment of the bileaflet surgical mitral valves (SMVs), supports previous work (Burriesci G et al 1999), showing a stented bileaflet bioprosthetic mitral prosthesis is feasible. In fact, the bileaflet SMVs also have an original combination of geometric features which mimic native valve morphology and thereby advance the study of nature-inspired mitral valve designs (section 2.1). Due to them exceeding minimum performance requirements (ISO 5840:2009) they have potential for technology transfer and therefore may initiate a new generation of surgical replacements designed specifically for the mitral position. Thus, the D-shaped bileaflet SMV, which requires minimal distortion to the D-shaped native mitral annulus compared to a circular device, potentially presents a paradigm shift from prioritising commercial profit over preservation of healthy natural physiological flow.

5.5.6.2 Bileaflet vs. trileaflet valves

For the first time functional performance of two and three leafleted bioprosthetic mitral valves were compared *in vitro*, opposed to *in silico* (Kheradvar et al 2012), thereby

advancing the study of bileaflet mitral valves. The *in vitro* data obtained cannot be compared precisely with *in vitro* data from another pulse duplicator, nor with *in vivo* data, although, in a broad sense, test parameters reported for similar devices *in vivo* and *in vitro* support the data obtained for the trileaflet and bileaflet valves respectively.

The proposed bileaflet valve was expected to exceed the trileaflet valve performance and, therefore, demonstrate its superiority compared to a commercially available circular alternative (Figure 1.10 and Figure 1.11). Although this was not shown to be the case it still exceeded minimum performance requirements (ISO 5840:2009). However, these findings relate only to their functional performance and therefore do not necessarily conflict with previous research which shows that two leaflets, rather than three, will generate more physiological left ventricle haemodynamics (Carmody et al 2006, Burriesci et al 2003). Furthermore, a two stent post design may be preferable due to relatively minimal disturbance to surrounding anatomy, most notably to the native mitral valve sub valvular apparatus, and associated mechanics, which crucially connect the native mitral valve to the left ventricle (Figure 1.1Figure 1.7Figure 1.8) and would theoretically lead to more physiological flow patterns (Figure 1.4Figure 1.9) and, therefore, less likely to cause blood damage. Furthermore, a D-shaped design is less likely to impede the aortic annulus (Figure 5.33).

In summary although the hypothesis (section 5.5.1) was not shown to be true for the surgical mitral valves made; overall the trileaflet valve had optimal functional performance, although the bileaflet valve was not worse for all of the bulk haemodynamic parameters measured. Furthermore, there are other expected advantages of a bileaflet, opposed to trileaflet, design in terms of more physiological left ventricle flow patterns, minimal interaction with myocardial morphology and dynamics and reduced risk of haemolysis and therefore a surgical bileaflet mitral valve device may still be preferable.

5.5.6.3 Solution to transcatheter reference valve predicament

Together, the two SMVs present an original and in fact first approach to providing a reference valve for a TMV (section 2.3.4). The trileaflet valve was indirectly the reference valve, i.e. it had to be compared to a surgical version of the UCL TMV to mitigate disparities in transvalvular regurgitation. The results demonstrated the bileaflet design strategy was successful in achieving optimal systolic performance, although consequently had poorer

diastolic performance, which is also likely if compared to circular TMVs in development (section 2.2).

In summary, the SMVs assessed present a design method for a bileaflet valve in line with international standards, and compare its functional performance to a commercially available and potentially relevant alternative prosthesis. The SMVs designed highlighted the difference in requirements of surgical and transcatheter devices, namely that a conical bileaflet design is best suited to a transcatheter device rather than a surgical device, and provided sufficient comparison with a relevant reference valve which confirmed the suitability of the UCL TMV leaflets.

5.5.6.4 Limitations

5.5.6.4.1 Left atrium

The effect of larger closing volumes, and therefore also energy losses (mJ), on the function of the left atrium (LA) in the trileaflet valve are unknown because the current rigid atrium prevents study of the extent to which smaller closing volumes in the bileaflet valve (section 5.5.1) are advantageous. More specifically, if the LA were capable of contraction, then its pressure-volume diagram would enable a more complete energy assessment of the devices, previously shown to be relevant by MacIsaac et al (1992) and Teien et al (1997). The former studied impact of mitral regurgitation on energy transfer from the left ventricle to LA and the latter showed energy associated with the LA to be at least as important as regurgitant volume in determining ventricular work required. Therefore, ideally atrial contraction would be included, which in fact is still emitted in even most recent pulsatile flow system designs (Leopaldi et al 2015).

5.5.6.4.2 Flow visualisation

Flow visualisation using the current pulse duplicator ventricle sac will not replicate *in vivo* flow patterns, most notably due to there being no sub-valvular components (Figure 1.2). Despite this it is still a valid tool for comparing devices, and as previously discussed can replicate pressures and flows observed *in vivo* (Table 5.4). Also as mentioned at the outset, dye injection is limited to providing a qualitative indication of flow patterns, a quantitative alternative is discussed in the following section.

5.6 Summary

This chapter described the equipment used and made to assess the prototypes, which included the design and manufacture of surgical mitral valves, designed to provide a relevant reference valve for the UCL TMV. Furthermore, it described the experimental conditions used to simulate the left side of a normal healthy adult heart and the parameters measured to assess prosthetic heart valve's performance, namely effective orifice area and regurgitation fraction. The minimum performance requirements are also expounded as well as the limitations of these methods.

The following chapter, chapter 6, will outline the main aim of the UCL TMVs, that is, to assess its potential as a treatment option for high-risk patients with severe mitral regurgitation. The design of the prototypes and their functional assessment are then described and the results presented and discussed.

Chapter 6 Transcatheter mitral valves 1st generation

This section describes the aim for the UCL TMV prototypes and the materials and methods used to make three prototypes. The aim of the functional assessment is clarified, details for which are in 0. The experimental results are presented, followed by a discussion and summary.

6.1 Aim

The aim of prototyping the UCL TMV (Figure 3.1) was to assess its potential as a treatment option for high-risk patients with severe mitral regurgitation, who are refused surgical interventions because they are too weak to undergo such an invasive procedure.

6.2 Design

This section describes advances made to the initial concept for the UCL TMV, previously described (section 1.4.4).

6.2.1 Leaflets

The pericardial leaflets were designed for optimal systolic performance, with acceptable levels of stress and maximal coaptation area (Chapter 4).

6.2.2 Wireframe

The wireframe was subsequently designed to fit the leaflets and was optimised (Bozkurt et al 2016) to provide adequate matching to the mitral valve anatomy, while minimising the stresses during loading in the delivery system (Figure 6.1).

The UCL TMV frames were thermo-mechanically formed (Lithotech Group Inc.) from a single 0.58 mm nitinol wire (Fort Wayne Metals). This manufacturing method is advantageous compared to laser-cutting them from metal tubes because laser cut tubes have heat affected zones susceptible to micro-cracking, which expose intrinsic draw lines resulting from the manufacturing process, serving as initiation sites for crack propagation. The wireframe was then collated in five locations using crimping sleeves to prevent rotation (Figure 6.1). Four sections of wire are held together with the annular medial sleeve, where

the wire begins and ends and just two sections of wire are contained within the other four sleeves.

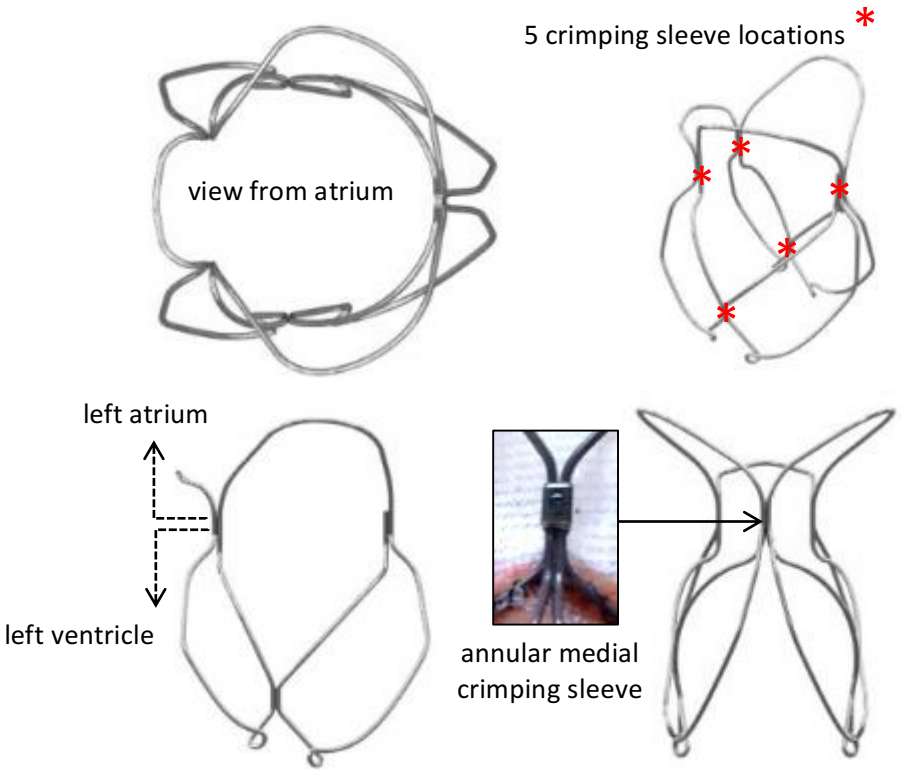

Figure 6.1: Optimised nitinol wireframe for the UCL transcatheter mitral valve, **(top left)** view from atrium, **(bottom left)** side view, **(bottom right)** made from a single wire starting and finishing at the annular medial crimping sleeve, and **(top right)** collated at four other points.

At present A_f is 4.8 ^{o}C, i.e. the transition temperature to which martensitic nitinol must be heated to completely transform it into its austenitic structure (section 3.3). This means when the frames are cooled below this transformation temperature its structure changes, enabling it to deform easily to fit inside the catheter, and then when later re-expanded *in vivo* at 37 ^{o}C it will return to the original shape. However, A_f is dependent on manufacturing processes and therefore will be subject to change as they are optimised.

6.2.3 Auxiliary parts

A pericardial sealing cuff (Figure 3.1) was designed to reduce paravalvular leakage and an appropriate polymeric mesh was sourced and selected for the skirt (section 3.2), which gently distributes an anchoring force over the annulus. Finally, as previously discussed (section 5.5.2), nylon was selected as the most appropriate thread for assembly.

6.3 Prototype

The cutting patterns for the leaflets (Figure 6.2), sealing cuff and skirt (Figure 6.3) were drawn using computer-aided design (CAD) 3-D modelling software Rhinoceros 4.0 (Robert McNeel & Associates) and printed onto the sticky side of overhead projector (OHP) acetate, except for the skirt pattern which was printed onto ordinary acetate. The patterns were then transferred onto their respective materials, cut out and assembled as follows.

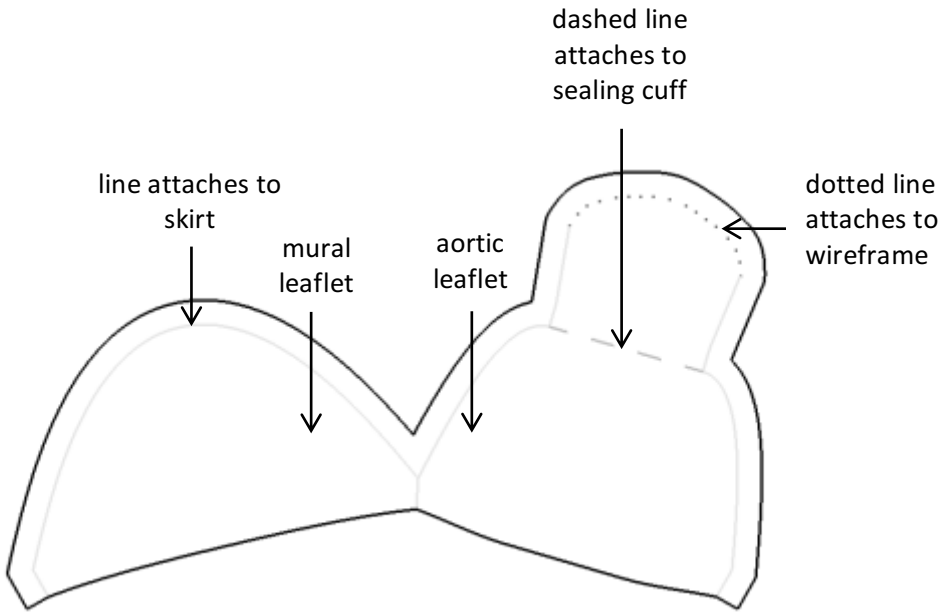

Figure 6.2: UCL transcatheter mitral valve leaflet cutting pattern indicating attachment sites to other parts.

The 0.4 mm thick BP leaflets (section 3.1.3) were double stitched to the skirt using nylon thread and the sides joined together, prior to inserting it inside the wireframe. The leaflet profile and skirt were then attached to the wireframe using nylon thread followed by the sealing cuff.

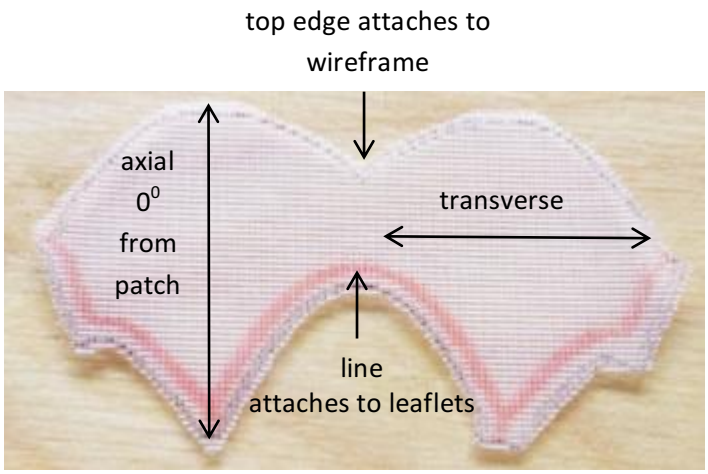

Figure 6.3: Skirt cutting pattern for PETKM2004, axial direction aligned with the 0o orientation of the patch sample (section 3.2.2).

6.4 Functional Assessment

6.4.1 Aims

The aim of the functional assessment of the UCL TMV was to determine firstly whether it met the international standard requirements and secondly to determine the effect of annulus size on its performance.

6.5 Results

This section presents the functional performance and regurgitant test results for the UCL TMV.

6.5.1 Functional performance

The mock native mitral valves (section 5.1.5) designed for assessing the TMVs successfully created a seal between the pulse duplicator's atrium and ventricle chambers and prevented migration of the prototypes (Figure 6.4, please see electronic version for a clearer image). The characteristic pressures and flows observed for a single cardiac cycle were previously shown in Figure 5.13 and the resulting test parameters for all tests are described below.

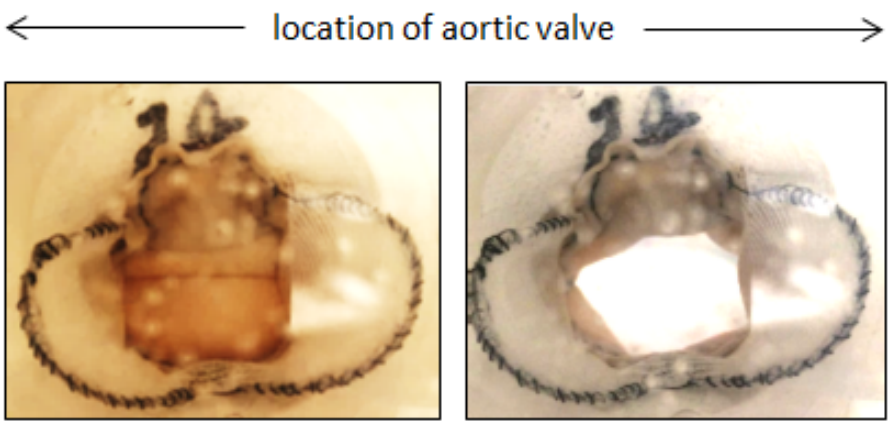

Figure 6.4: The UCL transcatheter mitral valve in the pulse duplicator functioning at a cardiac output of 5 lpm in a 24 mm holder **(left)** closed (systolic) and **(right)** open (diastolic).

6.5.1.1 Regurgitation fraction

The TMVs exceeded ISO 5840-3:2013 requirements at 5 lpm and, in general, the regurgitant fraction (RF) decreased as the CO increased (Figure 6.5). There was no significant difference between holder sizes although, on average, the RF was higher in a 25 mm annulus.

6.5.1.2 Effective orifice area

The TMVs exceeded the ISO 5840-3:2013 requirements and in general the effective orifice area (EOA) increased with CO and was larger in larger holders, although these variations were not significant due to the large variation in performance between the three prototypes made (Figure 6.5).

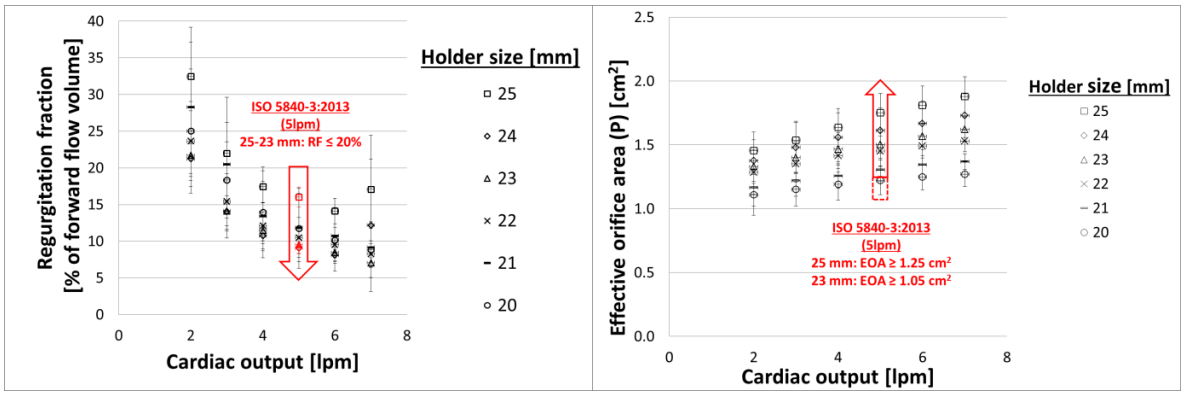

Figure 6.5: (left) regurgitation fraction **(right)** effective orifice area; average of 3 UCL transcatheter mitral valve prototypes in holder sizes 20-25 mm at cardiac outputs 2-7 lpm, arrow indicates that holder sizes 25 and 23 exceed ISO 5840-3:2013 requirements.

6.5.1.3 Mean diastolic transmitral pressure difference

In general the mean diastolic transmitral pressure difference (MDPD) increased with CO, although there was no statistically significant difference between holder sizes (Figure 6.6).

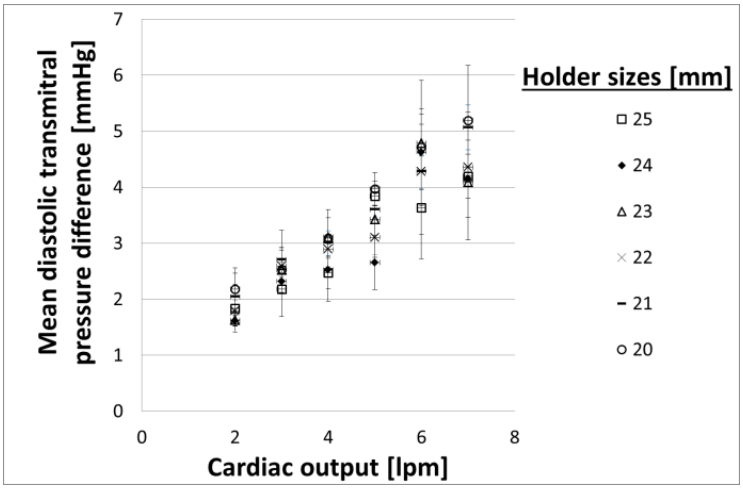

Figure 6.6: Mean diastolic transmitral pressure difference; average of 3 UCL transcatheter mitral valves in holder sizes 20-25 mm at cardiac outputs 2-7 lpm.

6.5.1.4 Reverse flow volumes

Most of the reverse flow volume (RFV) was due to leakage with more variable and in general higher RFVs in smaller holders (Appendix E, Figure E.1). For a CO of 5 lpm the minimum total RFV (5.7 ± 0.6 ml) occurred in transcatheter mitral valve two in a 21 mm holder and the maximum (12.2 ± 0.8 ml) was in transcatheter mitral valve three in a 25 mm holder.

There was no significant difference in the closing, leakage or total regurgitant volumes for COs between 2 and 7 lpm, with average values of 1.7 ± 0.4 ml, 8.1 ± 2.7 ml and 9.8 ± 2.9 ml respectively (Appendix E, Figures E.2-E.4). Although, based on average values, the leakage and total regurgitant volumes followed the same pattern, with maximum values in 25 mm holders with a peak value at 7 lpm and minimum values in 24 mm holders with higher and more variable performance in smaller holders.

6.5.1.5 Energy losses

Most of the energy loss (EL) occurs during diastole with minimal contribution from the closing phase (Appendix E, Figures E.5 and E.6). For a CO of 5 lpm the maximum total EL

(456 ± 10 mJ, 27 ± 1 %VE) occurred in TMV1 in a 20 mm holder and minimal losses (193 ± 9 mJ, 14 ± 1 %VE) occurred in TMV3 in a 24 mm holder, and decreased as holder size increased although losses in a 25 mm were similar to a 21 mm with more variable performance in a 20 mm. Similar patterns were observed for ELs across all COs, as well as for the diastolic and leakage ELs.

The diastolic EL increased with CO (Appendix E, Figures E.7 and E.8).

The closing EL in millijoules did not vary significantly with CO, with an average value of 15 ± 4 mJ, although as a %VE it tended to decrease as CO increased (Appendix E, Figures E.9 and E.10).

In general the leakage EL was not affected by CO, with an average value of 123 ± 47 mJ, however as a %VE it tended to decrease with CO (Appendix E, Figures E.11 and E.12).

The total EL in millijoules tended to increase with CO however as a %VE it tended to remained approximately constant (19 ± 3 %VE) (Appendix E, Figures E.13 and E.14).

6.5.2 Regurgitation tests

6.5.2.1 Reverse flows

The closing volume was not significantly affected by heart rate (HR) or mean back pressure (MBP), with an average value of 1.9 ± 0.3 ml (Appendix E, Figure E.15).

The leakage and total regurgitant volumes tended to decrease as heart rate increased and was higher for higher MBPs, with total minimum value for TMV2 at a HR of 120 bpm and MBP 80 mmHg (4.1 ± 0.6 ml) and a maximum value for TMV3 at a HR of 45 bpm and a MBP of 160 mmHg (57.8 ± 1.0 ml) (Appendix E, Figures E.16 and E.17).

In general the RF was not affected by HR and tended to increase with MBP, with a maximum value for TMV3 at a HR of 120 bpm and MBP of 160 mmHg (39 ± 1%) and a minimum value for TMV2 at a HR of 120 bpm and MBP of 80 mmHg (9 ± 1%) (Appendix E, Figure E.18).

6.5.2.2 Effective orifice area

The EOA tended to decrease as HR increased and was not significantly affected by MBP, with a maximum value for TMV3 at a HR of 45 bpm and MBP of 120 mmHg (1.73 ± 0.01 cm^2) and a minimum value for TMV2 at a HR of 120 bpm and MBP of 160 mmHg (1.30 ± 0.03 cm^2) (Appendix E, Figure E.19).

6.5.2.3 Diastolic energy losses

In general diastolic EL in millijoules decreased as HR increased and tended to be higher for higher MBPs, with a maximum value for TMV3 at a HR of 45 bpm and MBP of 160 mmHg (399 ± 4 mJ) and a minimum value for TMV1 at a HR of 120 bpm and MBP of 160 mmHg (70 ± 6 mJ) (Appendix E, Figure E.20).

However, as a %VE, the diastolic EL decreased as MBP increased with a maximum value for TMV3 at a HR of 45 bpm and MBP of 80 mmHg (13.8 ± 0.1 %VE) and a minimum value for TMV1 at a HR of 120 bpm and MBP of 160 mmHg (5.4 ± 0.2 %VE) (Appendix E, Figure E.21).

6.5.2.4 Closing energy losses

In general closing EL increased with HR and for HRs of 70 and 120 bpm also increased with MBP, with a maximum value for TMV3 at a HR of 120 bpm and MBP of 160 mmHg (67 ± 3 mJ) and a minimum value for TMV3 at a HR of 45 bpm and a MBP of 80 mmHg (6.5 ± 0.5 mJ) (Appendix E, Figure E.22).

The closing EL as a %VE also increased with HR, but there was no significant relationship with MBP, with a maximum value for TMV1 at a HR of 120 bpm and MBP 120 mmHg (3.2 ± 0.3 %VE) and a minimum for TMV3 at a HR 45 bpm and MBP 160 mmHg (0.2 ± 0.1 %VE) (Appendix E, Figure E.23).

6.5.2.5 Leakage energy losses

In general leakage energy losses decreased as HR increased and increased with MBP, with a minimum value in TMV2 at a HR of 120 bpm and a MBP 80 mmHg (33 ± 5 mJ, 4.7 ± 0.6 %VE) and a maximum for TMV3 at a HR of 45 bpm and a MBP 160 mmHg (1244 ± 19 mJ, 28.4 ± 0.5 %VE) (Appendix E, Figures E.24 and E.25).

6.5.2.6 Total energy loss

The total EL decreased as HR increased and tended to increase as MBP increased, with a minimum value for TMV1 at a HR of 120 bpm and a MBP of 80 mmHg (124 ± 23 mJ) and a maximum value for TMV3 at a HR of 45 bpm and a MBP of 160 mmHg (1657 ± 17 mJ) (Appendix E, Figure E.26).

However, in general, as a %VE total EL was not significantly affected by HR or MBP with an average value of 23 ± 1 %VE (Appendix E, Figure E.27).

6.6 Discussion

In this section the functional performance of the UCL TMV prototypes are discussed in terms of their systolic, diastolic and global performance, anomalies and comparison to another TMV in terms of transmitral pressure difference and implantation range is also discussed. After this, the failure modes and design flaws observed and their subsequent effect on test parameters are explained.

6.6.1 Functional performance

As expected, the functional performance of the UCL TMV was affected by annulus size. The TMV anchored securely in all holder sizes 20-25 mm and had optimal performance in a 24 mm holder in terms of regurgitation fraction and effective orifice area (Figure 6.5). On average the test parameters were ten times more variable between prototypes than across cardiac cycles, this is due to both the accuracy to which they were made as well as variability in placement in the annuluses, the latter being the main cause for this disparity being larger than observed in the SMVs, discussed in more detail below.

6.6.1.1 Systolic performance

The systolic performance of the UCL TMV is described by the RF, which includes reverse flow volumes in its calculation, and the leakage energy losses.

The prototypes met and exceeded the minimum performance requirements set for 25 mm and 23 mm devices[34] i.e. RFs ≤ 20%, with values of 16 ± 1.4% and 9.5 ± 1.2% respectively (no requirements are set for annulus sizes 20-22 mm). In fact, as previously mentioned,

[34] Minimum performance requirements are not set for 24 mm devices.

despite the variability of performance between individual valves being larger than between cardiac cycles, even the worst performing valves exceeded the standard; which were prototypes one and three when in holder sizes 25 and 23 mm respectively, associated with RFs of 17.5 ± 2.8% and 10.9 ± 0.5% respectively. However, the elderly patients in whom the device would initially be implanted tend to have lower resting COs of around 3 l/min (Brandfonbrener et al 1955) and so in practice the TMV will be functioning at suboptimal COs. The regurgitation tests demonstrated that the RF is relatively constant for mean back pressures (MBP) 80-160 mmHg and heart rates 45-120 bpm on average being 18 ± 2%.

The leakage energy loss as a percentage of ventricular energy follows a similar pattern to RF and therefore is arguably an equally good measure of systolic performance with values of 11.4 ± 1.1 %VE and 6.3 ± 1.1 %VE for 25 and 23 mm holders respectively.

6.6.1.2 Diastolic performance

The diastolic performance of the TMV is described by EOA, mean transmitral diastolic pressure difference (MDPD), and diastolic energy losses.

The prototypes exceeded the minimum performance requirements set for 25 and 23 mm TMVs i.e. EOAs ≥ 1.25 cm^2 and 1.05 cm^2 respectively, with values of 1.8 ± 0.2 cm^2 and 1.5 ± 0.1 cm^2 respectively (no requirements are set for annulus sizes 20-22 mm).

The diastolic performance is arguably best described by diastolic energy loss rather than MDPD because, although pressure difference during diastole quantifies resistance to forward flow, this pressure is not directly reflected in the peripheral circulatory system (unlike the ventricular pressure whilst the aortic valve is open), whereas the diastolic energy loss (mJ) is directly related to how much energy is required by the left ventricle and, therefore, is of more clinical relevance. Furthermore, the apparent advantageous increase in EOA with increased CO is misleading; the diastolic energy loss (%VE) on the other hand better represents true diastolic performance i.e. greater forward flow energy losses at higher COs.

6.6.1.3 Global performance

The global performance of the UCL TMV is described by total energy losses and was minimum for the 24 mm holder for COs between 2 and 6 lpm (Appendix E, Figures E.13 and E.14). The total energy loss was relatively constant for MBPs 80-160 mmHg and heart rates 45-120 bpm on average being 23 ± 1%VE, measured at 5 lpm which, as would be expected, is higher than the 15 ± 1%VE for normal healthy pulsatile flow conditions.

6.6.1.4 Anomalies

The majority of data plotted in section 6.5 is the average of three prototypes and their associated standard deviation. However, there were some anomalies, all relating to TMV3 in a 21 mm holder. These particular data points were identified because if included they caused the standard deviation for the three prototypes to be larger than the average value for the parameter i.e. the standard deviation statistic spanned into the negative regions of energy loss and closing volume, which are nonsensical and so were removed. The anomalies identified were as follows.

At 5 lpm TMV3 had an abnormally high closing energy loss of 73 mJ (4.6 %VE) compared to 14 and 10 mJ (0.7 and 0.9 %VE) for TMV1 and 2 respectively and therefore these were not included (Appendix E, Figures E.9 and E.10). For similar disparities between data points the closing energy losses (mJ and %VE) at 2 and 3 lpm and closing volume at 3 lpm (Appendix E, Figure E.2) and were also treated as anomalies and removed. All other data for TMV3, which also caused the three largest standard deviations between prototypes; for closing volumes in 21 mm holders at 2, 5 and 6 lpm (Appendix E, Figure E.2), were not removed because although very large, the standard deviation statistic still spanned meaningful closing volumes.

These elevated closing energy losses and closing volumes are most likely due to the native leaflets of the 21 mm holder not covering the TMV3 skirt mesh in a consistent way for all COs (Figure 6.7) and therefore, elevated paravalvular leakage occurred from the ventricle through the skirt mesh into the atrium as the leaflets closed. The greater significance of this feature in TMV3 compared to TMV2 and 1 may have been exacerbated by the slightly thinner sealing cuff and its assembly.

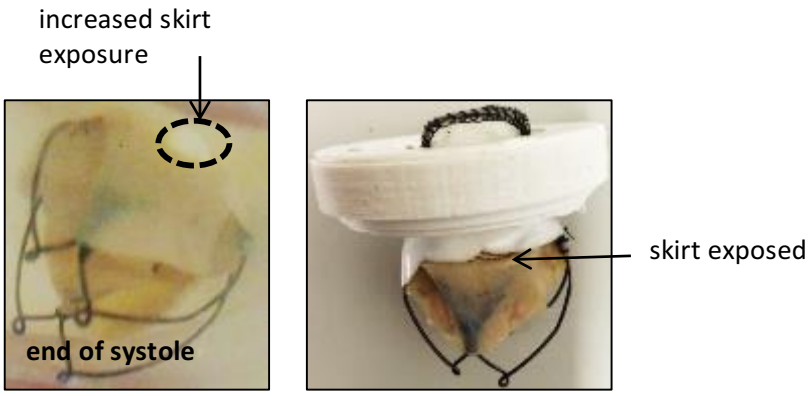

Figure 6.7: Skirt of TMV3 not covered by mock native leaflets associated with a 21 mm holder **(left)** exacerbated during systole **(right)** on bench top.

6.6.1.5 Comparisons to other transcatheter mitral valves

6.6.1.5.1 Functional performance

Pulse duplicator data for other TMVs have not been published. However, due to inevitable differences in pulse duplicators and exact testing parameters used, direct comparison would still not be appropriate (Simenauer et al 1987). The only comparative data available is for the Fortis (Edwards) TMV, which is reported to achieve a mean transmitral pressure difference (MPD) of ≤ 4 mmHg (Altisent et al 2015); however, no other pulsatile flow conditions were specified. Therefore, comparison with the MPD for the UCL TMV in a 24 mm holder at, for example, 5 lpm (6 ± 1 mmHg), is limited, although they do appear to have the same order of magnitude.

6.6.1.5.2 Implantation range

In terms of A2-P2 diameter (orthogonal to the inter-trigonal diameter, Figure 1.2), the proposed TMV is a 20 mm device suitable for annuluses between 15 and 19 mm, which is different to the 29 mm Fortis (Edwards) TMV which, due to its atrial flange, is only implanted into relatively larger native valves, between 30 and 44 mm (Bapat et al 2014) i.e. the major difference being that the UCL TMV requires an interference fit for anchorage. It is predicted that a greater interference fit between the UCL TMV and annulus will have a greater effect on the native valve/leaflets potentially leading to greater damage and increased risk of native leaflets occluding the left ventricle outflow tract (LVOT), depending on each patients' specific anatomy.

The Fortis was suitable for aortic and mural leaflet lengths < 23 mm and > 5 mm respectively. In fact, anatomical criteria for the left atrium minor and major diameters, left ventricle outflow tract width, aorta to device plane angle, left ventricular outflow tract clearance, left ventricle diameter at papillary muscle plane and left atrium height were also specified. The UCL TMV performed well for aortic, mural and commissure lengths of 17-23 mm, 9-12 mm, and 9-13 mm respectively. These lengths were associated with inter-trigonal holder sizes 20-25 mm and the 24 mm holder. The 26 mm TMV performed optimally in the 24 mm holder, which had aortic, mural and commissure lengths of 22, 11 and 12 mm respectively. The commissure length of the UCL TMV was of critical importance in reducing regurgitant flow. This was unlike the Fortis, which in fact is unsuitable for patients with predominantly commissural mitral regurgitation (Bapat et al 2014). Therefore, the commissure length should be included in the echocardiography inclusion criteria for the UCL TMV, which would be used to determine patient suitability, discussed further in the following section.

6.6.2 Design issues

6.6.2.1 Interaction between sealing cuff and mock native commissures

The main source of regurgitant flow was due to native leaflets not covering the skirt mesh (Figure 6.7), or there being a gap between them. In the first instance this was observed as elevated RF and total regurgitant volume in holder sizes 20 and 21 mm and secondly for a 25 mm holder, most notable at 7 lpm for which they were also elevated for the 24 mm holder.

Additional reverse flow occasionally occurred due to the sealing cuff being pushed towards the atrium during systole (Figure 6.8), which occurred in TMV1, with a most notably elevated RF in a 20 mm holder at 2 lpm (35 ± 1%) compared to TMV2 and 3 (22 ± 1% and 19 ± 1% respectively), for which this did not occur.

6.6.2.2 Interaction with ventricle

The TMV wireframe contacted the ventricle during systole for TMV2 and 3 for COs of 5, 6 and 7 lpm for all holder sizes as well as for TMV1 for all COs apart from 2 lpm (Figure 6.9). Considering that *in vivo* the ventricle sac would also be smaller for smaller annulus sizes this problem is likely to be more severe in smaller annuluses.

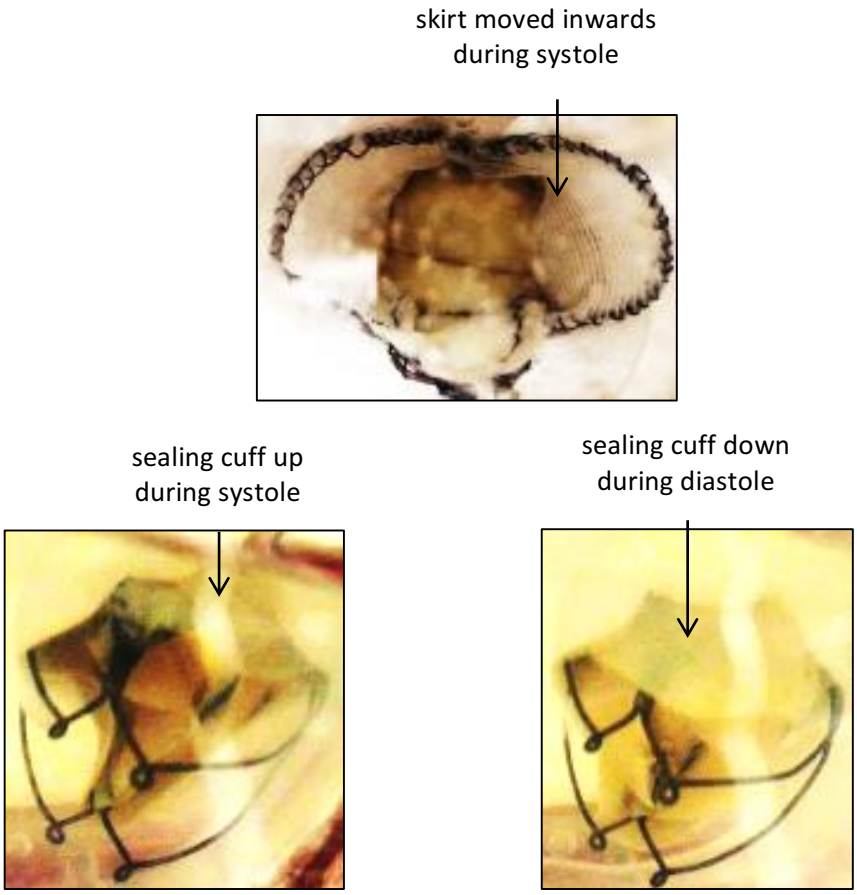

Figure 6.8: Dysfunction of sealing cuff in UCL transcatheter mitral valve one, in a 25 mm holder at 5 lpm **(top)** atrial view **(bottom):** *left;* ventricular view during systole, *right;* ventricular view during diastole.

Figure 6.9: Interaction between the frame of TMV2 in a 22 mm holder and ventricle sac at the end of systole **(left)** no contact at 2 lpm **(right)** most severe contact at 7 lpm.

6.7 Summary

This chapter outlined the main aim of the UCL TMVs, that is, to assess its potential as a treatment option for high-risk patients with severe mitral regurgitation. The design of the prototypes, in terms of their leaflets, wireframe, sealing cuff and skirt, and their functional assessment were described. The results were presented and discussed in terms of both the achievement of working prototypes and the design issues that still required attention.

The following chapter 7 further describes how and why the 1st generation device was developed into a 2nd generation device, for which preliminary results and discussion are provided.

Chapter 7 Transcatheter mitral valves 2nd generation

As discussed in section 6.6.2 and 0 a smaller frame for the UCL TMV was developed. In this chapter, the new wireframe design and initial results of the functional assessment of three prototypes are expounded and compared to the 1st generation of UCL TMVs. (The functional assessment conducted was the same as previously described in Chapter 6).

7.1 Design

The aim of the new wireframe design (Figure 7.1) was mainly to reduce interaction between the ventricle sac and frame during systole (Figure 6.9) and also has the added benefit that if a transseptal version is designed it would reduce vascular damage during implantation. This was achieved by making the petal shaped hoops smaller (Figure 6.1 compared to Figure 7.1).

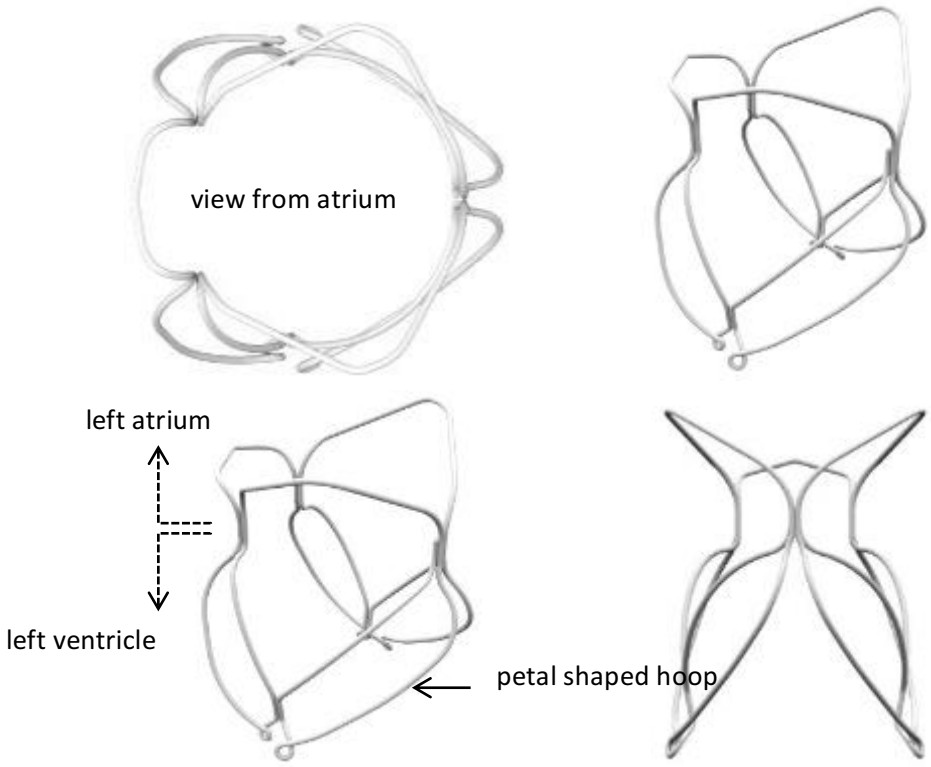

Figure 7.1: 2nd generation nitinol wireframe for the UCL transcatheter mitral valve with reduced size of petal shaped hoops, **(top left)** view from atrium, **(bottom left)** side view, **(bottom right)** front view **(top right)** perspective view.

The 2nd generation UCL TMV houses the same sized leaflets, and so is the same size device. However, the 2nd generation frame is shorter than the first; its deployed and crimped lengths being 33 and 45 mm, which are 7 and 8 mm shorter than the 1st generation respectively (Bozkurt et al 2016). Thus making potential vascular damage caused by the length of the 2nd generation UCL TMV frame less compared to the 1st as well as compared to the much longer CoreValve, which has a deployed height of 50-53 mm (Table 1.1).

7.2 Preliminary results and discussion

In this section the results for a cardiac output of 5 lpm are presented and discussed.

7.2.1 Effective orifice area

The 2nd generation UCL TMV still met and exceeded the ISO requirements for effective orifice area (EOA) (Figure 7.2). However, on average it had a smaller EOA compared to the first generation and overall there were similar standard deviations between prototypes. For example, for the 24 mm holder, the EOA for the 1st generation was 1.61 ± 0.18 cm^2 and for the 2nd generation it was only 1.32 ± 0.14 cm^2.

7.2.2 Regurgitant fraction

The 2nd generation UCL TMV still met and exceeded the ISO requirements for regurgitant fraction (RF) (Figure 7.2). However, on average it had larger RFs compared to the 1st generation and overall there was a smaller standard deviation between the 2nd generation prototypes. For example, for the 24 mm holder at a cardiac output of 5lpm, the RF for the

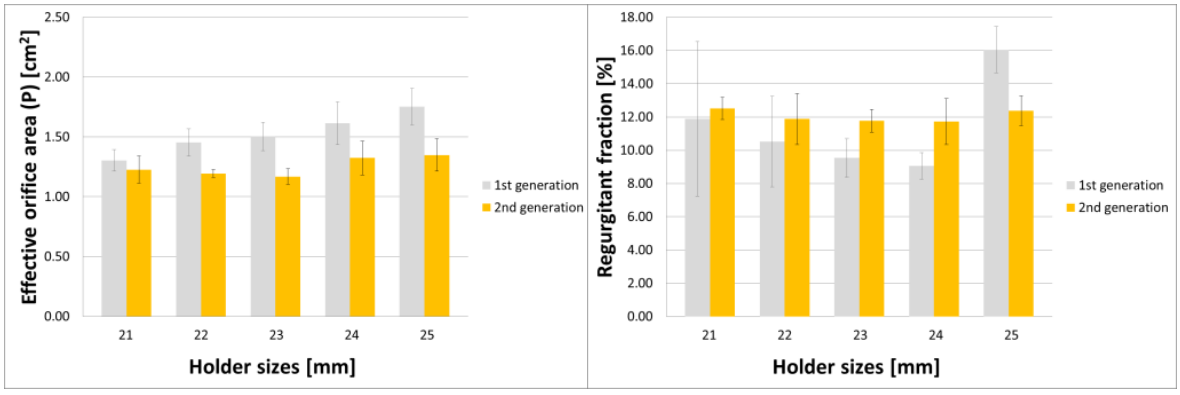

Figure 7.2: (left) effective orifice area **(right)** regurgitation fraction; for two generations of the UCL transcatheter mitral valve, both averages and standard deviations are for three prototypes.

1st generation was 9.1 ± 0.8% and for the 2nd generation it was 11.7 ± 1.4%.

7.3 Summary

This chapter demonstrated that the 2nd generation wireframe design for the UCL TMV achieved its aim to reduce interaction between the ventricle sac and frame during systole, as determined from visual observations. The new design also had the added benefit that if a transseptal version were designed it would reduce vascular damage during implantation and still meet the Internal Standard requirements (ISO 5840-3:2013). However, in terms of EOA and RF its performance was surpassed by the first generation. Although its performance could foreseeably improve as assembly methods are refined.

The following chapter, discusses the limitations of the work and future work. This includes a discussion of materials, leaflet design, prototyping, *in vitro* assessment as well as the future delivery system for the UCL TMV.

Chapter 8 Conclusions & Recommendations for Future Work

The aim of this project was to develop a proof of concept prototype of the UCL transcatheter mitral valve (TMV) by completing an initial design cycle consisting of design (Chapter 3 and 4), prototyping and testing (Chapters 6 and 7). This aim was achieved demonstrating both promising hydrodynamic performance (section 6.6.1) and durability (Chapters 6 and 7). In fact the *in vitro* results for the proof of concept 1st generation UCL TMV prototypes (Chapter 6) have already been utilised in the 2nd design cycle (Chapter 7), analysis for which is ongoing.

This final chapter discusses the main findings, limitations and recommendations for future work, including a discussion of the materials, leaflet design, prototyping and *in vitro* assessment.

8.1 Main findings

Conclusions in this section are discussed in the context of background information provided in 3, as well as other major concepts and recent developments, and advances made in the study of various subject areas. Areas of original contribution are highlighted and where broad conclusions support, add to or conflict with previous work are indicated.

The following sections 8.1.1 and 8.1.2 discuss the main contributions to the following areas of research:

- Nature-inspired conical leaflet design (Chapter 1, Figure 1.5, section 1.4.4)
- Thermomechanical properties of pericardium (Chapter 3, section 3.1.2.1)
- Design and making of mock native mitral valves (Chapter 5, section 5.1)
- Proof of concept and effective adaptation of the TAV frame for the UCL TMV, including optimal implantation site size and surpassing ISO 5840-3:2013 minimum performance requirements (Chapter 6, section 6.6)

8.1.1 Design

The two leafleted UCL TMV is a viable alternative to transcatheter repair techniques (section 1.4.1) for treating mitral regurgitation (Figure 1.8) in high-risk patients and due to its geometric similarity to the human mitral valve (Figure 1.1 and 1.3), may prove more

appropriate compared to circular TMVs in development (Table 2.1), minimising disturbance to natural kinetics of native mitral apparatus (Figure 1.7) and possibly resulting in more natural pressures and flows (Figure 1.4 and 1.9), thereby significantly advancing their development. Furthermore, there are only three other devices, the AccuFit, Direct Flow Mitral and Tresillo (Figure 2.8) which, like the UCL TMV, are retrievable and repositionable, features which were inherited for their success in the UCL TAV wireframe (section 1.4.3).

A novel design strategy, using a failure mode and effects analysis, was used to select optimal leaflets for the UCL TMV, which supports the approach suggested in ISO 5840-3:2013, this led to addition of conicity to the parametric leaflet design, which as well as design of the sealing cuff and selection of skirt material, was an original contribution to the initial design (section 1.4.4). In fact, the methods used to characterise the skirt mesh were also novel and could enable a more advanced study of mesh structures for other biological purposes.

In terms of the experimental design there were two major original contributions. Firstly, investigation into thermo-mechanical properties of pericardium was the first justification for *in vitro* testing of bioprosthetic heart valves at room temperature. In fact, the constitutive equation derived to show this improved on the accuracy achieved by previous equations used to describe the behaviour of pericardium. Secondly, design and methods for making mock native mitral valve implantation sites were an effective novel development in *in vitro* assessment of TMVs, for which no experimental equipment has previously been suggested.

8.1.2 Functional performance

For the first time, hydrodynamic functional performance data for a TMV, using internationally recognised pulsatile flow conditions are reported. The proposed TMV was shown to exceed minimum performance requirements set for nominal diameters of 23 and 25 mm (ISO 5840-3:2013) i.e. effective orifice areas (EOAs) ≥ 1.05 and 1.25 cm^2 and regurgitation fractions (RFs) ≤ 20%. It performed optimally in a 24 mm mock native mitral valve holder, with minimum total energy loss of 14.7 ± 1.6% of ventricular energy, an EOA of 1.61 ± 0.18 cm^2 and a RF of 9.1 ± 0.8% (here, the average values are for a cardiac output of 5 lpm and the standard deviations are, in worse cases, between three prototypes). In

other words, it achieved an EOA 41% greater and a RF 55% less than required. These *in vitro* assessments support previous research (section 2.2.4) which indicates TMVs can achieve good anchoring in a mitral orifice and have healthy diastolic and systolic performance. For the UCL TMV, regurgitation prevention using a sealing cuff was paramount to its good performance. The tests demonstrated the effective adaptation of the UCL TAV frame for the mitral position and that its functional performance was largely determined by native leaflet geometry, highlighting that more complex sizing algorithms are required for TMVs compared to TAVs and will be different for different TMV designs.

8.1.3 Summary of main achievements

To summarise, to address a currently untreated patient population of elderly people with severe mitral regurgitation a proof of concept for a 26 mm UCL transcatheter mitral valve has been provided which exceeds international standards and would foreseeably be suitable for patients with annulus sizes between 20 and 25 mm and to date has achieved *in vitro* durability up to two years. Furthermore, the *in vitro* results indicated design improvements required, which were implemented in the 2nd generation UCL TMV which still meets the international standards. In addition, the following three papers and three conferences resulted from the research:

- Preston-Maher GL, Torii R and Burriesci G. **A technical review of minimally invasive mitral valve replacements**. Cardiovascular Engineering and Technology. 6(2):174-184. Jun 2015. URL: http://dx.doi.org/10.1007/s13239-014-0203-9. (Chapter 2, section 2.4).
- Sturla F, Ronzoni M, Vitali M, Dimasi A, Vismara R, Preston-Maher G, Burriesci G, Votta E and Redaelli A. **Impact of different aortic valve calcification patterns on the outcome of transcatheter aortic valve implantation: a finite element study**. Journal of Biomechanics. 49(12):2520-2530, Aug 2016. URL: http://dx.doi.org/10.1016/ j.jbiomech.2016.03.036. (Chapter 3, section 3.1.2).
- Bozkurt S, Preston-Maher GL, Torii R and Burriesci G. **Design, analysis and testing of a novel mitral valve for transcatheter implantation.** Annals of Biomedical Engineering. Mar 2017. URL: http://dx.doi.org/10.1007/s10439-017-1828-2. (Chapter 6).
- Preston-Maher G, Bozkurt S, Rahmani B, Torii R, Mullen M and Burriesci G. **Development and hydrodynamic assessment of a novel transcatheter mitral valve.** European Society for Vascular Surgery Spring Meeting, London, UK, 13 May 2016 – 14 May 2016. 14 May 2016. (Chapter 6).

- Bozkurt S, Preston-Maher G, Torii R and Burriesci G. **A novel mitral valve for transcatheter implantation.** European Society of Biomechanics Conference, Lyon, France, 10 Jul 2016 – 13 Jul 2016. 10 Jul 2016. (Chapter 6).
- Bozkurt S, Preston-Maher GL, Rahmani B, Torii R, Burriesci G. **Design, Analysis and Hydrodynamic Assessment of a Novel Transcatheter Mitral Valve**. 28th Conference of the International Society for Medical Innovation and Technology, Delft, Netherland, 5-8 Oct 2016. 7 Oct 2016. (Chapter 6).

8.2 Limitations and recommendations for future work

8.2.1 Materials

8.2.1.1 Pericardium

The main limitation of using pericardium tissue in bioprosthetic heart valves is its durability and in the case of transcatheter valves maybe affected by crimping inside a catheter for delivery. More specifically, crimping duration is correlated with structural changes which maybe of clinical significance and therefore the duration and severity of crimping should ideally be minimised (Kiefer et al 2011). However, Kiefer et al (2011) did not study the influence of temperature at which the leaflets are crimped, therefore a further thermo-mechanical study of pericardium is required to determine the effect of crimping pericardial leaflets at 4 ^{o}C, and of particular relevance for retrievable devices, the effect of repeated crimping and unfolding at 37 ^{o}C.

The UCL Cardiovascular Engineering Group is currently investigating two alternatives to pericardial leaflets; genetically modified sources and nanocomposite polymers. The latter has shown promising results for the UCL TAV (Rahmani et al 2013, Rahmani et al 2012), achieving more than 400 million cardiac cycles *in vitro* and could foreseeably be applied to the UCL TMV. Most recently, a simpler approach was taken by Anssari-Benam et al (2016), whom simply addressed the durability issue by suggesting an alternative chemical treatment.

8.2.1.2 Polyester mesh

The current polyester mesh used for the UCL TMV skirt is sufficient for *in vitro* assessments. However further investigation is required to select a mesh structure that will be optimal in terms of tissue ingrowth, whilst still achieving the required extensibility.

8.2.1.3 Nitinol wire

The UCL TMV, like most other TMVs in development (Table 2.1), has nitinol components. Unfortunately, this will limit the number of patients suitable for the devices due to some having hypersensitivity to the nickel content of nitinol which occurs in approximately 15% of the population (Marks Jr. et al 2003), research into how to mitigate this is required.

8.2.2 Leaflet design using finite element analyses

All finite element models have a certain amount of unavoidable uncertainty due to their narrow depiction of reality partly due to omission of natural variability in mechanical properties of materials. Similarly, despite quality measures in place, there will be variations between mechanical properties in bioprosthetic heart valve leaflets.

In fact, pericardium tissue has an innate range of maximum tensile strengths and general tensile behaviour; mean tensile stress at rupture for porcine pericardium was reported to range between 2 and 20 MPa (Paez et al 2003, Zioupos et al Apr 1994) and the Young's Modulus of decellularized bovine pericardium was reported (even though it has a nonlinear relationship between strain and stress) to range between 60 and 100 MPa (Hulsmann et al 2012). Variability also occurs due to manufacturing methods, including variation in geometry of these handmade devices, operating environment and subsequent loading conditions. Therefore, the exact leaflet shape observable *in vitro* will differ from those predicted by FEA and subsequently so will predicted stress distributions. Despite this the FEAs of the bioprosthetic heart valve leaflets provided a useful prediction of their general ability to close, occlude the orifice and stress states are meaningful as an order of magnitude approximation. Furthermore, the simulations correctly predicted the curvature of the fully closed leaflets being towards the mural leaflet in the case of the transcatheter mitral valve prototype (Figure 4.14).

The boundary conditions for diseased native mitral valves and surrounding anatomy into which the TMV would be implanted i.e. their structure, material properties and forces they exert, were not modelled because, in general, their high complexity and variability throughout the cardiac cycle have not been quantified. In fact, exact values for forces in native mitral valves have only recently been recorded (Askov et al 2013) and although predictions for patient specific configuration of transcatheter aortic valves has recently been investigated (Bailey et al 2016, Capelli et al 2012) a patient specific approach is not appropriate when designing one device for a whole patient population. Instead boundary conditions were applied to the leaflets in their manufactured configuration, which still predicted the order of magnitude of the maximum principal stress (MPS), as recently expounded by Abbasi et al (2015) who reported that although the MPS for the SAPIEN TAV leaflets varies non-linearly with its expanded diameter, it remained within the same order of magnitude as 1 MPa. Also, simulating the leaflets in their manufactured configuration would still provide comparative values for coaptation areas. Furthermore, the native mitral valve boundary conditions may be subject to change once the proposed device is implanted. For example, the once reduced left ventricular systolic torsion, associated with mitral regurgitation (Ennis et al 2009), may increase as the ventricle re-models.

The absence of the frame[35] is a limitation of the simulations, causing an over estimation of the stresses that will occur due to the additional rigidity of the boundary conditions. It is also limited because the simulations do not predict the opening and closing dynamics.

The shell elements used were limited in that they could not represent shear, a possible alternative would be membrane or brick elements. However, the former were not appropriate for modelling the heart valve leaflets because they do not account for bending and the latter were unsuitable because five brick elements would be required to have five integration points through the thickness of the pericardium tissue (as done in the shell elements for representation of out-of-plane stresses); this would quintuplet the number of elements introducing bricks with a very small dimension, the latter being associated with very small time steps and subsequently long analysis times (Burriesci et al 1999).

[35] Modelling the frame was beyond the scope of this project.

The structural models were inherently limited in their ability to represent the physics involved in heart valve leaflet closure, which treated the geometry and pressure difference as inputs and resulting morphology and stress states as outputs. In reality, the physics is different; the working fluid interacts with the valve geometry and pressure differences are what result. Therefore, ideally pressure difference should be an output rather than an imposed boundary condition, which could be achieved by modelling a body of fluid moving in a closed system.

A structural model may also be surpassed by a fluid structure interaction (FSI) model in its ability to simulate the formation of vortices (Lau et al 2010); however the shear stresses induced on the leaflet surface by fluid flow are an order of magnitude less than shear stresses generated due to structural deformation. Therefore, pressure difference is considered to be the principal load causing leaflet deformation and, despite ignoring local pressure variation and fluid shear stresses due to blood flow, a time-dependent, spatially uniform pressure distribution across the leaflet surface, should yield reasonably accurate results (Chandran 2010). Omission of the ventricular vortex generated behind the aortic leaflet (Charonko et al 2013) is a likely explanation for why the model predicted opposite curvature of the closed leaflets in the case of the surgical mitral valve, which curved convexly towards the aortic leaflet rather than concaved (Figure 4.14).

Furthermore, leaflet closure duration *in silico* and *in vitro* were not expected to correlate either because it was previously demonstrated that due to lack of fluid inertia, a structural simulation of mitral leaflets will close approximately 16 times faster and take twice as long to open compared to experimental results, the latter being 400 and 40 ms respectively (Burriesci et al 1999). Nevertheless, the structural model did not entirely fail to represent the presence of a fluid; firstly, contact between leaflets was modelled as frictionless and, secondly, the role of inertia in reducing oscillations was represented by multiplying node velocities by a damping coefficient of 0.9965, previously used successfully by Burriesci et al (1999).

It is unlikely that numerical simulations would be able to predict a maximum leaflet length. More specifically, they fail to replicate the point at which further increase in leaflet length, and therefore also in their coaptation area, will result in a reduction of pressure between

them. Once this pressure reaches zero, any further increase in length would in fact actively separate the leaflets (Figure 8.1) reducing the coaptation area.

8.2.3 Haemodynamic assessment of valve leaflets

8.2.3.1 Software

The current ViViTest software does not calculate pressure-volume diagrams (Figure 1.9) automatically; manual processing of data is required. However, previous research has shown that altering the pressure-volume relationship directly is possible and useful for simulating both healthy and disease sates (Yokoyama et al 2010).

8.2.3.1.1 Mitral valve implantation sites

The mock native mitral valve implantation sites successfully assessed effect of annulus size on the functional performance of the UCL TMV. However, clinical relevance of the data is limited because the highly likely corresponding change in size of the patients' ventricle was not represented; the same standard ventricle sac was used for all annulus sizes. Ideally, ventricles with a smaller volume would be used for the smaller geometric orifice areas; scaled according to averaged native morphological findings (not published to date).

8.2.4 Bileaflet surgical mitral valve

This section discusses the future work for the bileaflet surgical mitral valve and adaptations to the pulse duplicator required to obtain flow visualisation data using particle image velocimetry (PIV).

The novel bileaflet surgical mitral valve (SMV) met the minimum performance requirements (section 5.4) and therefore, following durability assessment as per the requirements and protocol outlined in section 0, could eventually proceed to animal trials. If this were the case then the flange, designed specifically for *in vitro* assessment, would have to be converted to a suture ring, similar to that used for the Pericarbon MORE Mitral (Figure 1.10) and biocompatible materials for the stent and thread would be required.

8.2.4.1 Flow visualisation

The functional assessment of the SMVs showed they can replicate healthy pressures and flows and qualitative macro-scale features of the latter were viewed experimentally (Figure 5.31Figure 5.32). Further work is required to determine the quantitative micro-scale[36] fluid mechanics. For example, instantaneous velocity measurements would be essential for assessing the hemolytic[37] and thrombogenic[38] potential of prosthetic heart valves (ISO 14708, Adrian 1991). In the case of the SMVs presented in this thesis, more detailed flow visualisation would be essential for investigating the effect of conicity on flow separation, which according to Akins et al (2008) is heavily dependent on the ratio of the cross-sectional area from a smaller to larger vessel.

8.2.4.2 Particle image velocimetry

Particle image velocimetry (PIV) has previously been used to compare the ventricular flow associated with different mechanical mitral valve designs (Querzoli et al 2010). In PIV velocity data for a fluid is obtained by seeding it with tracer particles which can be illuminated using a laser. The displacement patterns of the particles are observed using video footage from a high speed camera, which is combined with the time between laser pulses to provide velocity data. This enables the quantification of stagnation zones as regions with low velocity and long residence times (Toninato et al 2016), which "*promote the formation of thrombi and concur to the development of lesions of embolic origin* " in a TAV device, and which in general occur more frequently in transcatheter replacements compared to surgical (Ducci et al 2013).

Optical distortions, observable using calibration grids (Barannyk et al 2015), will occur if the index of refraction (IR) of the materials through which the laser sheet passes do not match. For the current pulse duplicator (section 5.1), there are two materials, the acrylic housing and silicon ventricle sac, and two fluids, the distilled water outside the ventricle and buffered saline inside the ventricle, which should ideally have identical indices of refraction (Figure 8.2).

[36] Opossed to the attempted macro-scale observation.
[37] Red blood cell damage.
[38] Formation of blood clots which cause blockages and damage surrounding tissue.

In general there are algorithms to account for optical distortions; however these will not work well with the spherical, cylindrical and highly nonlinear deformations of the ventricle, which occur under typical operating conditions as it expands and contracts in less than one second for a complete cardiac cycle.

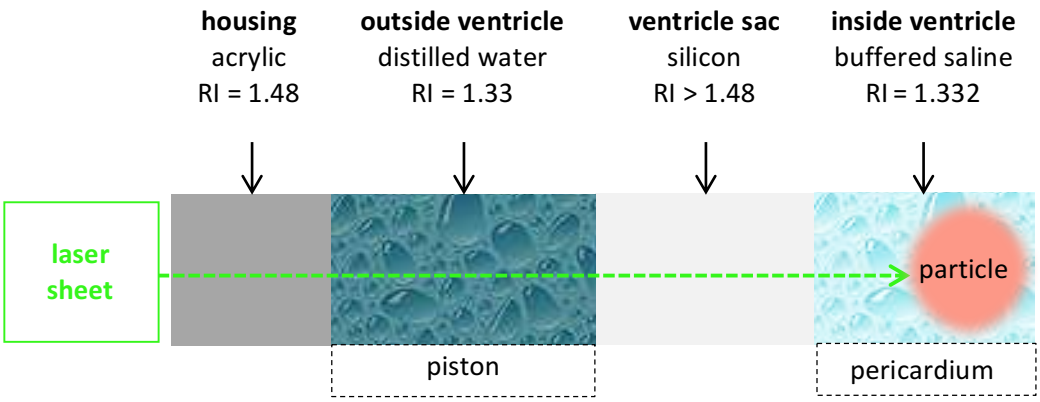

Figure 8.1: Refractive index (RI) matching problem for the current pulse duplicator, indicating the parts the fluids contact.

RI matching has previously been achieved by replacing the fluid in the ventricle with a mixture of deionized water (water with almost all of its mineral ions removed), viscous sugar alcohol (glycerin) and salt (sodium iodide (NaI), Barannyk et al 2015). However, NaI is not compatible with pericardium soft tissue and if used outside the ventricle its highly corrosive properties would damage the piston seal and viscoelastic impedance adapter. In fact, according to the manufactures manual the area outside the ventricle should only ever be filled with distilled water; any other fluid may cause damage. The ventricle sac could be replaced with one made from silicone that has the same RI as the housing stock acrylic or vice versa. Either way, the RI of all four materials must match and appropriate fluids and materials compatible with the machine parts and pericardial valves[39] remain undefined therefore conducting PIV would require the design and making of a new pulse duplicator system that also ideally includes clear visual access to the ventricle from numerous angles, similar to the rectangular tank set-up used by Falahatpisheh et al (2012).

[39] Fluorecent dyes could theoretically be used with lasers (or seeding particles) despite not achieving RI matching, and would still give a better visualisation. However, they are not compatible with pericardium and so were not used.

8.2.4.3 Clinical relevance

The analysis of blood flow dynamics is common in laboratories and is only recently being developed into flow-based indexes for early diagnosis of cardiac pathologies (Sengupta et al 2012). In fact, in a more general sense, Moraldo et al (2013) used doppler echocardiography[40] to measure the effective regurgitant orifice area (EROA) in patients with mitral regurgitation using the proximal isovelocity surface area (PISA) technique, which incidentally, as mentioned previously (section 2.3.1), is also a more relevant method for assessing the diastolic performance of mitral valves. Therefore, development of flow visualisation techniques for the mitral valves *in vitro* would enable the effective surface area to be measured rather than the current effective orifice area making their assessment more clinically relevant.

8.2.5 Pulse duplicator

The Cardiovascular Engineering Group at UCL is currently developing a more physiologically similar ventricular sac. This was made by firstly extracting the shape of the outer surface of a human left ventricle in the fully contracted position from a computerised tomographic (CT) scan (Figure 8.2). This was then printed as a solid artefact in 3D to act as a moulding surface which was dipped in liquid silicon to form a transparent silicon sac (Figure 8.2).

Figure 8.2: Human left ventricle **(left)** computerised Tomographic (CT) scan in its fully contracted state **(right)** *left*: mould to make ventricle sac *right*: silicon ventricle sac formed using mould.

[40] Doppler echocardiography is an ultrasound technology, i.e. high frequency sound waves, which enables one to see inside the body from the outside.

Furthermore, the ventricle was adapted to incorporate artificial papillary muscles for tethering the chordae tendineae of animal heart valves, the orientation of which can be adjusted (Figure 8.3).

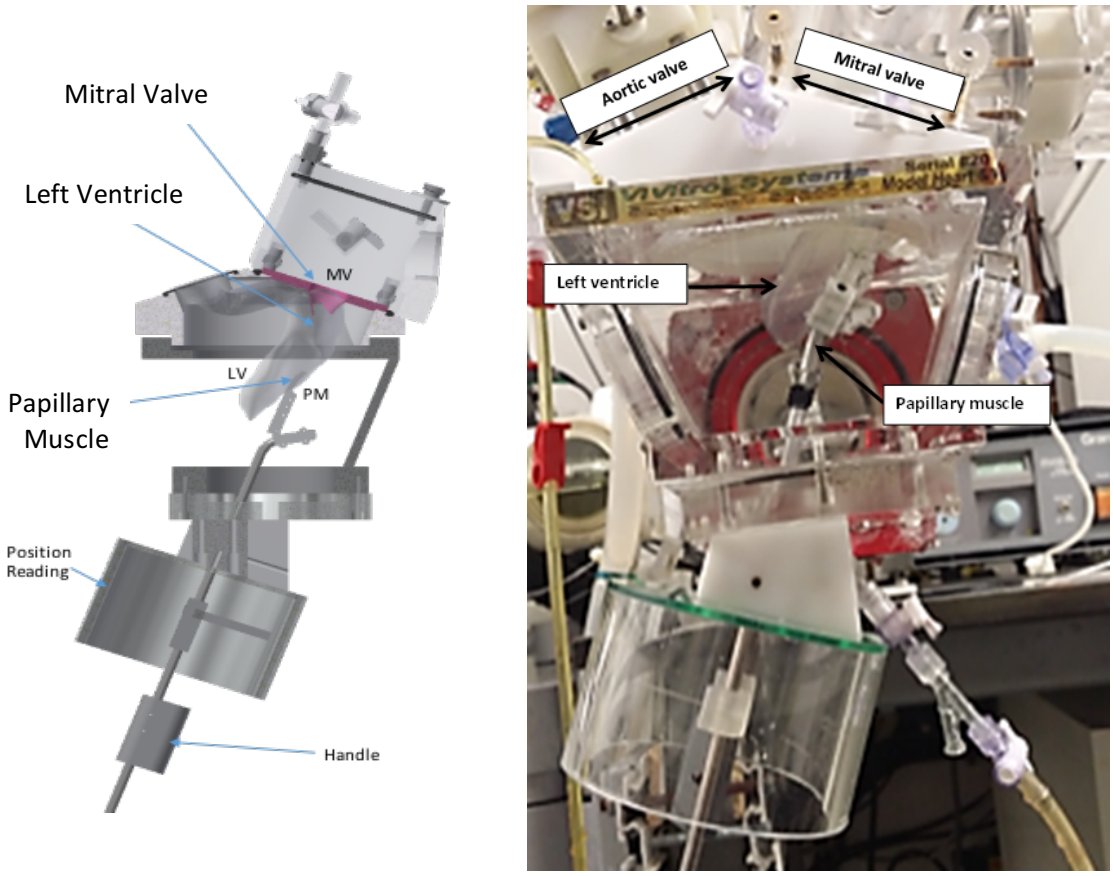

Figure 8.3: Physiologically similar ventricle sac with adaptable papillary muscles **(left)** schematic **(right)** adapted hydro-mechanical cardiovascular pulse duplicator system (ViVitro Superpump SP3891, ViVitro, BC, Canada).

8.2.6 Transcatheter mitral valve

This section discusses the ongoing development of the UCL TMV in terms of the new wireframe design and the functional assessment; more specifically the test temperature and anatomical inclusion criteria, the delivery system and lastly durability assessments.

8.2.6.1 Wireframe design

As discussed in section 6.6.2, the ventricle sac frequently touched the UCL TMV frame during systole and therefore to minimise this interaction, a smaller frame was developed and is currently being tested (6.7). However, repeated contact does not necessarily imply the frame is unsuitable; there are other commercially available surgical approaches, such as left ventricle assist devices (LVAD), which repeatedly connect with the ventricle wall without significant damage. In the case of the UCL TMV, *in vivo* assessment in animals will be required to determine whether this causes significant damage to the left ventricle and/or device.

8.2.6.2 Functional assessment

8.2.6.2.1 Test temperature

As per the investigation into thermo-mechanical properties of pericardium (section 3.1.2), assessing the functional performance of bioprosthetic heart valves at room temperature, rather than body temperature, does not significantly affect the mechanical properties of the pericardial leaflets. However, elevated temperatures will substantially affect the mechanical properties (rigidity) of nitinol frames and, therefore, once the optimal frame design and processing techniques (e.g. electropolishing or alternatives (Rokicki et al 2015)) have been finalised, new UCL TMV prototypes should be assessed at 37 ^{o}C.

8.2.6.2.2 Anatomical inclusion criteria

The UCL TMVs were tested in mock native mitral valve holders with inter-trigonal diameters between 20 and 25 mm, which identified the native commissural length as a critical parameter affecting their performance (section 6.6.2), i.e. if they are too short then the porous skirt mesh is exposed, greatly increasing regurgitant volumes. In the event of *in vivo* assessment, further clarification of native anatomy inclusion criteria, including when in the cardiac cycle these parameters should be measured, is required, some of which may be similar to that reported for the Fortis device (Bapat et al 2014).

8.2.6.3 Delivery system

The catheter based delivery system which facilitates crimping, multi-stage expansion (Figure 1.15), repositioning and retrieval of the proposed TMV, will be based on that developed for the UCL TAV (Rahmani et al 2016, Burriesci et al 2012), the main adaptation

being increasing catheter diameter. A minimal girth would minimise the invasivity of the transapical access required and if a transseptal version were designed, would minimise vascular damage. Therefore, further experimental work is required to determine the minimal crimped diameter achievable without damage to device or delivery system whilst maintaining ease of loading.

The proposed 26 mm UCL TMV had a deployed length of 40 mm and will be 53 mm long when crimped to a diameter of 8 mm (Bozkurt et al 2016). The same sized device but with a shorter frame which is only 33 mm long when deployed and 45 mm when crimped has been made and initial functional assessment results obtained (6.7). The aim of this design change was mainly to reduce interaction between ventricle sac and frame during systole, but also has the added benefit that if a transseptal version is designed would reduce vascular damage during implantation. In fact, potential vascular damage caused by the length of either of the UCL TMV frames would still be optimal compared to the much longer CoreValve, which has a deployed height of 50-53 mm (Table 1.1).

8.2.6.4 Durability assessment

8.2.6.4.1 Requirements

Further to the functional assessment of the UCL TMVs (0), the international standards (ISO 5840-3:2013) require that transcatheter heart valves remain functional for at least 200 million *in vitro* test cycles, equivalent to approximately 5 years *in vivo*. However, to meet the CE directive requirements, on route to acquiring the CE marking (Conformite Europeene i.e. European Conformity), only 8 million *in vitro* test cycles (90 days *in vivo*) are required prior to animal testing. In the United States the FDA (Food and Drug Administration; a federal agency of the United States Department of Health and Human Services) require a longer durability assessment of 12 million cycles (140 days *in vivo*) before animal studies can be undertaken. These regulations currently have to be satisfied independently, however, the WHO (World Health Organisation; a specialized agency of the United Nations) continues to promote the harmonization of regulations (Lamph 2012).

8.2.6.4.2 Protocol

The durability of the UCL TMV prototypes is currently being assessed inside optimal 24 mm mock native mitral valve holders using the BDC Laboratories' VDT-3600i heart valve durability tester (Figure 8.4) whilst in saline solution at 37 ^{o}C. The accelerated wear test

system is set to generate a heart rate of 20 Hz and peak differential pressure of 130 mmHg, which is slightly higher than the required normotensive 120 mmHg to account for machine oscillations and is maintained for at least 5% of each cycle for 95% or more of all test cycles. This higher than natural heart rate means that *in vitro* it takes only three months to simulate five years of *in vivo* function.

8.2.6.4.3 Results to date

TMV1 and TMV3 have passed 80 million cycles (equivalent to two years *in vivo*) and are still functional. Therefore, they would be considered durable enough for animal trials. The frame of TMV2 failed prior to reaching one million cycles, however this premature failure will foreseeably be rectified once the frames are electropolished, which will remove micro-cracks which act as initiation sites for failure. Tests are estimated to be completed by the end of 2016.

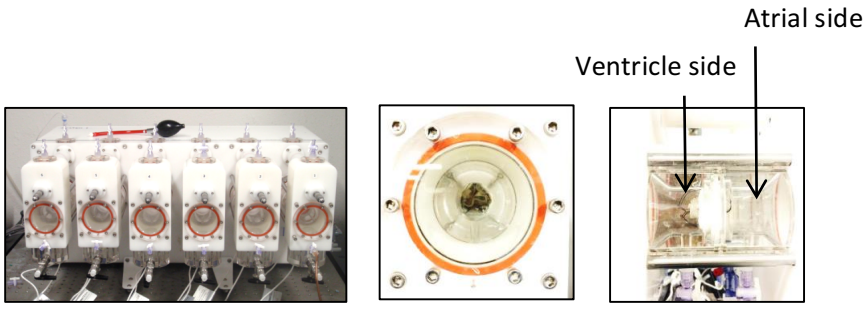

Figure 8.4: Heart valve durability tester (BDC Laboratories) **(left)** 6 stations of tester and the UCL TMV mounted viewed from **(middle)** ventricular side **(right)** side view.

8.2.6.4.4 Future work

The durability testing will continue until 200 million cycles/device failure and will continue to be paused every 40 million cycles, approximately 18 days, equivalent to 1 year *in vivo*, at which point the devices will be placed back in the pulse duplicator to confirm they are maintaining acceptable functional performance. Once the frame design and manufacturing methods have been optimised (namely, electropolishing methods) and the catheter delivery system is made, the devices will be crimped and released three times prior to repeating the durability assessment outlined above. Therefore, the current durability assessment is predominantly testing the leaflets and general assembly methods.

On successful completion of the durability assessments to the required standards, estimated to be completed by the end of 2016, animal trials could foreseeably be performed followed by human trials within the next 2-4 years.

References

Aaslid R, Levang O, Froysaker T, Skagseth E and Hall KV. “in situ” evaluation of the aortic pivoting disc valve prosthesis. *Scandinavian Cardiovascular Journal,* 9(2):81-84, 1975. doi: 10.3109/14017437509139179. URL: http://dx.doi.org/10.3109/ 14017437509139179.

Abbasi M and Azadani AN. Leaflet stress and strain distribution following incomplete transcatheter aortic valve expansion. *Journal of Biomechanics*, 48(13):3672-3680, Oct 2015. doi: 10.1016/j.jbiomech.2015.08.012. URL: http://dx.doi.org/10.1016/j.jbiomech. 2015.08.012Document.

Abdelghani M, Onuma Y, Zeng Y, Soliman OII, Ma J, Huo Y, Guidotti A, Nietlispach F, Maisano F and Serruys PW. The Sino Medical AccuFit transcatheter mitral valve implantation system. *EuroIntervention*, 11(1):W84-W85, Sep 2015. doi: 10.4244/EIJV11SWA26. URL: http://dx.doi.org/10.4244/EIJV11SWA26.

Adrian RJ. Particle-imaging techniques for experimental fluid mechanics. *Annual Review of Fluid Mechanics*, 23(1):261-304, 1991.

Akins CW, Travis B and Yoganathan AP. Energy loss for evaluating heart valve performance. *The Journal of Thoracic and Cardiovascular Surgery*, 136(4):820-833, Oct 2008. doi: 10.1016/j.jtcvs.2007.12.059. URL: http://dx.doi.org/10.1016/ j.jtcvs.2007.12.059.

Alfieri O, Maisano F, De Bonis M, Stefano PL, Torracca L, Oppizzi M, La Canna G and Miller DC. The double-orifice technique in mitral valve repair: A simple solution for complex problems. *Journal of Thoracic Cardiovascular Surgery*, 122(4):674-681, Oct 2001. doi: 10.1067/mtc.2001.117277. URL: http://dx.doi.org/10.1067/ mtc.2001.117277.

Alsoufi B, Al-Shahid M, Manlhiot C, Al-Amri M, McCrindle BW, Fadel B and Al-Halees Z. Mitral valve replacement with the Quattro stentless pericardial bio-prosthesis: mid-term clinical and echocardiographic follow up. *Journal of Heart Valve Disease*, 19(3):304-311, May 2010.

Altisent OAJ, Dumont E, Dagenais F, Senechal M, Bernier M, O’Connor K, Bilodeau S, Paradis JM, Campelo-Parada F, Puri R, del Trigo M and Rodes-Cabau J. Initial experience of

transcatheter mitral valve replacement with a novel transcatheter mitral valve procedural and 6-month follow-up results. *Journal of the American College of Cardiology*, 66(9):1011-1019, Sep 2015.

American College of Cardiology/American Heart Association 2006 Guidelines from the Management of Patients with Valvular Disease.

Anssari-Benam A, Barber AH and Bucchi A. Evaluation of bioprosthetic heart valve failure using a matrix-fibril shear stress transfer approach. *Journal of Materials Science: Materials in Medicine*, 27(2):1-11, Feb 2016. doi: 10.1007/s10856-015-5657-2. URL: http://dx.doi/org/10.1007/s10856-015-5657-2.

Askov JB, Honge JL, Jensen MO, Nygaard H, Hasenkam JM and Nielsen SL. Significance of force transfer in mitral valve-left ventricular interaction: In vivo assessment. *Journal of Thoracic and Cardiovascular Surgery*, 145(6):1635-1641.e1, Jun 2013. doi: 10.1016/j.jtcvs.2012.07.062. URL: http://dx.doi.org/10.1016/j.jtcvs. 2012.07.062.

Auricchio F, Conti M, Morganti S and Reali A. Simulation of transcatheter aortic valve implantation: a patient-specific finite element approach. *Computer Methods in Biomechanics and Biomedical Engineering,* 17(12):1347-1357, Sep 2014. doi: 10.1080/10255842.2012.746676. URL: http://dx.doi.org/10.1080/10255842.2012. 746676.

Axford J and O'Callaghan C. Medicine. Malden, Mass.: Blackwell Science; 2004.

Aybek T, Simon A, Dogan S, Greinecker GW and Mortiz A. Two years' clinical experience with a quadrileaflet stentless bioprosthesis in the mitral position. *Journal of Heart Valve Disease*, 9(5):667-673, 2000.

Bailey J, Curzen N and Bressloff NW. Assessing the impact of including leaflets in the simulation of TAVI deployment into a patient-specific aortic root. *Computer Methods in Biomechanics and Biomedical Engineering*, 19(7):733-744, May 2016. doi: 10.1080/10255842.2015.1058928.

Banai S, Jolicoeur EM, Schwartz M, Garceau P, Biner S, Tanguay JF, Cartier R, Verheye S, White CJ and Edelman E. Tiara: A novel catheter-based mitral valve bioprostheses: initial

experiments and short-term pre-clinical results. *Journal of the American College of Cardiology,* 60(15):1430-1431, Oct 2012. 10.1016/j.jacc.2012.05.047. URL: http://dx.doi.org/10.1016/j.jacc.2012.05.047.

Banai S, Verheye S, Cheung A, Schwartz M, Marko A, Lane R, Jolicoeur EM, Garceau P, Biner S, Tanguay JF, Edelman ER and White CJ. Transapical mitral implantation of the tiara bioprosthesis: Pre-clinical results. *JACC Cardiovascular Interventions*, 7(2):154-162, Feb 2014. doi: 10.1016/j.jcin.2013.10.009. URL: http://dx.doi.org/10.1016/j.jcin.2013.10.009.

Bapat V, Buellesfeld L, Peterson MD, Hancock J, Reineke D, Buller C, Carrel T, Praz F, Rajani R, Fam N, Kim H, Redwood S, Young C, Munns C, Windecker S and Thomas M. Transcatheter mitral valve implantation (TMVI) using the Edwards FORTIS device. *EuroIntervention*, 10:U120-U128, Sep 2014. doi: 10.4244/EIJV10SUA18. URL: http://dx.doi.org/10.4244/EIJV10SUA18.

Barannyk O and Oshkai P. The influence of the aortic root geometry on flow characteristics of a prosthetic heart valve. *Journal of Biomechanical Engineering*, 137(5):051005, May 2015. doi: 10.1115/1.4029747. URL: http://dx.doi.org/10.1115/1.4029747.

Bartel T, Muller S, Biviano A and Hahn RT. Why is intracardiac echocardiography helpful? Benefits, costs, and how to learn. *European Heart Journal*, 35(2):69-76, 2014. doi: 10.1093/eurheartj/eht411. URL: http://dx.doi.org/10.1093/ eurheartj/eht411.

Bellhouse BJ. Some fluid mechanic theories and their application to the design of heart valves and memebrane lungs. In *Cardiac Dynamics*, Baan J, Arntzenius AC and Yellin EL (Eds.), Martinus Nijhoff Publishers, 443-463, 1980. ISBN: 940098796X, 9789400987968.

Belytschko TB and Tsay CS. Explicit algorithms for nonlinear dynamics of shells. *American Society of Mechanical Engineers, Applied Mechanics Divison, AMD*, 48:209-231, Nov 1981.

Bernacca GM, Fisher AC, Wilkinson R, Mackay TG and Wheatley DJ. Calcification and stress distribution in bovine pericardial heart valves. *Journal of Biomedical Materials Research*, 26(7):959-966, Jul 1992. doi: 10.1002/jbm.820260710. URL: http://dx.doi.org/10.1002/jbm.820260710.

Black MM, Drury PJ and Tindale WB. A construction technique for minimising valve leaflet fatigue failure in pericardial valves. *Life Support Systems*, 2(1):89-91, 1984.

Black MM, Drury PJ, Tindale WB and Lawford PV. The Sheffield bicuspid valve: concept, design and in vitro and in vivo assessment. *Biologic and bioprosthetic valves: proceedings of the third international symposium*, 1986.

Black MM, Howard IC, Huang X, and Patterson EA. A three-dimensional analysis of a bioprosthetic heart valve. *Journal of Biomechanics*, 24(9):793–801, 1991. doi: 10.1016/0021-9290(91)90304-6. URL: http://dx.doi.org/10.1016/0021-9290(91) 90304-6.

Block PC. Percutaneous mitral valve repair: are they changing the guard? *Circulation*, 111(17):2154-2156, May 2005. doi: 10.1161/01.CIR.0000 165266.57397.B2. URL: http://dx.doi.org/10.1161/ 01.CIR. 0000165266.57397.B2.

Block PC and Palacios IF. Clinical and hemodynamic follow-up after percutaneous aortic valvuloplasty in the elderly. *American Journal of Cardiology,* 62(10):760-763, Oct 1988. doi: 10.1016/0002-9149(88)91218-0. URL: http://dx.doi.org/10.1016 /0002-9149(88)91218-0.

Block P, Hermann H and Whitlow P. Percutaneous edge-to-edge mitral valve repair using the Evalve MitraClip: initial experience with functional mitral regurgitation in the EVEREST I trial. *J Am Coll Cardiol*, 47(4):283A, 2006.

Bonhoeffer P, Boudjemline Y, Saliba Z, Merckx J, Aggoun Y, Bonnet D, Acar P, Le Bidois J, Sidi D and Kachaner J. Percutaneous replacement of pulmonary valve in a right-ventricular to pulmonary-artery prosthetic conduit with valve dysfunction. *Lancet*, 356(9239):1403-1405, Oct 2000.

Bozkurt S, Preston-Maher G, Torii R and Burriesci G. A novel mitral valve for transcatheter implantation. European Society of Biomechanics Conference, Lyon, France, 10 Jul 2016 – 13 Jul 2016. 10 Jul 2016.

Burriesci G and Bergamasco G. (2007). Annuloplasty prosthesis with an auxetic structure. Patent US8034103 (B2).

Burriesci G, Howard IC and Patterson EA. Influence of anisotropy on the mechanical behaviour of bioprosthetic heart valves. *Journal of Medical Engineering & Technology*, 23(6):203-215, Nov-Dec 1999.

Burriesci G, Carmody CJ, Howard CJ and Patterson EA. Simulazione numerica del comportamento emodinamico del ventricolo sinistro con interazione fluido-struttura. Presented at: XXXII National Congress of AIAS – Stress Analysis Italian Association, Salerno, Italy, 2003: n.032.

Burriesci G, Marincola FC and Zervides C. Design of a novel polymeric heart valve. *Journal of Medical Engineering & Technology*, 34(1):7-22, Jan 2010. doi: 10.3109/03091900903261241. URL: http://dx.doi.org/10.3109/030919009 03261241.

Burriesci G, Tzamtzis S and Seifalian AM. (2012). Prosthesis delivery system. Patent WO/2012/052718.

Burriesci G, Zervides C and Seifalian AM. (2010). Heart valve prosthesis. Patent WO2010112844 A1.

Brandfonbrener M, Landowne M and Shock NW. Changes in cardiac output with age. *Circulation*, 12(4):557-566, 1955.

Caimmi PP, Summa MD, Galloni M, Gastaldi L, Papillo B, Dato GMA, Agaccio G, Donegani E, Poletti G and Morea M. Twelve-year follow up with the Sorin Pericarbon Bioprosthesis in the Mitral Position. *Journal of Heart Valve Disease,* 7(4):400-406, Jul 1998.

Capelli C, Bosi GM, Cerri E, Nordmeyer J, Odenwald T, Bonhoeffer P, Migliavacca F, Taylor AM and Schievano S. Patient specific simulations of transcatheter aortic valve stent implantation. *Med Biol Eng Comput,* 50(2):183-192, Feb 2012. doi: 10.1007/s11517-012-0864-1. URL: http://dx.doi.org/10.1007/s11517-012-0864-1.

Carmody CJ, Burriesci G, Howard IC and Patterson EA. An approach to the simulation of fluid-structure interaction in the aortic valve. *Journal of Biomechanics,* 39(1):158-169, 2006.

doi: 10.1016/j.jbiomech.2004.10.038. URL: http://dx.doi.rg/10.1016/j.jbiomech.2004.10.038.

Chandran KB. Role of computational simulations in heart valve dynamics and design of valvular prostheses. *Cardiovascular Engineering and Technology*, 1(1):18-38, Mar 2010. doi: 10.1007/s13239-010-0002-x. URL: http://dx.doi.org/10.1007/s13239-010-0002-x.

Chandran KB, Kim SH and Han G. Stress distribution on the cusps of a polyurethane trileaflet heart valve prosthesis in the closed position. *J Biomechanics*, 24(6):385-387,389-395, 1991. doi: 10.1016/0021-9290(91)90027-K. URL: http://dx.doi.org/ 10.1016/0021-9290(91)90027-K.

Charonko JJ, Kumar R, Stewart K, Little WC and Vlachos PP. Vortices formed on mitral valve tips aid normal left ventricular filling. *Annals of Biomedical Engineering*, 41(5):1049-1061, May 2013. doi: 10.1007/s10439-013-0755-0. URL: http://dx.doi/org/10.1007/s10439-013-0755-0.

Cheung A, Webb J, Verheye S, Moss R, Boone R, Leipsic J, Ree R and Banai S. Short-term results of transapical transcatheter mitral valve implantation for mitral regurgitation. *Journal of the American College of Cardiology*, 64(17):1814-1819, Oct 2014. doi: 10.1016/j.jacc.2014.06.1208. URL: http://dx.doi.org/10.1016/ j.jacc.2014.06.1208.

Chiam PTL and Ruiz CE. Percutaneous transcatheter mitral valve repair. *JACC: Cardiovascular Interventions*, 4(1):1-13, Jan 2011. doi: 10.1016/j.jcin.2010.09.023. URL: http://dx.doi.org/10.1016/j.jcin.2010.09.023.

Claramunt R, Alvarez-Ayuso L, Garcia-Paez JM, Ros A and Casado MC. Changes in the mechanical properties of chemically treated bovine pericardium after a short uniaxial cyclic test. *Artificial Organs,* 37(2):183-188, Feb 2013. doi: 10.1111/j.1525-1594.2012.01538.x. URL: http://dx.doi.org/10.1111/j.1525-1594.2012.01538.x.

Claramunt R, García Páez JM, Alvarez L, Ros A and Casado MC. Fatigue behaviour of young ostrich pericardium. *Materials Science and Engineering C,* 32(6):1415-1420, Aug 2012. doi: 10.1016/j.msec.2012.04.020. URL: http://dx.doi.org/10.1016/ j.msec.2012.04.020.

Coats L and Bonhoeffer P. New percutaneous treatments for valve disease. *Heart,* 93(5):639-644, May 2007. doi: 10.1136/hrt.2005.074799. URL: http://dx.doi.org/10.1136/hrt.2005.074799.

Cohn LH. Minimally invasive valve surgery. *J Card Surg*, 16(3):260-5, 2001.

Cohn LH and Edmunds LH Jr, eds. Cardiac Surgery in the Adult. New York, NY: McGraw-Hill; 2003:987-997. ISBN: 0071593470, 9780071593472.

Dasi LP, Simon HA, Sucosky P and Yoganathan AP. Fluid mechanics of artificial heart valves. *Clinical and Experimental Pharmacology and Physiology,* 36(2):225-237, Feb 2009. doi: 10.1111/j.1440-1681.2008.05099.x. URL: http://dx.doi.org/10.1111/ j.1440-1681.2008.05099.x.

Davidson MJ and Baim DS. Percutaneous aortic valve interventions. In: Cohn LH, ed. Cardiac surgery in the adult. New York: McGraw-Hill, 2008;963-71.

Davidson MJ, White JK and Baim DS. Percutaneous therapies for valvular heart disease. *Cardiovascular Pathology,* 15(3):123-129, May 2006. doi: 10.1016/j.carpath.2006.02.004. URL: http://dx.doi.org/10.1016/j.carpath. 2006.02.004.

De Backer O, Piazza N, Banai S, Lutter G, Maisano F, Herrmann HC, Franzen OW and Sondergaard L. Percutaneous transcatheter mitral valve replacement. An overview of devices in preclinical and early clinical evaluation. *Circulation: Cardiovascular Interventions,* 7(3):400-409, Jun 2014. doi: 10.1161/CIRCINTERVENTIONS.114.001607. URL: http://dx.doi.org/10.1161/ CIRCINTERVENTIONS.114.001607.

De Bonis M. The “edge-to-edge” technique in mitral valve repair. *Heart Views*, 4:164-169, 2002.

De Bonis M, Lapenna E, Lorusso R, Buzzatti N, Gelsomino S, Taramasso M, Vizzardi E and Alfieri O. Very long-term results (up to 17 years) with the double-orifice mitral valve repair combined with ring annuloplasty for degenerative mitral regurgitation. *Journal of Thoracic*

and cardiovascular Surgery, 144(5):1019-1024, 2012. doi: 10.1016/j.jtcvs.2012.07.034. URL: http://dx.doi.org/10.1016/j.jtcvs.2012.07.034.

Dieter Liepsch. Biofluid Mechanics: Blood Flow in Large Vessels. Published by Springer-Verlag Berlin Heidelberg , 1990. ISBN 978-3-540-52730-5.

Ducas RA, Jassal DS, Zieroth SR, Kirkpatrick ID and Freed DH. Left ventricular outflow tract obstruction by a bioprosthetic mitral valve: Diagnosis by cardiac computed tomography. *Journal of Thoracic Imaging,* 24(2):132-135, May 2009. doi: 10.1097/RTI.0b013e31819ca79d. URL: http://dx.doi.org/10.1097/ RTI.0b013e31819ca79d.

Ducci A, Tzamtzis S, Mullen MJ and Burriesci G. Hemodynamics in the Valsalva sinuses after transcatheter aortic valve implantation (TAVI). *The Journal of heart valve disease,* 22(5):688-696, Sep 2013.

Dumesnil JG and Yoganathan AP. Valve prosthesis hemodynamics and the problem of high transprosthetic pressure gradients. *European Journal of Cardio-thoracic Surgery*, 6:S34-S38, Jan 1992. doi: 10.1093/ejcts/6.Supplement_1.S34. URL: http://dx.doi/org/10.1093/ejcts/6.Supplement_1.S34.

Dyverfeldt P, Kvitting JPE, Carlhall CJ, Boano G, Sigfidsson A, Hermansson U, Bolger AF, Engvall J and Ebbers T. Hemodynamic aspects of mitral regurgitation assessed by generalized phase-contrast MRI. *Journal of Magnetic Resonance Imaging*, 33(3):582-588, Mar 2011. doi: 10.1002/jmri.22407. URL: http://dx.doi/org/10.1002/jmri.22407.

Edwards MB and Taylor KM. Outcomes in nonagenarians after heart valve replacement operation. *Annals of Thoracic Surgery*, 75(3):830-834, Mar 2003. doi: 10.1016/S0003-4975(02)04558-7. URL: http://dx.doi.org/10.1016/S0003-4975(02)04558-7.

Ennis DB, Nguyen TC, Itoh A, Bothe W, Liang DH, Ingels NB and Miller DC. Reduced systolic torsion in chronic “pure” mitral regurgitation. *Circulation: Cardiovascular Imaging*, 2(2):85-92, Mar 2009. doi: 10.1161/CIRCIMAGING.108.785923. URL: http://dx.doi.org/10.1161/CIRCIMAGING.108.785923.

Falahatpisheh A and Kheradvar A. High-speed particle image velocimetry to assess cardiac fluid dynamics in vitro: from performance to validation. *European Journal of Mechanics, B/Fluid*, 35:2-8, Sep 2012. doi: 10.1016/j.euromechflu.2012.01.019. URL: http://dx.doi.org/10.1016/j.euromechflu.2012.01.019.

Fassa AA, Himbert D, Brochet E, Depoix JP, Cheong AP, Alkhoder S, Nataf P and Vahanian A. Transseptal transcatheter mitral valve implantation for severely calcified mitral stenosis. *JACC: Cardiovascular Interventions*, 7(6):696-697, Jun 2014. doi: 10.1016/j.jcin.2013.12.204. URL: http://dx.doi.org/10.1016/j.jcin.2013.12.204.

Fedak PWM, McCarthy PM and Bonow RO. Evolving concepts and technologies in mitral valve repair. *Circulation, 117*(7):963-974, Feb 2008. doi: 10.1161/CIRCULATIONAHA.107.702035. URL: http://dx.doi.org/10.1161/CIRCULATIONAHA.107.702035.

Feldman T, Wasserman HS, Herrmann HC, Gray W, Block PC, Whitlow P, Goar FS, Rodriguez L, Silvestry F, Schwartz A, Sanborn TA, Condado JA and Foster E. Percutaneous mitral valve repair using the edge-to-edge technique: Six-month results of the EVEREST phase I clinical trial. *Journal of the American College of Cardiology*, 46(11):2134-2140, Dec 2005. doi: 10.1016/j.jacc.2005.07.065. URL: http://dx.doi.org/10.1016/j.jacc.2005.07.065.

Gabbay S, McQueen DM, Yellin EL, Becker RM and Frater RW. In vitro hydrodynamic comparison of mitral valve prostheses at high flow rates. *Journal of Thoracic and Cardiovascular Surgery,* 76(6):771-787, 1978.

Ghanbari H, Kidane A, Burriesci G, Bonhoeffer P and Seifalian AM. Percutaneous Heart Valve Replacement: An Update. *Trends in Cardiovascular Medicine*, 18(4):117-125, May 2008. doi: 10.1016/j.tcm.2008.02.002. URL: http://dx.doi.org/10.1016/j.tcm.2008.02.002.

Ghanbari H, Viatge H, Kidane AG, Burriesci G, Tavakoli M and Seifalian AM. Polymeric heart valves: new materials, emerging hopes. *Trends in Biotechnology*, 27(6):359-367, Jun 2009. doi: 10.1016/j.tibtech.2009.03.002. URL: http://dx.doi.org/10.1016/j.tibtech.2009.03.002.

Gillespie MJ, Minakawa M, Morita M, Vergnat M, Koomalsingh KJ, Robb JD, Kondo N, Shuto T, Takebe M, Shimaoka T, McGarvey JR, Gorman RC and Gorman III JH. Sutureless mitral valve replacement: initial steps towards a percutaneous procedure. *Annals of Thoracic Surgery,* 96(2):670-674, Aug 2013. doi: 10.1016/j.athoracsur.2013.02.065. URL: http://dx.doi.org/10.1016/ j.athoracsur.2013.02.065.

Gogoladze G, Dellis SL, Donnino R, Ribakove G, Greenhouse DG, Galloway A and Grossi E. Analysis of the mitral coaptation zone in normal and functional regurgitant valves. *Annals of Thoracic Surgery*, 89(4):1158-1161, Apr 2010. doi: 10.1016/j.athoracsur.2009.12.061. URL: http://dx.doi.org/10.1016/ j.athoracsur.2009.12.061.

Goldberg L, Mekel J and Grigorov V. 'Quadrileaflet' mitral valve associated with paravalvular aneurysms and complicated by mitral incompetence: A case report of a rare pathology identified by 2-dimensional echocardiography. *Cardiovascular Journal of South Africa*, 13(5):241-245, Sep 2002.

Guerrero M, Greenbaum A and O'Neill W. First in human percutaneous implantation of a balloon expandable transcatheter heart valve in a severely stenosed native mitral valve. *Catheterization and Cardiovascular Interventions,* 83(7):E287-E2991, Jun 2014. doi: 10.1002/ccd.25441. URL: http://dx.doi.org/10.1002/ccd.25441.

Hacohen G. Prosthetic mitral valve with tissue anchors. 2011. Patent US 20110224785 A1.

Hallquist JO, LS-DYNA Theory Manual. Livermore Software Technology Corporation (LSTC), March 2006. URL: http://www.lstc.com/pdf/ls-dyna_theory_manual_2006.pdf.

Hamid MS, Saddah HN and Stein PD. Influence of stent height upon stresses on the cusps of closed bioprosthetic valves. *J Biomechanics*, 19(9):759-769, 1986. doi: 10.1016/0021-9290(86)90199-5. URL: http://dx.doi.org/10.1016/0021-9290(86) 90199-5.

Harris JL, Wells PB and Humphrey JD. Altered mechanical behaviour of epicardium, due to isothermal heating under biaxial isothermal loads. *Journal of Biomechanical Engineering*, 125(3);381-388, Jun 2003. doi: 10.1115/1.1567754. URL: http://dx.doi.org/10.1115/1.1567754.

Hasan R, Mahadevan VS, Schneider H and Clarke B. First in human transapical implantation of an inverted transcatheter aortic valve prosthesis to treat mitral valve stenosis. *Circulation*, 128(6):e74-e76, Aug 2013. doi: 10.1161/CIRCULATIONAHA.113.001466. URL: http://dx.doi.org/10.1161/ CIRCULATIONAHA.113.001466.

Helton TJ, Kapadia SR and Tuzcu EM. Clinical trial experience with transcatheter aortic valve insertion. *International Journal of Cardiovascular Imaging,* 27(8);1143-1154, Dec 2011. doi: 10.1007/s10554-011-9825-2. URL: http://dx.doi.org/10.1007/s10554-011-9825-2.

Herrmann HC. Transcatheter mitral valve implantation – The advantage of MIS-tMVI may make it the ideal choice for high-risk patients. Cardiac Interventions Today. 2009. August/September, Cover Story.

Herrmann HC, Kar S, Siegel R, Fail P, Loghin C, Lim S, Hahn R, Rogers JH, Bommer WJ, Wang A, Berke A, Lerakis S, Kramer P, Wong SC, Foster E, Glower D and Feldman T. Effect of percutaneous mitral repair with the MitraClip (R) device on mitral valve area and gradient. *Eurointervention,* 4(4):437-442, Jan 2009. doi: 10.4244/EIJV4I4A76. URL: http://dx.doi.org/10.4244/EIJV4I4A76.

Himbert D, Bouleti C, Lung B, Nejjari M, Brochet E, Depoix JP, Ghodbane W, Fassa AA, Nataf P and Vahanian A. Transcatheter valve replacement in patients with severe mitral valve disease and annular calcification. *Journal of the American College of Cardiology,* 64(23):2557-2558, 2014. doi: 10.1016/j.jacc.2014.09.047. URL: http://dx.doi.org/10.1016/j.jacc.2014.09.047.

Hoffmann G, Lutter G and Cremer J. Durability of Bioprosthetic Cardiac Valves. *Deutsches Arzteblatt International*, 105(8):143-148, Feb 2008. doi: 10.3238/arztebl.2008.0143. URL: http://dx.doi.org/10.3238/arztebl.2008.0143.

Hofmann B, Cichon R, Knaut M, Kappert U, Tugtekin SM, Aron W and Schuler S. Early experience with a quadrileaflet stentless mitral valve. *Annals of Thoracic Surgery*, 71(5):S323-S326, May 2001. doi: 10.1016/S0003-4975(01)02544-9. URL: http://dx.doi.org/10.1016/S0003-4975(01)02544-9.

Howard IC, Patterson EA and Yoxall A. On the opening mechanism of the aortic valve: some observations from simulations. *J. Med. Eng. Technol*, 27(6):259–266, Nov 2003. doi: 10.1080/0309190031000096621. URL: http://dx.doi.org/10.1080/ 0309190031000096621.

Huang X, Black MM, Howard IC and Patterson EA. A 2-dimensional finite-element analysis of a bioprosthetic heart-valve. *J. Biomech*, 23(8):753–762, 1990. doi: 10.1016/0021-9290(90)90022-U. URL: http://dx.doi.org/10.1016/0021-9290(90) 90022-U.

Huang X, Ackland GJ and Rabe KM. Crystal structures and shape-memory behaviour of NiTi. *Nature Materials*, 2(5):307-311, May 2003. doi: 10.1038/nmat884. URL: http://dx.doi.org/10.1038/nmat884.

Huang XY, Luo Y, Zhong Q, Su ML, Wang BL and Huang SH. Biomechanical analysis of stentless quadrileaflet pericardial mitral valve: Implications of morphologies. *Sensors and Transducers*, 161(12):460-465, 2013.

Hulsmann J, Grun K, El Amouri S, Barth M, Hornung K, Holzfub C, Lichtenberg A and Akhyari P. Transplantation material bovine pericardium biomechanical and immunogenic characteristics after decellularization vs. glutaraldehyde-fixing. *Xenotransplantation*, 19(5):286-297, Sep-Oct 2012. doi: 10.1111/j.1399-3089.2012.00719.x. URL: http://dx.doi.org/10.1111/j.1399-3089.2012.00719.x.

Iino K, Boldt J, Lozonschi L, Metzner A, Schoettler J, Petzina R, Cremer J and Lutter G. Off-pump Transapical mitral valve replacement: evaluation after one month. *European Journal of Cardio-thoracic Surgery,* 41(3):512-517, 2012. doi: 10.1093/ejcts/ezr106. URL: http://dx.doi.org/10.1093/ejcts/ezr106.

Inoue K, Owaki T, Nakamura T, Kitamura F and Miyamoto N. Clinical-application of transvenous mitral commissurotomy by a new balloon catheter. *Journal of Thoracic and Cardiovascular Surgery*, 87(3):394-402, 1984.

Ishihara T, Ferrans VJ, Boyce SW, Jones M and Roberts WC. Structure and classification of cuspal tears and perforations in porcine bioprosthetic cardiac valves implanted in patients.

The American Journal of Cardiology, 48(4):665-678, Oct 1981. doi: 10.1016/0002-9149(81)90145-4. URL: http://dx.doi.org/10.1016/0002-9149(81)90145-4.

Jensen MO, Hagege AA, Otsuji Y and Levine RA. The unsaddled annulus – biomechanical culprit in mitral valve prolapse? *Circulation*, 127(7):766-768, Feb 2013. doi: 10.1161/CIRCULATIONAHA.112.000628. URL: http://dx.doi.org/10.1161/CIRCULATIONAHA.112.000628.

Kapadia SR, Leon MB, Makkar RR, Tuzcu EM, Svensson LG, Kodali S, Webb JG, Mack MJ, Douglas PS, Thourani VH, Babaliaros VC, Herrmann HC, Szeto WY, Pichard AD, Williams MR, Fontana GP, Miller DC, Anderson WN, Smith CR, Akin JJ and Davidson MJ. 5-year outcomes of transcatheter aortic valve replacement compared with standard treatments for patients with inoperable aortic stenosis (PARTNER 1): A randomised controlled trial. *The Lancet*, 385(9986): 2485-2491, Jun 2015. doi: 10.1016/S0140-6736(15)60290-2. URL: http://dx.doi.org/10.1016/S0140-6736(15)60290-2.

Karnessis N and Burriesci G. Uniaxial and buckling mechanical response of auxetic cellular tubes. *Smart Materials and Structures*, 22(8):084008, Aug 2013. doi:10.1088/0964-1726/22/8/084008. URL: http://dx.doi.org/10.1088/0964-1726/22/8/084008.

Kaye DM, Byrne M, Alferness C and Power J. Feasibility and short-term efficacy of percutaneous mitral annular reduction for the therapy of heart failure-induced mitral regurgitation. *Circulation*, 108(15):1795-1797, Oct 2003. doi: 10.1161/01.CIR.0000096051.23734.28. URL: http://dx.doi.org/10.1161/01.CIR.0000096051.23734.28.

Kiefer P, Gruenwald F, Kempfert J, Aupperle H, Seeburger J, Mohr FW and Walther T. Crimping may affect the durability of transcatheter valves: An experimental analysis. *Annals of Thoracic Surgery*, 92(1):155-160, Jul 2011. doi: 10.1016/j.athoracsur.2011.03.020. URL: http://dx.doi.org/10.1016/j.athoracsur. 2011.03.020.

Kheradvar A, Assadi R, Falahatpisheh A and Sengupta PP. Assessment of transmitral vortex formation in patients with diastolic dysfunction. *Journal of the American Society of*

Echocardiography. 25(2):220-227, Feb 2012. doi: 10.1016/j.echo.2011.10.003. URL: http://dx.doi.org/10.1016/j.echo.2011.10.003.

Kheradvar A and Gharib M. Influence of ventricular pressure drop on mitral annulus dynamics through the process of vortex ring formation. *Annals of Biomedical Engineering*, 35(12):2050-2064, Dec 2007. doi: 10.1007/s10439-007-9382-y. URL: http://dx.doi.org/10.1007/s10439-007-9382-y.

Kheradvar A and Gharib M. On mitral valve dynamics and its connection to early diastolic flow. *Annals of Biomedical Engineering*, 37(1):1-13, Jan 2009. doi: 10.1007/s10439-008-9588-7. URL: http://dx.doi.org/10.1007/s10439-008-9588-7.

Kheradvar A, Kasalko J, Johnson D and Gharib M. An in vitro study of changing profile heights in mitral bioprostheses and their influence on flow. *ASAIO Journal,* 52(1):34-38, Jan 2006. doi: 10.1097/01.mat.0000191203.09932.8c. URL: http://dx.doi.org/10.1097/01.mat.0000191203.09932.8c.

Kheradvar A and Falahatpisheh. The effects of dynamic saddle annulus and leaflet length on transmitral flow pattern and leaflet stress of a bileaflet bioprosthetic mitral valve. *The Journal of Heart Valve Disease*, 21(2):225-233, Mar 2012.

Kheradvar A, Groves EM, Goergen CJ, Alavi SH, Tranquillo R, Simmons CA, Dasi LP, Grande-Allen KJ, Mofrad MRK, Falahatpisheh A, Griffith B, Baaijens F, Little SH and Canic S. Emerging trends in heart valve engineering: Part II. Novel and standard technologies for aortic valve replacement. *Annals of Biomedical Engineering*, 43(4):844-857, Apr 2015. doi: 10.1007/s10439-014-1191-5. URL: http://dx.doi.org/10.1007/s10439-014-1191-5.

Kheradvar A, Houle H, Pedrizzetti G, Tonti G, Belcik T, Ashraf M, Lindner JR, Gharib M and Sahn D. Echocardiographic particle image velocimetry: A novel technique for quantification of left ventricular blood vorticity pattern. *Journal of the American Society of Echocardiograph*, 23(1):86-94, Jan 2010. doi: 10.1016/j.echo.2009.09.007. URL: http://dx.doi.org/10.1016/j.echo.2009.09.007.

Kheradvar A, Milano M and Gharib M. Correlation between vortex ring formation and mitral annulus dynamics during ventricular rapid filling. *ASAIO Journal*, 53(1):8-16, Jan 2007. doi: 10.1097/01.mat.0000249870.44625.22. URL: http://dx.doi.org/10.1097/01.mat.0000249870.44625.22.

Klabunde RE. Cardiovascular Physiology Concepts Second Edition. Published by Lippincott Williams & Wilkins, 2011. ISBN: 9781451113846.

Körfer R, Schütt U, Minami K, Hartmann D, Körtke H and Lüth JU. Left ventricular function in heart valve surgery: a multidisciplinary challenge. *Journal of Heart valve Disease,* 4(2):S194-S197, 1995.

Krucinski S, Vesely I, Dokainish MA and Campbell G. Numerical simulation of leaflet flexure in bioprosthetic valves mounted on rigid and expansile stents. *Journal of Biomechanics,* 26(8):929-943, Aug 1993. doi: 10.1016/0021-9290(93)90055-J. URL: http://dx.doi.org/10.1016/0021-9290(93)90055-J.

Kuai X, Zhang J, Ren B, Liu F, Gong G and Zeng Y. Stress analysis on stentless quadrileaflet pericardial mitral valve. *Communications in Numerical Methods in Engineering*, 24(9):785-793, Sep 2008. doi: 10.1002/cnm.999. URL: http://dx.doi.org/10.1002/cnm.999.

Kuai XC, Ren BQ, Liu F and Gong GF. Stress analysis on stentless quadrileaflet pericardial mitral valve. *Chinese Journal of Biomedical Engineering*, 25(3):283-287, Jun 2006.

Kunzelman KS, Cochran RP, Verrier ED, Eberhart RC. Anatomic basis for mitral valve modelling. *The Journal of Heart Valve Disease*, 3(5):491-496, 1994.

Lally C, Reid AJ and Prendergast PJ. Elastic behaviour of porcine coronary artery tissue under uniaxial and equibiaxial tension. *Annals of Biomedical Engineering*, 32(10):1355-1364, Oct 2004. doi: 10.1114/B:ABME.0000042224.23927.ce. URL: http://dx.doi.org/10.1114/B:ABME.0000042224.23927.ce.

Lamph S. Regulation of medical devices outside of the European Union. *Journal of the Royal Society of Medicine*, 105(1):S12-21, Apr 2012.

Lancellotti P, Moura L, Pierard LA, Agricola E, Popescu BA, Tribouilloy C, Hagendorff A, Monin JL, Badano L, Zamorano JL, Sicari R, Vahanian A and Roelandt JRTC. European association of echocardiography recommendations for the assessment of valvular regurgitation. Part 2: mitral and tricuspid regurgitation (native valve disease). *European Journal of Echocardiography,* 11(4):307-332, May 2010. doi: 10.1093/ejechocard/jeq031. URL: http://dx.doi.org/10.1093/ejechocard/jeq031.

Laniado S and Yellin EL. Simultaneous recording of mitral valve echogram and transmitral flow. In *The mitral valve, a pluridisciplinary approach*, Kalmanson D (Ed.), Publishing Sciences Graoup Inc., 155-162, 1976. ISBN: 0884161161, 9780884161165.

Lau KD, Diaz V, Scamler P and Burriesci G. Mitral valve dynamics in structural and fluid-structure interaction models. *Medical Engineering and Physics*, 32(9):1057-1064, Nov 2010. doi: 10.1016/j.medengphy.2010.07.008. URL: http://dx.doi.org/10.1016/j.medengphy.2010.07.008.

Lee CSF and Talbot L. A fluid-mechanical study of the closure of heart valves. *Journal of Fluid Mechanics*, 91(1):41-63, Mar 1979. doi: 10.1017/S0022112079000033**.** URL: http://dx.doi.org/10.1017/S0022112079000033.

Leopaldi AM, Vismara R, van Tuijl S, Redaelli A, van de Vosse FN, Fiore GB and Rutten MCM. A novel passive left heart platform for device testing and research. *Medical Engineering and Physics*, 37(4):361-366. Apr 2015. doi: 10.1016/j.medengphy.2015.01.013. URL: http://dx.doi.org/10.1016/j.medengphy. 2015.01.013.

Leverett LB, Hellums JD, Alfrey CP and Lynch EC. Red blood cell damage by shear stress. *Biophysical Journal,* 12(3):257-273, Mar 1972.

Liao YB, Meng Y, Zhao ZG, Zuo ZL, Li YJ, Xiong TY, Cao JY, Xu YN, Feng Y and Chen M. Meta-analysis of the effectiveness and safety of transcatheter aortic valve implantation without balloon predilation. *American Journal of Cardiology,* 117(10):1629-1635, May 2016. doi: 10.1016/j.amjcard.2016.02.036. URL: http://dx.doi.org/10.1016/j.amjcard.2016.02.036.

Liddicoat JR, Mac Neill BD, Gillinov AM, Cohn WE, Chin CH, Prado AD, Pandian NG and Oesterle SN. Percutaneous mitral valve repair: A feasibility study in an ovine model of acute ischemic mitral regurgitation. *Catheterization and Cardiovascular Interventions*, 60(3):410-416, Nov 2003. doi: 10.1002/ccd.10662. URL: http://dx.doi.org/10.1002/ccd.10662.

Lin Z, Pike K, Schlun M, Zipse A and Draper J. Nitinol fatigue life for variable strain amplitude fatigue. *Journal of Materials Engineering and Performance,* 21(12):2628-2632, Dec 2012. doi: 10.1007/s11665-012-0387-9. URL: http://dx.doi.org/10.1007/s11665-012-0387-9.

Lloyd-Jones D, Adams RJ, Brown TM, Carnethon M, Dai S, De Simone G, et al. Heart disease and stroke statistics 2010 update: a report from the American heart association. *Circulation*, 121(7): 948-954, Feb 2010. doi: 10.1161/CIRCULATIONAHA.109.192666. URL: http://dx.doi.org/10.1161/ CIRCULATIONAHA.109.192666.

Lowe GDO. Virchow's triad revisited: Abnormal flow. *Pathophysiology of Haemostasis and Thrombosis*, 33(5-6):455-457, 2003. doi: 10.1159/000083845. URL: http://dx.doi.org/10.1159/000083845.

Lung B, Baron G, Butchart EG, Delahaye F, Gohlke-Bärwolf C, Levang OW, et al. A prospective survey of patients with valvular heart disease in Europe: The euro heart survey on valvular heart disease. *Eur Heart J*, 24(13):1231-1243, Jul 2003. doi: 10.1016/S0195-668X(03)00201-X. URL: http://dx.doi.org/10.1016/S0195-668X(03) 00201-X.

Lung B, Cormier B, Ducimetière P, Porte JM, Nallet O, Michel PL, Acar J and Vahanian A. Immediate results of percutaneous mitral commissurotomy. A predictive model on a series of 1514 patients. *Circulation*, 94(9):2124-2130, 1996.

Lutter G, Lozonschi L, Ebner A, Gallo S, Kall CM, Missov E and de Marchena E. First in human off pump transcatheter mitral valve replacement. *JACC: Cardiovascular Interventions*, 7(9):1077-1078, Sep 2014. doi: 10.1016/j.jcin.2014.06.007. URL: http://dx.doi.org/10.1016/j.jcin.2014.06.007.

Ma L, Tozzi P, Huber CH, Taub S, Gerelle G and von Segesser LK. Double-crowned valved stents for off-pump mitral valve replacement. *European Journal of Cardio-thoracic Surgery*,

28(2):194-198, Aug 2005. doi: 10.1016/j.ejcts.2004.12.068. URL: http://dx.doi.org/10.1016/j.ejcts.2004.12.068.

MacIsaac AI, McDonald IG, Kirsner RL, Graham SA and Tanzar D. Left ventricular energy in mitral regurgitation: a preliminary report. *Australian and New Zealand Journal of Medicine*, 22(5):532-540, Oct 1992.

Mahtabi MJ, Shamsaei N and Mitchell MR. Fatigue of Nitinol: The state-of-the-art and ongoing challenges. *Journal of the mechanical behaviour of biomedical materials,* 50:228-254, Oct 2015. doi: 10.1016/j.jmbbm.2015.06.010. URL: http://dx.doi.org/10.1016/j.jmbbm.2015.06.010.

Maisano F, Alfieri O, Banai S, Buchbinder M, Colombo A, Falk V, Feldman T, Franzen O, Herrmann H, Kar S, Kuck KH, Lutter G, Mack M, Nickenig G, Piazza N, Reisman M, Ruiz CE, Schofer J, Sondergaard L, Stone GW, Taramasso M, Thomas M, Vahanian A, Webb J, Windecker S and Leon MB. The future of transcatheter mitral valve interventions: Competitive or complementary role of repair vs. replacement? *European Heart Journal*, 36(26):1651-1659, 2015. doi: 10.1093/eurheartj/ehv123. URL: http://dx.doi.org/10.1093/eurheartj/ehv123.

Marks Jr. JG, Belsito DV, DeLeo VA, Fowler Jr. JF, Fransway AF, Maibach HI, Mathias CGT, Pratt MD, Rietschel RL, Sherertz EF, Storrs FJ and Taylor JS. North American contact dermatitis group patch-test results, 1998 to 2000. *American Journal of Contact Dermatitis*, 14(2):59-62, Jun 2003.

Masson JB, Kovac J, Schuler G, Ye J, Cheung A, Kapadia S, Tuzcu ME, Kodali S, Leon MB and Webb JG. Transcatheter aortic valve implantation review of the nature, management, and avoidance of procedural complications. *JACC Cardiovascular Interventions,* 2(9):811-820, Sep 2009. doi: 10.1016/j.jcin.2009.07.005. URL: http://dx.doi.org/10.1016/j.jcin.2009.07.005.

Mckay RG. The mansfield scientific aortic valvuloplasty registry - overview of acute hemodynamic-results and procedural complications. *Journal of the American College of Cardiology*, 17(2):485-491, Feb 1991.

Middlemost SJ, Barlow JB, Sussman MJ, van der Donck, Patel A and Manga P. The quadrileaflet mitral valve: follow-up in rheumatic heart disease. *Seminars in thoracic and cardiovascular surgery*, 11(4):183-185, Oct 1999.

Middlemost SJ and Manga P. The stentless quadrileaflet bovine pericardial mitral valve: Echocardiographic assessment. *Journal of Heart Valve Disease*, 8(2):180-185, Mar 1999.

Middlemost SJ and Manga P. The Quattro valve in rheumatic mitral valve disease: Four-year follow up. *Journal of Heart Valve Disease*, 12(6):758-763, Nov 2003.

Middlemost SJ, Patel A, Sussman M and Manga P. The Quattro valve and active infective endocarditis of the mitral valve. *Journal of Heart Valve Disease*, 9(4):544-551, Jul 2000.

Middlemost SJ, Sussman M, Patel A and Manga P. The stentless quadrileaflet bovine pericardial mitral valve: Early clinical results. *Journal of Heart Valve Disease*, 8(2):174-179, Mar 1999.

Mirabel M, Lung B, Baron G, Messika-Zeitoun D, Détaint D, Vanoverschelde JL, Butchart EG, Ravaud P and Vahanian A. What are the characteristics of patients with severe, symptomatic, mitral regurgitation who are denied surgery? *Eur Heart J*. 28(11):1358-1365, Jun 2007. doi: 10.1093/eurheartj/ehm001. URL: http://dx.doi.org/10.1093/eurheartj/ehm001.

Mirnajafi A, Zubiate B and Sacks MS. Effects of cyclic flexural fatigue on porcine bioprosthetic heart valve heterograft biomaterials. *Journal of Biomedical Materials Research Part A*, 94A(1):205-213, Jul 2010. doi: 10.1002/jbm.a.32659. URL: http://dx.doi.org/10.1002/jbm.a.32659.

Modi P, Hassan A and Chitwood WRJr. Minimally invasive mitral valve surgery: a systemic review and meta-analysis. *European Journal of Cardio-thoracic Surgery,* 34(5):943-952, Nov 2008. doi: 10.1016/j.ejcts.2008.07.057. URL: http://dx.doi.org/10.1016/j.ejcts.2008.07.057.

Moraldo M, Cecaro F, Shun-Shin M, Pabari PA, Davies JE, Xu XY, Hughes AD, Manisty C and Francis DP. Evidence-based recommendations for PISA measurements in mitral

regurgitation: Systemic review, clinical and in-vitro study. *International Journal of Cardiology*, 168(2):1220-1228, Sep 2013. doi: 10.1016/j.ijcard.2012.11.059. URL: http://dx.doi.org/10.1016/j.ijcard.2012.11.059.

Mullen MJ, Yap J, Tzamtzis S, Rahmani B, De Mel A, Seifalian A and Burriesci G. The TRISKELE Transcatheter Heart Valve. Euro PCR. Paris, France, 2014.

Navia JL, Brozzi N, Doi K, Garcia M, Al-Ruzeh S, Atik FA, Fukamachii K, Xu XF, Kamohara K, Gonzalez-Stawinski GV and Lytle B. Implantation technique and early echocardiographic performance of newly designed stentless mitral bioprosthesis. *ASAIO Journal*, 56(6):497-503, Nov 2010. doi: 10.1097/MAT.0b013e3181f67e0c. URL: http://dx.doi.org/10.1097/MAT.0b013e3181f67e0c.

Nishimura RA, Otto CM, Bonow RO, Carabello BA, Erwin JP, Guyton RA, O'Gara PT, Ruiz CE, Skubas NJ, Sorajja P, Sundt TM and Thomas JD. 2014 AHA/ACC guideline for the management of patients with valvular heart disease: executive summary. *Journal of the American College of Cardiology*, 63(2):2438–2488, Jun 2014. doi: 10.1016/j.jacc.2014.02.537. URL: http://dx.doi.org/10.1016/j.jacc.2014.02.537.

Nkomo VT, Gardin JM, Skelton TN, Gottdiener JS, Scott CG and Enriquez-Sarano M. Burden of valvular heart diseases: a population-based study. *Lancet*, 368(9540):1005-1011, Sep 2006. doi: 10.1016/S0140-6736(06)69208-8. URL: http://dx.doi.org/10.1016/S0140-6736(06)69208-8.

Osnabrugge RL, Kappetein AP, Reynolds MR and Cohen DJ. Cost-effectiveness of transcatheter valvular interventions: economic challenges. *Eurointervention*, 9(10):S48-54, Sep 2013.

Padala M, Hutchison RA, Croft LR, Jimenez JH, Gorman RC, Gorman III JH, Sacks MS and Yoganathan AP. Saddle shape of mitral annulus reduces systolic strains on the P2 segment of the posterior mitral leaflet. *Annals of Thoracic Surgery*, 88(5):1499-1505, Nov 2009. doi: 10.1016/j.athoracsur.2009.06.042. URL: http://dx.doi.org/10.1016/j.athoracsur.2009.06.042.

Padala M, Sacks MS, Liou SW, Balachandran K, He ZM and Yoganathan AP. Mechanics of the mitral valve strut chordae insertion region. *Journal of Biomechanical Engineering-Transactions of the ASME,* 132(8):081004, Aug 2010. doi: 10.1115/1.4001682. URL: http://dx.doi.org/10.1115/1.4001682.

Paez JMG, Herrero EJ, Sanmartin AC, Millan I, Cordon A, Maestro MM, Rocha A, Arenaz B and Castillo-Olivares JL. Comparison of the mechanical behaviours of biological tissues subjected to uniaxial tensile testing: pig, calf and ostrich pericardium sutured with Gore-Tex. *Biomaterials,* 24(9):1671-1679, Apr 2003. doi: 10.1016/S0142-9612(02)00536-7. URL: http://dx.doi.org/10.1016/S0142-9612(02)00536-7.

Pasipoularides A, Shu M, Shah A, Womack MS and Glower DD. Diastolic right ventricular filling vortex in normal and volume overload states. *American Journal of Physiology – Heart and Circulatory Physiology*, 284(4):H1064-H1072, Apr 2003.

Patterson EA, Howard IC and Thornton MA. A comparative study of linear and nonlinear simulations of the leaflets in a bioprosthetic heart valve during the cardiac cycle. *J. Med. Eng. Technol*, 20(3):95–108, May 1996.

Pedersen HD and Häggström J. Mitral valve prolapse in the dog: a model of mitral valve prolapse in man. *Cardiovascular Research,* 47(2):234-243, Aug 2000. doi: 10.1016/S0008-6363(00)00113-9. URL: http://dx.doi.org/10.1016/S0008-6363(00)00113-9.

Pendrizzetti G, Domenichini F and Giovanni T. On the left ventricular vortex reversal after mitral valve replacement. *Annals of Biomedical Engineering*, 38(3):769-773, Mar 2010. doi: 10.1007/s10439-010-9928-2. URL: http://dx.doi.org/10.1007/ s10439-010-9928-2.

Peskin CS and McQueen DM. A computer test chamber for the design and evaluation of prosthetic mitral valves. *Proc. AAMI*, 16, 80, 1981.

Preston-Maher GL, Torii R and Burriesci G. A technical review of minimally invasive mitral valve replacements. *Cardiovascular Engineering and Technology*, 6(2):174-184, Jun 2015. doi: 10.1007/s13239-014-0203-9. URL: http://dx.doi.org/10.1007/ s13239-014-0203-9.

Querzoli G, Fortini S and Cenedese A. Effect of the prosthetic mitral valve on vortex dynamics and turbulence of the left ventricular flow. *Physics of fluids*, 22(4):041901, Apr 2010. doi: 10.1063/1.3371720. URL: http://dx.doi.org/10.1063/1.3371720.

Rabbah JPM, Saikrishnan N, Siefert AW, Santhanakrishnan A and Yoganathan AP. Mechanics of health and functionally diseased mitral valves: A critical review. *Journal of Biomechanical Engineering*, 135(2):021009, 2013. doi: 10.1115/1.4023238. URL: http://dx.doi.org/10.1115/1.4023238.

Rabkin SW and Hsu PH. Mathematical and mechanical modelling of stress-strain relationship of pericardium. *American Journal of Physiology*, 229(4):896-900, 1975.

Rahmani B, Burriesci G, Mullen M, Seifalian A, Tzamtzis S and Yap J. A new generation transcatheter heart valve with a novel nanocomposite material and fully retrievable design. *JACC: Cardiovascular Interventions*, 60(17):B34-B34, Oct 2013.

Rahmani B, Tzamtzis S, Sherdian R, Mullen MJ, Yap J, Seifalian AM and Burriesci G. A new transcatheter heart valve concept (the TRISKELE): feasibility in an acute preclinical model. *EuroIntervention*, 12(7):148, Sep 2016. doi: 10.4244/EIJV12I7A148. URL: http://dx.doi.org/10.4244/EIJV12I7A148.

Rahmani B, Tzamtzis S, Ghanbari H, Burriesci G and Seifalian AM. Manufacturing and hydrodynamic assessment of a novel aortic valve made of a new nanocomposite polymer. *Journal of Biomechanics,* 45(7):1205-1211, Apr 2012. doi: 10.1016/j.jbiomech.2012.01.046. URL: http://dx.doi.org/10.1016/j.jbiomech. 2012.01.046.

Recusani F, Bargiggia GS, Yoganathan AP, Raisaro A, Valdes-Cruz LM, Sung HW, Bertucci C, Gallati M, Moises VA, Simpson IA, Tronconi L and Sahn DJ. A new method for quantification of regurgitant flow-rate using color doppler flow imaging of the flow convergence region proximal to a discrete orifice: An in vitro study. *Circulation*, 83(2):594-604, Feb 1991.

Reul H and Talkukder N. Heart valve mechanics. In *Quantitative cardiovascular studies*, Hwang NHC, Gross DR and Patel DJ (Eds.), Clinical and Research Applications of Engineering Principles. University Park Press, 527-564, 1979.

Reul H, Talukder N and Muller EW. Fluid mechanics of the natural mitral valve. *Journal of Biomechanics*, 14(5):361-372, 1981. doi: 10.1016/0021-9290(81)90046-4. URL: http://dx.doi.org/10.1016/0021-9290(81)90046-4.

Ribeiro HB, Doyle D, Urena M, Allende R, Amat-Santos I, Pasian S, Bilodeau S, Mohammadi S, Paradis JM, Delarochelliere R, Rodes-Cabau J and Dumont E. Transapical mitral implantation of a balloon-expandable valve in native mitral valve stenosis in a patient with previous transcatheter aortic valve replacement. *JACC: Cardiovascular Interventions*, 7(10):e137-e139, Oct 2014. doi: 10.1016/j.jcin.2014.02.024. URL: http://dx.doi.org/10.1016/j.jcin.2014.02.024.

Rodes-Cabau J, Dumont E, Boone RH, Larose E, Bagur R, Gurvitch R, Bedard F, Doyle D, De Larochelliere R, Jayasuria C, Villeneuve J, Marrero A, Cote M, Pibarot P and Webb JG. Cerebral embolism following transcatheter aortic valve implantation: comparison of transfemoral and transapical approaches. *Journal of the American College of Cardiology*, 57(1):18-28, Dec 2010. doi: 10.1016/j.jacc.2010.07.036. URL: http://dx.doi.org/10.1016/j.jacc.2010.07.036.

Rokicki R, Hryniewicz T, Pulletikurthi C, Rokosz K and Munroe N. Towards a better corrosion resistance and biocompatibility improvement of nitinol medical devices. *Journal of Materials Engineering and Performance*, 24(4):1634-1640, 2015. doi: 10.1007/s11665-015-1429-x. URL: http://dx.doi.org/10.1007/s11665-015-1429-x.

Roques F, Nashef SA, Michel P, Gauducheau E, de Vincentiis C, Baudet E, Cortina J, David M, Faichney A, Gavrielle F, Gams E, Harjula A, Jones MT, Pinna Pintor P, Salamon R and Thulin L. Risk factors and outcome in European cardiac surgery: analysis of the EuroSCORE multinational database of 19030 patients. *European Journal of Cardio-thoracic Surgery*, 15(6):816-823, Jun 1999. doi: 10.1016/S1010-7940(99)00106-2. URL: http://dx.doi.org/10.1016/S1010-7940(99)00106-2.

Sacks MS and Yoganathan AP. Heart valve function: a biomechanical perspective. *Philosophical transactions of the royal society*, 362:1369-1391, Jun 2007. doi: 10.1098/rstb.2007.2122. URL: http://dx.doi.org/10.1098/rstb.2007.2122.

Sastry SSS. Accepted practices in practical finite element analysis of structures. NAFEMS. 2010.

Scarpa F, Smith FC, Chambers B and Burriesci G. Mechanical and electromagnetic behaviour of auxetic honeycomb structures. *Aeronautical Journal*, 107(1069):175-183, Mar 2003.

Schlun M, Zipse A, Dreher G and Rebelo N. Effects of cyclic loading on the uniaxial behaviour of nitinol. *Journal of Materials Engineering and Performance*, 20(4-5):684-687, Jul 2011. doi: 10.1007/s11665-010-9790-2. URL: http://dx.doi.org/10.1007/s11665-010-9790-2.

Sengupta PP, Pedrizzetti G, Kilner PJ, Kheradvar A, Ebbers T, Tonti G, Fraser AG and Narula J. Emerging trends in CV flow visualization. *JACC: Cardiovascular Imaging*, 5(3):305-316, Mar 2012. doi: 10.1016/j.jcmg.2012.01.003. URL: http://dx.doi/org/10.1016/j.jcmg.2012.01.003.

Shah SR and Vyavahare NR. The effect of glycosaminoglycan stabilization on tissue buckling in bioprosthetic heart valves. *Biomaterials*, 29(11):1645–1653, Apr 2008. doi: 10.1016/j.biomaterials.2007.12.009. URL: http://dx.doi.org/10.1016/j.biomaterials.2007.12.009.

Siminiak T, Firek L, Jerzykowska O, Kałmucki P, Wołoszyn M, Smuszkiewicz P and Link R. Percutaneous valve repair for mitral regurgitation using the Carillon Mitral Contour System. Description of the method and case report. *Kardiologia Polska,* 65(3):272-278, 2007.

Simenauer PA and Chwirut DJ. Preliminary results of an interlaboratory comparison of prosthetic heart valve performance. Sixth Southern Biomedical Engineering Conference. Regent Hotel Dallas Texas. MN Monograph. October 23-24 1987.

Sinning JM, Mellert F, Schiller W, Wetz A, Nickenig G and Hammerstingl C. Transcatheter mitral valve replacement using a balloon-expandable prosthesis in a patient with calcified native mitral valve stenosis. *European Heart Journal,* 34(33):2609, Sep 2013. doi: 10.1093/eurheartj/eht254. URL: http://dx.doi.org/10.1093/eurheartj/eht254.

Smith FC, Scarpa F and Burriesci G. Simultaneous optimization of the electromagnetic and mechanical properties of honeycomb materials. *Smart Structures and Materials 2002: Smart Structures and Integrated Systems*, 4701:582-591, 2002. doi: 10.1117/12.474693. URL: http://dx.doi.org/10.1117/12.474693.

Smuts AN, Blaine DC, Scheffer C, Weich H, Doubell AF and Dellimore KH. Application of finite element analysis to the design of tissue leaflets for a percutaneous aortic valve. *Journal of the Mechanical Behaviour of Biomedical Materials*, 4(1):85-98, 2011. doi: 10.1016/j.jmbbm.2010.09.009. URL: http://dx.doi.org/10.1016/ j.jmbbm.2010.09.009.

Sondergaard L. Transcatheter Mitral Valve Implantation: CardiAQ. Presented at: TCT 2012, Miami, Florida, US, 22-26 Oct 2012.

Sondergaard L, Brooks M, Ihlemann N, Jonsson A, Holme S, Tang M, Terp K and Quadri A. Transcatheter mitral valve implantation via transapical approach an early experience. *European Journal of Cardio-Thoracic Surgery*, 48(6):873-878, 2015.

Steinberg DH, Castillo-Sang M and Powers ER. Advances in transcatheter valve therapies. *Journal of Cardiovascular Translational Research*, 7(4):375-386, Jun 2014. doi: 10.1007/s12265-014-9561-9. URL: http://dx.doi.org/10.1007/s12265-014-9561-9.

Stoeckel D, Pelton A and Duerig T. 2008. Self-expanding Nitinol stents for the treatment of vascular disease. *Shape Memory Alloys for Biomedical Applications*. Woodhead Publishing Limited. Chapter 10, pp. 237-256. ISBN: 1845695240, 9781845695248.

Sturla F, Ronzoni M, Vitali M, Dimasi A, Vismara R, Preston-Maher G, Burriesci G, Votta E and Redaelli A. Impact of different aortic valve calcification patterns on the outcome of transcatheter aortic valve implantation: a finite element study. *Journal of Biomechanics*, 49(12):2520-2530, Aug 2016. doi: 10.1016/j.jbiomech.2016.03.036. URL: http://dx.doi.org/10.1016/j.jbiomech. 2016.03.036.

Tsakiris AG, Gordon DA, Mathieu Y and Lipton I. Time-motion of both mitral leaflets early in diastole. In *The mitral valve, A pluridisciplinary approach*, Kalmanson D (Ed.), Publishing Science Group Inc., 27-32, 1976.

Tang GHL, Lansman SL, Cohen M, Spielvogel D, Cuomo L, Ahmad H and Dutta T. Transcatheter aortic valve replacement: current developments, ongoing issues, future outlook. *Cardiology in Review*, 21(2):55-76, Mar 2013. doi: 10.1097/CRD.0b013e318283bb3d. URL: http://dx.doi.org/10.1097/ CRD.0b013 e318283bb3d.

Taramasso M, Cioni M, Giacomini A, Michev I, Godino C, Montorfano M, Colombo A, Alfieri O and Masisano F. Emerging approaches of transcatheter valve repair/insertion. *Cardiology Research and Practice*, 1(1):540749, 2010. doi: 10.4061/2010/540749. URL: http://dx.doi.org/10.4061/2010/540749Document.

Teien DE, Jones M, Shiota T, Yamada I, Frithiof D and Sahn DJ. Left ventricular stroke work in mitral regurgitation: An animal experimental study. *Journal of Heart Valve Disease,* 6(6):613-620, Nov 1997.

Thubrikar MJ, Deck JD, Aouad J and Nolan SP. Role of mechanical stress in calcification of aortic bioprosthetic valves. *Journal of Thoracic and Cardiovascular Surgery,* 86(1):115-125, 1983.

Timek TA, Green GR, Tibayan FA, Lai DT, Rodriguez F, Liang D, Daughters GT, Ingels Jr NB and Miller DC. Aorto-mitral annular dynamics. *Annals of Thoracic Surgery,* 76(6):1944-1950, Dec 2003. doi: 10.1016/S0003-4975(03)01078-6. URL: http://dx.doi.org/10.1016/S0003-4975(03)01078-6.

Toninato R, Salmon J, Susin FM, Ducci A and Burriesci G. Physiological vortices in the sinuses of Valsalva: An *in vitro* approach for bio-prosthetic valves. *Journal of Biomechanics,* May 2016. doi: 10.1016/j.jbiomech.2016.05.027. URL: http://dx.doi.org/10.1016 /j.jbiomech.2016.05.027.

Trowbridge EA, Black MM and Daniel CL. The mechanical response of glutaraldehyde-fixed bovine pericardium to uniaxial load. *Journal of Materials Science*, 20(1):114-140, 1985. doi: 10.1007/BF00555905. URL: http://dx.doi.org/10.1007/BF00555905.

Tzamtzis S, Viquerat J, Yap J, Mullen MJ and Burriesci G. Numerical analysis of the radial force produced by the Medtronic-CoreValve and Edwards-SPAIEN after transcatheter aortic valve implantation (TAVI). *Medical Engineering and Physics*, 35(1):125-130, Jan 2013. doi: 10.1016/j.medengphy.2012.04.009. URL: http://dx.doi.org/10.1016/j.medengphy.2012.04.009.

US Census Bureau. Statistical Abstract of the US: 2006, Table 12.

Vahanian A and Palacios IF. Percutaneous approaches to valvular disease. *Circulation,* 109(13):1572-1579, Apr 2004. doi: 10.1161/01.CIR.0000124794.1680.E3. URL: http://dx.doi.org/10.1161/ 01.CIR.0000124794.1680.E3.

Van Mieghem NM, Piazza N, Anderson RH, Tzikas A, Nieman K, De Laat LE, McGhie JS, Geleijnse ML, Feldman T, Serruys PW and de Jaegere PP. Anatomy of the mitral Valvular complex and its implications for transcatheter interventions for mitral regurgitation. *Journal of the American College of Cardiology*, 56(8):617-626, Aug 2010. doi: 10.1016/j.jacc.2010.04.030. URL: http://dx.doi.org/10.1016/ j.jacc.2010.04.030.

Vesely I, Boughner D and Song T. Tissue buckling as a mechanism of bioprosthetic valve failure. *Annals of Thoracic Surgery,* 46(3):302–308, 1988.

Votta E, Caiani E, Veronesi F, Soncini M, Montevecchi FM and Redaelli A. Mitral valve finite-element modelling from ultrasound data: a pilot study for a new approach to understand mitral function and clinical scenarios. *Philosophical Transactions of the Royal Society A-Mathematical Physical and Engineering Sciences*, 366(1879):3411-3434, Sep 2008.

Vyavahare N, Ogle M, Choen FJ, Zand R, Gloechner DC, Sacks M and Levy RJ. Mechanisms of bioprosthetic heart valve failure: Fatigue causes collagen denaturation and glycosaminoglycan loss. *Journal of Biomedical Materials Research*, 46(1):44-50, 1999. doi: 10.1002/(SICI)1097-4636(199907)46:1<44::AID-JBM5>3.0.CO;2-D. URL: http://dx.doi.org /10.1002/(SICI)1097-4636(199907)46:1<44::AID-JBM5>3.0.CO;2-D.

Walker DK, Scotten LN, Hewgill DE, Racca RG and Brownlee RT. Development and in vitro assessment of a new two-leaflet replacement heart valve designed using computer-generated bubble surfaces. *Medical & Biological Engineering & Computing*, 21(1):31-38, Jan 1983. doi: 10.1007/BF02446403. URL: http://dx.doi.org/10.1007/BF02446403.

Walther T, Lehmann S, Falk V, Walther C, Doll N, Rastan A, Metz S, Schneider J, Gummert J and Mohr FW. Midterm results after stentless mitral valve replacement. *Circulation*, 108(10):II85-II89, Sep 2003.

Walther T, Walther C, Falk V, Kruger M, Dagge A, Diegeler A, Autschbach R and Mohr FW. Stentless mitral valve replacement using the quattro valve. *Seminars in thoracic and cardiovascular surgery*, 11(4):186-190, Oct 1999.

Walther T, Walther C, Falk V, Langebartels G, Kruger M, Dagge A, Diegeler A, Autschbach R and Mohr FW. Quadrileaflet stentless mitral valve replacement. *Thoracic and Cardiovascular Surgeon*, 47(6):357-360, Dec 1999.

Wang JG, Kuai XC, Ren BQ, Gong GF and Zhou XM. Reduced leaflet stress in the stentless quadrileaflet mitral valve: A finite element model. *PLoS ONE*, 8(7):e67683, Jul 2013. doi: 10.1371/journal.pone.0067683. URL: http://dx.doi.org/10.1371/journal.pone.0067683.

Wang Q and Sun W. Finite element modelling of mitral valve dynamics deformation using patient-specific multi-slice computed tomography scans. *Annals of Biomedical Engineering*, 41(1):142-153, 2013. doi: 10.1007/s10439-012-0620-6. URL: http://dx.doi.org/10.1007/s10439-012-0620-6.

Wertman B, Azarbal B, Riedl M and Tobis J. Adverse events associated with nickel allergy in patients undergoing percutaneous atrial septal defect or patent foramen ovale closure. *Journal of the American College of Cardiology*, 47(6):1226-1227, Mar 2006. doi: 10.1016/j.jacc.2005.12.017. URL: http://dx.doi.org/10.1016/j.jacc. 2005.12.017.

Wood S. Early results for transcatheter mitral valve replacement reveal complications and challenges for the long road ahead. Cardiovascular Research Foundation, website: www.tctmd.com, accessed 13/06/16.

Yoganathan AP and Travis BR. Fluid dynamics of prosthetic valves. In: Otto CM, ed. The practice of clinical echocardiography. 2nd ed. Philadelphia: WB Saunders; 2002:50-524. ISBN: 0721692044, 9780721692043.

Yokoyama Y, Kawaguchi O, Shinshi T, Steinseifer U and Takatani S. A new pulse duplicator with a passive fill ventricle for analysis of cardiac dynamics. *Journal of Artificial Organs*, 13(4):189-196, Dec 2010. doi: 10.1007/s10047-010-0518-8. URL: http://dx.doi.org/10.1007/s10047-010-0518-8.

Zajarias A and Cribier AG. Outcomes and safety of percutaneous aortic valve replacement. *Journal of the American College of Cardiology,* 53(20):1829-1836, May 2009. doi: 10.1016/j.jacc.2008.11.059. URL: http://dx.doi.org/10.1016/ j.jacc.2008.11.059.

Zioupos P and Barbenel JC. Mechanics of native bovine pericardium II A structure based model for the anisotropic mechanical behaviour of the tissue. *Biomaterials,* 15(5):374-382, Apr 1994. doi: 10.1016/0142-9612(94)90250-X. URL: http://dx.doi.org/10.1016/0142-9612(94)90250-X.

Zioupos P, Barbenel JC and Fisher J. Anisotropic elasticity and strength of glutaraldehyde fixed bovine pericardium for use in pericardial bioprosthetic valves. *Journal of Biomedical Materials Research*, 28(1):49-57, Jan 1994. doi: 10.1002/jbm.820280107. URL: http://dx.doi.org/10.1002/jbm.820280107.

Zou Y, Ferrari E and von Segesser LK. Off-pump transapical mitral valve-in-ring implantation. *European Journal of Cardio-thoracic Surgery,* 43(4):849-855, Apr 2013. doi: 10.1093/ejcts/ezs407. URL: http://dx.doi.org/10.1093/ejcts/ezs407.

Standards

ASTM INTERNATIONAL, Standard Test Method for Tension Testing of Nickel-Titanium Superelastic Materials. Designation: F 2516-07$^{\epsilon 2}$.

BSI, *British Standards BS EN ISO 5840:2009*, Cardiovascular implants – Cardiac valve prostheses (ISO 5840:2005), ISC 11.040.40.

BSI, *British Standard BS EN ISO 11137-1:2006,* Sterilization of health care products – radiation – Part 1: requirements for development validation and routine control of a sterilization process for medical devices, ISC 11.080.1.

BSI, *British Standards BS EN 12006-2:1998+A1:2009*, Non-active surgical implants – particular requirements for cardiac and vascular implants – Part 2: Vascular prostheses including cardiac valve conduits, ICS 11.040.40.

BSI, *British Standard BS EN ISO 14708*:2010, Implants for surgery, active implantable medical devices; Part 5. 2010: Particular requirements for circulatory support devices; section 6.106.2.2, Fluid dynamic analysis, p.8.

ISO, *International Standard ISO 5840-3:2013*, Cardiovascular implants – cardiac valve prostheses. Part 3: Heart valve substitutes implanted by transcatheter techniques.

ISO, *International Standard ISO 10993-1:2003,* Biological evaluation of medical devices – part 1: evaluation and testing, third edition.

U.S. Department of Health and Human Services, Food and Drug Administration, Center for Devices and Radiological Health, Circulatory Support and Prosthetic Devices Branch, Division of Cardiovascular Devices, Office of Device Evaluation. Draft guidance for industry and FDA staff. Heart valves – investigational device exemption (IDA) and premarket approval (PMA) applications. *DRAFT GUIDANCE.* 2010.

Appendix A

```
% This script analyses the data from a cyclic tensile test, with ten
% conditioning cycles and ten main cycles.
% The excel file should contain three columns; cycle number, nominal
strain
% standard force in columns A, B and C respectively, with no titles.
close all;
clear all;
%% Reading in the data and predefined variables
% input file name
str = input('Please enter the name of your excel file:  ' ,'s');
test_data = xlsread(str);
test_data_for_editing = test_data;
area = input('Please enter the cross sectional area of your specimen
in millimetres squared:  ');
original_length = input('Please enter the original length of the
gauge section your specimen in millimetres:  ');
% Input initial estimates for the parameters of the equation
display('Your data will be described with the following equation:
stress = Aln(1 + exp(B*strain - C)) + D*strain)')
A = input('Please enter an initial estimate for parameter A:  ');
B = input('Please enter an initial estimate for parameter B:  ');
C = input('Please enter an initial estimate for parameter C:  ');
D = input('Please enter an initial estimate for parameter D:  ');
%  Definition of matrices and creation of separate matrices for
separate      % cycles. Define two matrices for the data that is
associated with the     % zeroth cycle.
cycle_zero_start = zeros(length(test_data), 2);
cycle_zero_middle = zeros(length(test_data), 2);
% Define ten matrices, one for each conditioning cycle.
cycle_conditioning_1 = zeros(length(test_data), 2);
cycle_conditioning_2 = zeros(length(test_data), 2);
cycle_conditioning_3 = zeros(length(test_data), 2);
cycle_conditioning_4 = zeros(length(test_data), 2);
cycle_conditioning_5 = zeros(length(test_data), 2);
cycle_conditioning_6 = zeros(length(test_data), 2);
cycle_conditioning_7 = zeros(length(test_data), 2);
cycle_conditioning_8 = zeros(length(test_data), 2);
cycle_conditioning_9 = zeros(length(test_data), 2);
cycle_conditioning_10 = zeros(length(test_data), 2);
% Define ten matrices, one for each main cycle.
cycle_1 = zeros(length(test_data), 2);
cycle_2 = zeros(length(test_data), 2);
cycle_3 = zeros(length(test_data), 2);
cycle_4 = zeros(length(test_data), 2);
cycle_5 = zeros(length(test_data), 2);
cycle_6 = zeros(length(test_data), 2);
cycle_7 = zeros(length(test_data), 2);
cycle_8 = zeros(length(test_data), 2);
cycle_9 = zeros(length(test_data), 2);
cycle_10 = zeros(length(test_data), 2);
% Fill in the first row of the zeroth cycle.
cycle_zero_start(1,1:2)= test_data_for_editing(1,2:3);
% Remove this row from the test data. It has now been filed in the
correct
% place.
```

```
test_data_for_editing = removerows(test_data_for_editing, 1);
% Go through each row adding it to the zeroth cycle if there is a
zero in
% the first column.
% Fill the cycle zero start matrix
% This i denotes the row number of the cycle_zero_start matrix
i = 1;
while ((test_data_for_editing(1,1)) == 0)
cycle_zero_start(i+1,1:2)= test_data_for_editing(1,2:3);
  test_data_for_editing = removerows(test_data_for_editing, 1);
  i=i+1;
end
% Fill the conditioning cycle 1 matrix
i = 1;
while ((test_data_for_editing(1,1)) == 1)
 cycle_conditioning_1(i,1:2)= test_data_for_editing(1,2:3);
 test_data_for_editing = removerows(test_data_for_editing, 1);
 i=i+1;
end
% Fill the conditioning cycle 2 matrix
i = 1;
while ((test_data_for_editing(1,1)) == 2)
 cycle_conditioning_2(i,1:2)= test_data_for_editing(1,2:3);
 test_data_for_editing = removerows(test_data_for_editing, 1);
 i=i+1;
end
% Fill the conditioning cycle 3 matrix
i = 1;
while ((test_data_for_editing(1,1)) == 3)
 cycle_conditioning_3(i,1:2)= test_data_for_editing(1,2:3);
 test_data_for_editing = removerows(test_data_for_editing, 1);
 i=i+1;
end
% Fill the conditioning cycle 4 matrix
i = 1;
while ((test_data_for_editing(1,1)) == 4)
 cycle_conditioning_4(i,1:2)= test_data_for_editing(1,2:3);
 test_data_for_editing = removerows(test_data_for_editing, 1);
 i=i+1;
end
% Fill the conditioning cycle 5 matrix
i = 1;
while ((test_data_for_editing(1,1)) == 5)
 cycle_conditioning_5(i,1:2)= test_data_for_editing(1,2:3);
 test_data_for_editing = removerows(test_data_for_editing, 1);
 i=i+1;
end
% Fill the conditioning cycle 6 matrix
i = 1;
while ((test_data_for_editing(1,1)) == 6)
 cycle_conditioning_6(i,1:2)= test_data_for_editing(1,2:3);
 test_data_for_editing = removerows(test_data_for_editing, 1);
 i=i+1
end
% Fill the conditioning cycle 7 matrix
i = 1;
while ((test_data_for_editing(1,1)) == 7)
 cycle_conditioning_7(i,1:2)= test_data_for_editing(1,2:3);
 test_data_for_editing = removerows(test_data_for_editing, 1);
```

```
 i=i+1;
end
% Fill the conditioning cycle 8 matrix
i = 1;
while ((test_data_for_editing(1,1)) == 8)
 cycle_conditioning_8(i,1:2)= test_data_for_editing(1,2:3);
 test_data_for_editing = removerows(test_data_for_editing, 1);
 i=i+1;
end
% Fill the conditioning cycle 9 matrix
i = 1;
while ((test_data_for_editing(1,1)) == 9)
 cycle_conditioning_9(i,1:2)= test_data_for_editing(1,2:3);
 test_data_for_editing = removerows(test_data_for_editing, 1);
 i=i+1;
end
% Fill the conditioning cycle 10 matrix
i = 1;
while ((test_data_for_editing(1,1)) == 10)
 cycle_conditioning_10(i,1:2)= test_data_for_editing(1,2:3);
 test_data_for_editing = removerows(test_data_for_editing, 1);
 i=i+1;
end
% Fill the cycle zero middle
i = 1;
while ((test_data_for_editing(1,1)) == 0)
 cycle_zero_middle(i,1:2)= test_data_for_editing(1,2:3);
 test_data_for_editing = removerows(test_data_for_editing, 1);
 i=i+1;
end
% Fill the main cycle 1 matrix
i = 1;
while ((test_data_for_editing(1,1)) == 1)
 cycle_1(i,1:2)= test_data_for_editing(1,2:3);
 test_data_for_editing = removerows(test_data_for_editing, 1);
 i=i+1;
end
% Fill the main cycle 2 matrix
i = 1;
while ((test_data_for_editing(1,1)) == 2)
 cycle_2(i,1:2)= test_data_for_editing(1,2:3);
 test_data_for_editing = removerows(test_data_for_editing, 1);
 i=i+1;
end
% Fill the main cycle 3 matrix
i = 1;
while ((test_data_for_editing(1,1)) == 3)
 cycle_3(i,1:2)= test_data_for_editing(1,2:3);
 test_data_for_editing = removerows(test_data_for_editing, 1);
 i=i+1;
end
% Fill the main cycle 4 matrix
i = 1;
while ((test_data_for_editing(1,1)) == 4)
 cycle_4(i,1:2)= test_data_for_editing(1,2:3);
 test_data_for_editing = removerows(test_data_for_editing, 1);
 i=i+1;
end
% Fill the main cycle 5 matrix
```

```
i = 1;
while ((test_data_for_editing(1,1)) == 5)
 cycle_5(i,1:2)= test_data_for_editing(1,2:3);
 test_data_for_editing = removerows(test_data_for_editing, 1);
 i=i+1;
end
% Fill the main cycle 6 matrix
i = 1;
while ((test_data_for_editing(1,1)) == 6)
 cycle_6(i,1:2)= test_data_for_editing(1,2:3);
 test_data_for_editing = removerows(test_data_for_editing, 1);
 i=i+1;
end
% Fill the main cycle 7 matrix
i = 1;
while ((test_data_for_editing(1,1)) == 7)
 cycle_7(i,1:2)= test_data_for_editing(1,2:3);
 test_data_for_editing = removerows(test_data_for_editing, 1);
 i=i+1;
end
% Fill the main cycle 8 matrix
i = 1;
while ((test_data_for_editing(1,1)) == 8)
 cycle_8(i,1:2)= test_data_for_editing(1,2:3);
 test_data_for_editing = removerows(test_data_for_editing, 1);
 i=i+1;
end
% Fill the main cycle 9 matrix
i = 1;
while ((test_data_for_editing(1,1)) == 9)
 cycle_9(i,1:2)= test_data_for_editing(1,2:3);
 test_data_for_editing = removerows(test_data_for_editing, 1);
 i=i+1;
end
% Fill the main cycle 10 matrix
% This is what is left in the test_data_for_editing.
 cycle_10(1:(length(test_data_for_editing)),1:2)=
test_data_for_editing(:,2:3);
%% Extract just the loading data from the main cycles
% The end of the loading will occur at the maximum value of force,
which
% is the maximum value in column 2.
% Loading data for cycle  1
[num, idx] = max(cycle_1(:,2));
loading_cycle_1(1:idx,:) = cycle_1(1:idx,:);
% Loading data for cycle  2
[num, idx] = max(cycle_2(:,2));
loading_cycle_2(1:idx,:) = cycle_2(1:idx,:);
% Loading data for cycle  3
[num, idx] = max(cycle_3(:,2));
loading_cycle_3(1:idx,:) = cycle_3(1:idx,:);
% Loading data for cycle  4
[num, idx] = max(cycle_4(:,2));
loading_cycle_4(1:idx,:) = cycle_4(1:idx,:);
% Loading data for cycle  5
[num, idx] = max(cycle_5(:,2));
loading_cycle_5(1:idx,:) = cycle_5(1:idx,:);
% Loading data for cycle  6
[num, idx] = max(cycle_6(:,2));
```

```
loading_cycle_6(1:idx,:) = cycle_6(1:idx,:);
% Loading data for cycle  7
[num, idx] = max(cycle_7(:,2));
loading_cycle_7(1:idx,:) = cycle_7(1:idx,:);
% Loading data for cycle  8
[num, idx] = max(cycle_8(:,2));
loading_cycle_8(1:idx,:) = cycle_8(1:idx,:);
% Loading data for cycle  9
[num, idx] = max(cycle_9(:,2));
loading_cycle_9(1:idx,:) = cycle_9(1:idx,:);
% Loading data for cycle  10
[num, idx] = max(cycle_1(:,2));
loading_cycle_10(1:idx,:) = cycle_10(1:idx,:);
%% Smoothing the force data points to remove noise
% Only need to smooth the force data.
% Smoothing loading cycle 1 data
loading_cycle_1_smooth = loading_cycle_1;
loading_cycle_1_smooth(:,2)   =   smooth(loading_cycle_1_smooth(:,2),
10);
% Smoothing loading cycle 2 data
loading_cycle_2_smooth = loading_cycle_2;
loading_cycle_2_smooth(:,2)   =   smooth(loading_cycle_2_smooth(:,2),
10);
% Smoothing loading cycle 3 data
loading_cycle_3_smooth = loading_cycle_3;
loading_cycle_3_smooth(:,2)   =   smooth(loading_cycle_3_smooth(:,2),
10);
% Smoothing loading cycle 4 data
loading_cycle_4_smooth = loading_cycle_4;
loading_cycle_4_smooth(:,2)   =   smooth(loading_cycle_4_smooth(:,2),
10);
% Smoothing loading cycle 5 data
loading_cycle_5_smooth = loading_cycle_5;
loading_cycle_5_smooth(:,2)   =   smooth(loading_cycle_5_smooth(:,2),
10);
% Smoothing loading cycle 6 data
loading_cycle_6_smooth = loading_cycle_6;
loading_cycle_6_smooth(:,2)   =   smooth(loading_cycle_6_smooth(:,2),
10);
% Smoothing loading cycle 7 data
loading_cycle_7_smooth = loading_cycle_7;
loading_cycle_7_smooth(:,2)   =   smooth(loading_cycle_7_smooth(:,2),
10);
% Smoothing loading cycle 8 data
loading_cycle_8_smooth = loading_cycle_8;
loading_cycle_8_smooth(:,2)   =   smooth(loading_cycle_8_smooth(:,2),
10);
% Smoothing loading cycle 9 data
loading_cycle_9_smooth = loading_cycle_9;
loading_cycle_9_smooth(:,2)   =   smooth(loading_cycle_9_smooth(:,2),
10);
% Smoothing loading cycle 10 data
loading_cycle_10_smooth = loading_cycle_10;
loading_cycle_10_smooth(:,2)  =  smooth(loading_cycle_10_smooth(:,2),
10);
%% Zero the smoothed loading data
% Zeroing the data for cycle 1
for i=1:length(loading_cycle_1_smooth)
% Zero extension data
```

```
loading_cycle_1_smooth_zeroed  (i,1)  =  loading_cycle_1_smooth(i,1)-
loading_cycle_1_smooth(1,1);
% Zero force data
loading_cycle_1_smooth_zeroed  (i,2)  =  loading_cycle_1_smooth(i,2)-
loading_cycle_1_smooth(1,2);
end
% Zeroing the data for cycle 2
for i=1:length(loading_cycle_2_smooth)
% Zero extension data
loading_cycle_2_smooth_zeroed  (i,1)  =  loading_cycle_2_smooth(i,1)-
loading_cycle_2_smooth(1,1);
% Zero force data
loading_cycle_2_smooth_zeroed  (i,2)  =  loading_cycle_2_smooth(i,2)-
loading_cycle_2_smooth(1,2);
end
% Zeroing the data for cycle 3
for i=1:length(loading_cycle_3_smooth)
% Zero extension data
loading_cycle_3_smooth_zeroed  (i,1)  =  loading_cycle_3_smooth(i,1)-
loading_cycle_3_smooth(1,1);
% Zero force data
loading_cycle_3_smooth_zeroed  (i,2)  =  loading_cycle_3_smooth(i,2)-
loading_cycle_3_smooth(1,2);
end
% Zeroing the data for cycle 4
for i=1:length(loading_cycle_4_smooth)
% Zero extension data
loading_cycle_4_smooth_zeroed  (i,1)  =  loading_cycle_4_smooth(i,1)-
loading_cycle_4_smooth(1,1);
% Zero force data
loading_cycle_4_smooth_zeroed  (i,2)  =  loading_cycle_4_smooth(i,2)-
loading_cycle_4_smooth(1,2);
end
% Zeroing the data for cycle 5
for i=1:length(loading_cycle_5_smooth)
% Zero extension data
loading_cycle_5_smooth_zeroed  (i,1)  =  loading_cycle_5_smooth(i,1)-
loading_cycle_5_smooth(1,1);
% Zero force data
loading_cycle_5_smooth_zeroed  (i,2)  =  loading_cycle_5_smooth(i,2)-
loading_cycle_5_smooth(1,2);
end
% Zeroing the data for cycle 6
for i=1:length(loading_cycle_6_smooth)
% Zero extension data
loading_cycle_6_smooth_zeroed  (i,1)  =  loading_cycle_6_smooth(i,1)-
loading_cycle_6_smooth(1,1);
% Zero force data
loading_cycle_6_smooth_zeroed  (i,2)  =  loading_cycle_6_smooth(i,2)-
loading_cycle_6_smooth(1,2);
end
% Zeroing the data for cycle 7
for i=1:length(loading_cycle_7_smooth)
% Zero extension data
loading_cycle_7_smooth_zeroed  (i,1)  =  loading_cycle_7_smooth(i,1)-
loading_cycle_7_smooth(1,1);
% Zero force data
loading_cycle_7_smooth_zeroed  (i,2)  =  loading_cycle_7_smooth(i,2)-
loading_cycle_7_smooth(1,2);
```

```
end
% Zeroing the data for cycle 8
for i=1:length(loading_cycle_8_smooth)
% Zero extension data
loading_cycle_8_smooth_zeroed  (i,1)  =  loading_cycle_8_smooth(i,1)-
loading_cycle_8_smooth(1,1);
% Zero force data
loading_cycle_8_smooth_zeroed  (i,2)  =  loading_cycle_8_smooth(i,2)-
loading_cycle_8_smooth(1,2);
end
% Zeroing the data for cycle 9
for i=1:length(loading_cycle_9_smooth)
% Zero extension data
loading_cycle_9_smooth_zeroed  (i,1)  =  loading_cycle_9_smooth(i,1)-
loading_cycle_9_smooth(1,1);
% Zero force data
loading_cycle_9_smooth_zeroed  (i,2)  =  loading_cycle_9_smooth(i,2)-
loading_cycle_9_smooth(1,2);
end
% Zeroing the data for cycle 10
for i=1:length(loading_cycle_10_smooth)
% Zero extension data
loading_cycle_10_smooth_zeroed (i,1) = loading_cycle_10_smooth(i,1)-
loading_cycle_10_smooth(1,1);
% Zero force data
loading_cycle_10_smooth_zeroed (i,2) = loading_cycle_10_smooth(i,2)-
loading_cycle_10_smooth(1,2);
end
%% Convert extension to strain and force to stress
%  Converting  extensions  to  strain  by  dividing  by  the  original
length; for example 20 mm.
cycle_1_strain_stress(:,1)=
loading_cycle_1_smooth_zeroed(:,1)/original_length;
cycle_2_strain_stress(:,1)=
loading_cycle_2_smooth_zeroed(:,1)/original_length;
cycle_3_strain_stress(:,1)=
loading_cycle_3_smooth_zeroed(:,1)/original_length;
cycle_4_strain_stress(:,1)=
loading_cycle_4_smooth_zeroed(:,1)/original_length;
cycle_5_strain_stress(:,1)=
loading_cycle_5_smooth_zeroed(:,1)/original_length;
cycle_6_strain_stress(:,1)=
loading_cycle_6_smooth_zeroed(:,1)/original_length;
cycle_7_strain_stress(:,1)=
loading_cycle_7_smooth_zeroed(:,1)/original_length;
cycle_8_strain_stress(:,1)=
loading_cycle_8_smooth_zeroed(:,1)/original_length;
cycle_9_strain_stress(:,1)=
loading_cycle_9_smooth_zeroed(:,1)/original_length;
cycle_10_strain_stress(:,1)=
loading_cycle_10_smooth_zeroed(:,1)/original_length;
% Converting force to stress by dividing by area. This area will be
%  different  for  each  sample  tested  and  should  be  defined  at  the
beginning  % of this script.
cycle_1_strain_stress(:,2)= loading_cycle_1_smooth_zeroed(:,2)/area;
cycle_2_strain_stress(:,2)= loading_cycle_2_smooth_zeroed(:,2)/area;
cycle_3_strain_stress(:,2)= loading_cycle_3_smooth_zeroed(:,2)/area;
cycle_4_strain_stress(:,2)= loading_cycle_4_smooth_zeroed(:,2)/area;
cycle_5_strain_stress(:,2)= loading_cycle_5_smooth_zeroed(:,2)/area;
```

```
cycle_6_strain_stress(:,2)= loading_cycle_6_smooth_zeroed(:,2)/area;
cycle_7_strain_stress(:,2)= loading_cycle_7_smooth_zeroed(:,2)/area;
cycle_8_strain_stress(:,2)= loading_cycle_8_smooth_zeroed(:,2)/area;
cycle_9_strain_stress(:,2)= loading_cycle_9_smooth_zeroed(:,2)/area;
cycle_10_strain_stress(:,2)=
loading_cycle_10_smooth_zeroed(:,2)/area;
%% Plot the real data for cycle 10
strain = cycle_10_strain_stress(:,1);
stress = cycle_10_strain_stress(:,2);
fig1 = figure(1);
set(fig1,'name', 'Real Data');
plot(strain,stress, 'r');
title('Real Data: Stress vs Strain', 'FontWeight', 'bold');
xlabel('Strain');
ylabel('Stress [MPa]');
%% Solving nonlinear curve fitting (data-fitting) problems in least-
squares % sense.'lsqcurvefit' enables you to fit a parameterised
nonlinear function % to data easily. You can use lsqnonlin as well,
lsqcurvefit is simply a    % convenient way to call lsqnonlin for
curve fitting.
% Define a fitting function
% In order to fit the parameters to the data using lsqcurvefit you
need to
% define a fitting function. Define the fitting function PREDICTED
as an
% anonymous function.
strain_predicted_solver = 0:0.0001:0.4;
predicted     =     @(a,strain_predicted_solver)     a(1)*log(1     +
exp(a(2)*strain_predicted_solver         -         a(3)))         +
a(4)*strain_predicted_solver;
% provide initial estimates for parameters
% To fit the model to the data, lsqcurvefit needs an initial
estimate 'a0'
% for the parameters
a0 = [A;B;C;D];
% Run the solver

[ahat,resnorm,residual,exitflag,output,lambda,jacobian]            =
lsqcurvefit(predicted,a0,strain,stress);
% View the resulting least-squares estimate
ahat;
%% plot the predicted data using the equation derived in
sigmoid_curve.m
% The 'sigmoid_curve.m' script is available on request.
% Note; the real values of strain are used to predict the values of
stress
strain_predicted = 0:0.0001:0.4;
stress_predicted = ahat(1)*log(1 + exp(ahat(2)*strain_predicted -
ahat(3))) + ahat(4)*strain_predicted;
'FontWeight', 'bold');
fig3 = figure(3);
set(fig3,'name', 'Comparison Between the Real Data and Predicted
Data');
plot(strain,stress, 'r');
hold on;
plot(strain_predicted,stress_predicted, 'g');
title('Comparison Between the Real Data (red) and Predicted Data
(green)', 'FontWeight', 'bold');
xlabel('Strain');
```

```
ylabel('Stress [MPa]');
%% Plot the derivative the derived equation
derivative = diff(stress_predicted)./diff(strain_predicted);
derivative = derivative';
% Slight adjustment to the strain range in order to make the
matrices the
% same size to let us plot the derivative
strain_predicted_derivative = 0.0001:0.0001:0.4;
strain_predicted_derivative = strain_predicted_derivative';
fig4 = figure(4);
set(fig4,'name', 'Derivative of Derived Equation');
plot(strain_predicted_derivative, derivative);
title('Derivative of Derived Equation', 'FontWeight', 'bold');
xlabel('Strain');
ylabel('Derivative');
x_start = strain_predicted_derivative(1);
y_start = derivative(1);
text(x_start,y_start , ['(x = ',num2str(x_start), ' , y = ',
num2str(y_start),
')\rightarrow\bullet'],'HorizontalAlignment','right', 'Color',[1 0.5
0]);
x_end = strain_predicted_derivative(end);
y_end = derivative(end);
text(x_end,y_end , ['(x = ',num2str(x_end), ' , y = ',
num2str(y_end),
')\rightarrow\bullet'],'HorizontalAlignment','right', 'Color',[1 0.5
0]);
%% Plot the second derivative the derived equation
second_derivative =
diff(derivative)./diff(strain_predicted_derivative);
second_derivative = second_derivative';
strain_predicted_derivative_derivative = 0.0002:0.0001:0.4;
fig5 = figure(5);
set(fig5,'name', 'Second Derivative of Derived Equation');
plot(strain_predicted_derivative_derivative, second_derivative);
title('Second Derivative of Derived Equation', 'FontWeight',
'bold');
xlabel('Strain');
ylabel('Second Derivative');
%% Find where the maximum of the second derivative occurs
% pks gives the maximum y-value
[pks, locs] = findpeaks(second_derivative);
% We want the strain value at this maximum y value
strain_at_which_maximum_occurs =
strain_predicted_derivative_derivative(second_derivative==max(second
_derivative(:)));
text(strain_at_which_maximum_occurs, pks, ['Maximum: (x = ',
num2str(strain_at_which_maximum_occurs), ', y = ', num2str(pks), ')
\rightarrow\bullet'],'HorizontalAlignment','right', 'Color',[1 0.5
0]);
X = ['The strain at which the maximum of the second derivative
occurs is: ', strain_at_which_maximum_occurs];
disp(X);
%% Plot the derived equation
% This has been moved here so that this figure appears first on the
screen
fig2 = figure(2);
set(fig2,'units', 'normalized', 'OuterPosition', [0 0 1 1],'name',
'Derived Equation');
```

```
plot(strain_predicted,stress_predicted, 'g');
axis([0 0.4 0 3]);
title('Predicted Stress vs Strain', 'FontWeight', 'bold');
xlabel('Strain');
ylabel('Stress [MPa]');
text('units',     'normalized',     'position',     [0.1,     0.75],
'string','General Equation: \sigma = Alog(1 + exp(B\epsilon - C) +
D\epsilon)', 'Color',[1 0.5 0]);
text('units',     'normalized',     'position',     [0.1,     0.7],
'string',['Derived Equation: \sigma =' , num2str(ahat(1)), 'log(1 +
exp(',  num2str(ahat(2)),'\epsilon  -  ',  num2str(ahat(3)),')  +  ',
num2str(ahat(4)), '\epsilon)'], 'Color',[1 0.5 0]);
text('units',  'normalized','position',  [0.1,  0.55],'string','Final
Parameters:', 'Color',[1 0.5 0]);
text('units',  'normalized','position',  [0.1,  0.5],'string',['A:  ',
num2str(ahat(1))], 'Color',[1 0.5 0]);
text('units', 'normalized','position', [0.1, 0.45],'string',['B: ',
num2str(ahat(2))], 'Color',[1 0.5 0]);
text('units',  'normalized','position',  [0.1,  0.4],'string',['C:  ',
num2str(ahat(3))], 'Color',[1 0.5 0]);
text('units', 'normalized','position', [0.1, 0.35],'string',['D: ',
num2str(ahat(4))], 'Color',[1 0.5 0]);
```

Appendix B

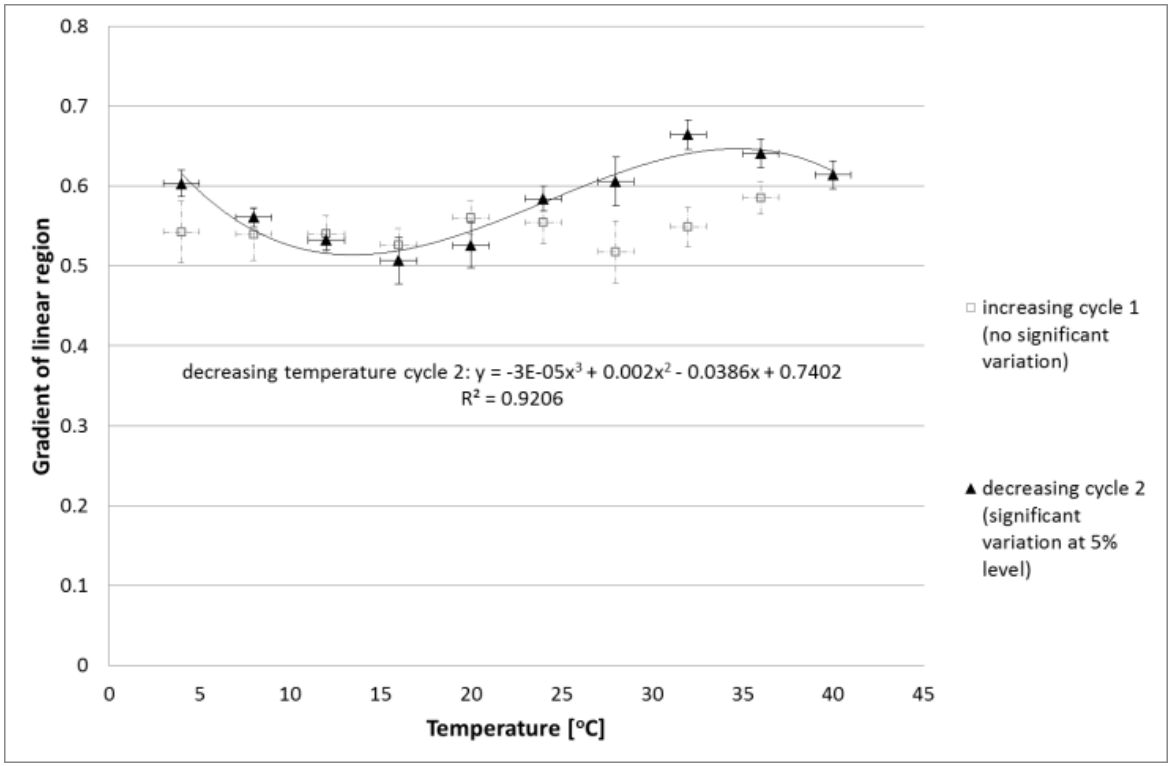

Figure B.1: Thermo-mechanical properties of bovine pericardium, relationship between the gradient of the linear region and temperature for dumbbell 2 on day 21.

Table B.1: Thermo-mechanical properties of bovine pericardium, statistical significance of the third order polynomial relationship between the gradient of the linear region and temperature.

Hypothesis rejected based on a paired Student's t-test	Number of cycles per data set	p-value
$T10_{40} = T12_{32}$	6	4.8×10^{-3}
$T12_{32} = T13_{28}$	5	3.7×10^{-3}
$T13_{28} = T15_{20}$	5	1.5×10^{-2}
$T15_{20} = T19_{4}$	5	4.0×10^{-3}
$T11_{36} = T14_{24}$	6	9.9×10^{-4}
$T14_{24} = T16_{16}$	6	6.2×10^{-4}
$T16_{16} = T18_{8}$	5	2.3×10^{-2}
$T16_{16} = T19_{4}$	5	1.9×10^{-4}
$T19_{4} = T17_{12}$	4	5.2×10^{-5}
Key: $T10_{40}$ = test 10 at 40 ^{o}C.		

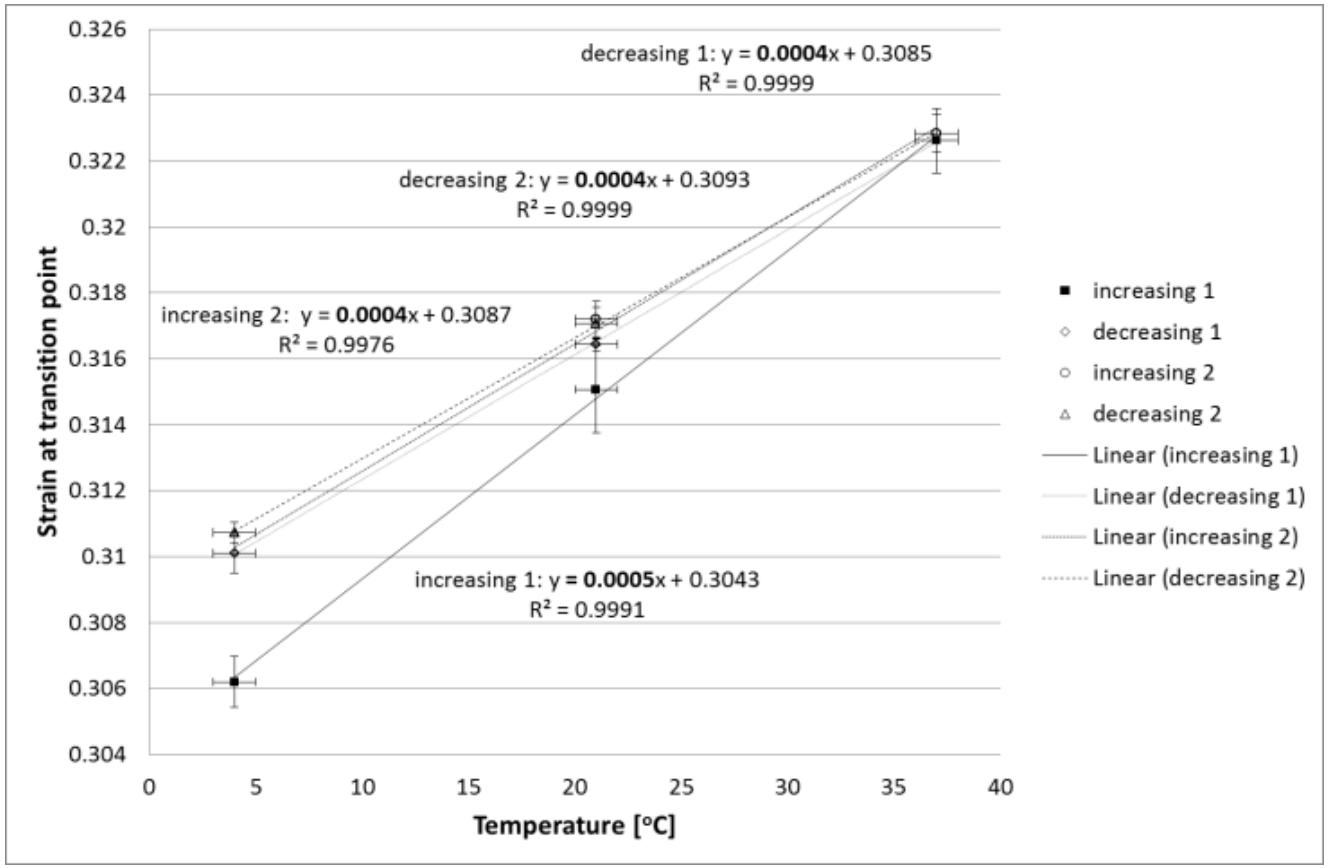

Figure B.2: Relationship between temperature and the strain at transition point for sample 1 when cycled between 3 different temperatures twice.

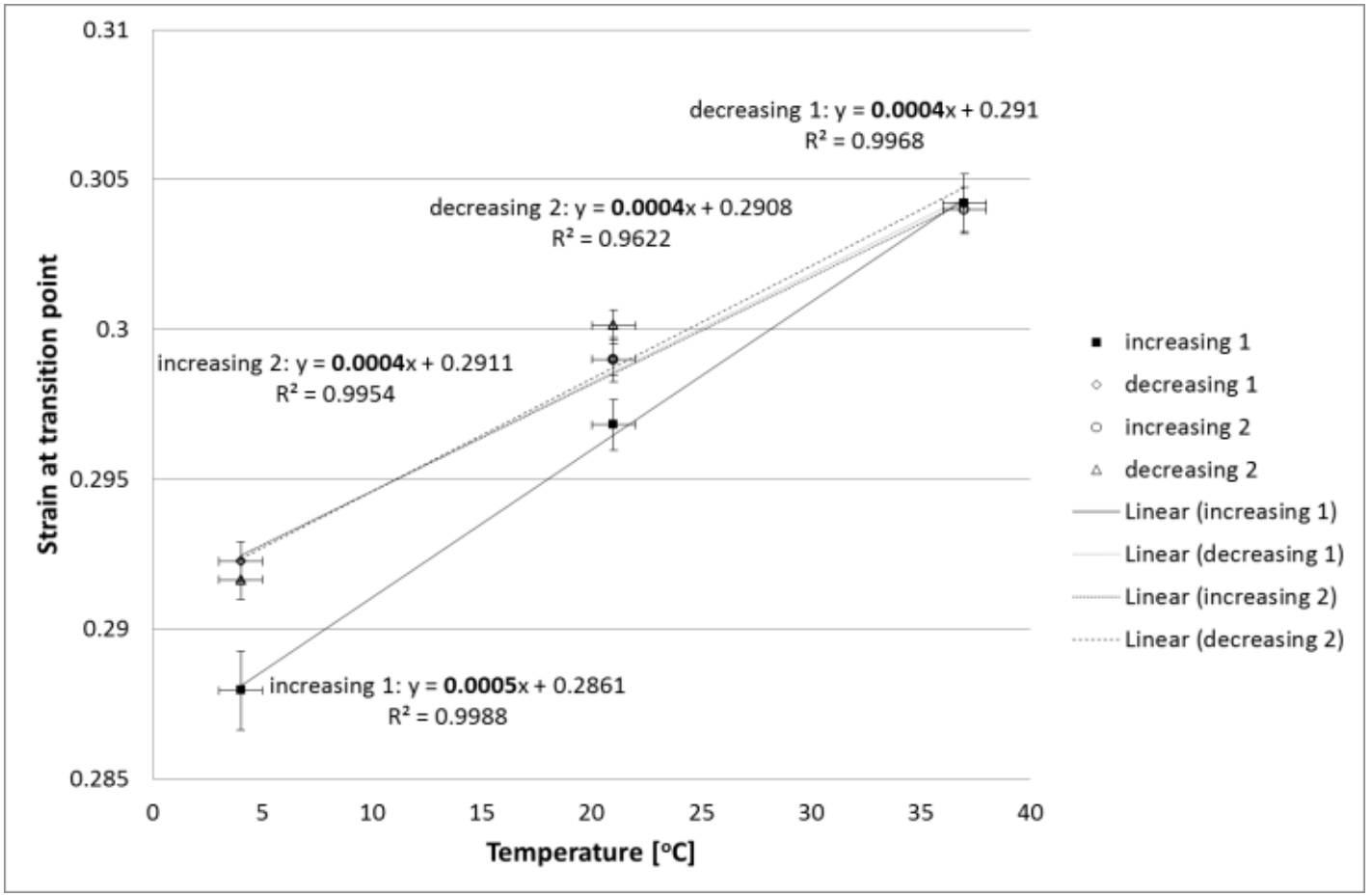

Figure B.3: Relationship between temperature and the transition point for sample 2 when cycled between 3 different temperatures twice.

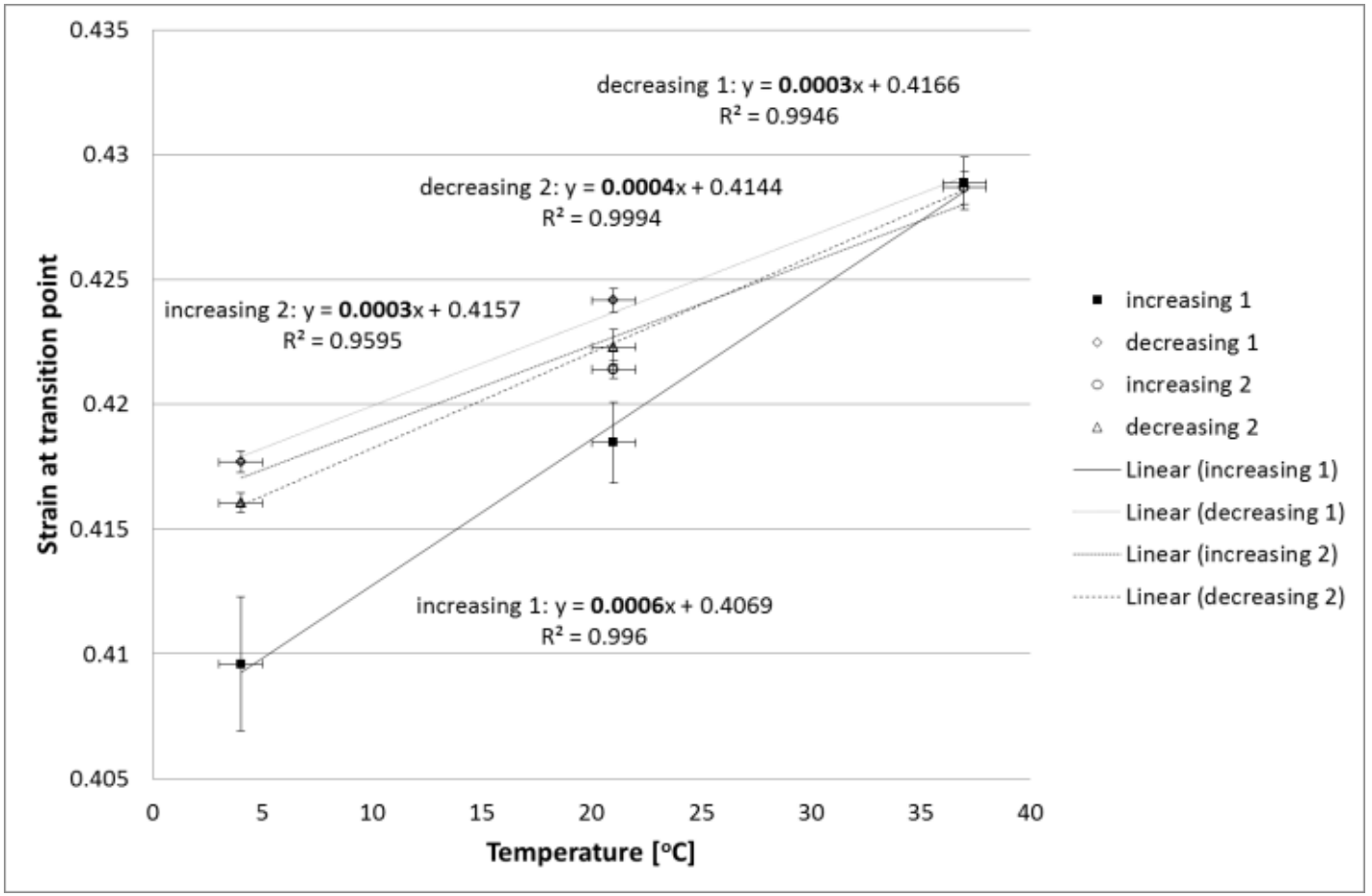

Figure B.4: Relationship between temperature and the transition point for sample 3 when cycled between 3 different temperatures twice.

Table B.2: Thermo-mechanical properties of bovine pericardium, Student's t-tests for significance of the increase in transition point with temperature for three dumbbells.

Dumbbell number	Hypothesis rejected based on a paired Student's t-test	Number of cycles included in calculation	p-values
1	$TP_4 = TP_{21}$	13	1.5×10^{-10}
	$TP_{21} = TP_{37}$		8.5×10^{-13}
	$TP_4 = TP_{37}$		9.2×10^{-13}
2	$TP_4 = TP_{21}$	14	3.0×10^{-11}
	$TP_{21} = TP_{37}$		1.5×10^{-10}
	$TP_4 = TP_{37}$		1.4×10^{-11}
2 (21 days later)	$TP_4 = TP_{20}$	10	1.7×10^{-8}
	$TP_{20} = TP_{36}$		1.8×10^{-8}
	$TP_4 = TP_{36}$		3.1×10^{-9}
3	$TP_4 = TP_{21}$	11	4.6×10^{-8}
	$TP_{21} = TP_{37}$		8.2×10^{-6}
	$TP_4 = TP_{37}$		4.7×10^{-7}
Key: TP_4 = strain at the transition point for $4^{o}C$			

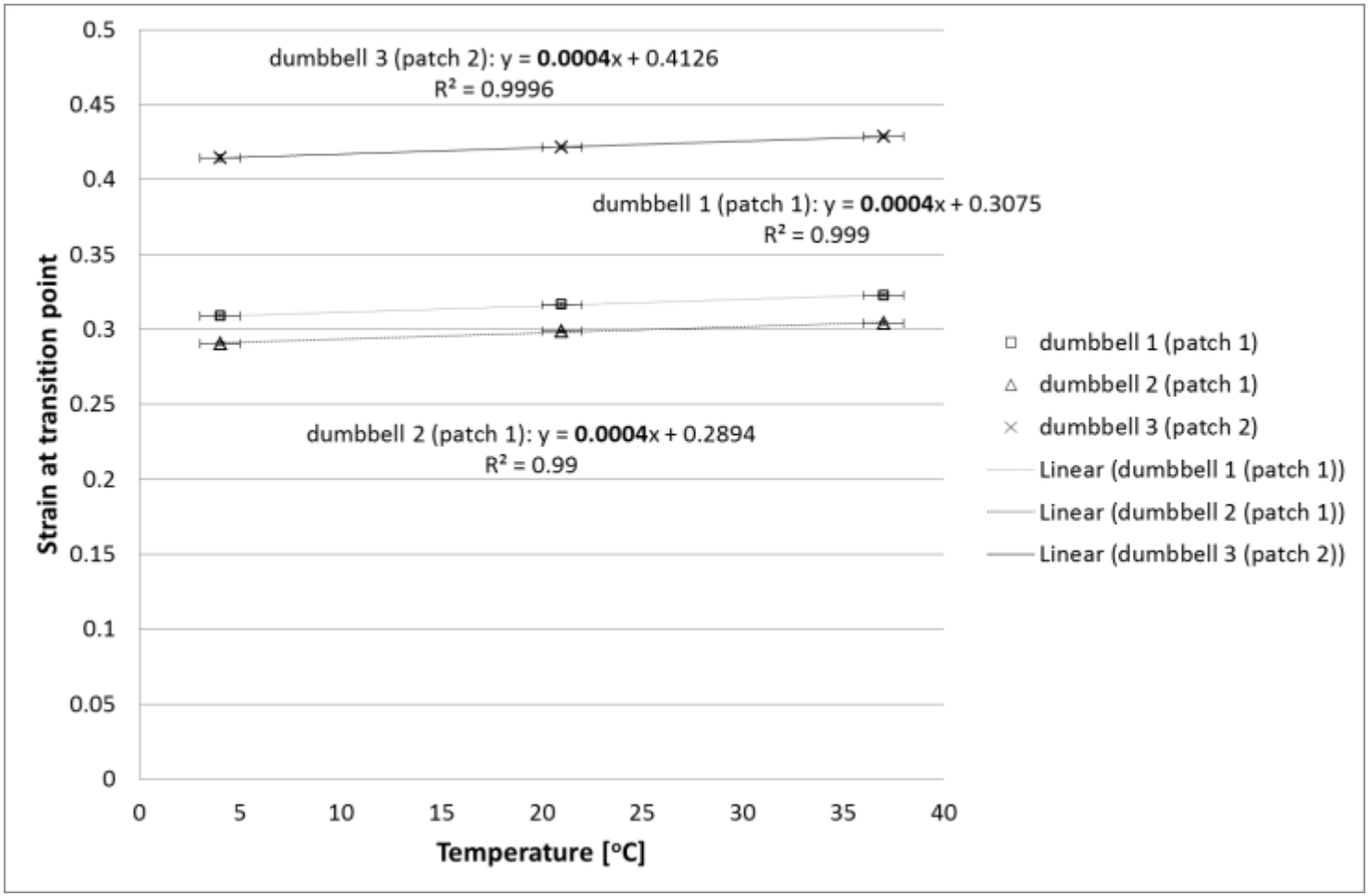

Figure B.5: Transition point for three different temperatures and dumbbells from two different patches of pericardium.

Table B.3: Thermo-mechanical properties of bovine pericardium statistical significance of variation in transition point between dumbbells and greater variation between patches.

Temperature (^{o}C)	Hypothesis rejected based on a paired Student's t-test	p-values
4	$TP_{db1} = TP_{db2}$	9.5×10^{-13}
	$TP_{db1} = TP_{db3}$	2.6×10^{-18}
	$TP_{db2} = TP_{db3}$	1.1×10^{-16}
21	$TP_{db1} = TP_{db2}$	3.2×10^{-16}
	$TP_{db1} = TP_{db3}$	3.3×10^{-19}
	$TP_{db2} = TP_{db3}$	2.7×10^{-18}
37	$TP_{db1} = TP_{db2}$	3.1×10^{-15}
	$TP_{db1} = TP_{db3}$	3.6×10^{-21}
	$TP_{db2} = TP_{db3}$	1.6×10^{-22}
Key: TP_{db1} = strain at transition point for dumbbell 1. Note: dumbbell 1 and 2 are from the same patch and dumbbell 3 is from a different patch.		

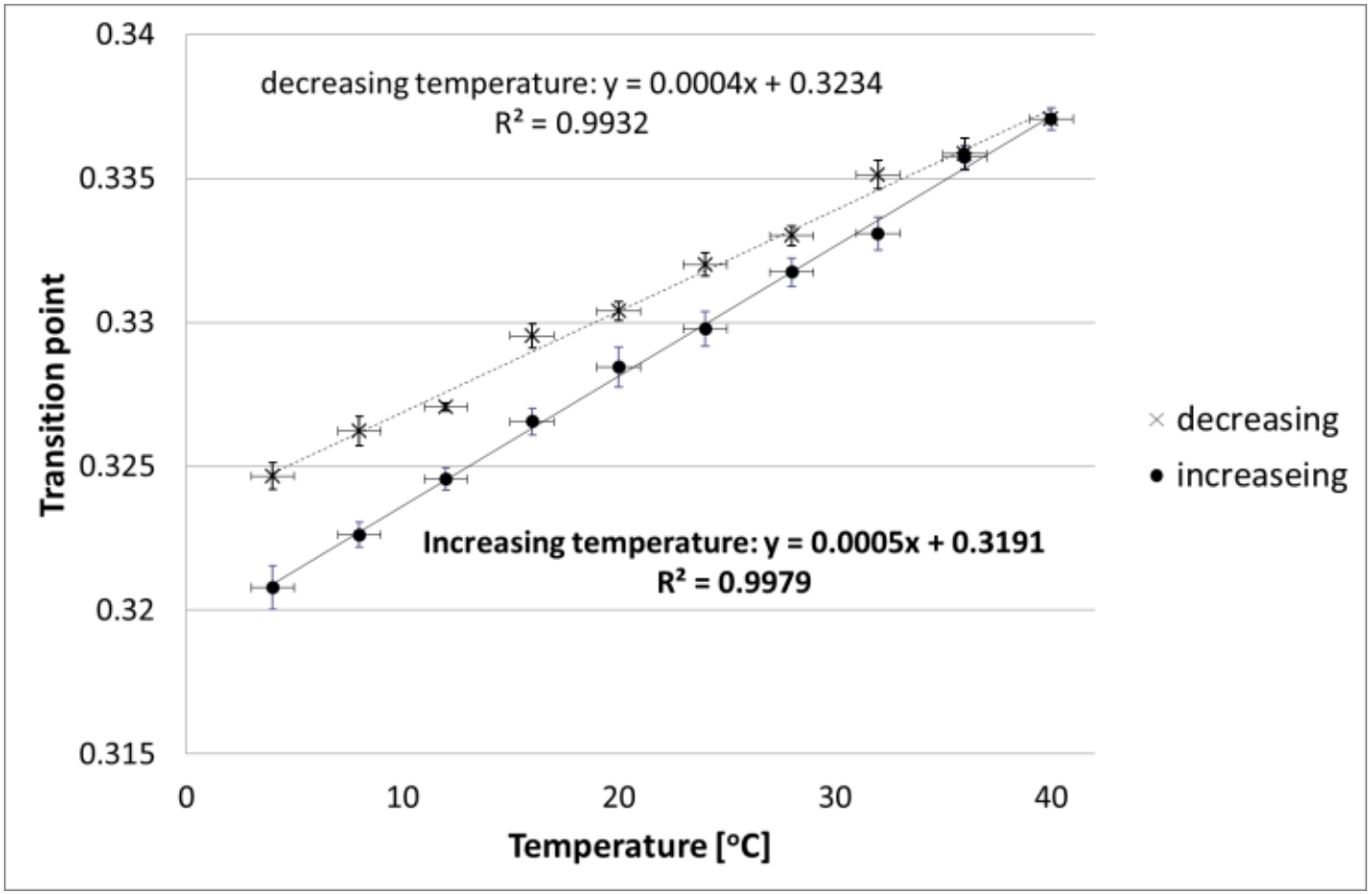

Figure B.6: Relationship between temperature and the transition point for sample 2 when cycled between 10 different temperatures once on day 21.

Table B.4: Thermo-mechanical properties of bovine pericardium; increase in transition point due to cyclic temperature changes.

Temperature	Dumbbell number	p-value for null hypothesis[41] $TP_{c1} = TP_{rc}$
4	1	7.0×10^{-3}
	2	5.8×10^{-4}
	2 (day21)	6.0×10^{-5}
	3	8.9×10^{-4}
21	1	2.0×10^{-2}
	2	2.2×10^{-2}
	2 (day21)	3.8×10^{-4}
	3	6.2×10^{-4}
TP_{c1} = transition point for cycle 1, TP_{rc} = transition point for remaining cycles.		

Table B.5: Change in thermo-mechanical properties of bovine pericardium in terms of its transition point (increases) after 21 days stored in PBS at 4°C.

Hypothesis rejected based on a paired Student's t-test	p-values
$TP4_{d1} = TP4_{d21}$	6.6×10^{-17}
$TP21/20_{d1} = TP21/20_{d21}$	6.2×10^{-17}
$TP36/37_{d1} = TP36/37_{d21}$	2.5×10^{-14}
Key: $TP4_{d1}$ = strain at transition point at 4°C on day 1, TP36/37 = on day 1 it was measured at 36 °C and on day 21 it was measured at 37 °C, however the temperature error was ±1 °C so was not significant.	

[41] A null hypothesis is a general statement that there is no relationship between two measured phenomena.

Table B.6: Thermo-mechanical properties of bovine pericardium statistical significance of variation in hysteresis between dumbbells and greater variation between patches.

Temperature (^{o}C)	Hypothesis rejected based on a paired Student's t-test	p-values
4	$H_{db1} = H_{db2}$	1.4×10^{-2}
	$H_{db1} = H_{db3}$	2.5×10^{-8}
	$H_{db2} = H_{db3}$	7.3×10^{-10}
21	$H_{db1} = H_{db2}$	4.7×10^{-2}
	$H_{db1} = H_{db3}$	1.2×10^{-12}
	$H_{db2} = H_{db3}$	1.5×10^{-13}
37	$H_{db1} = H_{db2}$	2.5×10^{-2}
	$H_{db1} = H_{db3}$	4.4×10^{-7}
	$H_{db2} = H_{db3}$	1.6×10^{-6}

Key: H_{db1} = hysteresis for dumbbell 1.
Note: dumbbell 1 and 2 are from the same patch and dumbbell 3 is from a different patch.

Appendix C

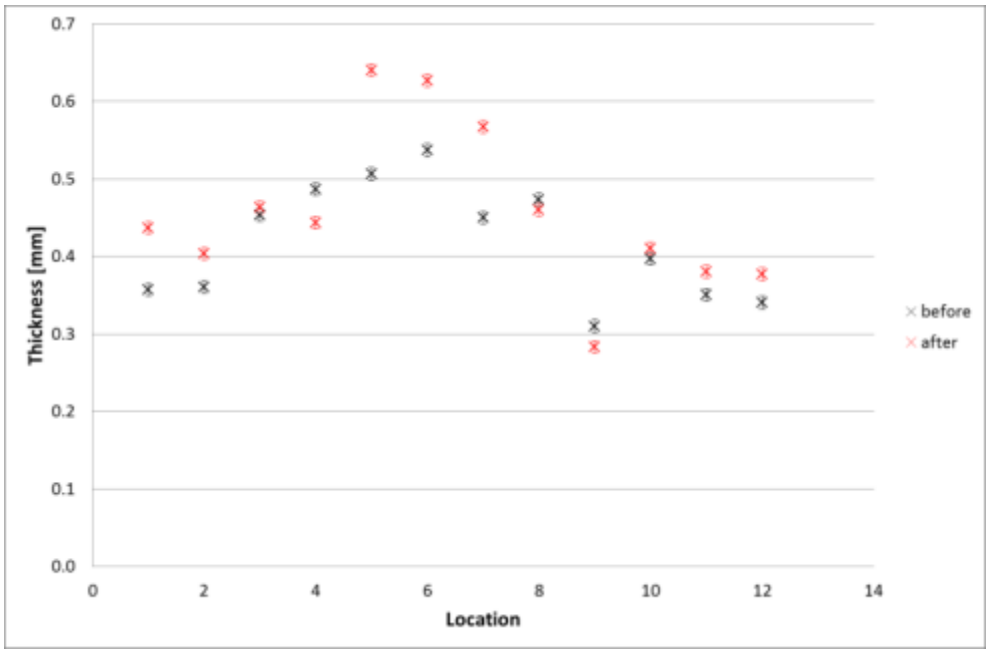

Figure C.1: Effect of fixation on the thickness of bovine pericardium patch 3 in 12 locations.

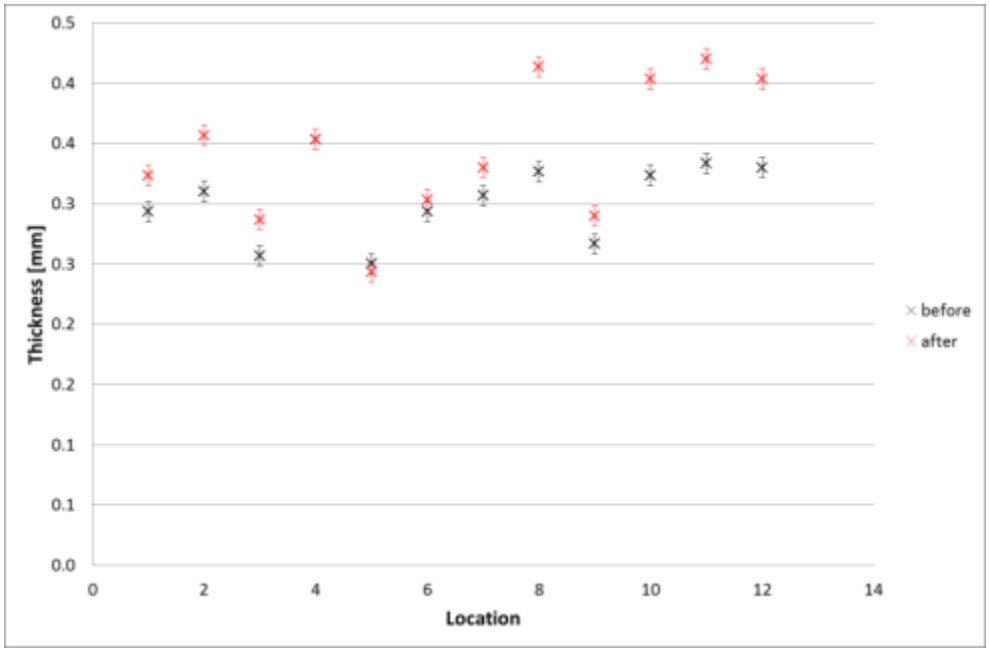

Figure C.2: Effect of fixation on the thickness of bovine pericardium patch 2 in 12 locations.

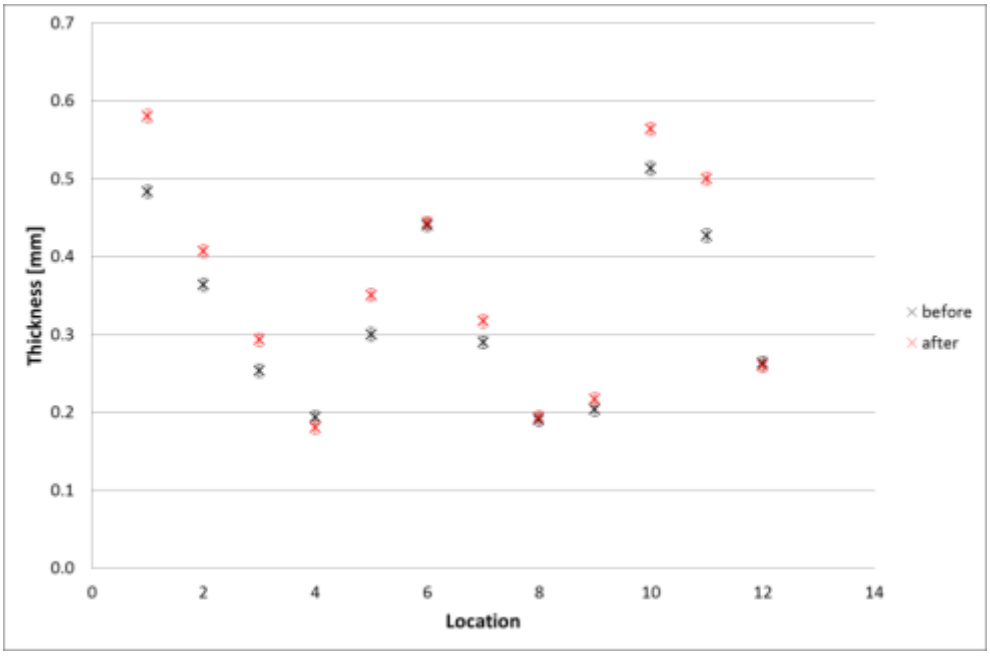

Figure C.3: Effect of fixation on the thickness of bovine pericardium patch 4 in 12 locations.

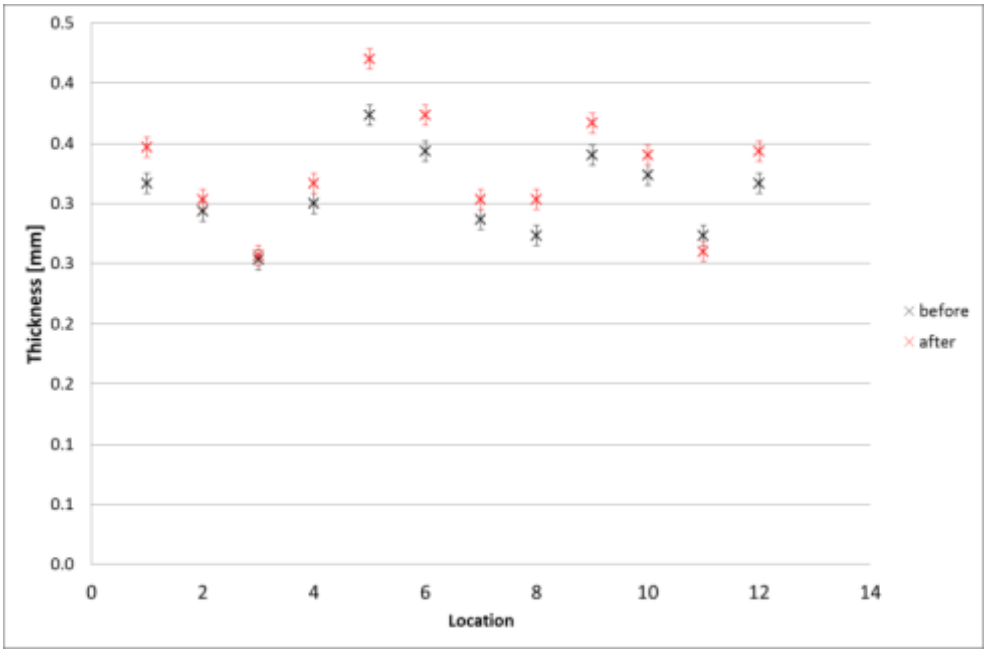

Figure C.4: Effect of fixation on the thickness of bovine pericardium patch 5 in 12 locations.

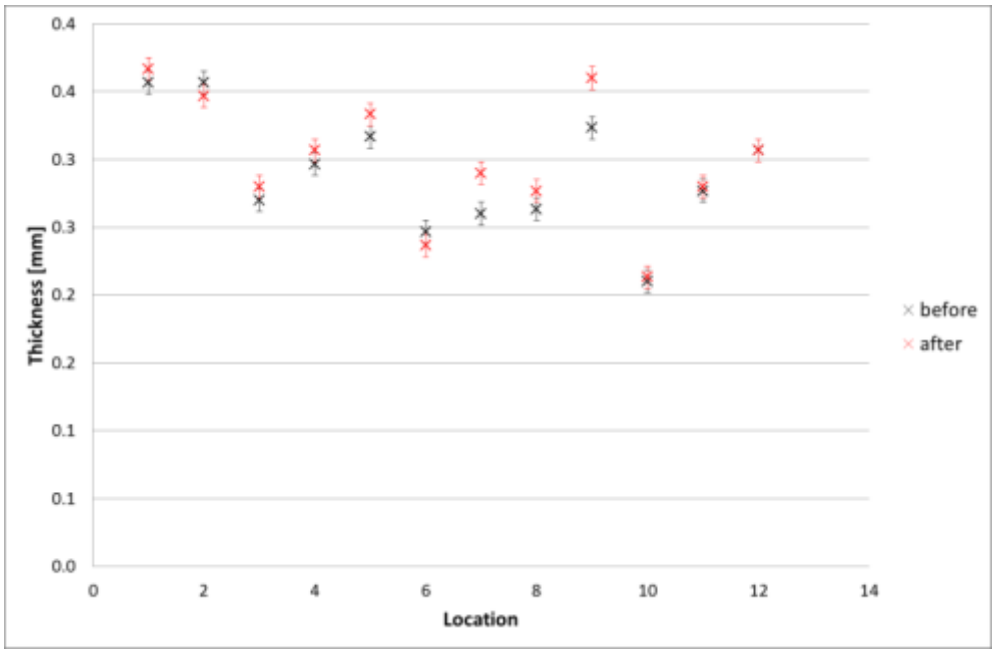

Figure C.5: Effect of fixation on the thickness of bovine pericardium patch 8 in 12 locations.

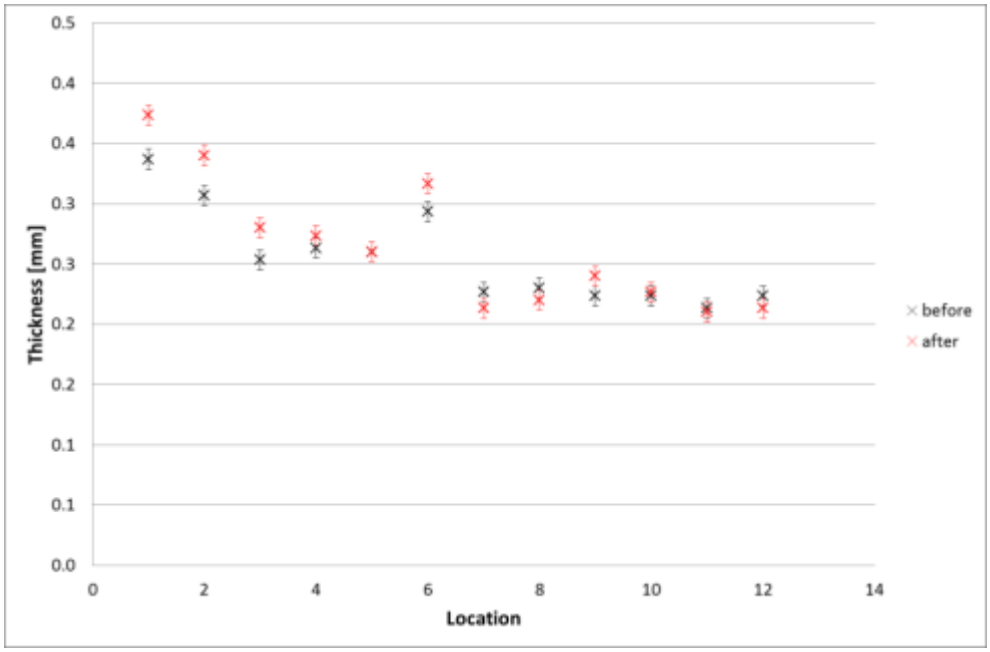

Figure C.6: Effect of fixation on the thickness of bovine pericardium patch 6 in 12 locations.

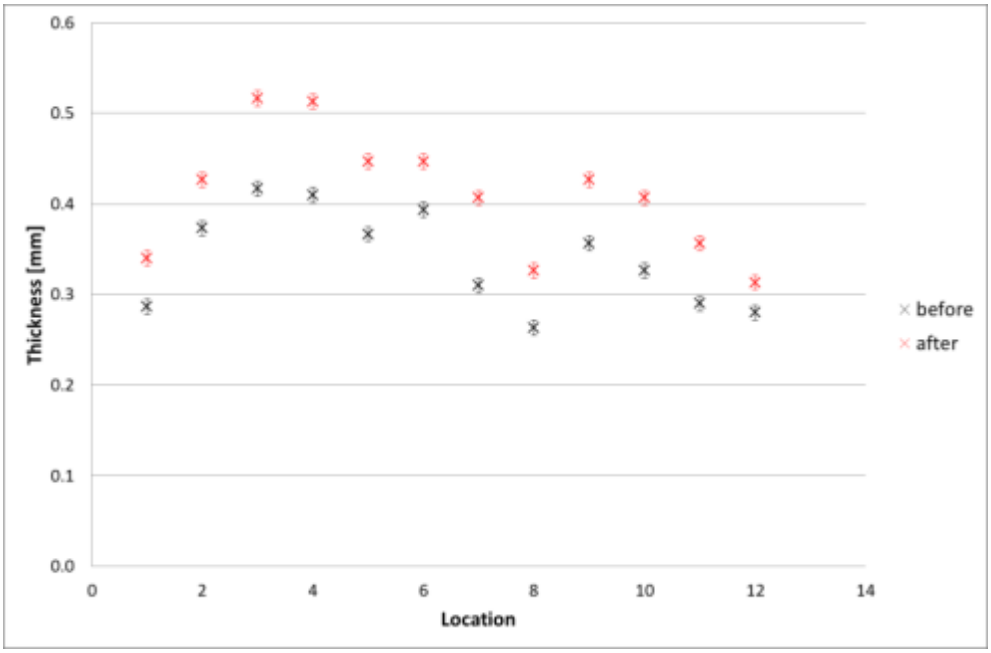

Figure C.7: Effect of fixation on the thickness of bovine pericardium patch 7 in 12 locations.

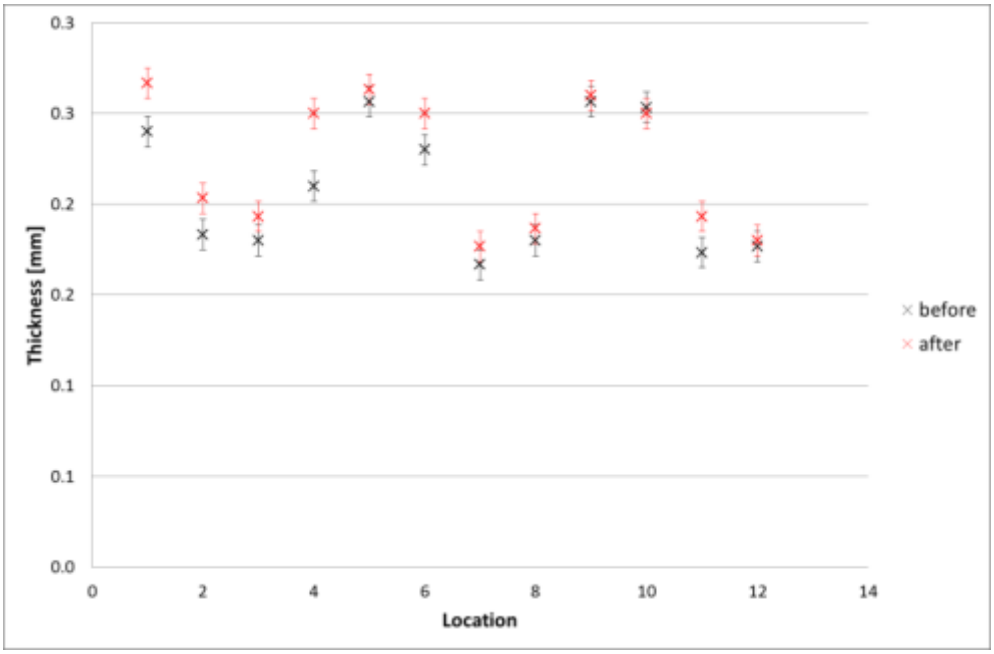

Figure C.8: Effect of fixation on the thickness of bovine pericardium patch 9 in 12 locations.

Appendix D

```
$# LS-DYNA Keyword file
*KEYWORD
*TITLE
This keyword file will simulate the closure of a pair of pericardial mitral valve
leaflets
*DATABASE_FORMAT
$ Define the output format for binary files
$[1] output format
$[2] word size of the binary output files
$--------1---------2-----------------------------------------
$------IFORM---IBINARY-------------------------------------
         0         0
$
$*******************************************************************************
$***************************** CONTROL CARDS ***********************************
$*******************************************************************************
$
*CONTROL_TERMINATION
$ Stop the job
$[1] termination time
$[2] termination cycle
$[3]  reduction  factor  for  initial  time  step  size  to  determine  minimum  time  step
TSMIN.
$[4] percent change in energy ratio for termination of calculation
$[5] percent change in the total mass for termination of calculation
$[6] flag for a non-solution run
$--------1---------2---------3---------4---------5---------6---------
$------ENDTIM----ENDCYC----DTMIN----ENDENG----ENDMAS-----NOSOL-------
  6.82E-01
*CONTROL_TIMESTEP
$ Set structural time step size control using different options
$ CARD1
$[1] initial time step size
$[2] scale factor for computed time step
$[3] basis of time size calculation for 4-node shell elements
$[4] shell element minimum time step assignment
$[5] time step size for mass scaled solutions
$[6] load curve ID that limits the maximum time step size (optional)
$[7]   erosion   flag   for   solid,   t-shell   and   SPH   elements   when   TSMIN   (see
*CONTROL_TERMINATION) is reached
$[8] limit mass scaling to the first step and fix the mass vector according to the
time steps once
$--------1---------2---------3---------4---------5---------6---------7---------8-----
----
$-----DTINIT----TSSFAC------ISDO-----TSLIMT----DT2MS-----LCTM------ERODE-----MSIST---
----
         0       0.9         1
$ CARD2
$[1] reduction factor for initial time step size to determine the minimum time step
size permitted
$[2] load curve specifying DT2MS as a function of time during the explicit solutions
phase
$[3] flag for selective mass scaling if and only if mass scaling active
$--------1---------2---------3---------
$-----DT2MSF----DT2MSL-----IMSCL-------
         0         0         0
*CONTROL_CONTACT
$ Change defaults for computation with contact surfaces
$ CARD1
$[1] scale factor for sliding interface penalties, SLSFAC. (default = 0.1)
$[2] scale factor for rigid wall penalties, which treat nodal points interacting with
rigid walls, RWPNAL.
$[3]  initial  penetration  check  in  contact  surfaces  with  indication  of  initial
penetration in output files. (1 - no checking)
$[4] shell thickness considered in type surface to surface and node to surface type
contact options, where options 1 and 2 below activate the new contact algorithms. (0
= thickness is not considered)
$[5] penalty stiffness value option. (0 - the default is set to 1)
$[6]  shell  thickness  changes  considered  in  single  surface  contact.  (0  =  no
consideration (default))
```

```
$[7] optional automatic reorientation of contact interface segments during
initialization (1 - active for automated (part) input only. Contact surfaces are
given by *PART definitions.)
$--------1---------2---------3---------4---------5---------6---------7---------8-----
----
$-----SLSFAC----RWPNAL----ISLCHK----SHLTHK----PENOPT----THKCHG-----ORIEN----ENMASS---
----
  0.100000     0.000         1         0         0         0         1         0
$ CARD2
$[1] storage per contact interface for user supplied interface control subroutine,
see Appendix F.
$[2] storage per contact interface for user supplied interface friction subroutine,
see Appendix G.
$[3] number of cycles between contact searching using three dimensional bucket
searches.
$[4] flag for intermittent searching in old surface-to-surface contact using the
interval specified as NSBCS above. (0 = off)
$[5] contact surface maximum penetration check multiplier (0 - default is set to 4)
$[6] flag for using actual shell thickness in single surface contact logic-types 4,
13, 15 and 26. (0 = actual shell thickness is not used in the contacts (default))
$[7] time step size override for eroding contact. (0 = contact time size may control
Dt)
$[8] bypass projection of slave nodes to master surface in types (0 = eliminate gaps
by projection nodes)
$--------1---------2---------3---------4---------5---------6---------7---------8-----
----
$----USRSTR-----USRFRC-----NSBCS----INTERM-----XPENE-----SSTHK------ECDT---TIEDPRJ---
----
         0         0         0         0  4.000000         0         0         0
$ CARD3
$[1] default static coefficient of friction (see *PART_CONTACT)
$[2] default dynamic coefficient of friction (see *PART_CONTACT)
$[3] default exponential decay coefficient (see *PART_CONTACT)
$[4] default viscous friction coefficient (see *PART_CONTACT)
$[5] default contact thickness (see *PART_CONTACT)
$[6] default thickness scale factor (see *PART_CONTACT)
$[7] default local penalty scale factor (see *PART_CONTACT)
$--------1---------2---------3---------4---------5---------6---------7---------
$------SFRIC-----DFRIC------EDC-------VFC-------TH-------TH_SF----PEN_SF-------
     0.000     0.000     0.000     0.000     0.000     0.000     0.000
$ CARD4
$[1] ignore initial penetrations in the *CONTACT_AUTOMATIC options. (0 = move nodes
to eliminate initial penetrations in the model definition)
$[2] flag to activate the calculation of frictional sliding energy. (0 = do not
calculate)
$[3] flag not to display stationary rigid wall by default. (0 = generate 4 extra
nodes and 1 shell element to visualize stationary planar rigid wall)
$[4] flag to output each beam spot weld slave node and its master segment for contact
type: *CONTACT_SPOTWELD into the D3HSP file. (0 = no, do not write out this
information)
$[5] if a spot weld node or face, which is related to a *MAT_SPOTWELD beam or solid
element, respectively, cannot be found on the master surface, should an error
termination occur? (0 = no, continue calculation)
$[6] if the nodes of a spot weld beam or solid element are attached to a shell
element that fails and are deleted, then the attached spot weld element is deleted if
this flag is on. (0 = no, do not delete the spot weld beam or solid element)
$[7] optional thickness scale factor
$--------1---------2---------3---------4---------5---------6---------7---------
$-----IGNORE----FRCENG---SKIPRWG----OUTSEG---SPOTSTP---SPOTDEL---SPOTHIN-------
         0         0         0         0         0         0     0.000
$ CARD5
$[1] symmetry plane option default for automatic segment generation when contact is
defined by part IDs. (0 = off)
$[2] flag to use one-way node to surface erosion. (0 = use one way algorithm)
$[3] flag to add rigid wall gap stiffness, see parameter RWGDTH below. (1 = add gap
stiffness, 2  = do not add gap stiffness)
$[4] death time for gap stiffness. After this time the gap stiffness is no longer
added.
$[5] rigid wall penalty scale factor for contact with deformable parts during
implicit calculations.
$[6] invokes the covariant formulation of Konyukhov and Schweizerhof in the FORMING
contact option. (0 = standard formulation (default))
$[7] spot weld radius scale factor for neighbour segment thinning. (0 = neighbour
segments not thinned (default)).
```

```
$[8] flag for offsetting thermal contact surfaces for thick thermal shells. (0 = no
offset)
$--------1---------2---------3---------4---------5---------6---------7---------8-----
----
$-------ISYM----NSEROD----RWGAPS----RWGDTH-----RWKSF-----ICOV-----SWRADF-------
ITHOFF----
         0         0         0     0.000  1.000000         0     0.000         0
$ CARD6
$[1] flag for assuming edge shape for shells when measuring penetration. (0 = shells
are assumed round (default))
$[2] flag to choose the method for calculating the penalty stiffness. (0 = based on
material density and segment dimensions (default))
$[3] thermal contact heat transfer methodology. ( 0 = default set to 1)
$[4]  tied constraint offset contact update option. (0 = update velocities and
displacements from accelerations)
$[5] option to output contact forces to RDFORC for all 2 surface force transducer
surfaces overlap. (0 = output to the first force transducer that matches (default))
$[6] unused
$[7] optional shell thickness scale factor for contact with rigid walls.
$--------1---------2---------3---------4---------5---------6---------7---------
$-----SHLEDG----PSTIFF----ITHCNT----TDCNOF-----FTALL----UNUSED----SHLTRW-------
         0         0         0         0         0         0     0.000
*CONTROL_ENERGY
$ Provides control for energy dissipation options
$CARD1
$[1] Hourglass energy calculation option. This option requires significant additional
storage and increases cost by ten percent. (1 - hourglass energy is not computed -
default)
$[2]  Rigidwall  energy  (a.k.a.  stonewall  energy)  dissipation  option.  (1  -  energy
dissipation is not computed)
$[3] Sliding interface energy dissipation option (this parameter is always set to 2
if contact is active. The option SLNTEN=1 is not available). (1 - energy dissipation
is not computed)
$[4]  Rayleigh  energy  dissipation  option  (damping  energy  dissipation).  (1  -  energy
dissipation is not computed - default)
$--------1---------2---------3---------4---------
$-------HGEN------RWEN----SLNTEN-----RYLEN-------
         2         2         1         1
*CONTROL_ACCURACY
$ Define control parameters that can improve the accuracy of the calculation
$ CARD1
$[1] Global flag for 2nd order objective stress updates.
$[2] Invariant node numbering for shell and solid elements. (4 - on for shell, thick
shell and solid elements)
$[3] Part set ID for objective stress updates
$--------1---------2---------3----------
$-------OSU-------INN-----PIDOSU--------
         1          4          0                                                    0
0
*CONTROL_BULK_VISCOSITY
$ Reset the default values of the bulk viscosity coefficients globally. This may be
advisable for shock wave propagation and some materials.
$ CARD1
$[1] default quadratic viscosity coefficient
$[2] default linear viscosity coefficient
$[3]  default  bulk  viscosity  type,  IBQ  (Default  =  1).  (-2  -  internal  energy
dissipation by the viscosity in the shell elements is computed and included in the
overall energy balance)
$[4] beam bulk viscosity type (Default = 0)
$--------1---------2---------3---------4---------
$-------Q1---------Q2-------TYPE-----BTYPE-------
       1.5      0.06        -2
*CONTROL_SHELL
$ Provide controls for computing shell response
$ CARD1
$[1] shell element warpage angle in degrees
$[2] automatic sorting of triangular shell elements to treat degenerate quadrilateral
shell elements as CO or DKT triangular shells
$[3] shell normal update option
$[4] shell thickness change option for deformable shells
$[5] default shell formulation
$[6] warping stiffness for Belytschko-Tsay shells
$[7] plane stress plasticity option (applies to materials 3, 18, 19 and 24)
```

```
$[8] projection method for the warping stiffness in the Belytschko-Tsay shell (the
BWC option above) and the Belytschko-Wong-Chiang elements
$--------1---------2---------3---------4---------5---------6---------7---------8-----
----
$-----WRPANG-----ESORT-----IRNXX----ISTUPD----THEORY------BWC------MITER------PROJ---
----
     0.000         1                   1         2
$ CARD2
$[1] define a scale factor for the rotary shell mass
$[2] default shell through thickness numerical integration rule
$[3] laminated shell theory is available for all thin shell and thick shell materials
except those that use the Green-Lagrange strain
$[4] coordinate system for the type 6 shell element
$[5] thermal shell option
$--------1---------2---------3---------4---------5---------6---------7---------
$----ROTASCL----INTGRD----LAMSHT----CSTYP6----THSHEL----NFAIL1----NFAIL4-------
  0.000000         0         0         0
*CONTROL_OUTPUT
$ Set miscellaneous output parameters. This keyword does not control the information,
such as the stress and strain tensors, which is written into the binary databases.
$ For the latter, see the keyword *DATABASE_EXTENT_BINARY
$ CARD1
$[1] print suppression during input phase flag for the "d3hsp" file
$[2] print suppression during input phase flag for echo file
$[3] flag to update reference node coordinates for beam formulations 1, 2 and 11
$[4]  flag to average or filter nodal accelerations output to file "nodout" and the
time history database "d3thdt"
$[5] output interval for interface file written per *INTERFACE_COMPONENT_option
$[6] flag controlling output of initial time step sizes for elements to d3hsp
$[7] problem status report interval steps to the "d3hsp" file. This flag is ignored
if the "glstat" file is written, see *DATABASE_GLSTAT
$[8] number of time steps interval for flushing I/O buffers
$--------1---------2---------3---------4---------5---------6---------7---------8-----
----
$------NPOPT----NEECHO----NREFUP----IACCOP-----OPIFS----IPNINT----IKEDIT----IFLUSH---
----
         0         0         0         0         0         0       125         0
$ CARD2
$[1] default print flag for "rbdout" and "matsum" files
$[2] output erode internal and kinetic energy into the "matsum" file
$[3] output ten connectivity nodes into "d3plot" database
$[4] maximum number of each error/warning message
$[5] flag to output digitized curve data to message and d3hsp files
$[6] output interval for recorded motions from *INTERFACE_SSI_AUX
$--------1---------2---------3---------4---------5---------6---------7---------8-----
----
$------IPRTF----IERODE-----TET10----MSGMAX----IPCURV------GMDT-------
         0         0         0         0         0
*CONTROL_HOURGLASS
$ Redefine values of hourglass control type and coefficient
$[1] default hourglass type (1 - standard LSDYNA, 3 - Flanagan-Belytschko with exact
volume integration) for shells viscous type (1=2=3) for explicit or stiffness
hourglass control (4=5)
$[2] default hourglass coefficient (0.1 - default). Note QH that exceeds 0.15 may
cause instabilities.
$--------1---------2---------
$-------IHQ-------QH---------
         3    0.2475
*DAMPING_GLOBAL
$ define mass weighted nodal damping that applies globally to the nodes of deformable
bodies and to the mass center of the rigid bodies
$[1] load curve ID which specifies the system damping constant. EQ.0: a constant
damping factor as defined by VALDMP is used
$[2] system damping constant
$[3] scale factor
$[4] scale factor
$[5] scale factor
$[6] scale factor
$[7] scale factor
$[8] scale factor
$--------1---------2---------3---------4---------5---------6---------7---------8
$------LCID-----VALDMP------STX-------STY-------STZ-------SRX-------SRY-------SRZ
         0    0.9965
$
```

```
$*******************************************************************************
$***************************** SECTION ***************************************
$*******************************************************************************
$
*SECTION_SHELL
$ define section properties for shell elements
$ CARD1
$[1] section ID
$[2] element formulation options (2 - Belytschko-Tsay)
$[3]  shear correction factor which scales the transverse shear stress. A suggested
value is 5/6 for isotropic materials.
$[4] number of through thickness integration points (3 - 3 point)
$[5] printout option (2 - resultants at plan points and fibre lengths)
$[6] quadrature rule or integration rule ID, see *INTEGRATION_SHELL
$[7] flag for orthotropic/anisotropic layered composite material model
$[8] not used (obsolete)
$--------1---------2---------3---------4---------5---------6---------7---------8-----
----
$------SECID----ELFORM------SHRF------NIP------PROPT---QR/IRID-----ICOMP-----SETYP---
----
         1         2  0.833333         5         2
$ CARD2
$[1]  shell  thickness  at  node  n1,  unless  the  thickness  is  defined  on  the
*ELEMENT_SHELL_OPTION card
$[2] shell thickness at node n2
$[3] shell thickness at node n3
$[4] shell thickness at node n4
$[5] location of reference surface for three dimensional shell elements
$[6] non-structural mass per unit area
$[7] treatment of through thickness strain
$[8] edge node set required for shell type seatbelts
$--------1---------2---------3---------4---------5---------6---------7---------8-----
----
$--------T1--------T2--------T3--------T4-------NLOC-----MAREA------IDOF----EDGSET---
----
       0.4       0.4       0.4       0.4
*SECTION_SHELL
$ Define section properties for shell elements
$ CARD1
$[1] section ID
$[2] element formulation options (2 - Belytschko-Tsay)
$[3]  shear correction factor which scales the transverse shear stress. A suggested
value is 5/6 for isotropic materials.
$[4] number of through thickness integration points (3 - 3 point)
$[5] printout option (2 - resultants at plan points and fibre lengths)
$[6] quadrature rule or integration rule ID, see *INTEGRATION_SHELL
$[7] flag for orthotropic/anisotropic layered composite material model
$[8] not used (obsolete)
$--------1---------2---------3---------4---------5---------6---------7---------8-----
----
$------SECID----ELFORM------SHRF------NIP------PROPT---QR/IRID-----ICOMP-----SETYP---
----
         2         2  0.833333         5         2
$ CARD2
$[1]  shell  thickness  at  node  n1,  unless  the  thickness  is  defined  on  the
*ELEMENT_SHELL_OPTION card
$[2] shell thickness at node n2
$[3] shell thickness at node n3
$[4] shell thickness at node n4
$[5] location of reference surface for three dimensional shell elements
$[6] non-structural mass per unit area
$[7] treatment of through thickness strain
$[8] edge node set required for shell type seatbelts
$--------1---------2---------3---------4---------5---------6---------7---------8-----
----
$--------T1--------T2--------T3--------T4-------NLOC-----MAREA------IDOF----EDGSET---
----
       0.4       0.4       0.4       0.4
$
$*******************************************************************************
$*****************************  MATERIALS  *************************************

$*******************************************************************************
$
```

```
*MAT_OGDEN_RUBBER_TITLE
Pericardium parameters from experimental data
$ This is also material type 77. This material provides the Ogden [1984] rubber model
combined optionally with linear viscoelasticity as outlines by Christensen [1980]
$ CARD1
$[1] material identification
$[2] mass density
$[3] poissons ratio (>=0.49 is recommended; smaller values may not work and should
not be used.)
$[4] order of fit to the Ogden model
$[5] number of prony series terms in fit
$[6] shear modulus for frequency independent damping
$[7] limit stress for frequency independent frictional damping
$--------1---------2---------3---------4---------5---------6---------7---------
$-------MID--------RO---------PR---------N---------NV---------G---------SIGF-------
         1 1.2000E-9  0.499900         0         0     0.000     0.000
$ CARD2
$[1-8] the ith shear modulus
$--------1---------2---------3---------4---------5---------6---------7---------8-----
----
$-------MU1-------MU2-------MU3-------MU4-------MU5-------MU6-------MU7-------MU8----
----
 7.5600E-6 5.6700E-4     0.000     0.000     0.000     0.000     0.000     0.000
$ CARD3
$[1-8] the ith exponent
$--------1---------2---------3---------4---------5---------6---------7---------8-----
----
$-----ALPHA1----ALPHA2----ALPHA3----ALPHA-----ALPHA-----ALPHA-----ALPHA7----ALPHA8---
----
 26.255711 26.255711     0.000     0.000     0.000     0.000     0.000     0.000
$
$*******************************************************************************
$***************************** PART ****************************************
$*******************************************************************************
$
*PART
                                                                          Shell
$ Define parts, i.e., combine material information, section properties, hourglass
type, thermal properties, and a flag for part adaptivity
$ CARD1
$[1] part identification
$[2] section identification defined in the *SECTION section
$[3] material identification defined in the *MAT section
$[4] equation of state identification in the *EOS section
$[5] hourglass/bulk viscosity identification defined in the *HOURGLASS section
$[6] part initialization for gravity loading
$[7] indication if this part is adapted or not
$[8] thermal material property identification defined in the *MAT_THERMAL section
$--------1---------2---------3---------4---------5---------6---------7---------8-----
----
$-------PID------SECID------MID------EOSID------HGID------GRAV----ADPOPT------TMID---
----
         1         1         1         0         0         0         0         0
*PART
                                                                        Shell
$ Define parts, i.e., combine material information, section properties, hourglass
type, thermal properties, and a flag for part adaptivity
$ CARD1
$[1] part identification
$[2] section identification defined in the *SECTION section
$[3] material identification defined in the *MAT section
$[4] equation of state identification in the *EOS section
$[5] hourglass/bulk viscosity identification defined in the *HOURGLASS section
$[6] part initialization for gravity loading
$[7] indication if this part is adapted or not
$[8] thermal material property identification defined in the *MAT_THERMAL section
$--------1---------2---------3---------4---------5---------6---------7---------8-----
----
$-------PID------SECID------MID------EOSID------HGID------GRAV----ADPOPT------TMID---
----
         2         2         1         0         0         0         0         0
$
$*******************************************************************************
$***************************** NODES ***************************************
```

```
$*********************************************************************************
$
*NODE
$ Define a node and its coordinates in the global coordinate system
$ CARD1
$[1] node number
$[2] x coordinate
$[3] y coordinate
$[4] z coordinate
$[5] translational constraint
$[6] rotational constraint
$------1---------------2---------------3---------------4----------5----------6-------
---
$-----NID-------------X---------------Y---------------Z---------TC---------RC-------
---
… etc.
$
$ *********************************************************************************
$***************************** ELEMENTS ******************************************
$ *********************************************************************************
$
*ELEMENT_SHELL
$ Define three, four, six and eight node elements including 3D shells, membranes, 2D
plane stress, plane strain and axisymmetric solids
$ CARD1
$[1] element ID
$[2] part ID, see *PART
$[3] nodal point 1
$[4] nodal point 2
$[5] nodal point 3
$[6] nodal point 4
$[7-10] mid-side nodes for eight node shell
$------1-------2-------3-------4-------5-------6-------7-------8---------9------10---
----
$-----EID-----PID-----N1------N2------N3------N4------N5------N6--------N7------N8---
----
… etc.
*DEFINE_COORDINATE_SYSTEM
$ Define a local coordinate system
$ CARD1
$[1] coordinate system ID
$[2] X-coordinate of origin
$[3] Y-coordinate of origin
$[4] Z-coordinate of origin
$[5] X-coordinate of point on local x-axis
$[6] Y-coordinate of point on local x-axis
$[7] Z-coordinate of point on local x-axis
$[8]  coordinate  system  ID  applied  to  the  coordinates  used  to  define  the  current
system
$--------1---------2---------3---------4---------5---------6---------7---------8-----
----
$-------CID-------XO--------YO--------ZO--------XL--------YL--------ZL--------CIDL---
----
        26         0         0         0         1         0         0
$ CARD2
$[1] X-coordinate of point in local x-y plane
$[2] Y-coordinate of point in local x-y plane
$[3] Z-coordinate of point in local x-y plane
$--------1---------2---------3---------
$-------XP--------YP--------ZP---------
         0         1         0
$
$*********************************************************************************
$***************************** SETS **********************************************
$*********************************************************************************
$
*SET_SEGMENT
$ Define a set of quadrilateral and triangular segments with optional identical or
unique attributes
$ CARD1
$[1] set identification
$[2] first nodal attribute default value
$[3] second nodal attribute default value
$[4] third nodal attribute default value
```

```
$[5] fourth nodal attribute default value
$[6] this field is used by a non-mechanics solver to create a set defined on that
solver's mesh. By default, the set refers to the mechanics mesh (MECH)
$--------1---------2---------3---------4---------5---------6---------7---------8-----
----
$-------SID-------DA1-------DA2-------DA3-------DA4-----SOLVER------
$----leaflet_1_aortic----
         1
$ CARD2
$[1-6] Node ID n
$--------1---------2---------3---------4---------
$-------N1--------N2--------N3--------N4---------
… etc.
*SET_SEGMENT
$ Define a set of quadrilateral and triangular segments with optional identical or
unique attributes
$ CARD1
$[1] set identification
$[2] first nodal attribute default value
$[3] second nodal attribute default value
$[4] third nodal attribute default value
$[5] fourth nodal attribute default value
$[6] this field is used by a non-mechanics solver to create a set defined on that
solver's mesh. By default, the set refers to the mechanics mesh (MECH)
$--------1---------2---------3---------4---------5---------6---------7---------8-----
----
$-------SID-------DA1-------DA2-------DA3-------DA4-----SOLVER------
$----leaflet_2_mural----
         2
$ CARD2
$[1-6] Node ID n
$--------1---------2---------3---------4---------
$-------N1--------N2--------N3--------N4---------
… etc.
*SET_NODE_LIST_TITLE
Edges of leaflets fixed to frame
$ Define a nodal set with some identical or unique attributes
$ CARD1
$[1] set identification
$[2] first nodal attribute default value
$[3] second nodal attribute default value
$[4] third nodal attribute default value
$[5] fourth nodal attribute default value
$[6] this field is used by a non-mechanics solver to create a set defined on that
solver's mesh. By default, the set refers to the mechanics mesh (MECH)
$--------1---------2---------3---------4---------5---------6---------7---------8-----
----
$-------SID-------DA1-------DA2-------DA3-------DA4-----SOLVER------
         3
$ CARD2
$[1-6] Node ID n
$--------1---------2---------3---------4---------5---------6---------7---------8-----
----
$-------NID1------NID2------NID3------NID4------NID5------NID6------NID7------NID8---
----
… etc.
$
$*******************************************************************************
$***************************** CURVES ******************************************
$*******************************************************************************
$
*DEFINE_CURVE
$ Define a curve [for example, load (ordinate value) versus time (abscissa value)],
often referred to as a load curve
$ This is the pressure difference across the mitral valve, derived from pulse
duplicator data
$ CARD1
$[1] load curve ID
$[2] stress initialization by dynamic relaxation
$[3] scale factor for abscissa value
$[4] scale factor for ordinate value (function)
$[5] offset for abscissa values
$[6] offset for ordinate values (function)
$[7] data type
```

```
$--------1---------2---------3---------4---------5---------6---------7---------
$-------LCID------SIDR------SFA-------SFO-------OFFA------OFFO----DATTYP-------
         1         0         0         0         0         0         0
$CARD2
$[1] abscissa values
$[2] ordinate (function) values
$------------------1-------------------2-------------------
$-----------------A1------------------O1-------------------
… etc.
*DEFINE_CURVE
$ Define a curve [for example, load (ordinate value) versus time (abscissa value)],
often referred to as a load curve
$ CARD1
$[1] load curve ID
$[2] stress initialization by dynamic relaxation
$[3] scale factor for abscissa value
$[4] scale factor for ordinate value (function)
$[5] offset for abscissa values
$[6] offset for ordinate values (function)
$[7] data type
$--------1---------2---------3---------4---------5---------6---------7---------
$-------LCID------SIDR------SFA-------SFO-------OFFA------OFFO----DATTYP-------
         2         0         0         0         0         0         0
$CARD2
$[1] abscissa values
$[2] ordinate (function) values
$------------------1-------------------2-------------------
$-----------------A1------------------O1-------------------
… etc.
$
$*******************************************************************************
********
$*****************************                   LOADING                    CONDITIONS
****************************************
$*******************************************************************************
********
$
*LOAD_SEGMENT_SET
$ APPLYS TRANSMITRAL PRESSURE DIFFERENCE TO LEAFLET1
$ Apply the distributed pressure load over each segment in a segment set.
$ CARD1
$[1] Segment set ID, see *SET_SEGMENT
$[2] Load curve ID (see *DEFINE_CURVE) or function ID (see *DEFINE_FUNCTION)
$[3] Load curve scale factor
$[4] Arrival time for pressure or birth time of pressure
$--------1---------2---------3---------4---------
$-------SSID------LCID------SF--------AT---------
         1         1         0         0         0
*LOAD_SEGMENT_SET
$ APPLYS TRANSMITRAL PRESSURE DIFFERENCE TO LEAFLET2
$ Apply the distributed pressure load over each segment in a segment set.
$ CARD1
$[1] Segment set ID, see *SET_SEGMENT
$[2] Load curve ID (see *DEFINE_CURVE) or function ID (see *DEFINE_FUNCTION)
$[3] Load curve scale factor
$[4] Arrival time for pressure or birth time of pressure
$--------1---------2---------3---------4---------
$-------SSID------LCID------SF--------AT---------
         2         2         0         0         0
$
$*******************************************************************************
********
$*****************************       BOUNDARY       CONDITIONS       &       CONTACT
*****************************
$*******************************************************************************
********
$ Key word *BOUNDARY provides a way of defining imposed motions on boundary nodes.
*BOUNDARY_SPC_SET
$ Define nodal single point constraints for the edge of the leaflets fixed onto the
frame
$ CARD1
$[1] node ID or nodal set ID, see *SET_NODE
$[2] coordinate system ID, see *DEFINE-COORDINATE_SYSTEM
$[3] insert 1 for translational constraint in local x-direction
```

```
$[4] insert 1 for translational constraint in local y-direction
$[5] insert 1 for translational constraint in local z-direction
$[6] insert 1 for rotational constraint about local x-axis
$[7] insert 1 for rotational constraint about local y-axis
$[8] insert 1 for rotational constraint about local z-axis
$--------1---------2---------3---------4---------5---------6---------7---------8-----
----
$-----NID/NSI-----CID-------DOFX------DOFY------DOFZ-----DOFRX-----DOFRY-----DOFRZ---
----
         3        26         1         1         1
*CONTACT_AUTOMATIC_SINGLE_SURFACE
$ Define a contact interface
$ Contact type - AUTOMATIC
$ CARD1
$[1] slave segment, node set ID, par set ID, part ID or shell element set ID. (0 =
all part IDs are included for single surface contact, automatic single surface and
eroding single surface)
$[2] master segment set IC, part set ID, part ID or shell element set ID. (0 = for
single surface contact, automatic single surface, and eroding single surface)
$[3] ID type of SSID (5 - include all for single surface definition)
$[4] ID type of MSID (0 - segment set ID)
$[5] include in contact definition only those slave nodes/segments within box SBOXID
$[6] include in contact definition only those master segments within box MBOXID
$[7] include the slave side in the *DATABASE_NCFORC and the *DATABASE _BINARY_INTFOR
interface force files (1 = slave side forces included)
$[8] include the master side in the *DATABASE_NCFORC and the *DATABASE_BINARY_INTFOR
interface force files (1 = master side forces included)
$--------1---------2---------3---------4---------5---------6---------7---------8-----
----
$-------SSID------MSID-----SSTYP-----MSTYP----SBOXID----MBOXID------SPR-------MPR----
----
         0         0         5         0         0         0         0         0
$ CARD2
$[1] static coefficient of friction if FS is >0 and not equal to 2
$[2] dynamic coefficient of friction
$[3] exponential decay coefficient
$[4] coefficient for viscous friction
$[5] viscous damping coefficient in percent of critical
$[6] small penetration in contact search option
$[7] birth time (contact surface becomes active at this time) (0 = birth time is
inactive, i.e. contact is always active)
$[8] death time (contact surface is deactivated at this time)
$--------1---------2---------3---------4---------5---------6---------7---------8-----
----
$-------FS--------FD--------DC--------VC--------VDC-----PENCHK------BT--------DT-----
----
         0         0         0         0        10         0         0         0
$ CARD3
$[1] scale factor on default slave penalty stiffness when SOFT=0 or SOFT=2, see also
*CONTROL_ CONTACT
$[2] scale factor on default master penalty stiffness when SOFT=0 or SOFT=2, see also
*CONTROL_CONTACT
$[3] optional thickness for slave surface (overrides true thickness)
$[4] optional thickness for master surface (overrides true thickness)
$[5] scale factor for slave surface thickness (scales default thickness)
$[6] scale factor for master surface thickness (scales default thickness)
$[7] coulomb friction scale factor
$[8] viscous friction scale factor
$--------1---------2---------3---------4---------5---------6---------7---------8-----
----
$-------SFS-------SFM-------SST-------MST-------SFST------SFMT------FSF-------VSF----
----
         0         0         0         0         0         0         0         0
$ CARD4
$--------1---------2---------3---------4---------5---------6---------7---------
         2       0.1         0         0         3         5         0         0
$ CARD5
$--------1---------2---------3---------4---------5---------6---------7---------
         0         0         0         0         0         0         0         0
$
$*******************************************************************************
$*****************************  DATABASE  ***************************************

$*******************************************************************************
```

```
$
*DATABASE_EXTENT_BINARY
$ Control to some extent the content of specific output databases
$ CARD1
$[1] number of additional integration point history variables written to the binary
database for solid elements
$[2] number of additional integration point history variables written to the binary
database for both shell and thick shell elements for each integration point, see
NEIPH above
$[3] number of shell integration points written to the binary database, see also
*INTEGRATION_SHELL
$[4] set to 1 to dump strain tensors for solid, shell and thick shell elements for
plotting by LS-PREPOST and ASCII file ELOUT
$[5] flag for including stress tensor in the shell LS-DYNA database
$[6] flag for including the effective plastic strains in the shell LS-DYNA database
$[7] flag for including stress resultants in the shell LS-DYNA database
$[8] flag for including shell internal energy density and thickness in the LS-DYNA
database
$--------1---------2---------3---------4---------5---------6---------7---------8-----
----
$------NEIPH-----NEIPS----MAXINT----STRFLG----SIGFLG----EPSFLG----RLTFLG----ENGFLG---
---
         0         0         5         1
$ CARD2
$[1] orthotropic and anisotropic material stress and strain output in local material
coordinate system for solids, shells and thick shells
$[2] every plot state for "d3plot" database is written to a separate file
$[3] number of beam integration points for output
$[4] data compression to eliminate rigid body data
$[5] output shell hourglass energy density
$[6] output shell element time step, mass or added mass
$[7] material energy write option for D3THDT database
$[8] output solid part ID list containing ale materials
$--------1---------2---------3---------4---------5---------6---------7---------8-----
----
$-----CMPFLG----IEVERP----BEAMIP-----DCOMP------SHGE-----STSSZ----N3THDT---IALEMAT---
----
         1
*DATABASE_BINARY_D3PLOT
$ Options for binary output files with the default names given
$ D3PLOT - Dt for complete output states. See also *DATABASE_EXTENT_BINARY
$ CARD1
$[1] DT - time interval between outputs. CYCL - output interval in time steps (a time
step is a cycle). (1 - i.e. one result for each second of the simulation)
$[2] NR - number of running restart files, RUNRSF, written in a cyclical fashion.
LCDT - optional load curve ID specifying time interval between dumps
$[3] option flag for *DATABASE_BINARY_D3PLOT or D3PART
$[4] DT=ENDTIME/NPLTC applies to D3PLOT and D3PART only. This overrides the DT
specified in the first field
$[5] SET_PART ID for D3PART and D3PLOT only
$--------1---------2---------3---------4---------5---------
$----DT/CYCL---LCDT/NR------BEAM-----NPLTC----PSETID-------
   1.00E-3         0         1         0         0
$ CARD2
$[1] This option applies to the D3PLOT file only. Flag to govern behaviour of the
plot frequency load curve defined by LCDT
$--------1---------
$------IOOPT-------
         0
*DATABASE_BINARY_D3DUMP
$ Options for binary output files with default names
$ D3DUMP - binary output files. Define output frequency in cycles
$ CARD1
$[1] DT - time interval between outputs. CYCL - output interval in time steps (a time
step is a cycle)
$[2] NR - number of running restart files, RUNRSF, written in a cyclical fashion.
LCDT - optional load curve ID specifying time interval between dumps
$[3] option flag for *DATABASE_BINARY_D3PLOT or D3PART
$[4] DT=ENDTIME/NPLTC applies to D3PLOT and D3PART only. This overrides the DT
specified in the first field
$[5] SET_PART ID for D3PART and D3PLOT only
$--------1---------2---------3---------4---------5---------
$----DT/CYCL---LCDT/NR------BEAM-----NPLTC----PSETID-------
     20000
```

```
*DATABASE_BINARY_D3THDT
$ Options for binary output files with default names
$ D3THDT - dt for time history data of element subsets. See *DATABASE_HISTORY
$ CARD1
$[1] DT - time interval between outputs. CYCL - output interval in time steps (a time
step is a cycle)
$--------1---------2---------
$----DT/CYCL---LCDT/NR------
 2.0000E-4
*DATABASE_BINARY_RUNRSF
$ Options for binary output files with default names
$ RUNRSF - binary output restart file. Define output frequency in cycles
$ CARD1
$[1] DT - time interval between outputs. CYCL - output interval in time steps (a time
step is a cycle)
$--------1---------
$----DT/CYCL---
     99999
*DATABASE_BINARY_XTFILE
$ Options for binary output files with default names
$ XTFILE - flag to specify output of extra time  history data to XTFILE at same time
as D3THDT file. The following card is left black for this option
$ CARD1
$[1] DT - time interval between outputs. CYCL - output interval in time steps (a time
step is a cycle)
$--------1---------2---------3---------4---------
$----DT/CYCL---LCDT/NR------BEAM-----NPLTC-------
     0.000         0         0         0
*DATABASE_GLSTAT
$ Global data. Always obtained if SSSTAT file is activated
  0.000682         0         0         0         0         0                   0
*END
```

Appendix E

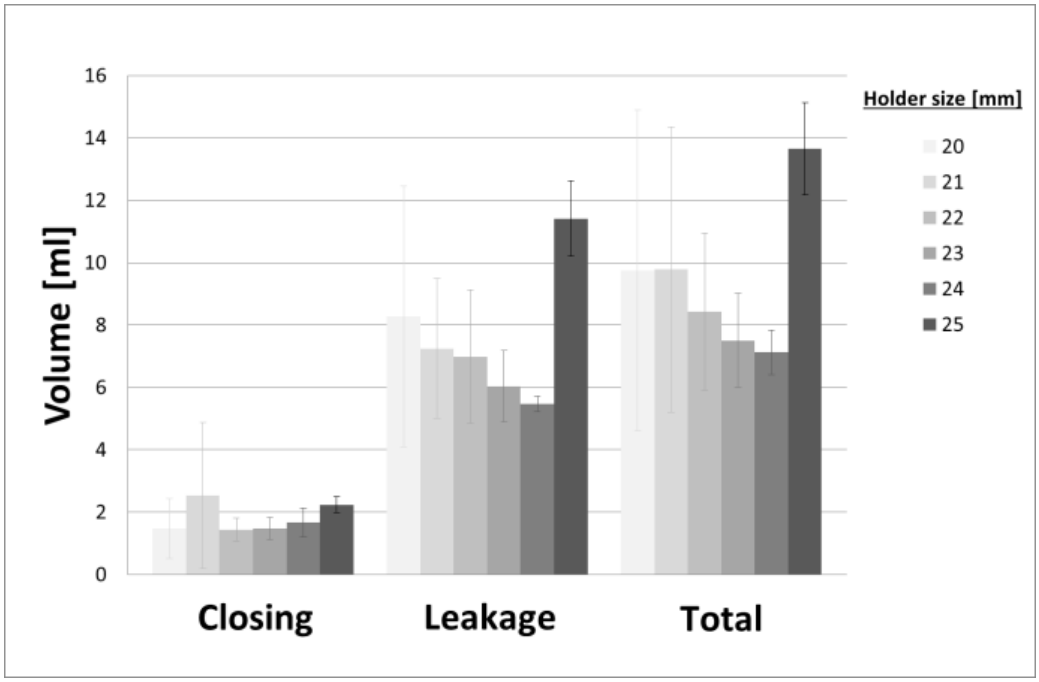

Figure E.1: Reverse flow volumes in millilitres; average of 3 UCL transcatheter mitral valves in holder sizes 20-25 mm at a cardiac output of 5 lpm.

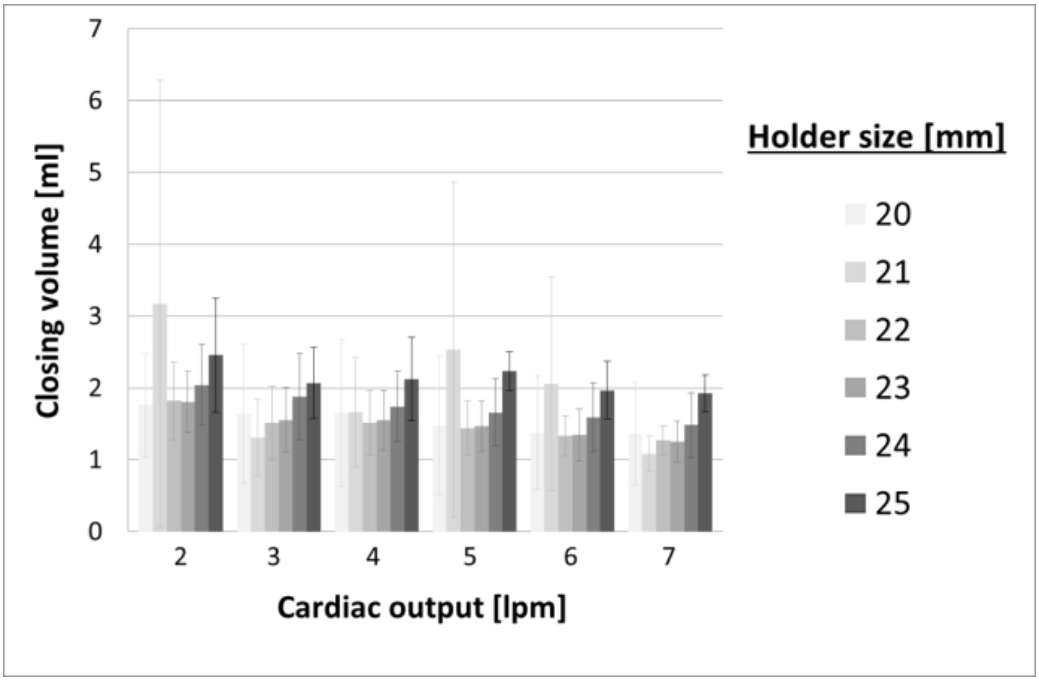

Figure E.2: Closing volumes for the UCL transcatheter mitral valve at six different cardiac outputs in holder sizes 20-25 mm, average of three prototypes.

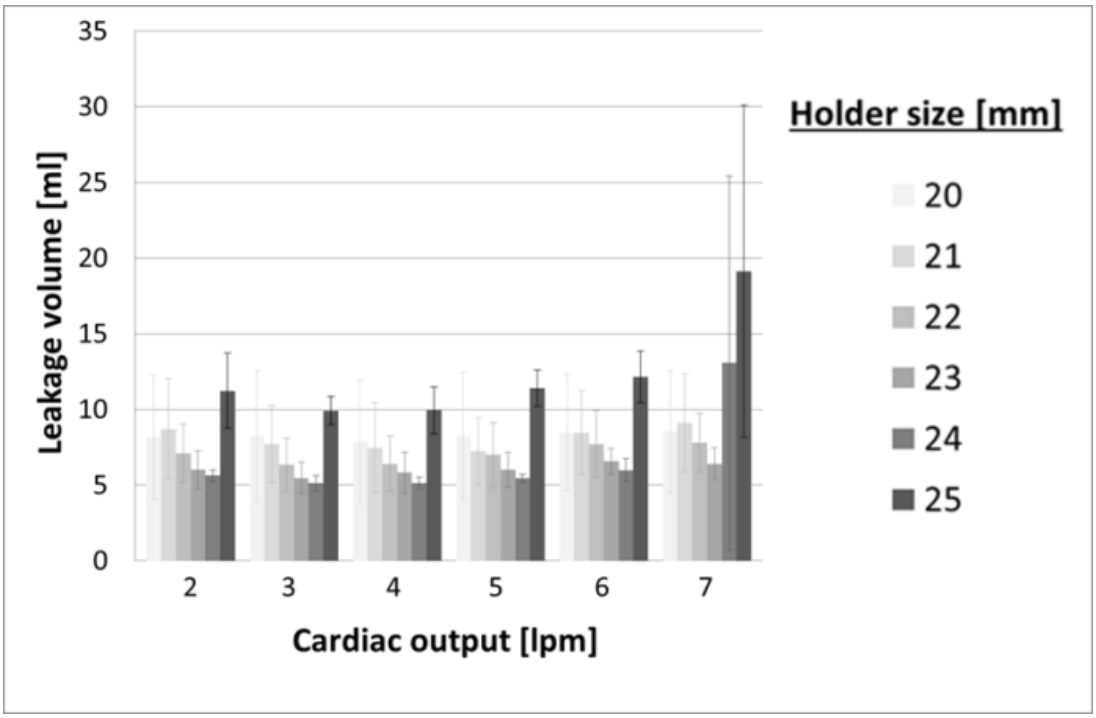

Figure E.3: Leakage volume for the UCL transcatheter mitral valve at six different cardiac outputs in holder sizes 20-25 mm, average of three prototypes.

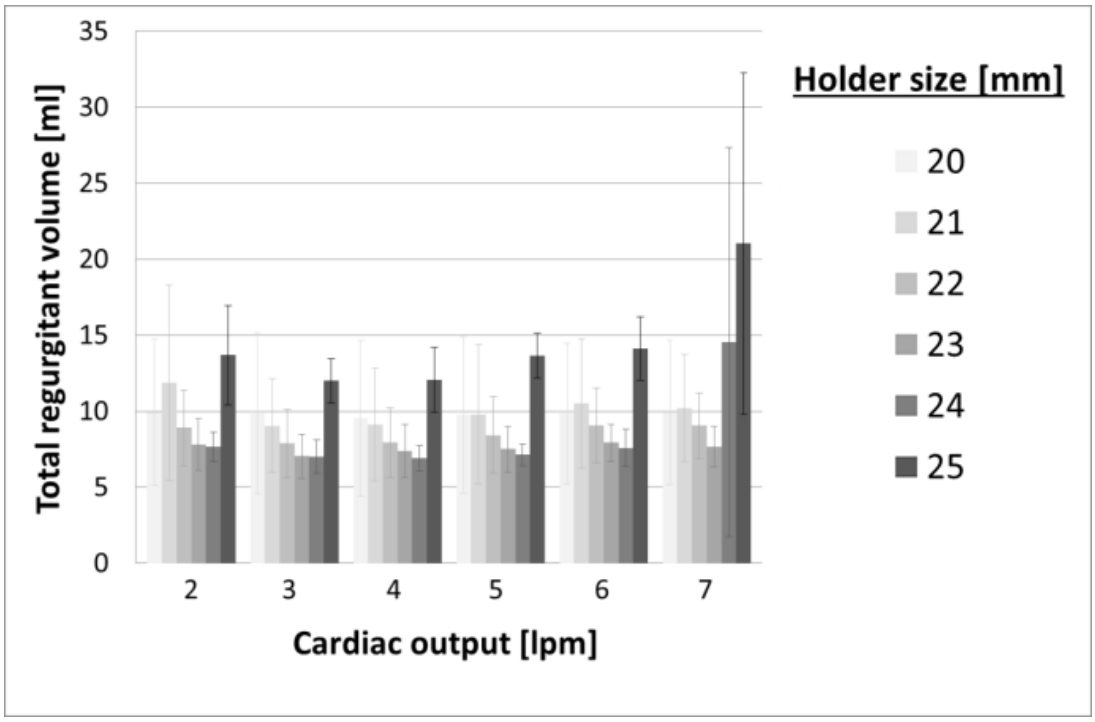

Figure E.4: Total regurgitant volume for the UCL transcatheter mitral valve at six different cardiac outputs in holder sizes 20-25 mm, average of three prototypes.

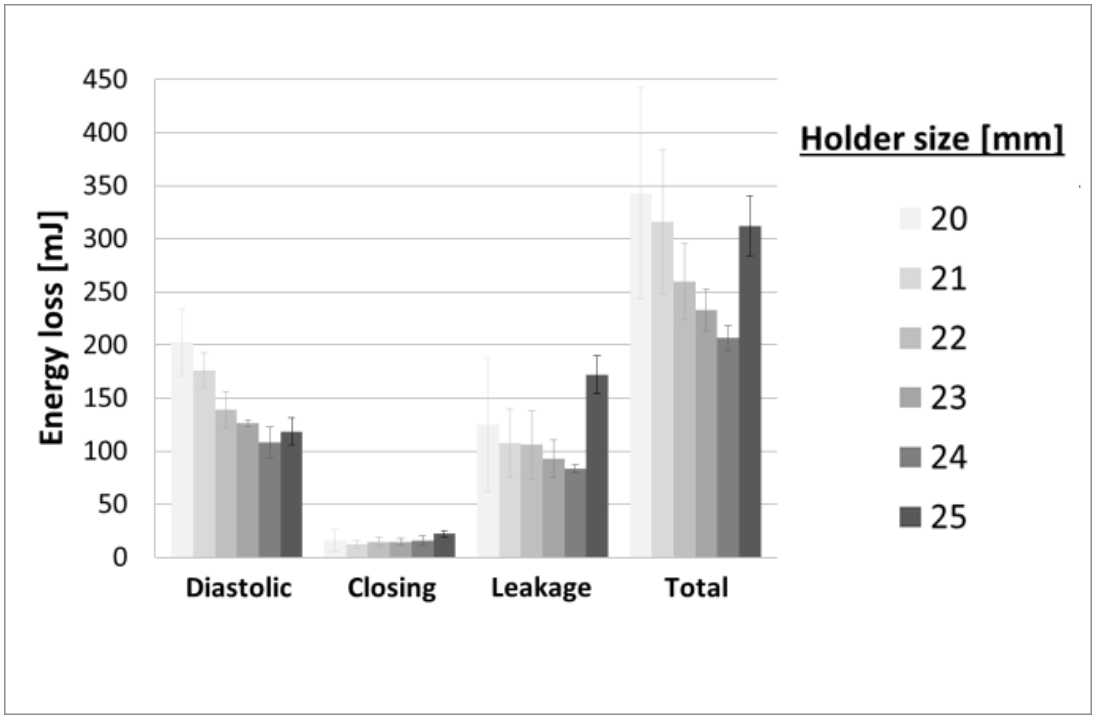

Figure E.5: Energy losses in millijoules; average of 3 UCL transcatheter mitral valves in holder sizes 20-25 mm at a cardiac output of 5 lpm.

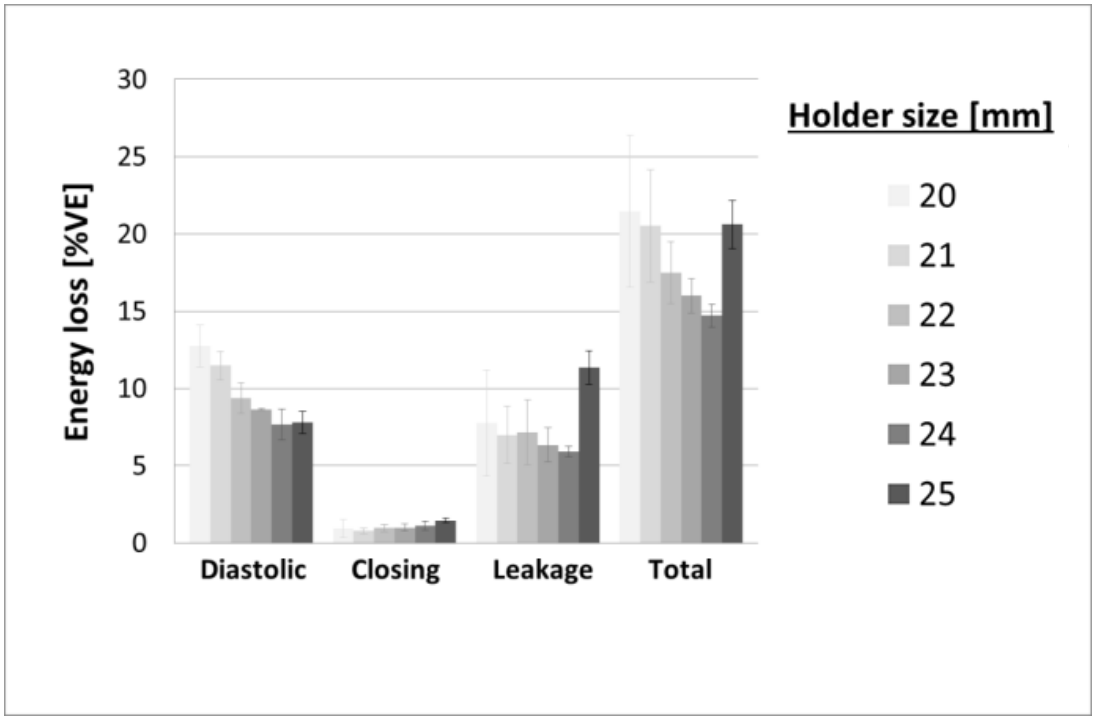

Figure E.6: Energy losses as a percentage of ventricular energy; average of 3 UCL transcatheter mitral valves in holder sizes 20-25 mm at a cardiac output of 5 lpm.

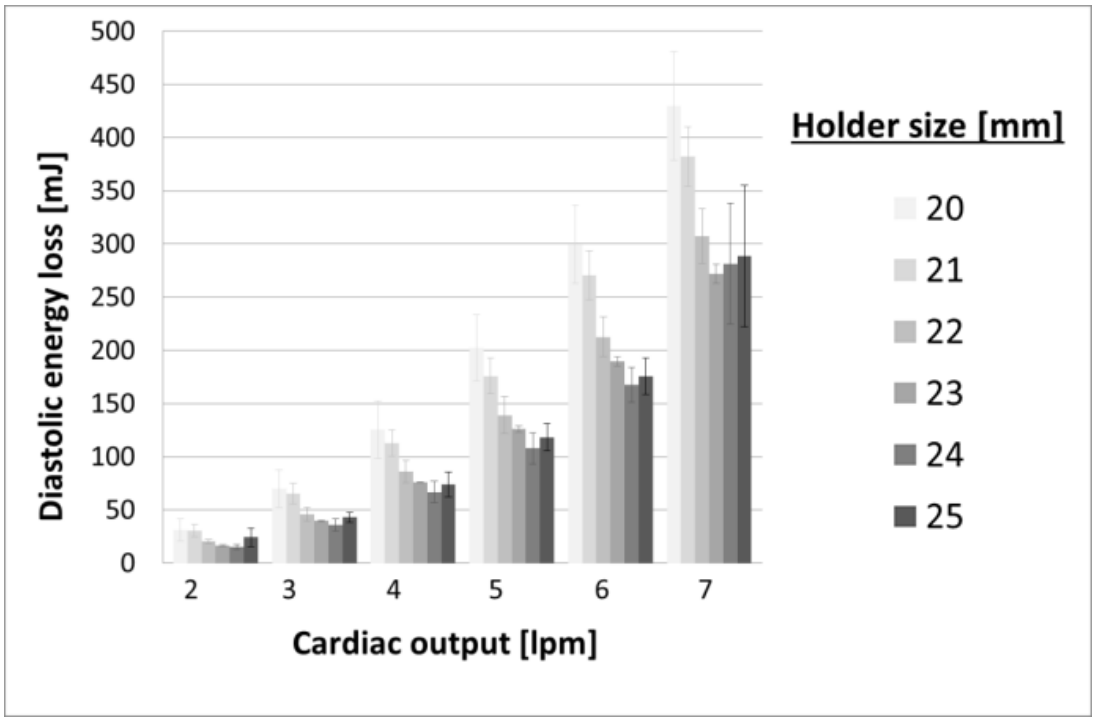

Figure E.7: Diastolic energy losses in millijoules for the UCL transcatheter mitral valve at six different cardiac outputs in holder sizes 20-25 mm, average of three prototypes.

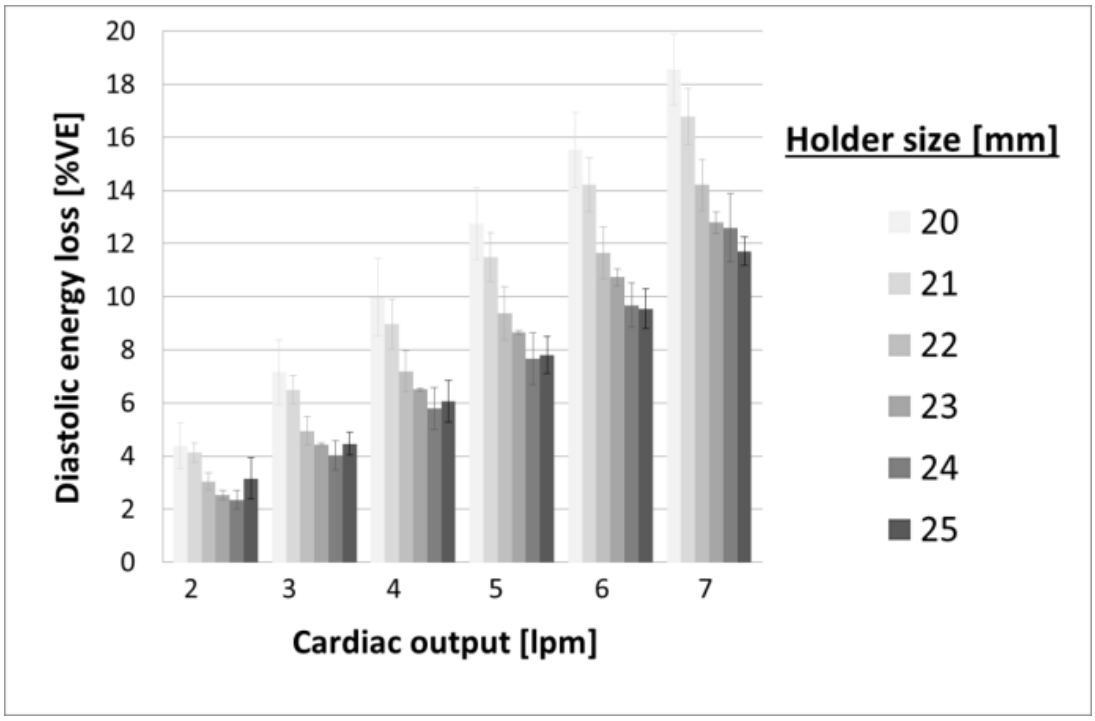

Figure E.8: Diastolic energy losses as a percentage of ventricular energy for the UCL transcatheter mitral valve at six different cardiac outputs in holder sizes 20-25 mm, average of three prototypes.

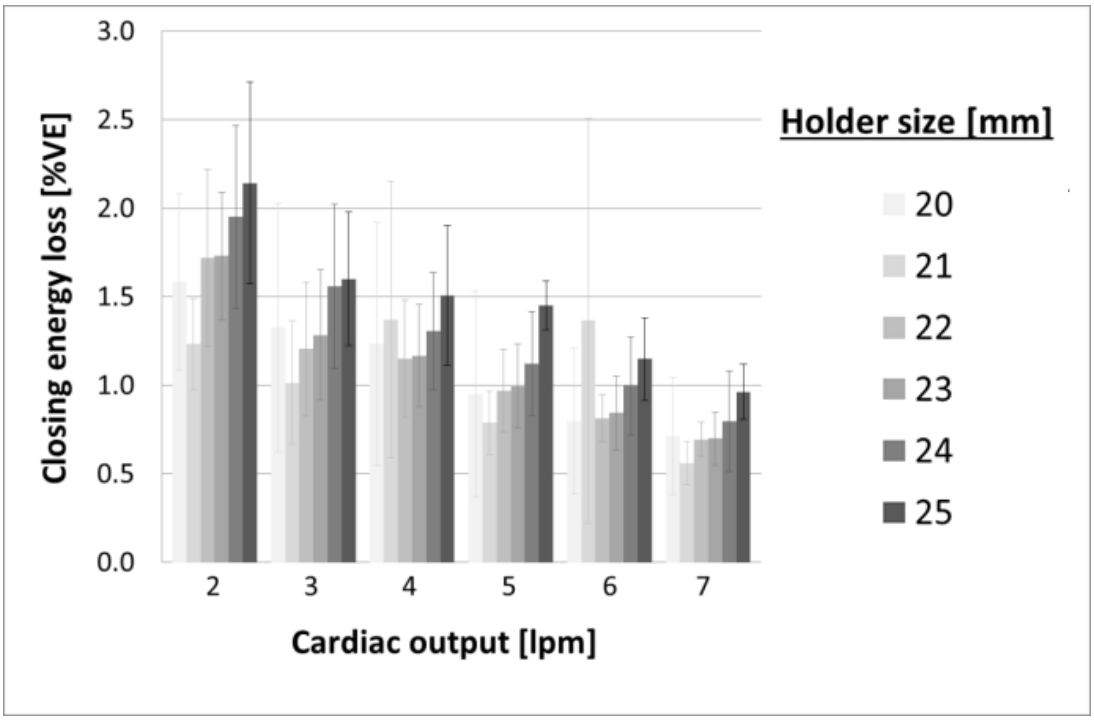

Figure E.9: Closing energy losses as a percentage of ventricular energy for the UCL transcatheter mitral valve at six different cardiac outputs in holder sizes 20-25 mm, average of three prototypes.

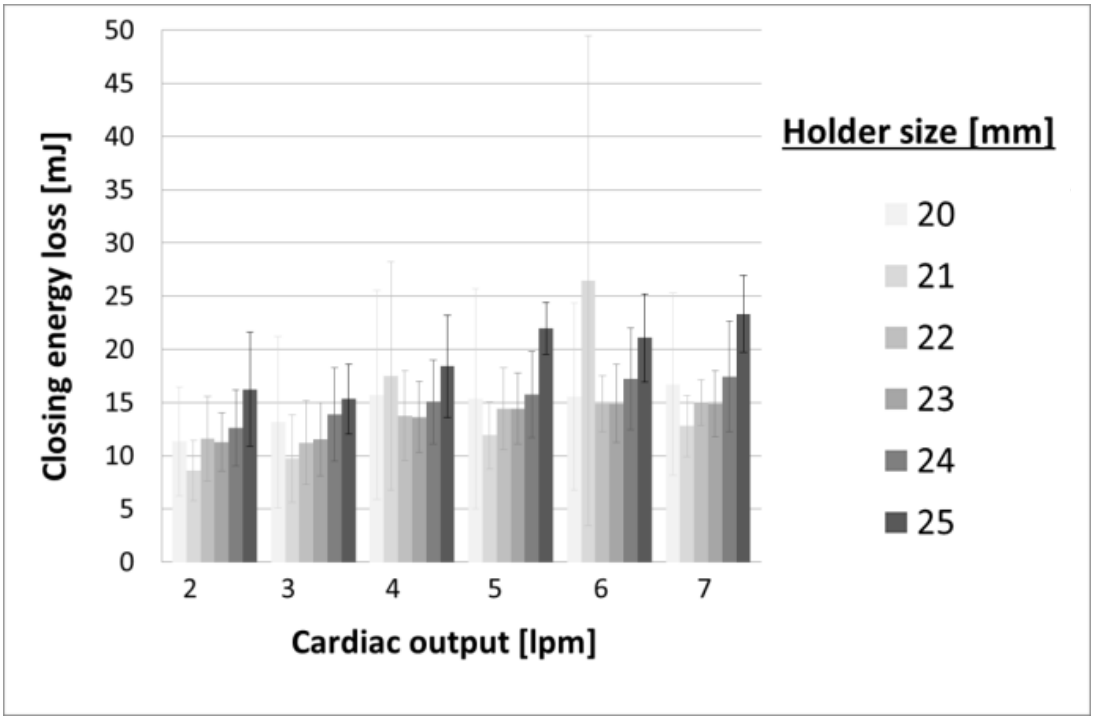

Figure E.10: Closing energy losses in millijoules for the UCL transcatheter mitral valve at six different cardiac outputs in holder sizes 20-25 mm, average of three prototypes.

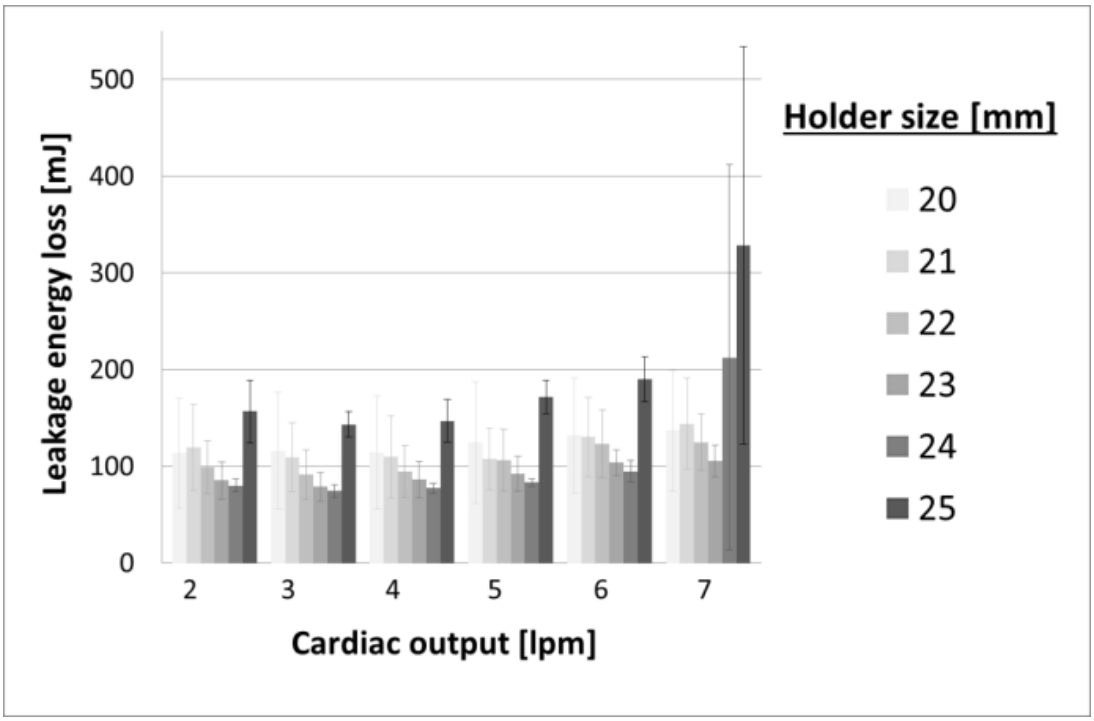

Figure E.113: Leakage energy losses in millijoules for the UCL transcatheter mitral valve at six different cardiac outputs in holder sizes 20-25 mm, average of three prototypes.

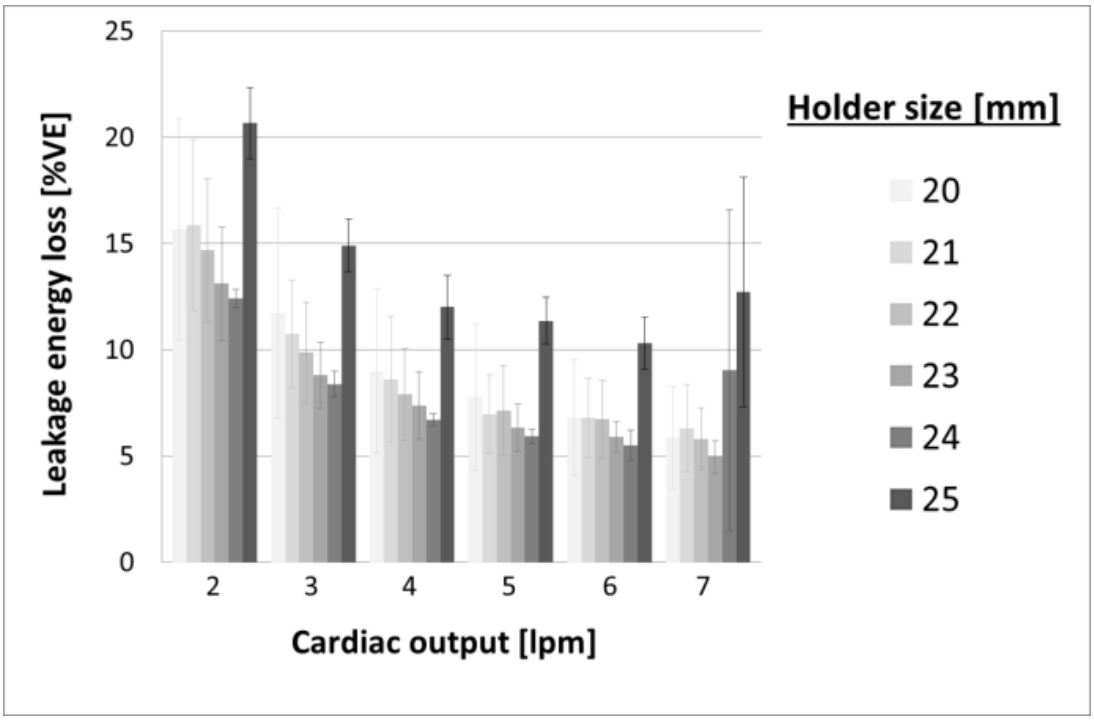

Figure E.12: Leakage energy losses as a percentage of ventricular energy for the UCL transcatheter mitral valve at six different cardiac outputs in holder sizes 20-25 mm, average of three prototypes.

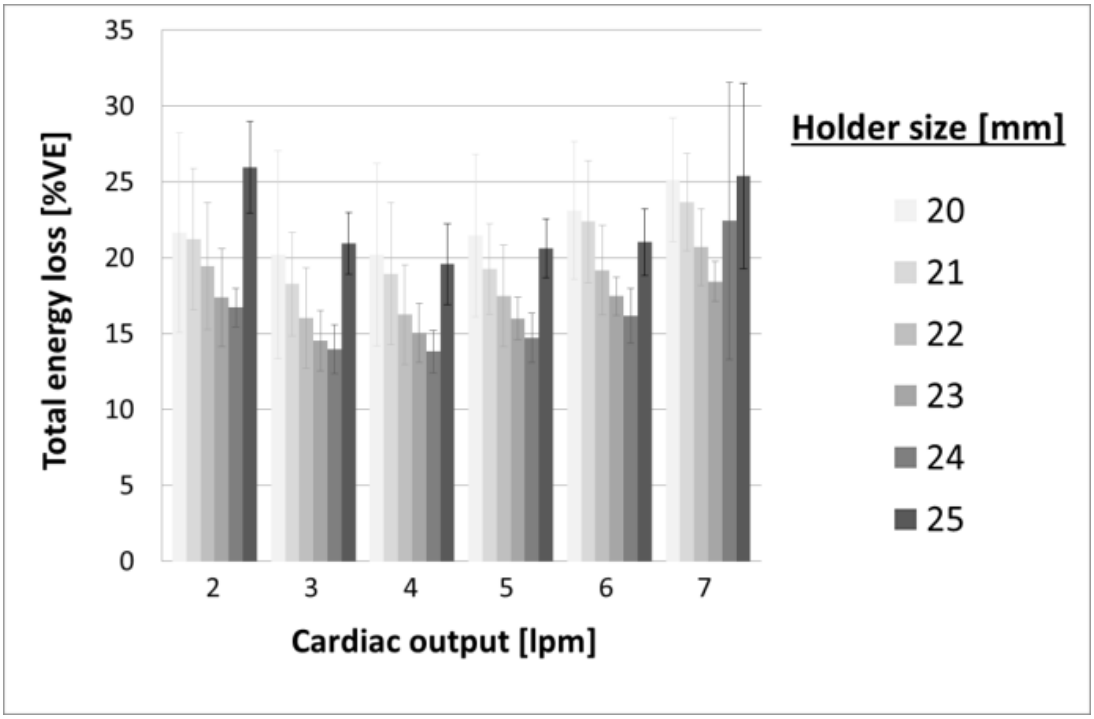

Figure E.13: Total energy losses as a percentage of ventricular energy for the UCL transcatheter mitral valve at six different cardiac outputs in holder sizes 20-25 mm, average of three prototypes.

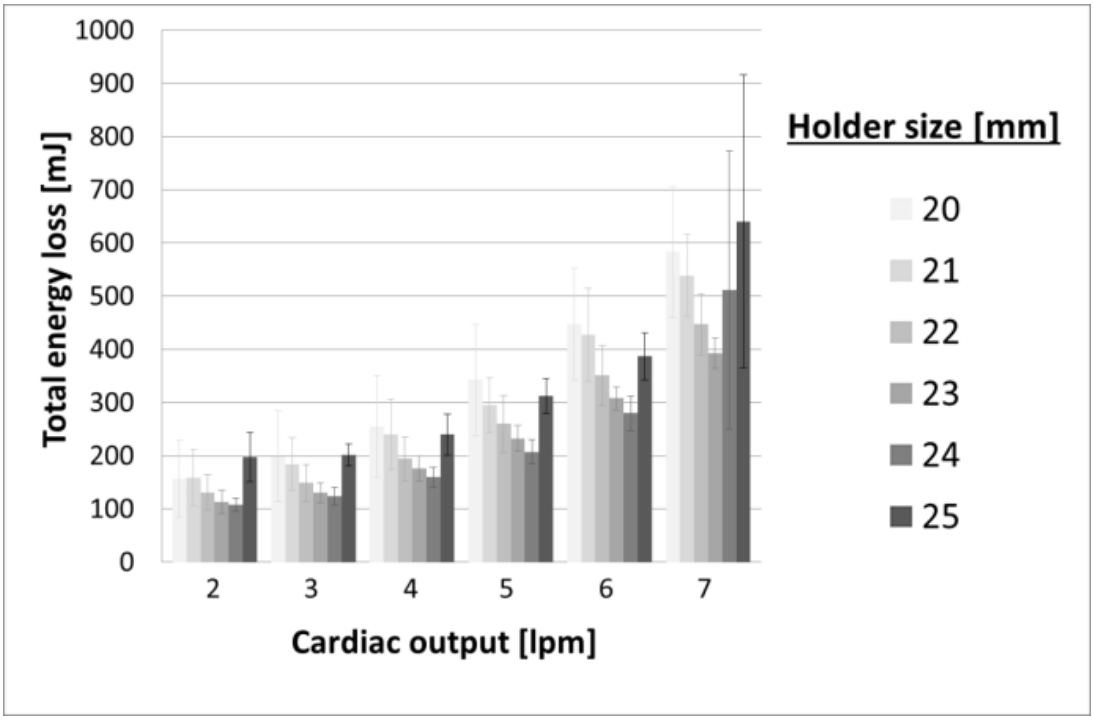

Figure E.14: Total energy losses in millijoules for the UCL transcatheter mitral valve at six different cardiac outputs in holder sizes 20-25 mm, average of three prototypes.

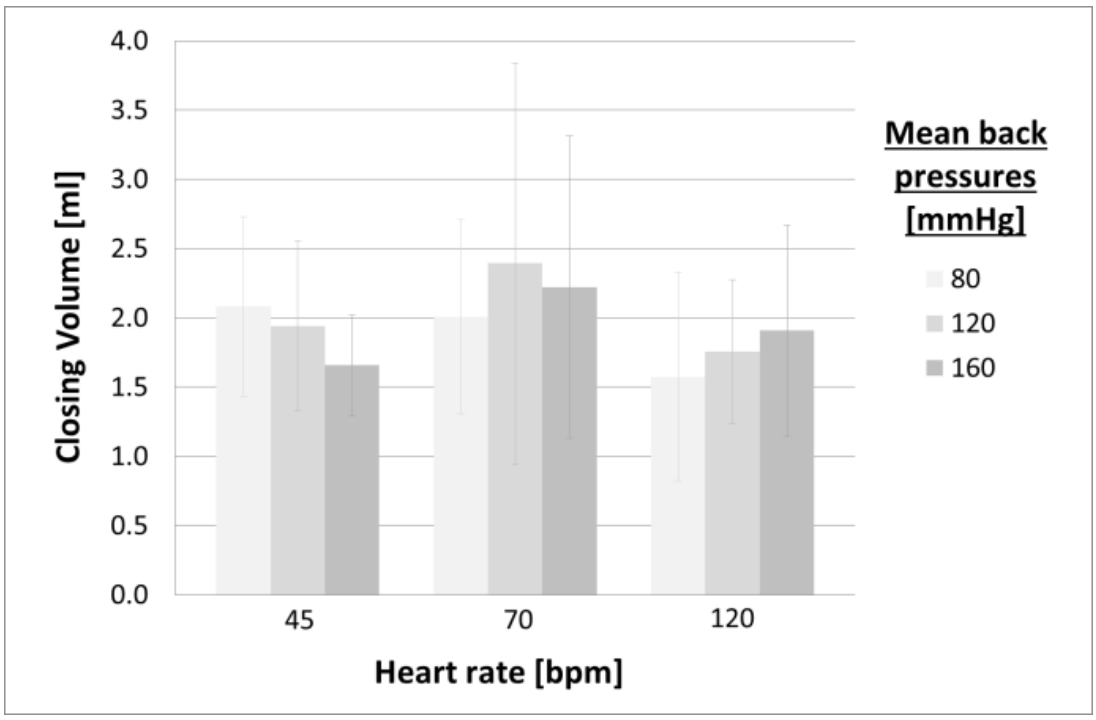

Figure E.15: Closing volume for three mean back pressures for three simulated heart rates, average of three UCL transcatheter mitral valve prototypes in a 24 mm holder.

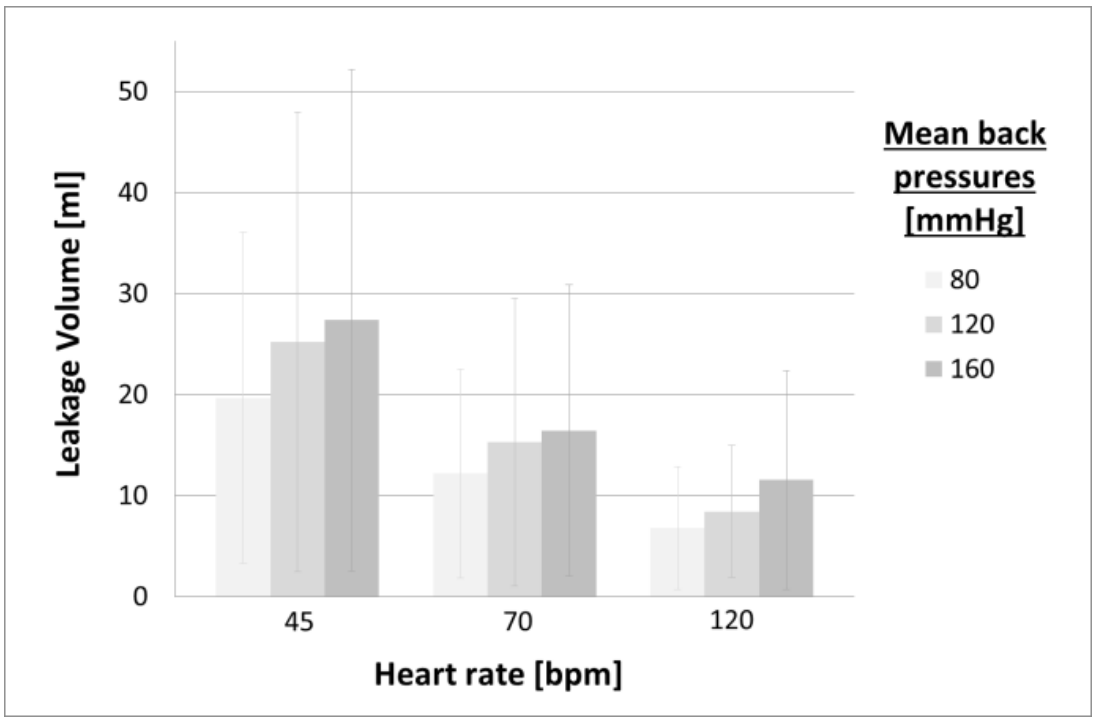

Figure E.16: Leakage volume for three mean back pressures for three simulated heart rates, average of three UCL transcatheter mitral valve prototypes in a 24 mm holder.

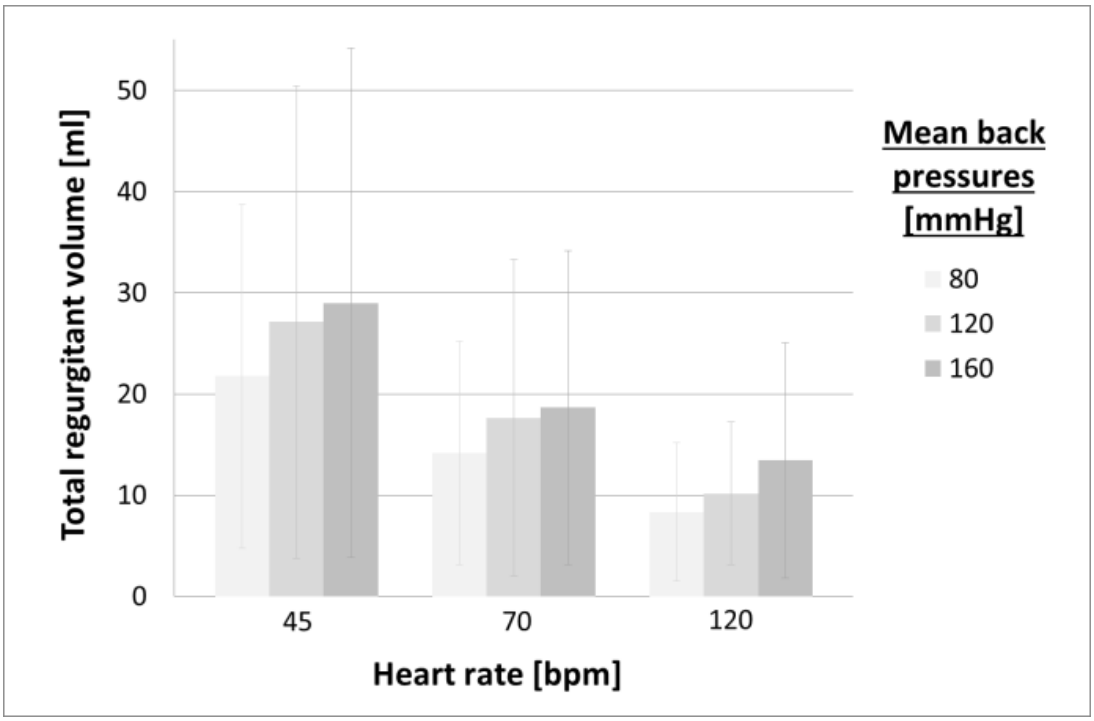

Figure E.17: Total regurgitant volumes for three mean back pressures for three simulated heart rates, average of three UCL transcatheter mitral valve prototypes in a 24 mm holder.

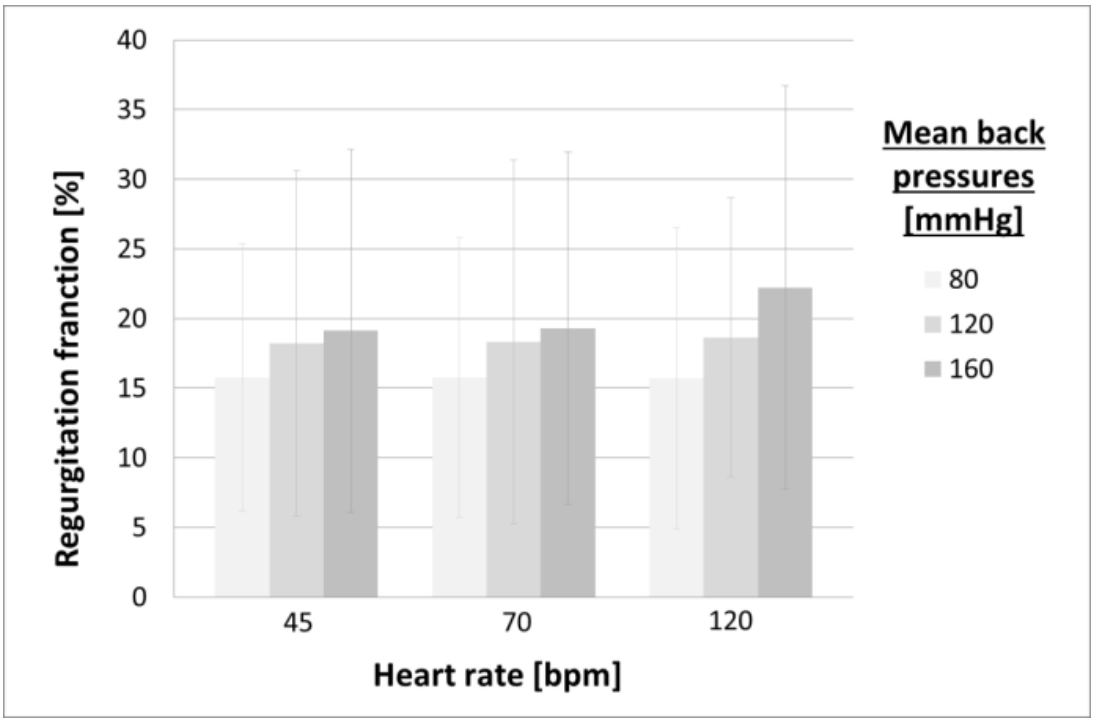

Figure E.18: Regurgitation fraction for three mean back pressures for three simulated heart rates, average of three UCL transcatheter mitral valve prototypes in a 24 mm holder.

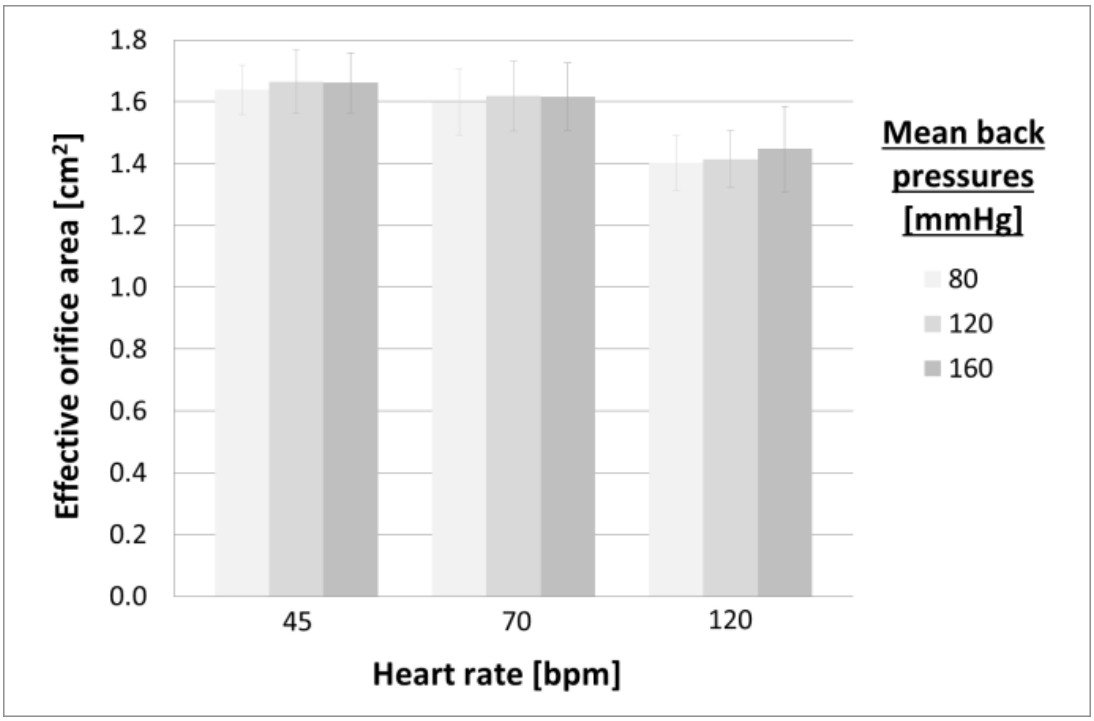

Figure E.19: Effective orifice area for three different mean back pressures for three simulated heart rates, average of three UCL transcatheter mitral valve prototypes in a 24 mm holder.

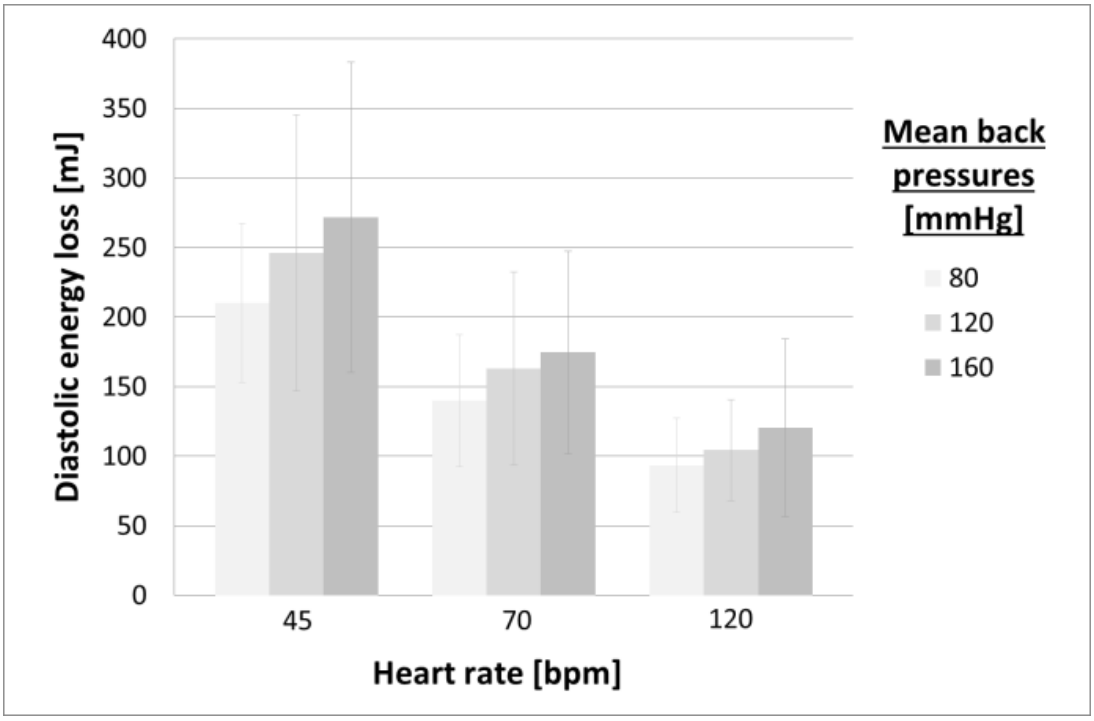

Figure E.204: Diastolic energy loss in millijoules for three mean back pressures for three simulated heart rates, average of three UCL transcatheter mitral valve prototypes in a 24 mm holder.

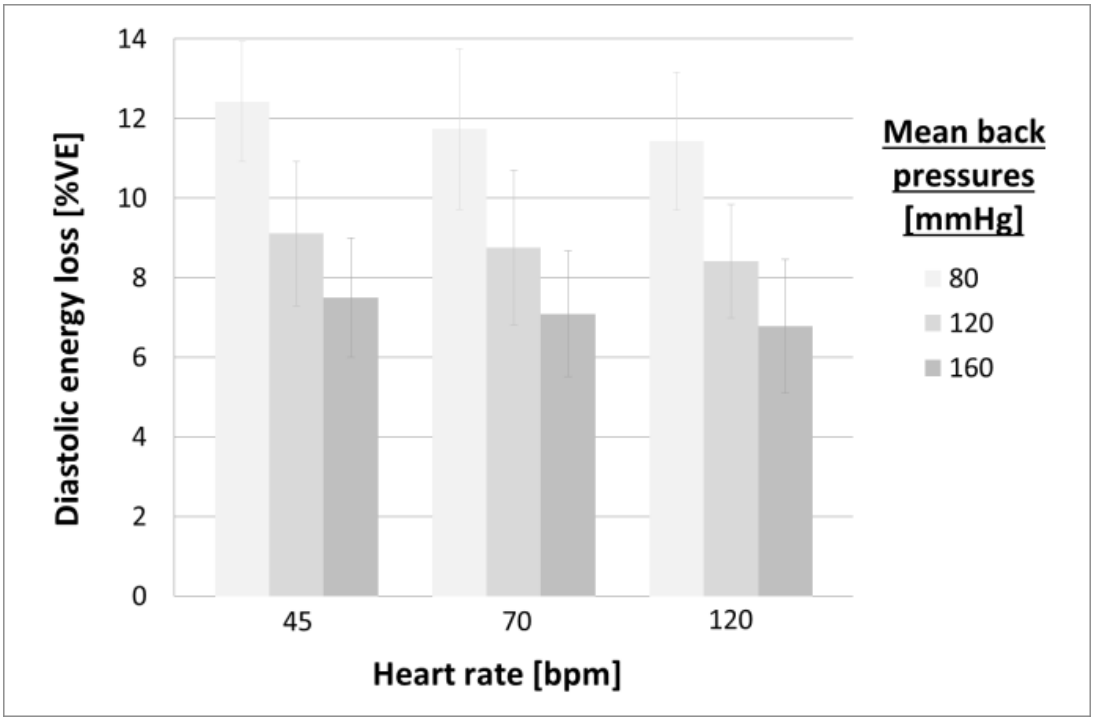

Figure E.21: Diastolic energy loss as a percentage of ventricular energy for three mean back pressures for three simulated heart rates, average of three UCL transcatheter mitral valve prototypes in a 24 mm holder.

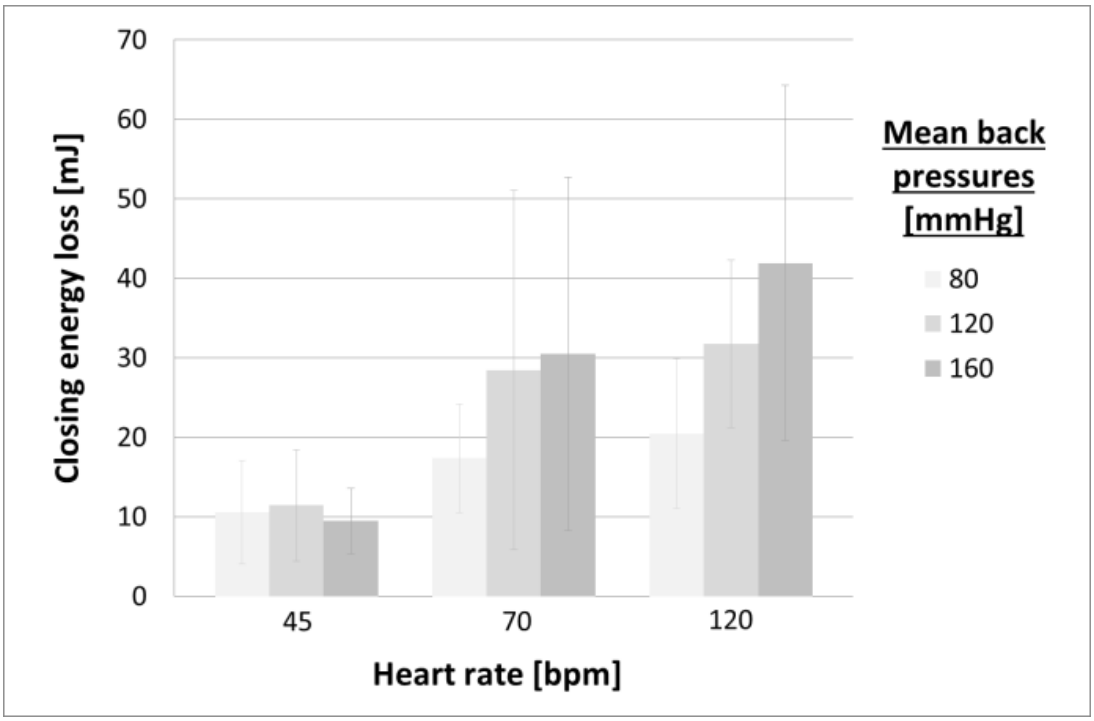

Figure E.22: Closing energy loss in millijoules for three mean back pressures for three simulated heart rates, average of three UCL transcatheter mitral valve prototypes in a 24 mm holder.

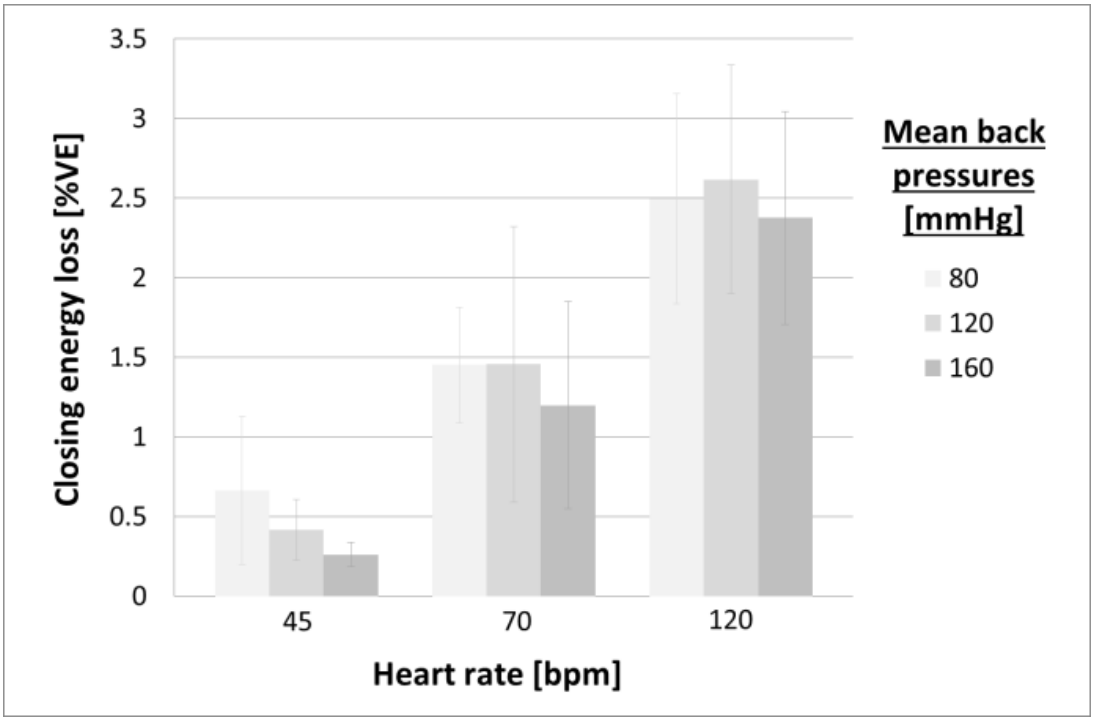

Figure E.23: Closing energy loss as a percentage of ventricular energy for three mean back pressures for three simulated heart rates, average of three UCL transcatheter mitral valve prototypes in a 24 mm holder.

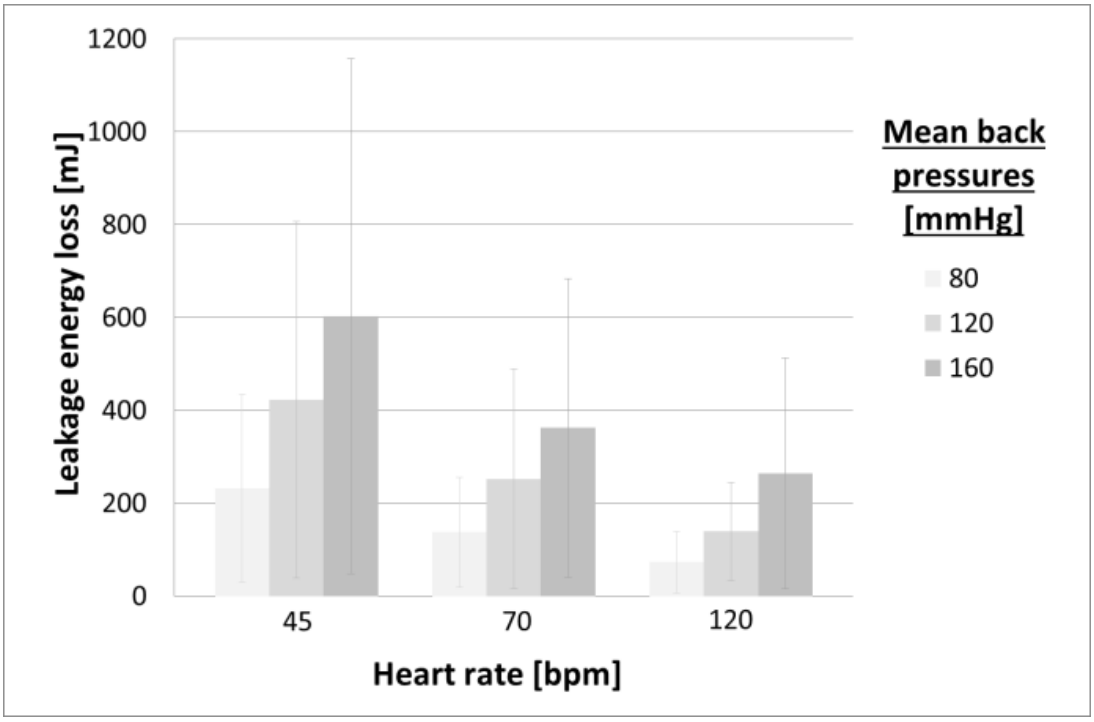

Figure E.24: Leakage energy loss in millijoules for three mean back pressures for three simulated heart rates, average of three UCL transcatheter mitral valve prototypes in a 24 mm holder.

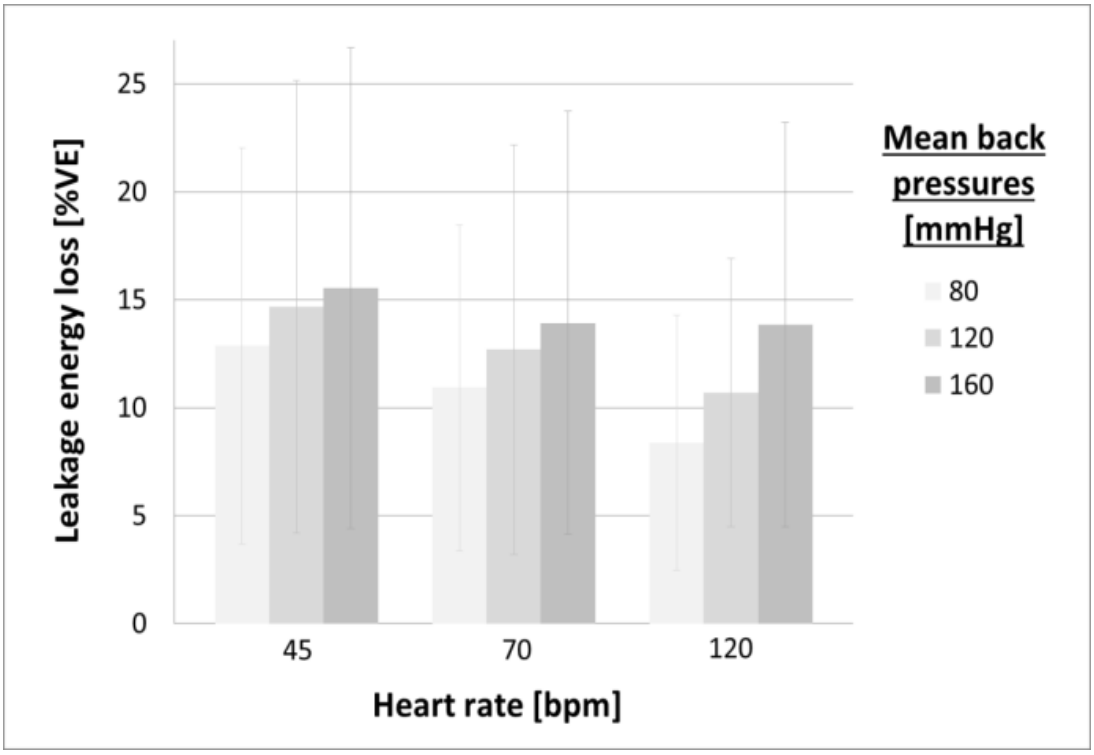

Figure E.255: Leakage energy loss as a percentage of ventricular energy for three mean back pressures for three simulated heart rates, average of three UCL transcatheter mitral valve prototypes in a 24 mm holder.

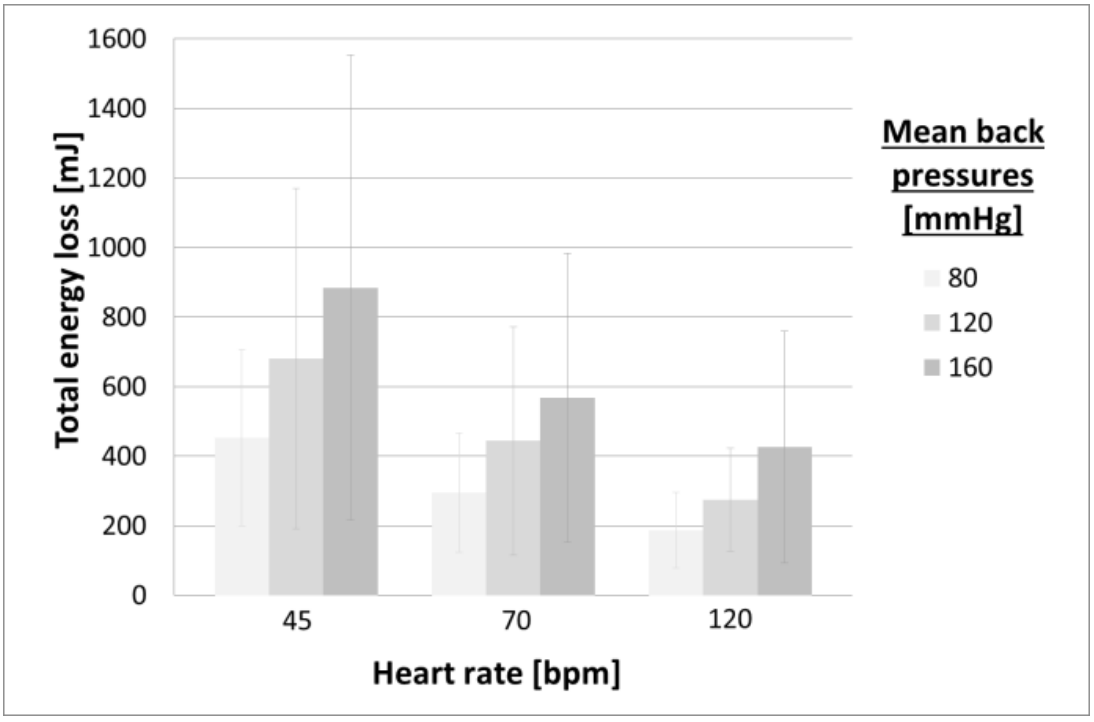

Figure E.26: Total energy loss in millijoules for three mean back pressures for three simulated heart rates, average of three UCL transcatheter mitral valve prototypes in a 24

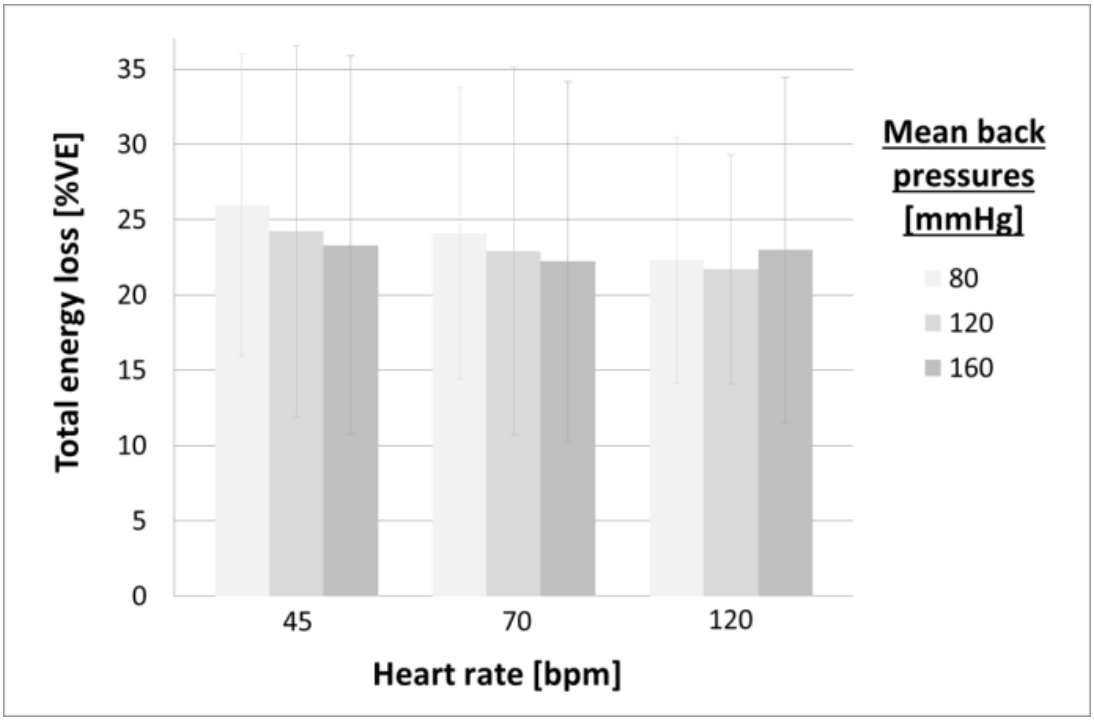

Figure E.27: Total energy loss as a percentage of ventricular energy for three mean back pressures for three simulated heart rates, average of three UCL transcatheter mitral valve